UNIVERSITÉ DE GRENOBLE

# THÈSE

Pour obtenir le grade de

## DOCTEUR DE L'UNIVERSITÉ DE GRENOBLE

Spécialité : **Sciences de la Terre, de l'Univers et de l'Environnement**

Arrêté ministériel : 7 août 2006


Présentée par

## Alaa HAMZE

Thèse dirigée par **Philippe GUEGUEN** et
codirigée par **Laurent BAILLET**

préparée au sein du **Laboratoire ISTerre (Institut des Sciences de la Terre)**
dans **l'École Doctorale Terre Univers Environnement**


# Détection et localisation de changements dans une structure : application numérique et expérimentale.

Thèse soutenue publiquement le **« 24 mai 2013 »**,
devant le jury composé de :

**Monsieur, Philippe, GUEGUEN**
Directeur de Recherche, IFSTTAR / ISTerre, Directeur de thèse
**Monsieur, Laurent, BAILLET**
Professeur, UJF / ISTerre, Co-directeur de thèse
**Monsieur, Jean-François, SEMBLAT**
Ingénieur TPE, Prof Associé Ecole Polytechnique, IFSTTAR, Rapporteur
**Monsieur, Georges, JACQUET-RICHARDET**
Professeur, INSA / Lyon, Rapporteur
**Monsieur, Denis, JONGMANS**
Professeur, UJF / ISTerre, Président
**Monsieur, Jacques, HARB**
Professeur Associé, Université Notre-Dame / Liban, Examinateur

# Résumé

La détection d'endommagements et de changements des propriétés élastiques dans des structures, utilisant les variations des paramètres dynamiques, fait l'objet d'une attention particulière depuis plusieurs années dans les domaines du génie mécanique et du génie civil.

Le principe général repose sur le fait que la variation des propriétés physiques (e.g. rigidité, masse, module d'Young, conditions aux limites) entraîne une variation des caractéristiques dynamiques de la structure (e.g. fréquences de résonance, amortissements modaux et déformées modales).

La présence d'endommagement provoque ainsi une diminution de la rigidité de la structure, c'est-à-dire une augmentation de sa flexibilité et de son amortissement que l'on retrouve dans la forme des modes et les valeurs des fréquences. Utilisant le changement de ces informations entre un état sain et un état endommagé, plusieurs méthodes non-destructives ont été proposées dans la littérature afin d'identifier et de localiser ces endommagements.

Ces pratiques et ces activités sont d'une importance considérable puisqu'elles permettent en premier lieu d'anticiper et donc d'éviter des ruptures dans les structures, toujours catastrophiques, et plus généralement de mettre en place des plans de maintenances prédictives, en lien avec le suivi sur le long terme de leur intégrité (Structural Health Monitoring). Ces méthodes de surveillance se popularisent également du fait de la réduction des coûts des instrumentations, liés à l'apparition de nouveaux équipements à bas coût, ayant des performances satisfaisantes.

L'objectif de ce travail est de tester les différentes solutions permettant la détection, la localisation et la quantification des changements dans des structures simples. Plusieurs méthodes ont été testées et une approche nouvelle a été proposée basée sur l'utilisation de la méthode des perturbations. Trois approches ont été suivies: une modélisation par éléments finis (analyse modale), une simulation numériques par éléments finis (analyse temporelle) et enfin des analyses expérimentales sur des poutres en Plexiglas au laboratoire, les trois volets de ce travail ayant permis de tester la sensibilité des méthodes non-destructives (NDE) globales et locales pour la détection et la localisation. Les changements ont été associés à une variation locale du module de Young (E), numériquement pour les solutions numériques et par chauffage local sur des sections de la poutre dans le volet expérimental. Dans tous les cas, nous sommes en situations réelles afin de proposer l'identification des caractéristiques modales par des méthodes opérationnelles (Operative Modal Analysis) telles que la méthode du décrément aléatoire et la méthode de décomposition dans le domaine fréquentiel (Frequency Domain Decomposition).

Les résultats d'identification ont montré une très bonne corrélation entre les valeurs numériques et les valeurs expérimentales obtenues : fréquences de résonance et déformés modale. Pour identifier l'endommagement, les méthodes de localisation basées sur la courbure des déformées propres, la matrice de flexibilité, la courbure de flexibilité et enfin sur la méthode d'inversion des modes ont été employées. D'après les résultats obtenus, la méthode d'inversion se montre efficace dans le cas de variations modales faibles et transitoires, alors que la méthode de la courbure de flexibilité donne généralement de bons résultats et apparait robuste lorsque les variations sont plus prononcées.

**Mots clés :** Eléments finis, analyse modale, analyse temporelle, vibrations ambiantes, méthodes non-destructives (NDE), détection, localisation, quantification, expériences, endommagement.

# Abstract

The detection of damage and changes in elastic properties of structures, using the variation of dynamic parameters, has been the subject of special attention for several years in the fields of mechanical and civil engineering. The general principle is based on the fact that the variation of physical properties (e.g. stiffness, mass, Young's modulus, boundary conditions) leads to a change in the dynamic characteristics of structures (e.g. resonance frequencies, modal damping and mode shapes).

The presence of damage causes a decrease in the rigidity of structures, which give rise to an increase in flexibility and damping, which can be seen in mode shapes and frequency values. Using the change of this information between a healthy and damaged condition, several non-destructive methods have been proposed in the literature in order to identify and locate the damage.

These practices and activities are of considerable importance. They allow us to anticipate and avoid breaks in structures, which are always catastrophic, and more generally, they allow us to establish the plans of a predictive maintenance, along with monitoring of the long-term of integrity (Structural Health monitoring). These monitoring methods are equally us popular because of the low cost of instrumentation, related to the appearance of new equipment at low cost, having the satisfactory performance.

The objective of this work is to test different solutions, allow for detection, localization and quantification of changes in simple structures. Several methods have been tested and a new approach is proposed based on the use of the perturbation method. Three approaches are followed: finite element modeling (modal analysis), finite element numerical simulation (temporal analysis), and finally, experimental analysis of a Plexiglas beam in the laboratory. These three scopes of work have allowed us to test the sensitivity of global and local non-destructive methods (NDE) for detection and localization of damage.

Changes associated with a local variation of Young's modulus (E) are tested numerically in modal and temporal analysis, and shown experimentally in local heating on the sections of beam. In all cases, we are in real life situations, where we identify modal characteristics by operational methods (Operative Modal Analysis) such as the random decrement technique and the method of decomposition in the frequency domain (Frequency Domain Decomposition).

The results show a very good correlation between the numerical and experimental values obtained: resonant frequencies and mode shapes. For identifying damage, localization methods based on the curvature of mode shape, flexibility matrix, curvature of flexibility, and finally on the method of inversion of modes are employed. According to the results, the method of inversion proves effective in the case where modal variation is low and transient, whereas, the curvature of flexibility (ULS method) usually gives good results and appears robust when the changes are more pronounced.

**Keywords:** Finite element, modal analysis, time analysis, ambient vibrations, methods non-destructive (NDE), detection, localization, quantification, experiences, damage.

*À ma femme Mona HAMZE*

*À ma mère et mon père*

# Remerciements

***Je voudrais tout d'abord exprimer ma gratitude envers la région Rhône Alpes. C'est assez rare, mais c'est grâce à elle que j'ai pu étudier pendant les trois ans dans des conditions privilégiées.***

***Je voudrais remercier tous ceux qui m'ont aidé à mener ce travail de thèse. Je tiens à remercier chaleureusement les membres du jury de thèse, Jean-François SEMBLAT, Georges JACQUET-RICHARDET, Denis JONGMANS et Jacques HARB qui ont donné de leur temps pour évaluer cette thèse.***

***Je tiens à remercier particulièrement mes encadrant de thèse : Philippe GUEGUEN et Laurent BAILLET, pour leur temps, leurs contributions et de m'avoir encadré durant tout ce travail de recherche.***

***Je voudrais aussi remercier Philippe ROUX pour ces idées et sa participation active. Je pense aux personnels techniques du laboratoire : Adeline RICHARD et Benjamin VIAL pour ses conseils et son soutien matériel.***

***Je remercie également le directeur de laboratoire Philippe CARDIN, le directeur de l'équipe risque Pierre-Yves BARD et le directeur de l'école doctorale Jean BRAUN et le secrétaire de l'école doctorale Christine BIGOT pour ces conseils pédagogiques.***

***Merci à Vincent CLERC, Julie BECASSE, EYMARD, Thomas PLANES, Mathieu PERRAULT, Pierre BOTTELIN, Johanes CHANDRA, Javed IQBAL, Boumediene DERRAS, Guénolé MAINSANT, Abbas SENOUCI, Christelle SALAMEH, Nancy SALLOUM, Sophie BEAUPRETRE, Walid KASSAB, Elias EL HABER et enfin Rachid ALOUANI.***

***Merci à l'accueil chaleureuse par l'ISTerre surtout l'ambiance familiale et amicale.***

***Un grand merci à Mona HAMZE, ma femme, pour sa patience et à qui je dédie ce travail.***

***Mes sincères remerciements s'adressent également à mon beau père, ma belle mère, à Ali FARHAT et à Anji el ZEIN.***

***Enfin, je dédie ce manuscrit à mes parents, ma femme, mon beau frère (Abou Hassan KRAIKER), mes frères et sœurs.***

# Table des matières

**CHAPITRE I** ..... **1**

INTRODUCTION GENERALE ..... 1

**CHAPITRE II** ..... **10**

METHODS FOR DETECTION AND LOCALIZATION OF CHANGES ..... 10
II.1 INTRODUCTION ..... 11
II.2 THEORETICAL SOLUTION OF THE CANTILEVER BEAM ..... 12
II.3 EFFECT OF CHANGES ON THE MODAL PARAMETERS ..... 16
II.4-GLOBAL METHODS FOR DETECTION ..... 17
*II.4.1 Frequency variation ..... 17*
*II.4.2 Modal Assurance Criterion (MAC) ..... 22*
II.5-LOCAL METHODS FOR DETECTION ..... 23
*II.5.1 - Methods Based on Mode Shape Curvature ..... 23*
*II.5.1.1 - Mode Shape Curvature Method (MSC) ..... 23*
*II.5.1.2 - Mode Shape Curvature Squared Method (MSCS) ..... 25*
*II.5.2 - Methods Based on Changes in Flexibility ..... 25*
*II.5.2.1 - Change in flexibility method (CIF) ..... 26*
*II.5.2.2 - Change in uniform load surface curvature (ULS) ..... 27*

**CHAPITRE III** ..... **29**

DETECTION AND LOCALIZATION OF CHANGES: THE EFFICIENCY OF METHODS USING EIGENMODES MODELING ..... 29
III.1-INTRODUCTION ..... 30
III.2-THE MODELS ..... 30
III.3- COMPARATIVE STUDY OF DAMAGE DETECTION ALGORITHM FOR BEAMS ..... 33
*III.3.1. – Global methods for detecting changes ..... 33*
*III.3.2. – Local methods for detection and localization ..... 38*
*III.3.2.1 – Comparing the four methods for scenarios S2, S3, S4 and S5 ..... 39*
*III.3.2.2 – Comparing the four methods for scenarios S6 and S7 ..... 44*
*III.3.2.3 – Comparing the four methods for scenario S8 ..... 47*
*III.3.2.4 – Comparing the four methods for multiple damage location - scenarios S9, S10 and S11 ..... 48*
*III.3.3 – Performance of the ULS method ..... 51*
*III.3.3.1 – Frequency ratio versus ULS localization ..... 51*
*III.3.3.2 – LV3 objective of the NDE-ULS method ..... 51*
III.4- CONCLUSIONS ..... 54

**CHAPTER IV** ..... **56**

DETECTION AND LOCALIZATION OF DAMAGE USING TIME DOMAIN MODELLING ..... 56
IV.1-INTRODUCTION ..... 57
IV.2-NUMERICAL SIMULATION ..... 57
*IV.2.1-Finite element discretization for a 1-D clamped-free beam ..... 57*
*IV.2.2-Equations of Motion of the Beam ..... 58*
*IV.2.3-Newmark Method ..... 59*

*IV.2.4-Description of numerical simulation with random noise excitation* ..... *59*
IV.3 – DATA PROCESSING WITH SIGNAL PROCESSING TOOLS (FFT, FDD, AND RDT) ..... 61
*IV.3.1 – Fast Fourier Transform analysis - FFT* ..... *62*
*IV.3.2- Frequency Domain Decomposition (FDD)* ..... *63*
*IV.3.2.1 – Theoretical background* ..... *65*
*IV.3.2.2 – Data processing description by Frequency Domain Decomposition (FDD)* ... *68*
*IV.3.3- Frequency analysis using the Random Decrement Technique (RDT)* ..... *70*
*IV.3.3.1 – Theoretical background* ..... *70*
*IV.3.2.2 – Data processing description by RDT* ..... *72*
IV.4 – DETECTION AND LOCALIZATION OF DAMAGES USING FFT, RDT AND FDD FROM SYNTHETIC EXPERIMENTS ..... 76
*IV.4.1 – Global detection using the frequency ratio FR* ..... *77*
*IV.4.2 – Global detection using the MAC value* ..... *77*
*IV.4.3 – Localization of damage using NDE methods* ..... *78*
*IV.4.3.1 – Single damage detection and localization. Scenarios S2, S3, S4 and S5* ..... *78*
*IV.4.3.2 – Single damage detection and localization. Scenarios S6 and S7* ..... *80*
*IV.4.3.3 – Large and multiple damage detection and localization – Scenarios S8 and S9* ..... *81*
*IV.4.3.4 – Multiple damage detection and localization - Scenarios S10 and S11* ..... *82*
*IV.4.3.5 – Conclusions on the NDE methods using mode shapes extracted from FDD* ... *82*
IV.5 – STRUCTURAL DAMAGE LOCALIZATION AND MONITORING THROUGH PERTURBATION THEORY 84
*IV.5.1 – Theoretical approach for a one-dimensional clamped–free beam under bending* ..... *85*
*IV.5.2 – Finite-element discretization for a one-dimensional clamped–free beam* ..... *89*
*IV.5.3 – A synthetic experiment with ambient-noise excitation.* ..... *94*
*IV.5.4 – Discussion and conclusions* ..... *97*
IV.6 – CONCLUSIONS ..... 99

**CHAPTER V ..... 101**

DETECTION AND LOCALIZATION OF DAMAGE USING THE EXPERIMENTAL RESULTS ..... 101
V.1-INTRODUCTION ..... 102
V.2- EXPERIMENTS ..... 103
V.3 – DETECTION OF DAMAGE FOR EXPERIMENTS 1 AND 2 ..... 107
*V.3.1 – Detection of changes using a single recording at the top – Experiment 1* ..... *108*
*V.3.2 – Detection of changes using a single recording at the top – Experiment 2* ..... *111*
*V.3.2 – Localization of damage using ULS and perturbation theory for experiment E1* ..... *113*
V.4 – DETECTION AND LOCALIZATION OF DAMAGE FOR EXPERIMENT 3 ..... 117
V.5 – CONCLUSIONS ..... 123
**CONCLUSION GENERALE ET PERSPECTIVES** ..... 125
**BIBLIOGRAPHIE** ..... 129

# Table des figures

**Figure I. 1 :** Types d'endommagements visés par la SHM (Structural Health Monitoring). Source: Roach and Neidigk 2011. ..... 2
**Figure I. 2 :** Etudes des effets thermiques sur le pont Z-24 (a : site d'étude Z-24 ; b : Evolution de la première fréquence propre en fonction de la température). Source : Peeters et al.2001. ..... 6
**Figure I. 3 :** Evolution de la première fréquence propre avec la température sur le pont d'Alamosa pendant une période de 24 heures. Source : Farrar et al.1997. ..... 6

**Figure II. 1 :** Clamped-free beam: coordinates and mechanical properties. $m$: the mass per unit length, $E$: the Young's modulus of elasticity, $I$ : the moment of inertia of the cross section, $S$ : the section area , $G$ : the shear modulus , $L$ : the length of beam. ..... 13
**Figure II. 2 :** First three vibration modes of a cantilever beam. ..... 15
**Figure II. 3 :** Evolution of two natural frequencies of the Millikan Library, South California from Clinton et al. (2006). Dashed lines are east-west natural frequencies; dashed-dotted lines are north-south natural frequencies, all from forced vibration testing. Shaded area is the likely region of natural frequencies taking into consideration errors in measurement, caused by unknown shaker weight configuration and weather conditions for each test, and experimental error. Crosses indicate the actual time of a forced vibration measurement. Circles indicate the natural frequency estimated from the strong motion recording of the event, with the number in italics giving the peak acceleration recorded for the event (cm/sec2). ..... 20
**Figure II. 4 :** (a) Photo of Factor building taken from the northeast side of the building, and (b) diagram of Factor building sensor locations. Arrows show polarities of sensors on each floor. (From Kholer et al. 2005). ..... 20
**Figure II. 5 :** Change in fundamental horizontal mode natural frequency before and after the Yorba Linda earthquake. The frequency peaks were measured from 100-second acceleration segments from either 12th or 13th floor waveforms before and after the earthquake, band-pass filtered for frequencies between 0.45 and 0.65 Hz. A least-squares fit to a Gaussian was used to find the central frequency peak. (From Kholer et al. (2005)). ..... 21

**Figure III. 1:** Clamped-free beam model in 1D with modal analysis using FEM by RDM6. 32
**Figure III. 2 :** Sensitivity of the four first modes with the position of the damage varying from the bottom to the top of the beam (Scenario S1). The black curves correspond to the frequency ratio (FR) normalized to the maximum, the red curve corresponds the square of the curvature of the mode shapes (normalized) and A, B and C correspond to the position of the damage corresponding to scenarios listed in Table III.3. a) Mode 1; b) Mode 2; c) Mode 3; d) Mode 4. ..... 34
**Figure III. 3:** The first eleven mode shapes (bending modes) obtained by modal analysis using RDM6. Blue curve: undamaged state; Red curve: damage at A (S2); red, Black curve: damage at B (S6); Green curve: damage at C (S7) with damage severity a=0.9. ..... 35
**Figure III. 4:** Frequency ratio (FR) normalized versus four damage severities at the bottom of beam (point A - 30-33.5 cm) using modal analysis (FEM) – Scenario S2, S3, S4 and S5. ..... 37

**Figure III. 5:** Global MAC value for four damage severities at the bottom of beam (position A - 30-33.5 cm) using modal analysis (FEM) and considering several number of modes. ..... 37
**Figure III. 6:** Example of the theoretical and estimated position of damage along the beam (node), using the ULS method for the S2 scenario. ..... 39
**Figure III. 7:** Theoretical (in blue) and estimated position of damage along the beam (node), using the MSC method for the scenario S2 (a), S3 (b), S4 (c) and S5 (d) using the first mode shape (red curve) and the first eight mode shapes (black curve). ..... 40
**Figure III. 8 :** same as Fig. III.7, for the MSCS method. ..... 41
**Figure III. 9 :** same as Fig. III.7, for the CIF method. ..... 41
**Figure III. 10:** same as Fig. III.7, for the ULS method. ..... 42
**Figure III. 11:** Correlation values $C_{AB}$ for the four methods (a: MSC; b: MSCS; c: CIF; d: ULS) considering the four damage severities at position A (scenario S2, S3, S4 and S5) and several numbers of modes. ..... 43
**Figure III. 12:** Peak values of the Normalized Damage Index (NDI) evaluated by the four methods (green: MSC; yellow: CIF; blue: MSCS; red: ULS) and considering the four damage severities at position A (scenario S2, S3, S4 and S5). ..... 44
**Figure III. 13:** Theoretical (in blue) and estimated position of damage along the beam, using the MSC (a), MSCS (b), CIF (c) and ULS (d) methods for the S6 scenario using the first mode shape (red curve) and the first eight mode shapes (black curve). ..... 45
**Figure III. 14:** Same as Fig. III.13, for the S7 scenario. ..... 45
**Figure III. 15:** Correlation values $C_{AB}$ for the four methods (blue: MSC; red: MSCS; green: CIF; black: ULS) considering a=0.9 damage severity at position B (scenario S6, upper row)) and at position C (scenario S7, lower row). ..... 46
**Figure III. 16:** Theoretical (in blue) and estimated position of damage along the beam, using the MSC (a), MSC (b), CIF (c) and ULS (d) methods for the S8 scenario using the first mode shape (red curve) and the first eight mode shapes (black curve). ..... 47
**Figure III. 17:** Correlation values $C_{AB}$ for the four methods (blue: MSC; red: MSCS; green: CIF; black: ULS) considering a=*0.9* damage severity at position D (scenario S8, wide damage). ..... 48
**Figure III. 18:** Theoretical (in blue) and estimated position of damage along the beam, using the MSC (a), MSC (b), CIF (c) and ULS (d) methods for the S8 scenario using the first mode shape (red curve) and the first eight mode shapes (black curve). ..... 49
**Figure III. 19:** Correlation values $C_{AB}$ for the four methods (blue: MSC; red: MSCS; green: CIF; black: ULS) considering a=*0.9* damage severity at positions A, B and C (scenario S9). 50
**Figure III. 20:** Estimated position of damage along the beam, using the ULS methods for the S10 (blue) and S11 (red) scenarios (multiple damage with different a coefficient) using the five first mode shapes. ..... 50
**Figure III. 21:** Amplitude and localization of damage using ULS method (multi-color legend) and the local method based on the frequency shift (Frequency Ratio FR, blue thick curve) considering damaged sections sliding along the beam and one (upper), three (middle) and five (lower) modes for the detection. ..... 52
**Figure III. 22:** Estimated position of damage along the beam, and variation of the amplitude of the ULS damage value for the S2 (blue), S3 (red), S4 (black) and S5 (green) scenario considering the five first modes. ..... 53
**Figure III. 23:** Summary of the performance of the ULS method considering the first five modes, for Scenarios S2 (orange), S6 (black), S7 (magenta), S8 (yellow) and S9 (green), keeping the same damage severity (*a=0.9*). ..... 53
**Figure III. 24:** Correlation values $C_{AB}$ for the four methods (a: MSC; b: MSCS; c: CIF; d: ULS) considering all the scenarios of Tab. III.3 (see figures for legends). ..... 55

**Figure IV. 1:** (a) Finite element model of the 1-D beam discretized by *j=1, nb* Euler-Bernouilli finite elements. $\boldsymbol{ui}$ is the transverse displacement and $\boldsymbol{\theta i}$ the rotation of node *i*. (b) The global stiffness matrix *K* is obtained by assembling the contribution of all the nb element stiffness matrices, *j=1,nb*.from Baillet et al. (2013). ..... 58
**Figure IV. 2:** Sketch of the clamped-free beam model with sensor positions. ..... 60
**Figure IV. 3:** Time-history of the beam motion recorded at the clamped (a) and free end (c) extremities of the beam, with frequency responses (b, clamped; d, free). The eleven peaks correspond to the modal frequencies of the beam. ..... 62
**Figure IV. 4:** Evolution of the spectral amplitude of the synthetics computed at the 29 sensors and representing the shapes of the 11 first modes of the initial (undamaged) beam. ..... 63
**Figure IV. 5:** (a) Modal analysis results using ambient vibration test on City Hall of Grenoble by FDD method (b) numerical modeling on City Hall of Grenoble. from Michel et al (2010). ..... 65
**Figure IV. 6:** Singular values of the PSD matrix of the response of the S1, S2, S3, S4 and S5 scenarios. ..... 70
**Figure IV. 7:** First eleven mode shapes for Scenario 1 extracted from FDD method. ..... 71
**Figure IV. 8:** Changes in normalized frequency for mode 2 to 8 versus time and tracked by the RDT method for Scenario 1 and 5. ..... 74
**Figure IV. 9:** Variation of the frequency assessment for mode 1 depending on the length of the time windows used for computing the RDT methods. ..... 75
**Figure IV. 10:** Accurate of frequency measurements by random decrement technique (RDT) depending on the length of the recording on several buildings of Grenoble (after Dunand, 2005). ..... 75
**Figure IV. 11:** Optimization of RDT tested using SDOF response to ambient vibrations. .... 76
**Figure IV. 12:** Frequency ratio (FR) normalized versus four damage severities for the first eleven mode shapes using modal analysis (blue curve) and time analysis (red curve) at the bottom of beam at position A (30-33.5 cm) Scenario S2 to S5. ..... 77
**Figure IV. 13:** (a) Global assessment of MAC with four damage severities using time analysis at **position** A (S2 to S5). (b) Comparison between modal analysis and time analysis. ..... 78
**Figure IV. 14:** Damage detection process for testing the NDE methods. ..... 78
**Figure IV. 15:** Variation of the $\boldsymbol{CAB}$ for a single and narrow damage (Scenario S2 to S5) according to the number of modes. (a) MSC; (b) MSCS; (c) CIF; (d) ULS. ..... 80
**Figure IV. 16:** Variation of the $\boldsymbol{CAB}$ for a single and narrow damage (Scenario S6, upper row; Scenario S7, lower row) according to the number of modes and the NDE. methodsMSC; (b) MSCS; (c) CIF; (d) ULS. ..... 81
**Figure IV. 17 :** Variation of the $\boldsymbol{CAB}$ for a large (Scenario S8, upper row) and multiple (Scenario S9, lower row) damage scenarios according to the number of modes and the NDE methods. ..... 83
**Figure IV. 18:** Estimated position of damage along the beam, using the ULS methods for the case # 10 (blue) and # 11 (red) scenarios (with three different damage severity a). ..... 83
**Figure IV. 19:** Summary of the relevancy of the ULS methods applied using modes and frequencies extracted by FDD like experimental methods. A) LV3 of the NDE objective, evaluating the amount of damage (Scenarios S2, S3, S4 and S5). B) Performance of the ULS method considering the first five modes for S5, S6, S7, S8 and S9 scenario, keeping the same severity of damage (a=0.9). C) Comparing the $\boldsymbol{CAB}$ values computed considering the ULS method with modal and time analysis considering S5, S6, S7, S8 and S9 scenarios of damage, keeping the same severity of damage (a=0.9). ..... 84

**Figure IV. 20 :** Representation of (a) the modal deformation $\varphi nx$, and (b) the sensitivity kernel of the relative frequency change $\frac{\delta\omega n}{\omega n}$, for the first five modes and the 10-m-long clamped–free beam. In (b), the gray arrow corresponds to the position of the stiffness perturbation at x = 2.3 m (see Fig. IV.21). The two dashed lines show the stiffness perturbation interval scanned step-by-step in Figure IV.27, between x = 2.25 m and x = 7.5 m. ..... 91
**Figure IV. 21 :** Relative frequency shift $\frac{\delta\omega n}{\omega n}$ of the natural frequencies of the beam *versus* mode number for a stiffness perturbation $\delta EI$ at x = 2.3 m. ..... 91
**Figure IV. 22:** Inversion result obtained with the perturbation approach for a local stiffness perturbation $\delta EI$, (a) at x = 2.3 m (gray arrow), and (b) at both x = 2.3 m and x = 4.3 m (gray arrows). ..... 92
**Figure IV. 23:** Model-based deconvolution result obtained for a local stiffness perturbation $\delta EI$, (a) at x = 2.3 m (gray arrow), and (b) at both x = 2.3 m and x = 4.3 m (gray arrows). ... 94
**Figure IV.24:** Model-based deconvolution result obtained for an extended stiffness perturbation between x = 1 m and x = 3 m (gray arrows) and for (a) the first 10 modes and (b) the first 5 modes. ..... 95
**Figure IV. 25:** Relative change $\Delta G/G$ of the inversion kernel matrix G for a stiffness perturbation associated to (a) a local perturbation (at x = 2.3 m), and (b) an extended perturbation (between x = 1 m and x = 3 m). The change in G is clearly associated with the higher-order modes for an extended perturbation. ..... 95
**Figure IV. 26:** Signal recorded at the top of the beam for synthetic noise excitation generated at the beam base. ..... 96
**Figure IV. 27:** Continuous track of the frequency change from the RDT algorithm for modes 1 to 6 [panels (a) to (f)] in response to a step-by-step perturbation of the stiffness beam from t = 3476 s to t = 12524 s in intervals of 476 s. ..... 97
**Figure IV. 28:** Representation of the spatial-temporal (a) inversion and (b) model-based deconvolution in response to step-by-step perturbations of the stiffness beam. In both panels, the red line corresponds to the localization of the time-evolving perturbation. The color bar in (a) is the estimation of the stiffness perturbation. The deconvolution is normalized in (b)..... 98

**Figure V. 1 :** Experimental bed test for detection and localization of changes used in this work (a) Clamped-free beam set up tested in the laboratory. (b) Sketch diagram with geometric dimensions and accelerometer layout. ..... 104
**Figure V. 2 :** Time-history of the beam motion recorded at the top (left) and its Fast Fourier Transform (right). ..... 105
**Figure V. 3 :** Evolution of the spectral amplitude of the experimental data computed at the 29 sensors and representing the shapes of the 9 first modes of the initial (undamaged) beam (excepted for the fundamental mode). The black line is the numerical mode shapes from Chap. III. ..... 106
**Figure V. 4 :** Example of a random decrement signature corresponding to mode 5, obtained by RDT from recording at the top of the beam. ..... 107
**Figure V. 5 :** RDT applied to the beam considered for the experiment E1, with three positions of changes (A, B and C) tested successively. The data used for this experience is provided by the sensor located at the top of the beam. ..... 108
**Figure V. 6 :** Time variation of the normalized frequencies of modes 4 to 9 computed by RDT using sensor located at the top of the beam (free condition) for experiment E1. A, B and

C mark the time when the heat flow was applied for 30 seconds at positions A,B and C respectively..... 109
**Figure V. 7 :** Example of fitting curve applied at points A, B and C after stopping the heat flow. The data corresponds to the vibration recorded at the top of the beam; the frequency is tracked with RDT and normalized by the average frequency of the undamaged state. ..... 110
**Figure V. 8 :** RDT applied to the beam considered for the experiment E2, with one position of change (position A) and 6 amounts of damage reproduced by the time duration of the heat flow exposure (from 10 to 60 seconds). Data used for this experience are provided by the sensor located at the top of the beam. ..... 112
**Figure V. 9 :** Time variation of the normalized frequencies of modes 4 to 9 computed by RDT using sensor located at the top of the beam (free condition) for experience E2. The heat flow was applied for 10 to 60 seconds at position A. ..... 112
**Figure V. 10 :** Frequency ratio (FR) of the 9 first modes for 10s to 60 seconds of heat flow exposure, applied at the bottom of the beam (**position** A)..... 113
**Figure V. 11 :** First five singular values (upper row) and mode shapes (lower row) of the beam extracted from ambient vibrations recorded on the beam using the 29 accelerometers, corresponding to the undamaged and damage (positions A, B and C) of the experiment E1. ..... 114
**Figure V. 12 :** Localization of the damage at position A, B and C using the ULS method and considering modes 2 to 5 for experiment E1..... 115
**Figure V. 13 :** Results of the damage localization method applied to the experimental data (experience E1) for the three cases of change (a: at position A; b: at position B; c: at position C), where the heat flow applied at 2, 4 and 6 hours from the beginning of the experiment corresponds to the numbers of recording following: 240, 480 and 720 respectively (each record duration is 10 s, a total of records is 960). ..... 117
**Figure V. 14 :** Experimental setup with faster prototype. ..... 117
**Figure V. 15 :** Evolution of the spectral amplitude of the experimental data computed at the 29 sensors and representing the shapes of the 9 first modes of the initial (undamaged) beam (excepted for the fundamental mode). The black line is the numerical mode shapes from Chap. III. ..... 118
**Figure V. 16 :** Time variation of the normalized frequencies of modes 2 to 9 computed by RDT using sensor located at the top of the beam (free condition) for experience E3. The heat flow was applied for 12 minutes at *x=40.5 cm*. ..... 120
**Figure V. 17 :** Singular values of the PSD matrix of the recordings provided by the 29 accelerometers along the height of the beam computed through the FDD methods..... 121
**Figure V. 18 :** First five mode shapes of the beam extracted from ambient vibrations recorded using the 29 accelerometers, corresponding to the undamaged (A) and damaged (A*) states of the experiment E3..... 122
**Figure V. 19 :** Summary of the performance of the ULS methods to locate the damage at the bottom of the beam (*x=40.5 cm*) using modes and frequencies extracted by FDD from the experiment E3. (a) Mode 2; (b) Mode 3; (c) Mode 4; (d) Mode 5; (e) Modes 2 to 5. ..... 122

# Liste des tableaux

**Table III. 1 :** Geometric and material properties of cantilever beam. ..... 31
**Table III. 2 :** Comparison of theoretical modal frequencies versus modal analysis using Finite element modeling by RDM6 of the clamped-free beam. ..... 32
**Table III. 3 :** Damage scenarios applied to the clamped-free beam using Finite element modeling. The values of the table correspond to '*a*', the damage severity parameter; the position of damage (POD) along the beam are presented on the first column. ..... 33
**Table III. 4 :** Frequency ratio (FR) for four damage severities (scenario S2, S3, S4, S5) at point A (30-33.5 cm) / ( ) is the value of MAC. ..... 36

**Table IV. 1 :** Damage scenarios applied to the clamped-free beam using time domain modeling. ..... 61
**Table IV. 2 :** Natural Frequencies (Hz) by modeling (RDM6) and numerical simulation ..... 63
**Table IV. 3 :** Natural Frequencies (Hz) corresponding to Scenarios 1 and 5 extracted by the FDD and RDT methods. ..... 74

**Table V. 1 :** Geometric and material properties of cantilever beam. ..... 103
**Table V. 2 :** Natural Frequencies (Hz) obtained by numerical and experimental analysis. .. 106
**Table V. 3 :** Variation coefficient (CV %) of the frequency value of the first 9 modes obtained using the RDT and considering the first part of the experience (unchanged beam condition before heating). ..... 108
**Table V. 4 :** β value of the time recovery of the modal frequencies computed using the RDT and observed after stopping the heat flow at position A, B and C, using the same time of heating of 30 seconds. ..... 110
**Table V. 5 :** Variation coefficient (CV %) of the frequency value of the first 9 modes obtained using the RDT and considering the first part of the experience (unchanged beam condition before heating). ..... 111
**Table V. 6 :** Natural Frequencies (Hz) obtained by experimental analysis for experiment 1 and 3 respectively before applying the damage (heat flow) in both cases correspond to intact beam. ..... 119
**Table V. 7 :** Variation coefficient (CV %) of the frequency value of the first 9 modes obtained using the RDT and considering the first part of the experience (unchanged beam condition before heating). ..... 120
**Table V. 8 :** Natural frequencies of undamaged and damaged beam for the first five modes. Frequency ratio (FR) calculated by Eq. III.7 and Modal Assurance Criterion (MAC) calculated by Eq. II.30. ..... 121

# CHAPITRE I

# Introduction générale

La surveillance de l'intégrité des structures (ou SHM, pour ***Structural Health Monitoring***) en lien avec l'identification des dommages structurels s'est particulièrement développée de la part des communautés scientifiques et techniques au cours des dernières décennies. Cette situation a concerné la conception, le développement et l'implémentation de techniques pour la détection, la localisation et l'estimation d'endommagements ou de changements dans une structure existante. En effet, cette surveillance est cruciale car une défaillance structurelle imprévue peut causer aussi bien une catastrophe économique qu'une perte de vies humaines.

Les systèmes SHM sont développés pour répondre à cet enjeu : *"SHM is the key technology to enable the transition from traditional schedule-driven maintenance to Condition-Based Maintenance"* (Chang, 2011).

Les 10 dernières années ont vu une augmentation rapide de la quantité de recherches portant sur la SHM (Structural Health Monitoring) à cause de l'augmentation des données et des moyens de calculs. Une vaste revue sur les méthodes de surveillance peut être trouvée dans la littérature (Doebling et al. 1996,1998 ; Hemez et al. 2001).

L'objectif de la SHM est de surveiller en temps réel (real-time) ou à intervalles réguliers l'intégrité d'une structure, au travers de la détection de fissures ou de corrosion des éléments constituant la structure. Parmi les systèmes et les ouvrages nécessitant une inspection régulière et une surveillance fréquente, on peut citer les plateformes pétrolières, les ponts et les bâtiments, les avions ou les véhicules spatiaux et plus récemment les parcs d'éoliennes.

Ces ouvrages sont constamment soumis à des agressions environnementales ou des événements extrêmes (tremblement de terre, Tsunami, vent violent, houle, augmentation et diminution de la température, trafic autoroutier), entraînant un vieillissement de leurs éléments (fatigue) ou de leurs matériaux constitutifs, sous l'action de leur fonctionnement normal, de l'évolution de leurs conditions d'exploitation ou des chargements exceptionnels.

Près de 60 % des applications de Structural Health Monitoring (SHM) dans le monde sont utilisée pour la surveillance des ponts en temps réel. Depuis peu, aux Etats-Unis, un nombre important de ponts a été remplacé car la surveillance a permis de découvrir que ces derniers étaient structurellement défectueux à cause du vieillissement (Chase. 2001).

Dans l'industrie aéronautique, 14% des accidents sont dus à des problèmes de maintenance, 4% sont liés à la présence d'endommagements (Balageas 2006). Roach and Neidigk (2011) ont effectué une enquête statistique en collaboration avec la Federal Aviation Administration (FAA) aux Etats-Unis.

Cette mission s'est basée sur les réponses de 455 personnes travaillant chez des constructeurs aéronautiques, compagnies aériennes et compagnies de maintenance. 61% de ces participants trouvent qu'il est très important de développer des systèmes SHM dans l'industrie aéronautique.

D'après la figure I.1, nous voyons que les participants à cette enquête sont très intéressés par la détection des endommagements de types fissure, délaminage, décollement, corrosion et impact.

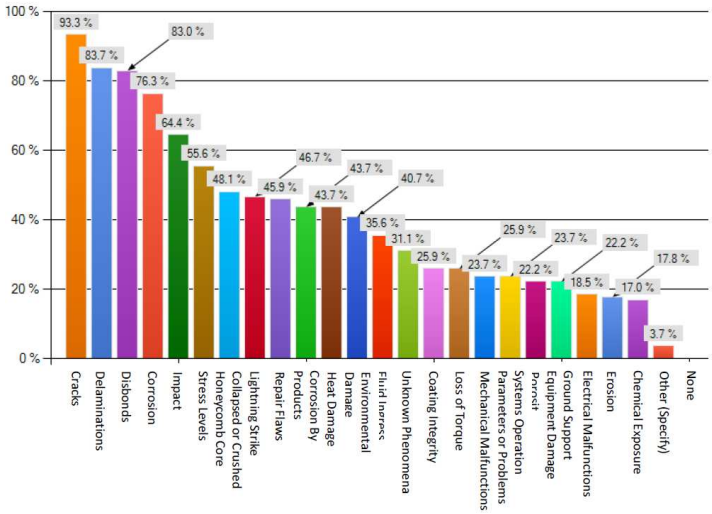


**Figure I. 1 :** Types d'endommagements visés par la SHM (Structural Health Monitoring).
Source: Roach and Neidigk 2011.

D'une manière générale, il y a deux types de techniques d'inspection des dommages utilisés : les techniques non destructives et celles destructives. La première est généralement la plus utilisée pour surveiller l'intégrité des structures ou des matériaux sans les dégrader (contrairement à la deuxième technique). On peut citer les techniques les plus connues comme les contrôles par rayons X, les techniques à base d'ultrasons, les émissions acoustiques, les courants de corrosion, etc.… Les méthodes de SHM sont généralement divisées en deux catégories: les méthodes locales et globales.

La première catégorie comprend des méthodes destinées à fournir des informations sur une région relativement petite du système analysé en utilisant des mesures locales. De plus, il est nécessaire que les capteurs soient situés à proximité du lieu d'endommagement. Dans la littérature, il est possible de trouver certains travaux portant sur une application expérimentale. Ce travail utilise la thermographie infrarouge (IR-thermography) comme technique non destructive (NDT).

La thermographie infrarouge (IR-thermography) permettent d'échauffer le matériau à partir des méthodes optiques telles que les lampes flashs ou halogènes, sans contact avec la pièce et en temps réel. Elle peut être utilisée pour suivi l'endommagement lors d'essais mécaniques mais également en contrôle non destructif. La thermographie est donc utilisée pour détecter la présence de défauts dus à la fabrication, à des chocs ou au service, à la fois dans les matériaux homogènes et les composites (Meola, 2004 ; Genest, 2009).

L'analyse des contraintes thermo élastiques (thermoelastic stress analysis : TSA) à l'aide de la thermographie infrarouge a été confirmée comme l'une des techniques efficaces non destructives d'évaluation des contraintes. Les fissures peuvent aussi être détectées et évaluées à partir des champs de contraintes singulières dues aux fissures.

Une autre application plus quantitative de la méthode par thermographie, proposée dans la littérature, a été faite dans le but de surveiller la réponse thermique de différents matériaux

pendant des chargements statiques ou en fatigue sur des bancs expérimentaux et de la relier à leur vie en fatigue (Risitano, 2010).

Récemment, la détection des dommages à travers les ondes ultrasonores guidées, telles que des ondes de Lamb, a été appliquée souvent en raison de la possibilité d'inspecter de grandes structures composites.

La détection des dommages par la propagation des ondes de Lamb avec des capteurs de plaquette piézoélectrique active (PWAS) est l'une des technologies émergentes de surveillance de la santé structurale. Les PWAS pourraient être des bons candidats pour détecter la corrosion des éléments métalliques (Giurgiutiu, 2008). Une nouvelle technique à base de titane-zircon de plomb piézoélectrique (PZT) comme capteurs semble avoir le potentiel pour améliorer significativement la surveillance de la santé structurale (SHM). Ces capteurs sont petits, légers, peu coûteux et peuvent être produits avec des géométries différentes. Ils peuvent être ensuite collés à la surface des structures, placés à l'intérieur des structures et ils peuvent même être intégrés entre les couches structurales et non structurales d'une construction complète (Giurgiutiu, 2008).

La deuxième catégorie consiste généralement en l'utilisation des modes à basse fréquence. Elle utilise des mesures réalisées à partir d'un ensemble de capteurs dispersés dans la structure pour obtenir des informations globales sur l'état du système. Il n'est pas nécessaire que les capteurs soient situés à proximité du site d'endommagement.

Evidemment, ces deux approches (locale et globale) sont complémentaires et le choix optimal de la méthode dépend fortement de la nature du problème et de la configuration des réseaux de capteurs utilisés. L'inspection régulière de l'état des structures permet de détecter des défauts éventuels et d'assurer la fiabilité de ces ouvrages pour l'usage quotidien. Le besoin de méthodes globales d'évaluation quantitative de l'endommagement d'un ouvrage complexe a conduit au développement et à la recherche de méthodes examinant les changements des caractéristiques vibratoires en continu.

L'accroissement des activités de recherche dans ce domaine pour le génie civil est le résultat de plusieurs facteurs. En premier lieu, le besoin d'essais, de contrôles et d'évaluations pour s'assurer de la sécurité des structures et des systèmes utilisés est un enjeu sociétal fort et l'expertise dans ce domaine ne peut être basée sur des approximations ou des simplifications. La mesure permet ainsi de lever pas mal d'ambiguïtés et apporte une représentation physique d'une situation, limitant l'interprétation et le jugement d'expert.

En second lieu, le vieillissement des parcs d'ouvrages et l'importance des coûts de réparation militent en faveur du développement de techniques de détection de changements et de dommages ou de détériorations précoces afin de cibler au mieux les renforcements ou réparations.

Enfin, les avancées technologiques des matériels de mesure et d'informatique ont largement contribué aux récentes améliorations dans la détection par analyse vibratoire. Le coût des capteurs a toujours été une limite au nombre de capteurs déployés. Il y a trente ans, l'utilisation d'un à trois accéléromètres sur une structure était une pratique courante considérée comme acceptable. Aujourd'hui, le prix des capteurs permet de placer près d'une centaine de capteurs sur une seule et même structure.

La technique non destructive d'évaluation (NDE) de dommages via des capteurs intégrés (cas de fibres optiques dans des composites par exemple) ou collés (accéléromètres acoustiques ou sismiques) à la structure, permet une surveillance fiable et efficace en continu. Par ailleurs, l'un des grands avantages des méthodes vibratoires repose sur la possibilité d'utiliser des vibrations ambiantes comme source d'excitation, présentes en condition réelle sur les bâtiments, ponts et les versants instables (falaise rocheuse).

Ces dispositifs de surveillance (capteurs et chaine d'acquisition) simplifiés permettent un suivi plus rapide et plus automatisé de la structure, sans la solliciter (mesure de la vibration ambiante de la structure en temps réel).

L'idée générale du SHM est que la variation des propriétés physiques (rigidité, masse et amortissement) entraînent une variation des caractéristiques dynamiques de la structure (fréquences de résonances, coefficient d'amortissement et déformées modales). De ce fait, les modifications pouvant intervenir sur les propriétés physiques ou mécaniques doivent être détectables au travers des changements des paramètres modaux.

La présence d'endommagement ou d'une fissure provoque une variation locale de la rigidité de la structure, qui se reporte sur l'ensemble du comportement mécanique de la structure. La réduction dans la rigidité réduit les fréquences et affecte des déformées modales, c'est-à-dire augmente la flexibilité (Ulm et al. 1993). À partir de la réponse dynamique mesurée sur le système, l'extraction de caractéristiques est le processus d'identification des propriétés sensibles permettant de distinguer entre les états sains et endommagés du système (Farrar et al. 2001).

Une définition générale de l'endommagement est donnée par Sohn et al. (2003) comme *"…changes introduced into a system that adversely affect its current or future performance. Implicit in this definition is the concept that damage is not meaningful without a comparison between two different states of the system, one of which is assumed to represent the initial, and often undamaged, state."*

Les vibrations ambiantes sont utilisées pour l'identification des structures de génie civil depuis les années 30 en Californie (USA). Carder (1936) a réalisé un grand nombre de mesures dans les bâtiments californiens et il a proposé ensuite une relation entre hauteur et période de vibration des bâtiments, relation encore utilisée dans les codes de génie parasismique américains.

En France, on peut citer notamment les travaux récents de C. Michel (Michel et al. 2008 ; Michel et al. 2010a), d'autres de Farsi (1996), Boutin et al. (1999) et Dunand (2005), études ayant pour but d'utiliser ces mesures ambiantes pour analyser la vulnérabilité des bâtiments existants. De nombreuses études ont été décrites dans la littérature sur le changement de fréquence dans la structure (Farrar et al.1997; Peeters et al.2001 ; Clinton et al.2006 ; Mikael et al.2013). D'après ces études, les auteurs ont considéré que la fréquence est un bon indicateur d'endommagement.

Récemment, Clinton et al. 2006 ont étudié l'évolution des deux premières fréquences de résonance de la Millikan Library, un grand bâtiment en Californie du Sud. La diminution de ses fréquences de résonance a été causée par divers séismes qui ont endommagé le bâtiment entre 1967 et 2003. Une baisse permanente des fréquences (21.4 % sur la composante Est-ouest et 12.1 % sur la composante Nord-sud) a été observée. Etant donné que la masse de la

structure reste à peu près constante au cours du temps, cette décroissance des fréquences de résonance (la perte en rigidité de la structure) a été interprétée comme une diminution de la rigidité du système provoquée par l'endommagement du bâtiment. Pour que les endommagements soient détectés avec un seuil de confiance important dans les structures, il faudrait que les fréquences propres varient d'au moins 5% (Creed, 1988).

Il existe de nombreuses sources autres que les dommages causant des variations dans les caractéristiques dynamiques d'une structure et dans le bruit mesuré, telles que la non-linéarité dans le système, les variations de température, l'absorption d'humidité, les interactions structure-sol, le vent, etc.… Elles peuvent produire une modification significative des paramètres modaux des structures (Guo et al. 2007).

Trifunac et al. (2001) rappellent que la chute de fréquence observée au cours des séismes ne peut pas seulement être due à l'endommagement dans la structure elle-même. Elle est aussi influencée par l'interaction sol-structure et la non-linéarité du sol. Les vibrations causées par le vent, peuvent modifier le comportement dynamique d'un ouvrage en altérant ses caractéristiques d'amortissement (Fujino & Yoshida 2002).

Clinton et al. (2006) ont aussi étudié l'effet du vent et des précipitations de pluie sur le même bâtiment ML (Millikan Library). Cette étude montre que la fréquence chute de 3 % lors de fortes rafales de vent, et que des précipitations intenses de pluie augmentent la fréquence fondamentale Est-ouest et la fréquence de torsion de l'ordre de 3% pendant quelques heures.

Li et al. (2010) montrent des écarts de 3% mesurés sur le pont haubané Tianjin Yonghe en Chine sur une durée de deux semaines. Des études expérimentales ont été effectuées sur le pont Z-24 en Suisse (Figure I.2.a), ces études ont été réalisées par l'EMPA (laboratoire Fédéral d'Essai des Matériaux et de Recherche) et l'université de Louvain (Peeters et al. 2001).

Les résultats de cette étude (pont Z-24) ont mené à des informations intéressantes et complémentaires sur la sensibilité des paramètres modaux dus aux variations climatiques (augmentation de la température). En particulier, il a été noté un changement de l'ordre de 10 % sur la première fréquence propre (Figure I.2.b) pour une variation thermique variant de -5 à 35 °C.

D'autre part ils ont montré qu'un changement de température de l'ordre de 15 °C (entre 15 et 30 °C), peut causer un changement de fréquence de 2.5 %. Ce changement est expliqué par une variation du module d'élasticité de l'asphalte au-dessous de 0°C, et peut également être expliqué par une modification des conditions de liaisons consécutives aux variations dimensionnelles du tablier lorsque les joints de dilatation ne fonctionnent pas correctement.

Cette diminution de la fréquence en fonction de l'augmentation de la température trouvée (Figure I.1.b) sur le pont Z-24 n'est pas une règle en soi. Ainsi, à titre de contre –exemple, Farrar et al. (1997) ont étudié le pont d'Alamosa Canyon au Nouveau-Mexique (USA), le résultat montre une augmentation de la première fréquence avec l'augmentation de la température (Figure I.3), et une variation de l'ordre de 5 % pendant 24 heures de surveillance.

Récemment, Mikael et al. (2013) ont montré sur des bâtiments différents des relations fréquences/températures fluctuantes, ne permettant de définir des généralités sur la réponse de ces ouvrages aux conditions environnementales.

(a) (b)

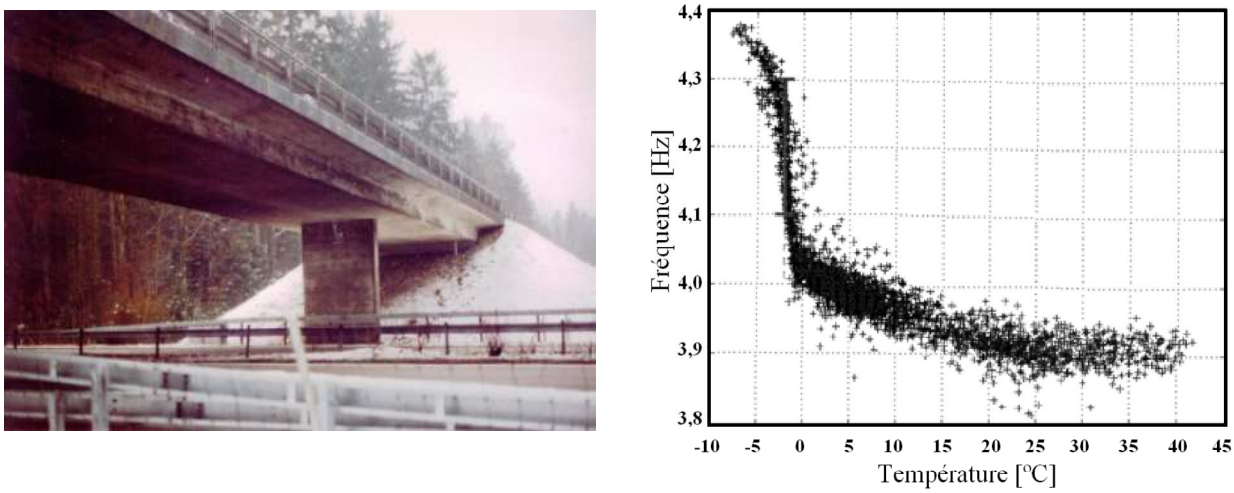


**Figure I. 2 :** Etudes des effets thermiques sur le pont Z-24 (a : site d'étude Z-24 ; b : Evolution de la première fréquence propre en fonction de la température). Source : Peeters et al.2001.

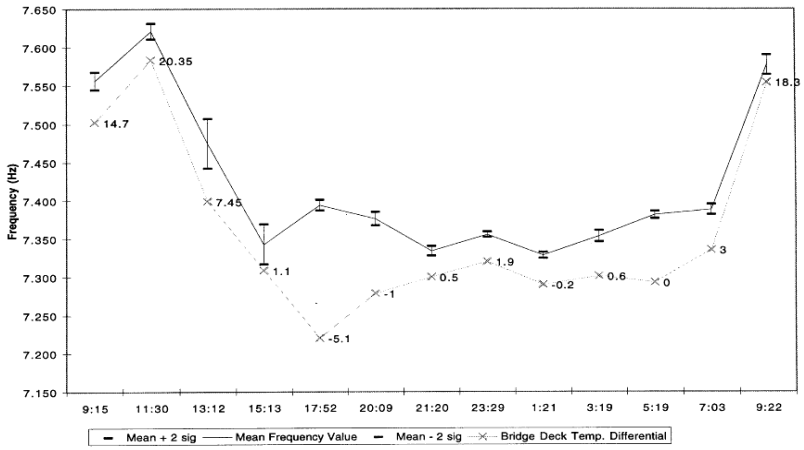


**Figure I. 3 :** Evolution de la première fréquence propre avec la température sur le pont d'Alamosa pendant une période de 24 heures. Source : Farrar et al.1997.

Fox (1992) a montré que les changements des fréquences propres sont des indicateurs peu sensibles dans le cas d'une poutre fissurée à la scie. Srinivasan and Kot (1992) sont arrivés aux mêmes conclusions dans le cas des plaques endommagées.

En général, les effets d'un endommagement dans une structure peuvent être classés comme linéaires ou non linéaires. Une situation d'endommagement sera dite linéaire, si la structure initialement élastique linéaire reste élastique linéaire après l'endommagement. Les changements des propriétés modales sont causés par le changement des géométries et / ou des propriétés matérielles de la structure, mais la réponse de la structure peut être toujours modélisée en utilisant les équations linéaires du mouvement.

L'endommagement sera non linéaire, si la structure initialement élastique linéaire se comporte de façon non linéaire après qu'un endommagement se soit produit. Un exemple d'endommagement non linéaire est la formation d'une fissure de fatigue qui s'ouvre et se ferme sous l'environnement normal de vibration.

Le suivi de l'état de santé des structures (SHM) est défini par l'ensemble du processus suivant :

La définition des objectifs du système de suivi (structure ou ouvrage), la détermination des caractéristiques du système (paramètres modaux), la récupération d'informations, l'extraction d'indicateurs pertinents sur l'état de santé, le diagnostic (évaluation de l'état présent), et enfin le pronostic (prédiction de l'état futur).

Il existe différents niveaux d'exigence sur les performances du dispositif de surveillance. Rytter et al. (1993) ont défini, la surveillance de l'intégrité des structures comme un processus à quatre étapes:

− Détection (niveau I)
− Localisation (niveau II)
− Quantification (niveau III)
− Prédiction (niveau IV)

Le niveau I fournit uniquement l'information concernant la détermination de l'existence d'un endommagement dans la structure. Pour de nombreuses applications pratiques, cela est suffisant. Le niveau II consiste à déterminer l'emplacement ou la localisation de l'endommagement. Le niveau III consiste à quantifier la sévérité d'un endommagement. Cette étape fait appel à des modèles d'endommagement, détectés, localisés et classés, dont le but est de décrire l'endommagement par des paramètres, tels que la longueur de la fissure, le diamètre d'un impact, la taille d'un délaminage ou la diminution de la rigidité sur le comportement dynamique de la structure (Chang et al. 2007).

Le dernier niveau (IV) a pour objectif de prédire l'évolution future de l'endommagement et d'estimer la durée de vie résiduelle de la structure. Cette étape nécessite une combinaison du modèle structurel global avec des modèles de lésions locales (Inman et al. 2005).

Sohn et al. (2003) et Worden and Dulieu-Barton (2004) ont ajouté une étape supplémentaire c'est la classification de l'endommagement entre les niveaux II et III.

Selon eux, la surveillance de l'intégrité des structures doit s'effectuer selon la procédure en cinq étapes. L'objectif principal de ces cinq niveaux est de prédire efficacement la durée de vie restante de la structure ainsi que l'information concernant le type de dommage. La classification devient alors une étape importante, avant l'estimation de la sévérité des endommagements.

Quand les endommagements se présentent dans une structure, la rigidité en flexion aux endroits des endommagements est réduite tandis qu'en même temps la courbure de forme de modes augmente (voir l'équation II.31), cette dernière est calculée par l'intégration numérique de la forme du mode (voir l'équation II.32). De plus, Chance et al. (1994) ont proposé d'utiliser les déformations au lieu de la mesure directe de la courbure, parce que le calcul de la courbure obtenu par des déformées propres peut aboutir à des erreurs inacceptables. Avec cette nouvelle façon d'obtenir la courbure, les résultats sont beaucoup améliorés.
Ho and Ewins (2000) ont étudié d'autres variations des caractéristiques basées sur des formes de modes comme la pente des formes des modes et le carré de la courbure des formes des

modes. Ils ont conclu que la caractéristique basée sur le carré de la courbure des formes des modes donne des meilleurs résultats.

Une autre méthode de détection d'endommagement a été proposée par Stubbs et al. (1992), basée sur le rapport entre l'énergie de déformation modale des éléments avant et après l'endommagement. Les formes des modes mesurées ont d'abord été différenciées pour obtenir des courbures des formes des modes et ensuite interpolées pour obtenir la courbure, afin de calculer l'énergie de déformation modale.

Le point fort de cette méthode est que la détection et la localisation de l'endommagement peuvent être obtenues avec un petit nombre de modes de vibration (Humar et al. 2006), lorsque cet indicateur est négatif, cela indique l'absence de l'endommagement dans la structure.

Farrar and Doebling (1999) ont réussi à utiliser l'énergie de déformation modale pour localiser les endommagements d'un pont. Ils ont constaté que l'utilisation de cette caractéristique est meilleure que la comparaison directe des courbures des formes des modes pour la localisation des endommagements.

Cependant, Worden et al. (2001) ont prouvé que les résultats de la localisation dépendent de l'emplacement des capteurs et l'échantillonnage des modes. Parc et al. (1998) ont comparé trois méthodes pour obtenir la matrice de flexibilité pour la détection de l'endommagement structural : une méthode de sous-structuration, une méthode basée sur la déformation et une méthode basée sur la contrainte. Ces méthodes ont été appliquées sur un bâtiment de dix étages, un pont et un moteur. Les résultats ont suggéré que ces techniques pourraient correctement localiser les endommagements.

Enfin une combinaison des méthodes de courbure des déformées modales et de flexibilité est effectuée par Zhang et Aktan (1995). L'idée générale est que la perte de rigidité locale produit une augmentation de courbure au même point. Le changement de courbure s'obtient alors par la flexibilité au lieu de déformées modales.

Certains chercheurs ont conclu que les déformées modales sont plus sensibles à la présence de l'endommagement que les fréquences propres (Biswas et al. 1990 ; Salane and Baldwin, 1990 ; Mazurek and Dewolf, 1990). Par contre, Alampalli et al. (1995) et Salawu and Williams (1995) mettent en évidence dans certains cas que les changements des déformées modales sont moins sensibles aux endommagements que les changements fréquentiels.

Une autre difficulté est qu'en pratique, les fréquences et leurs fluctuations peuvent être facilement suivies dans le temps, avec une précision très élevée, tandis que les formes modales sont plus sensibles aux erreurs de mesures et d'expérimentations. Par ailleurs, la surveillance de la santé structurale nécessite la connaissance de l'état initial pour détecter des changements dans le système ou bien de supposer un modèle théorique de comportement.

L'objectif global de cette thèse est de tester des méthodes de suivi de l'intégrité des structures (SHM), pour révéler et détecter les changements des propriétés mécaniques dues à une diminution locale du module d'Young (E).

Les principaux objectifs sont :

- Etre capable de détecter l'endommagement dans une structure
- Etre capable de localiser l'endommagement dans une structure
- Etre capable de quantifier la sévérité d'un endommagement

Ce manuscrit est divisé en cinq chapitres :

- Le chapitre I, constitue brièvement un état de l'art des méthodes de surveillance de l'intégrité des structures (SHM).
- Le chapitre II rappelle quelques notions théoriques sur la poutre encastrée-libre. Puis les descriptions des algorithmes non-destructifs d'évaluation (NDE) avec leurs applications dans la littérature pour détecter et localiser l'endommagement sont présentées. Ces méthodes seront utilisées dans les trois chapitres suivants, en gardant à l'esprit la volonté de tester des méthodes efficaces sur le terrain.
- Le chapitre III présente la modélisation d'une poutre encastrée libre en dynamique linéaire (analyse modale fréquentielle) sur laquelle est testée l'efficacité des méthodes NDE en prenant en compte plusieurs modes pour détecter, localiser et quantifier l'endommagement. La position de l'endommagement selon différentes configurations (unique, large et multiple) avec différentes sévérités de dégâts est testée.
- Le chapitre IV est consacré à la simulation numérique (analyse temporelle) en dynamique non-linéaire (Eléments Finis), en se plaçant cette fois en conditions expérimentales (excitation avec du bruit). Les variations fréquentielles en fonction du temps dues à un endommagement local sur la poutre sont obtenues par la technique du décrément aléatoire (RDT), et on vérifie la capacité de la méthode FDD (Frequency Domain Decomposition) à extraire les paramètres modaux. Les informations extraites de ces deux méthodes sont ensuite utilisées par les méthodes NDE afin d'évaluer leur faisabilité sous l'effet des vibrations ambiantes.
- Enfin, le chapitre V porte sur l'application expérimentale de la surveillance de l'intégrité (SHM) d'une poutre encastrée libre en plexiglas, pour atteindre les trois principaux objectifs définis précédemment : détecter, localiser et quantifier l'endommagement avec les méthodes NDE sur des vraies données.

# CHAPITRE II

# METHODS FOR DETECTION AND LOCALIZATION OF CHANGES

**Abstract:** In this chapter, several methods for the detection and localization of changes or damage in structures are presented and discussed. A large panel of methods exists in the scientific literature, several being applied and tested on numerical modeling that give access to some information not available using experimental approaches. By consequence, only methods applicable to field-testing are presented here, considering the global methods for detection of damage and local methods for localization. Most of the methods are based on the modal parameters variations of the structure. After reminding the main goal of the non-destructive evaluation methods, the theoretical model used for representing the building/structure behavior is discussed first through the continuous beam principle, for the bending/cantilever beam case. Then the effects of changes on the modal parameters are presented and the general methods (local and global) used in this work are discussed and presented.

## II.1 Introduction

For the last two decades, several researches have been conducted on non-destructive evaluation of damage (NDE), based on monitoring the change of the dynamic response of a structure. They have received considerable attention in mechanical industries, aerospace and civil engineering. The basic idea is that changing the characteristics of stiffness, mass or energy of a system can alter its dynamic response (Doebling et al, 1996; Farrar et Worden, 2007). Modal parameters (frequencies, damping and mode shapes) are sensitive to changes, resulting from changing boundary conditions (e.g., soil-structure interaction), design properties (e.g., strengthening) or elastic properties of the material (e.g. the Young's modulus) (Maeck et al., 2000). Moreover, changing the physical properties of a system (e.g., stiffness, attenuation or mass) causes a variation in the modal parameters of the structure. These variations can then be directly related with damages or loss of integrity, a decrease in the stiffness resulting in a decrease of frequency and therefore an increase in its flexibility.

Rytter (1993) classified the NDE methods into 4 levels based on their objectives: level 1 is the detection of damage, level 2 corresponds to the identification of the damage location, level 3 is the quantification of the damage severity, and level 4 is the prognosis of integrity of the structure.

The first level (LV1) is to detect if changes have occurred. The analysis of the damage related to the variation of the fundamental frequency of the buildings was a common practice in earthquake engineering since, as supported by Farrar et al. (2001), frequencies are certainly the modal parameter most sensitive to changes, especially because the loss of stiffness directly impacts the frequency values. Data was collected and processed for understanding the variations of the modal parameters during and after earthquakes, in correlation with the shaking level and the damage observed (Celebi et al., 1993; Ivanovic et al., 2000; Dunand et al., 2006; Clinton et al., 2006; Michel et al., 2010). The second level (LV2) is to detect if changes have occurred and simultaneously determine the location of damage. For example, variation of frequencies may only reflect a global change of the system properties and it is not often sufficient to locate the origin of changing within the structure. For that reason, damage detection methods have been developed based on the mode shape analysis. The experimental assessment of mode shapes is sometimes insufficiently precise to detect and locate small variations, compared to the sensitivity of the modal frequencies analysis. The third level (LV3) is to detect if changes have occurred, determine the location of damage as well as estimate the severity of damage. Few applications of LV3 are available in practice, while the estimate of the severity may contribute significantly to the action of the decision makers in case of an emergency after an extreme event.

In the most cases, structural damage detection is focused of a compare among the response from an undamaged and a damaged state. Several methods have been described in the literature to identify and locate damages, most of them are based on comparisons between a damaged and an undamaged condition and efficiency to severe damage. Structural Health Monitoring application using vibration techniques focused on mode shape derivatives as

indications of damage. For instance, the change in flexibility method (Pandey and Biswas, 1994), the curvature methods of mode shapes (Pandey et al., 1991) and the method of curvature flexibility (Zhang and Aktan, 1995) are quantitative methods. Farrar and Doebling (1999) presented the change in curvature of the Uniform Load Surface (ULS) to determine the location of damage. Wahab and De Roeck (1999) applied a curvature-based method to the Z24 Bridge in Switzerland successfully. They concluded that the use of modal curvature to locate damage in civil engineering structures seemed promising. Ho and Ewinx (2000) state that higher derivatives of mode shapes are more sensitive to damage. Hamey et al. (2004) assessed several damage algorithms in composite beams with several possible damage configurations using directly measured curvature mode shape. Just-Agosto et al. (2007) used the mode shape curvature data and a properly trained neural network scheme to implement successfully damage detection for composite sandwich beam.

After describing the theoretical solution of the cantilever beam used in this thesis, several methods found in the scientific literature will be presented, based on the variation of the mode shapes and frequencies between damaged and undamaged conditions. Local and global methods will be discussed and then applied to theoretical and experimental analysis, shown in Chap. III and IV.

## II.2 Theoretical solution of the Cantilever beam

The theoretical dynamic properties of the cantilever beam are described herein. In the case of a slender structure or a continuous beam of uniform section, the mass and stiffness can be distributed over the length of the beam and the equations of motion, for an Euler-Bernoulli beam system under free vibration, can be expressed as (Clough & Penzien, 1993):

$$m(x)\frac{\partial^2 u}{\partial t^2} + \frac{\partial^2}{\partial x^2}\left[EI(x)\frac{\partial^2 u}{\partial x^2}\right] = 0 \qquad \text{(II.1)}$$

where the transverse displacement $u(x,t)$ is function of time $t$ and the position $x$ along the length of the beam (Figure II.1). $m(x)$ is the mass per unit length, $E$ is the Young's modulus, $I$ is the moment of inertia of the cross section around "z", $EI$ and $m$ being considered as constant according to direction $x$.

A general solution of this equation has the following form:

$$u(x,t) = \varphi(x)q(t) \qquad \text{(II.2)}$$

where $\varphi(x)$ is a function of the mode shapes, and $q(t)$ is the amplitude in the time.

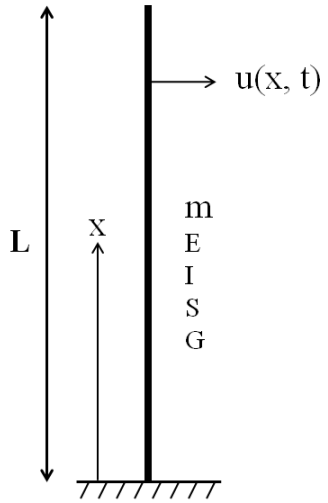


**Figure II. 1 :** Clamped-free beam: coordinates and mechanical properties. $m$: the mass per unit length, $E$: the Young's modulus of elasticity, $I$ : the moment of inertia of the cross section, $S$ : the section area , $G$ : the shear modulus , $L$ : the length of beam.

The above governing equation II.1 can be re-written as:

$$m(x)\varphi(x)\ddot{q}(t) + q(t)[EI(x)\varphi''(x)]'' = 0 \qquad \text{(II.3)}$$

Separating the two variables in the above partial differential equation will lead to two ordinary differential equations, such as:

$$\ddot{q}(t) + \omega^2\, q(t) = 0 \qquad \text{(II.4)}$$

$$[EI(x)\varphi''(x)]'' - \omega^2 m(x)\varphi(x) = 0 \qquad \text{(II.5)}$$

where $\omega$ is the angular frequency of the beam, such as $\omega^2 = {}^{k}/_{m}$.

Eq. II.4 is governing by the time function $q(t)$ which has the same form as the equation governing the free vibration of a single-degree-of-freedom (SDOF) system, with natural frequency $\omega$, and Eq. II.5 defines the eigenvalue problem together with the boundary conditions of the beam.

For a beam with uniform mass and stiffness (Chopra 1995), the second equation can be simplified as

$$\frac{\partial^4\varphi(x)}{\partial x^4} - \beta^4\varphi(x) = 0 \qquad \text{(II.6)}$$

where

$$\beta^4 = \frac{\omega^2 m}{EI} \quad \text{(II.7)}$$

The general solution of the aforementioned partial differential equation can be expressed as

$$\varphi(x) = C_1 \sin\beta x + C_2 \cos\beta x + C_3 \sinh\beta x + C_4 \cosh\beta x \quad \text{(II.8)}$$

where $C_1$, $C_2$, $C_3$ and $C_4$ are four constants to be determined.

In the case of a cantilever beam, the boundary conditions at the fixed support and the free end can provide the following four extra equations:

$$\begin{cases} \varphi(x) = 0 \\ \frac{\partial\varphi(x)}{\partial x} = 0 \end{cases} \quad \text{at } x = 0 \quad \text{(II.9)}$$

$$\begin{cases} M(x) = EI\frac{\partial^2\varphi(x)}{\partial x^2} = 0 \\ V(x) = EI\frac{\partial^3\varphi(x)}{\partial x^3} = 0 \end{cases} \quad \text{at the free end for } x = L \quad \text{(II.10)}$$

where $L$ is the length of the beam, $M(x)$ is the bending moment at location $x$, $V(x)$ is the base shear force at location $x$. Substituting the boundary condition equations (Eq. II.9 and II.10) into the general solution (Eq. II.8), we obtained the following equations:

$$C_4 = -C_2 \quad \text{(II.11)}$$
$$C_3 = -C_1 \quad \text{(II.12)}$$
$$C_1(\sin\beta L + \sinh\beta L) + C_2(\cos\beta L + \cosh\beta L) = 0 \quad \text{(II.13)}$$
$$C_1(\cos\beta L + \cosh\beta L) + C_2(-\sin\beta L + \sinh\beta L) = 0 \quad \text{(II.14)}$$

Equations (II.13) and (II.14) can be further transformed into a matrix form, i.e.:

$$\begin{bmatrix} \sin\beta L + \sinh\beta L & \cos\beta L + \cosh\beta L \\ \cos\beta L + \cosh\beta L & -\sin\beta L + \sinh\beta L \end{bmatrix} \begin{bmatrix} C_1 \\ C_2 \end{bmatrix} = \begin{bmatrix} 0 \\ 0 \end{bmatrix} \quad \text{(II.15)}$$

For a non-trivial solution, the determinate of the matrix must be zero. This leads to

$$1 + \cos\beta L \cdot \cosh\beta L = 0 \quad \text{(II.16)}$$

The numerical solutions which satisfy the equation (II.14) are as follows:

$\beta_n L = 1.8751, 4.6941, 7.8548, and\ 10.9960$ , for $n = 1,2,3,4$ respectively (II.17)

$\beta_n L \approx (2n-1)\frac{\pi}{2}$, for $n > 3$ (II.18)

Finally, by substituting equations (II.17) and (II.18) into equation (II.7), the natural frequencies $\omega_n$ of a cantilever Euler-Bernoulli beam with uniform mass and stiffness distribution can be determined from the following equation:

$\omega_n = \frac{(\beta_n L)^2}{L^2}\sqrt{\frac{EI}{m}}, n = 1,2,3, \ldots$ (II.19)

The expression of mode shape corresponding to each natural frequency can also be developed by combining equations (II.8) and (II.11) – (II.14). Finally, the shapes of the different modes are given in the following equation (Chopra, 2007):

$\varphi_n(x) = C_1\left[\cosh\beta_n x - \cos\beta_n x - \frac{\cosh\beta_n L + \cos\beta_n L}{\sinh\beta_n L + \sin\beta_n L}(\sinh\beta_n - \sin\beta_n\ x)\right]$ (II.20)

where $C_1$ is a constant equal to the vibration amplitude at this specific frequency.

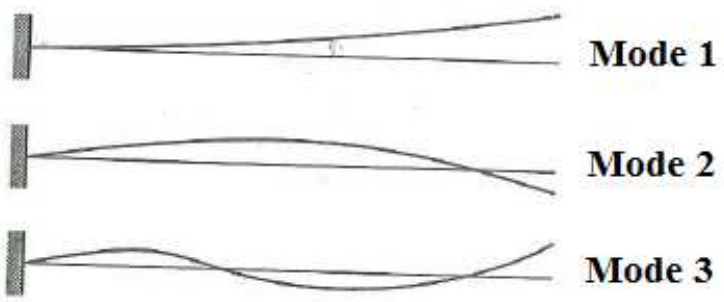


**Figure II. 2 :** First three vibration modes of a cantilever beam.

As indicated in equation (II.19), the natural frequency of each mode is proportional to the inverse of the squares of the length of the cantilever beam and to the stiffness and mass values. Then the frequencies have the following values:

$f_n = \frac{(\beta_n L)^2}{2\pi L^2}\sqrt{\frac{EI}{m}}$ (II.21)

$f_1 = \frac{0.5595}{L^2}\sqrt{\frac{EI}{m}}$ , $\frac{f_n}{f_1} = 0.7(2n-1)^2$ for $n > 1$ (II.22)

The ratio of the frequencies divide by the first frequency is:

$\frac{f_2}{f_1} = 6.3 \quad \frac{f_3}{f_1} = 17.5 \quad \frac{f_4}{f_1} = 34.3$ (II.23)

This distribution (6.3, 17.5, and 34.3) of frequencies is a characteristic of a clamped-free beam in bending.

## II.3 Effect of changes on the modal parameters

When a civil engineering structure is damaged, its mechanical properties are affected. This is the case for example of seismic damage for which the elements of the structure (walls, roofs, columns and beams) suffered cracks, changing the global Young's modulus (EI) of the structure. This is also the case when the connection between beams and columns or walls and roofs are damaged, reducing then the global strength and stiffness of the structure. A decrease in stiffness will result in a change of modal characteristics, namely frequencies, mode shapes and damping. Indeed, considering the case of an undamped cantilever beam, frequencies and mode shapes of the deformed beam are governed by the following equation:

$$(K - \lambda M)\phi = 0 \qquad \text{(II.24)}$$

That is the eigenvalues formulation of the global equation of the Cantilever beam (Eq. II.5). In this equation, *K* is the discrete multi DoFs system stiffness matrix (related with *EI*), *M* is the mass matrix and $\lambda$ and $\phi$ the eigenvalues and eigenvectors of the system, with $\lambda = \omega^2$.

Considering the same system after changing of its physical properties, Eq. II.24 becomes:

$$(K^* - \lambda^* M^*)\phi^* = 0 \qquad \text{(II.25)}$$

We can rewrite $K^*$ as function of *K*, by introducing the variation of stiffness $\delta K$ between the undamaged and damaged states such as $K^* = K + \delta K$. The same expression can be used for the mass, the eigenvectors and eigenvalues. Considering the fact that the damage does not produce variation of mass ($\delta M = 0$), and finally substituting into Equation II.24 the variations of the physical properties, we obtain the equation:

$$[(K + \delta K) - (\lambda + \delta\lambda)M)](\phi + \delta\phi) = 0 \qquad \text{(II.26)}$$

and

$$(K - M\lambda)(\phi + \delta\phi) + \delta K\phi + \delta K\delta\phi - \delta\lambda M\phi - \delta\lambda M\delta\phi = 0 \qquad \text{(II.27)}$$

From the Equation II.24, for a given non-trivial solution of $\phi$, we have $K - \lambda M = 0$. Moreover, by neglecting the second order term and by multiplying by $\phi^T$ the left part, Equation II.27 becomes:

$$\delta\lambda = \frac{\phi^T \delta K \phi}{\phi^T M\phi + \phi^T M\delta\phi} = \delta(\omega^2) = 2\omega\delta\omega \qquad \text{(II.28)}$$

Finally can be expressed as (Clough & Penzien, 1993) and Perrault (2013):

$$\delta\omega = \frac{1}{2\omega}\frac{\phi^T \delta K \phi}{\phi^T M \phi + \phi^T M \delta\phi} \quad \text{(II.29)}$$

For a multi-degree of freedom (MDOF) system, the frequency vector and stiffness and mass matrices are:

$$\delta\omega = \begin{Bmatrix} \delta\omega_1 \\ \vdots \\ \delta\omega_n \end{Bmatrix}; \quad \phi^T \delta K \phi = \begin{bmatrix} \delta k_1 & \dots & 0 \\ \vdots & \ddots & \vdots \\ 0 & \dots & \delta k_n \end{bmatrix}; \quad \phi^T M \phi = \begin{bmatrix} m_1 & \dots & 0 \\ \vdots & \ddots & \vdots \\ 0 & \dots & m_n \end{bmatrix};$$

Equation II.29 traduces that a stiffness changing is directly related with a frequency and mode shape variations, and a decrease of stiffness (i.e., $\delta K < 0$) produce a decrease of frequency. Almost all NDE methods for detecting and localizing the changes (or damage) use these fundamental properties by tracking the variation of mode shapes and frequencies between before and after an extreme event such as an earthquake. These methods will be applied for this work.

## II.4-Global methods for detection

### II.4.1 Frequency variation

Natural frequency-based methods use the natural frequency change of structures as the basic feature for damage detection. The choice of the natural frequency change is attractive because the natural frequencies can be conveniently measured from just a few accessible points on the structure and are usually less contaminated by experimental noise. However, several limitations must be accounted for such as complexity in structural modeling and damage and non-uniqueness of the solutions. The frequency changes caused by damage may be usually very small and may be buried in the changes caused by environmental and operational conditions (Clinton et al., 2006; Todorovska and Al Rjoub, 2006; Mikael et al., 2013) or by the wandering of the building motion in the mode shape bell, producing variation of frequency related to input signal (Michel and Gueguen, 2010). For this reason, the greatest success in the use of natural frequency shifts for damage identification of very small changes is in small simple laboratory structures with only single damage locations, under controlled experimental condition. Nevertheless, in case of strong damage such as those produced by earthquake, the frequency shift is a simple and operative marker that can be used (e.g., Dunand et al., 2004; Celebi et al., Clinton et al., 2006).

Most of new developments were supported by the use of ambient vibrations AV. AV are produced by the wind (low frequencies <1 Hz), internal sources (machinery, lift at high frequencies) and seismic noise (broadband). AV have been commonly used to monitor structures in civil, mechanical and aerospace engineering communities for a long time. The use of AV methods provides relevant informations on the elastic characteristics of the

building at reducing cost. AV modal analysis based methods provide also an effective tool for short- and/or long-term health monitoring of buildings, such as those due to ageing effect or after an extreme event, mainly by comparing initial and final values of frequencies, damping and mode shapes (Dunand et al., 2004). Most of the previous studies conducted in civil engineering structures (e.g., Clinton et al. 2006; Deraemaker et al., 2008; Hua et al., 2007; Nayeri et al., 2008; Mikael et al., 2013) have shown that the temperature is the most significant cause of variability of modal frequencies. Most of scientific papers dealing with experimental and in-situ data are focused on the fundamental frequency tracking. For instance, experimental and numerical analysis showed the efficiency of frequency analysis for damage detection considering fundamental mode and overtones (e.g., Kim and Stubbs, 2003; Xu et al., 2007). Nevertheless, the variation of the parameters of each mode will not be affected in the same manner, depending on the position, the amplitude and the nature of the damage (Baillet et al., 2013). Moreover, a major difficulty to overcome is that the damage can be very localized and it may not significantly influence the overall response of a structure evaluated only with the fundamental frequency.

As aforementioned, the presence of damage, i.e. a crack or a diminution of the Young's modulus, in cantilever-type structures causes local variation in the stiffness and results in a decrease in the natural frequencies of the structure. The natural frequency is proportional to the square root of stiffness, thus a relatively large stiffness change is required before significant frequency change can be detected. The extent of the drop in the natural frequency depends on the location and position of damage with respect to the mode shape of a particular mode of vibration (Moradalizadeh, 1990).

Askeegard and Mossing (1988) investigated seasonal changes of modal parameters of a reinforced concrete (RC) footbridge over a period of three years. They observed about 10% changes in frequency and concluded that this was mainly due to variation of ambient temperature. Farrar et al (1997) found that the first eigenfrequency of the Alamosa Canyon Bridge was subjected to changes of approximately 5% during a 24 hour time period. They also attributed it to the variation of temperature.

Peeters and de Roeck (1998) reported changes in the first four eigenfrequencies of the Z24 Bridge are in the range of 14-18%. These changes were mainly due to the increased elastic modulus of the asphalt at temperatures below zero Celsius degrees. Alampalli (1998) reported that the second and third eigenfrequencies of a small bridge were subjected to an increase of 40-50% due to freezing of the supports.

From their observations of forced and ambient vibration tests on the Hakucho Bridge, Fujino et al (2000) identified that the natural frequency of the first vertical bending mode decreased noticeably as the wind speed increased. In conjunction with temperature changes, other ambient conditions such as cloud cover, humidity, direction of temperature change, etc. were observed to affect bridge boundary conditions significantly (Aktan el al 1997).

Morassi (2001) presented single crack identification in a vibrating rod based on the knowledge of the damage-induced shifts in a pair of natural frequencies. The analysis is based on an explicit expression of the frequency sensitivity to damage and enables non uniform bars under general boundary conditions to be considered. Some of the results are also valid for cracked beams in bending. Messina et al. (1998) and Williams and Messina (1999) presented a technique capable of tackling multiple damage location and identification based on natural frequency shifts. The method was based on using a linearized sensitivity of frequency shifts to damage and assumed changes in stiffness only. The algorithm was successfully verified experimentally on three beams in laboratory with up to two damage locations. Surendra *et al*. (2000) proposed that frequency shifts be used for predicting the fatigue life of a structure by correlating the rate of decrease of the first natural frequency with the fatigue life.

In buildings, considered before as less sensitive to the wandering, few publications are focused on the frequency shift due to boundary condition. Recently, Clinton et al. (2006) studied the evolution of the first two resonance frequencies (East-West and North-South) of the Millikan Library in south California since its construction in 1967, putting in evidence a drop of frequency due to the seismic events more or less strong. Clinton et al. (2006) processed continuous ambient vibration records to study the drop in the natural frequency of buildings, resulting from a decrease in system stiffness with the progressive damaging during earthquakes.

Figure II.2 shows the reduction of the two natural frequencies in the Californian building observed by Clinton et al. (2006) for various earthquakes, forced experiment and ambient vibrations analysis since 1967. The two frequencies decrease 21.4% on the East-west component and 12.1% on the North-south component; this loss of the two natural frequencies indicates the loss of stiffness of the structure and was interpreted as an indicator of structural damage, being given the mass of the structure remains constant over time.

In the same study, Clinton et al. (2006) have shown, by analyzing two-year-long continuous records from the Caltech's Millikan Library, which the natural frequencies of a building can change significantly due to environmental factors, such as rainfall, wind speed, and temperature.

Dunand et al. (2006) showed the same trend considering several Californian buildings and they also concluded on a decrease of at least 30% of stiffness during the co-seismic time, without producing permanent shift related with damage. The physical reason explaining this recovery after extreme event is related to the opening and closing process of the pre-existing cracks, producing a temporary shift of frequency.

This has been also observed during the Yorba Linda earthquake recorded at the Factor building (Kholer et al., 2005), a 17-story moment-resisting steel-frame structure with an embedded 72-channel accelerometer network. This is certainly the most heavily and densely instrumented building in North America (Figure II.3).

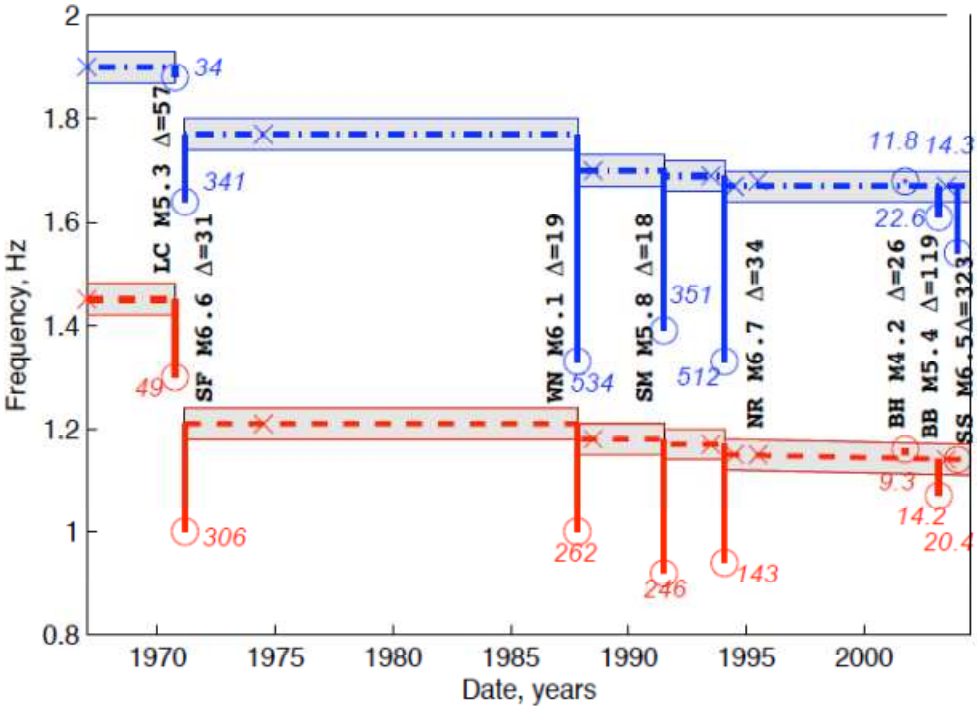


**Figure II. 3 :** Evolution of two natural frequencies of the Millikan Library, South California from Clinton et al. (2006). Dashed lines are east-west natural frequencies; dashed-dotted lines are north-south natural frequencies, all from forced vibration testing. Shaded area is the likely region of natural frequencies taking into consideration errors in measurement, caused by unknown shaker weight configuration and weather conditions for each test, and experimental error. Crosses indicate the actual time of a forced vibration measurement. Circles indicate the natural frequency estimated from the strong motion recording of the event, with the number in italics giving the peak acceleration recorded for the event (cm/sec2).

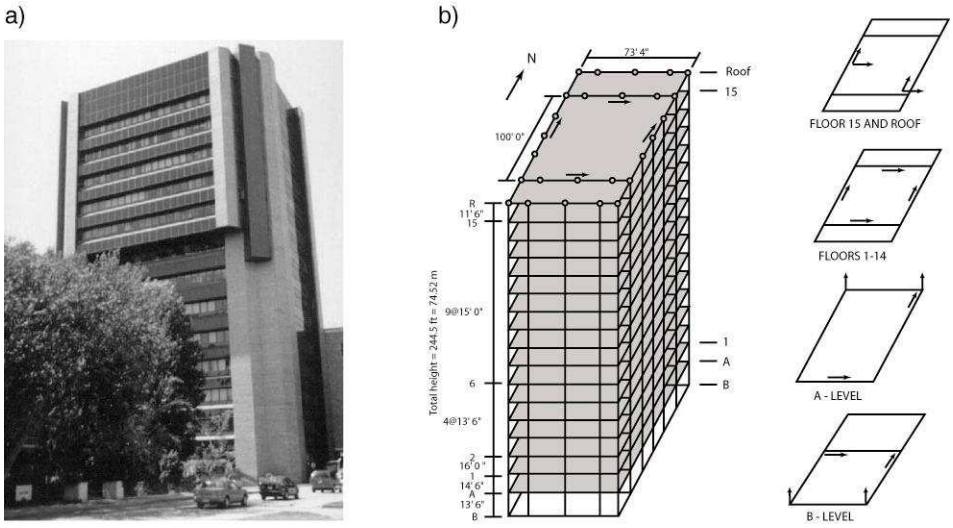


**Figure II. 4 :** (a) Photo of Factor building taken from the northeast side of the building, and (b) diagram of Factor building sensor locations. Arrows show polarities of sensors on each floor. (From Kholer et al. 2005).

This local earthquake recorded by the Factor building sensors occurred on 3 September 2002 near Yorba Linda, California, with local magnitude ($M_L$= 4.7 ). For example in Figure II.4 observed by Kohler et al. (2005), the frequency of the first mode of deformation decreases by about 10%, but the frequency recovers the pre-earthquake ambient vibration levels within 5 minutes after the Yorba Linda earthquake has occurred.

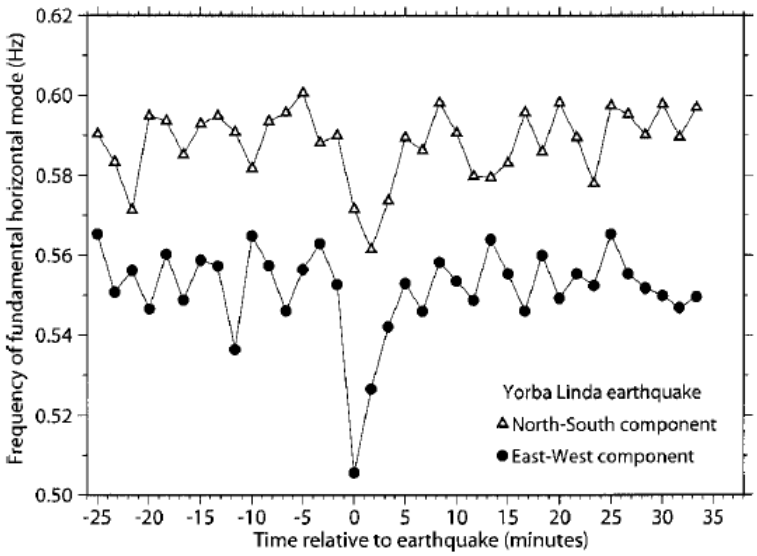


**Figure II. 5 :** Change in fundamental horizontal mode natural frequency before and after the Yorba Linda earthquake. The frequency peaks were measured from 100-second acceleration segments from either 12th or 13th floor waveforms before and after the earthquake, band-pass filtered for frequencies between 0.45 and 0.65 Hz. A least-squares fit to a Gaussian was used to find the central frequency peak. (From Kholer et al. (2005)).

The results showed that measurable softening effects are occurring for small earthquakes due to changes in the stiffness of the building or soil when amplitudes get larger as reported by Kohler et al. (2005). In fact, the variation observed during this earthquake may have several origins, since the frequency measured at the top of the structure is the apparent frequency of the soil-structure system, i.e. the flexible-based structure including soil-structure interaction. It is well known that the apparent frequency is related to the shear-wave velocity Vs of the soil. The same building resting on a stiff or a soft soil has two different apparent frequencies. We can also imagine that during an event (even moderate event), slight decrease of Vs can be observed, producing a decrease of the soil-structure frequency and then the apparent frequency recorded at the top of the building. Natural frequencies of a soil-structure system are known to vary under different levels of excitation and recent researches (Clinton et al., 2006; Kohler et al., 2005) indicated that during small shaking events, there is a measurable change in recorded natural frequencies of various types of structures.

This observation has been reported by Todorovska and Trifunac (2007) who analyzed the shift of the fixed-based and the flexible-based frequencies during the lifetime of one

Californian building, showing the soil-structure effects on the frequency shift. Also reported by Michel et al. (2011) who analyzed the decrease of the apparent frequency with respect to the fixed-based frequency at the City-Hall building in Grenoble, concluding the soil-structure influence on the frequency shift even for small-to-moderate earthquakes; and by Todorovska and Al Rjoub (2006) who interpreted the frequency wandering of the Milikan Library in California being influenced by the rain falls and the water content variation of the soil.

Recent initiatives started, taking advantage of the reduced cost of new instruments (such as MEMS sensor, Micro-Electro-Mechanical Systems), to increase the number of buildings monitored. For example, the Quake Catcher Network (QCN, Cochran et al., 2009) employs existing networked laptops and desktops to form a dense, distributed computing seismic network installed in buildings, schools etc... The QCN capitalizes on the main advantage of distributed computing—achieving large numbers of processors with low infrastructure costs—to provide a dense, large-scale seismic network. While MEMS accelerometers are less sensitive than typical broadband or short-period sensors, a higher number of stations is advantageous for both the study of earthquakes, structural health monitoring and, potentially, earthquake crisis management.

In fact, Dunand et al. (2004) contributed to assessing the building post-seismic integrity using single AV recording at the building top shaken by the Boumerdes (Algeria) Earthquake of May 21, 2003. They showed how the frequency shift evaluated using AV could be used to complement and improve seismic survey of damaged buildings.

In conclusion, the focus on the use of frequency change-based damage identification method can be successfully applied to simple structures with small cracks (typically, a slender beam-type structure with an artificially induced crack) in a controlled laboratory condition. However, its applications for real complex structures or multiple/ severe damage detection are promising, the accuracy of the frequency value recorded by ambient vibrations being a key-point for recording small changes. Mikael et al. (2013) on real buildings and Baillet et al. (2013) on models showed how small frequency shifts could be detected (less than 0.1%) using the Random Decrement Technique.

### II.4.2 Modal Assurance Criterion (MAC)

Compared to using natural frequencies, the advantages of using the mode shapes as a basic feature for damage detection are obvious. First, the mode shapes contain local information, which makes them more sensitive to local damages and enables them to be used directly in multiple damage detection. Second, the mode shapes are less sensitive to environmental effects, such as temperature, than natural frequencies Farrar et al. (1997).

A Modal Assurance Criterion (MAC) sometimes referred to as a modal correlation coefficient is calculated to quantify the correlation between two mode shapes (Allemang and Brown, 1982). It is often utilized to compare mode shapes derived from analytical models and measurements as quality criterion.

The MAC value is a global index of damage detection and gives information about which modes have been changed the most. Thus, the reduction of a MAC value may be an indication of damage. Let us suppose that $[\phi_A]$ and $[\phi_B]$ are matrices made-up of $m_A$ and $m_B$ mode shapes measured in *n* measurement points. These are thus matrices of dimension n × $m_A$ and n × $m_B$. For the $i = 1,2,\dots,m_A$ and $j = 1,2,\dots,m_B$ mode shapes, the MAC is defined as:

$$MAC_{ij} = \frac{\left|\sum_{k=1}^{n}(\phi_A)_k^i\,(\phi_B)_k^j\right|^2}{\sum_{k=1}^{n}\left([\phi_A]_k^i\right)^2\,\sum_{k=1}^{n}\left([\phi_B]_k^j\right)^2} \qquad \text{(II.30)}$$

Where, $[\phi_A]_k^i$ and $[\phi_B]_k^j$ are the $k^{th}$ component of mode shapes $[\phi_A]^i$ and $[\phi_B]^j$. The MAC coefficient presents the correlation degree between $i^{th}$ and $j^{th}$ mode shapes in A and B, and the diagonal value of MAC matrix varies from 0 to 1. The MAC value can be considered as a measure of the similarity of two mode shapes. A MAC value of 1 is a perfect match and a value of 0 means they are completely dissimilar. Thus, the reduction of a MAC value may be an indication of damage.

Ewins (1985) points out that, in practice, correlated modes will yield a value greater than 0.9, and uncorrelated modes will yield a value less than 0.05. Salawu and Williams (1995) tested a reinforced concrete bridge before and after repair. Although the results show the first seven natural frequencies shifted by less than 3%, but the MAC values showed substantial change leading the authors to argue that comparison of mode shapes is a more robust technique for damage detection than shifts in natural frequencies. Ndambi et al. (2002) presented a comparative study of damage detection methods based on laboratory tests of two cracked RC beams. Among several methods for detecting damage, they used the frequency and MAC values. The results show that (1) the eigenfrequency evolutions can follow the damage severity but are not influenced by the crack damage locations; (2) the MAC factors are, in contrast, less sensitive to crack damage compared with eigenfrequencies.

## II.5-Local methods for detection

### II.5.1 - Methods Based on Mode Shape Curvature

#### II.5.1.1 - Mode Shape Curvature Method (MSC)

Following Allemang et al (1982), Pandey et al. (1991), Ratcliffe (1997) used the change in mode shape curvature (MSC) as an indicator of damage, assuming that structural damage affects the structure's stiffness matrix (Equation II.29). It has been reported that damage of the structure causes a change in mode shape curvature and can be considered as a good indicator for detecting and localizing the damage. According to elementary beam theory, the curvature at a location *x* along a beam, $v''$(x), is:

$$v'' = \frac{M(x)}{EI} \tag{II.31}$$

where *M(x)* is the bending moment at location *x*, *E* is the Young's modulus of elasticity and *I* is the moment of inertia of the cross section. It is evident from Eq. (II.31) that any reduction in flexural rigidity (*EI*) due to damage will lead to an increase in curvature, and that the difference between pre- and post-damage curvature mode shapes will be largest at the location of damage. The curvatures, usually calculated by numerical differentiation of displacement mode shapes at equally spaced measurement points, is expressed as

$$\phi''_{i,j} = \frac{\phi_{(i+1),j} - 2\phi_{i,j} + \phi_{(i-1),j}}{h^2} \tag{II.32}$$

where $\phi''_{i,j}$ represents the modal curvature, first subscript *i* represents node number, second subscript *j* represents the corresponding mode shape number, *h* represents element length as the beam is discretized with elements of equal length (distance between the nodes) and $\phi_{i,j}$ represents the mass normalized modal value for the i$^{th}$ node in the j$^{th}$ mode.

The location of the damage is assessed by the largest computed absolute changes in MSCs of the damaged and undamaged structure as given by:

$$MSC_i = \sum_{j=1}^{N} \Delta\phi''_{i,j} = \sum_{j=1}^{N} \left| \left(\phi''^{*}_{i,j}\right) - \left(\phi''_{i,j}\right) \right| \tag{II.33}$$

where $\phi''$ and $\phi''^{*}$ stand for the mode shape second derivative of undamaged and damaged state, respectively, *N* is the number of measured mode shape curvature vectors, index *i* represents the measured point number and *j* is the mode shape number.

By plotting the difference in MSCs between the intact and the damaged case, a peak appears at the damaged element indicating the presence of changes. The curvature values are computed from the displacement mode shape using the central difference operator from Eq. (II.32). For example, Pandey et al. (1991) found that the modal curvature is far more sensitive damage indicator than the MAC (Modal Assurance Criterion). The most popular approach is the utilization of only a few lower order curvature modes to identify the damage location. Result showed that the difference of curvature mode shapes from undamaged and damaged structure can be a good indicator of damage. Pandey et al. (1991) used a finite element model (FEM) for a cantilever clamped-free beam model to demonstrate the applicability of the method, with a reduction in Young's modulus (E) of 50% at one third of the span. MSC has been successfully used so far for identification of various damages in the isotropic beams by Maia et al (2003), Palacz et al (2002), laminated composite beams by Lestari et al (2007), Hamey et al (2004), or wooden beam by Parloo et al (2003). Salawu and Williams (1994) compared the performance of both curvature and displacement mode shapes for locating damage, which confirmed the advantage of curvature mode in locating damage as compared to the displacement mode.

An important remark could be observed from the results of Pandey *et al*. (1991) that is, the difference in *MSCs* between the intact and the damaged beam showed not only a high peak at the fault position but also some small peaks at different undamaged locations for the higher modes, introducing some false detections. This can cause confusion to the analyst in a practical application in which one does not known in advantage the location of cracks or damage. One conclusion is the value of MSC using a large number of modes is strongly dependent on the position of the damage. Hence, in order to reduce the possibility of false alarms, Pandey et al. (1991) concluded that a few number of the first curvature mode shapes must be used for damage identification.

The sensitivity and the effectiveness of MSC method were also questioned by several researchers with experimental evidence showing that the modal curvature by itself cannot locate small damages (Ratcliffe, 2000). For example, Abdel Wahab and De Roeck (1999) investigated the accuracy of using the central difference approximation to compute the MSC based on finite element analysis. The authors suggested that a fine mesh is required to derive the modal curvature correctly for the higher modes and that the first mode will provide the most reliable curvature in practical application due to the limited number of sensors needed.

### II.5.1.2 - Mode Shape Curvature Squared Method (MSCS)

Ho and Ewins (2000) stated that higher derivatives of mode shapes are more sensitive to damage and they proposed the mode shape curvature squared (MSCS) method for improving the localization of the damage. This method is an improvement on the MSC, and it is mathematically expressed as

$$MSCS_i = \sum_{j=1}^{N} \Delta(\phi''_{i,j})^2 = \sum_{j=1}^{N} \left| \left(\phi''^{\,*}_{i,j}\right)^2 - \left(\phi''_{i,j}\right)^2 \right| \qquad \text{(II.34)}$$

In this case, in the same manner as MSC method, the location of damage by MSCS is identified as the place where the absolute difference between curvatures of the damaged and the undamaged structure is maximum. The changes in the curvature mode shape increase with the increasing size of damage and this information can be used to obtain also the amount of damage in the structure. Pandey, et al. (1991) did not present a means to quantify when changes in curvature are indicative of damage, hence, some engineering judgment is required when examining plots of the change of curvature as a function of position. For multiple modes, the absolute values of change in curvature associated with each mode can be summed to yield a damage parameter for a particular location.

### II.5.2 - Methods Based on Changes in Flexibility

Change in flexibility matrix (CIF) and change in uniform load surface curvature (ULS) are two basic algorithms based on changes in flexibility of a beam.

The basic advantage of the methods is that damage localization requires only the first few modes of the structure (typically the lowest frequency modes). Typically, damage is detected using flexibility matrices by comparing the flexibility matrix computed using the modes of the damaged structure to the flexibility matrix computed using the modes of the undamaged structure or the flexibility matrix from a FE model. Because of the inverse relationship to the square of the modal frequencies, the measured flexibility matrix is most sensitive to changes of the modes in the lower frequency range. The flexibility matrix converges rapidly with increasing values of frequency, an advantage of using flexibility instead of stiffness.

### II.5.2.1 - Change in flexibility method (CIF)

As an alternative for using changes in the modal parameters of a structure for detecting damage, the modal flexibility matrix includes the influence of both the mode shapes and the natural frequencies. Pandey and Biswas (1994) presented a damage detection and location method based on changes in the measured flexibility of the structure. This method takes into account the flexibility of the structure before and after damage. Only a few numbers of resonant frequencies and modes are needed. This procedure is tested with numerical examples and then with experimental data collected on a wide flange steel beam. Results of the numerical and experimental examples show that estimates of the damage condition and the location of the damage could be obtained from just the first two measured modes of the structure (Pandey and Biswas, 1995).

Raghavendrachar and Aktan (1992) also calculated flexibility using the mode shapes and conclude that it is a superior indicator to examine the raw mode shape data. They noted that higher modes would reveal local damage but that these higher modes are more difficult to identify experimentally on a real case structure such as a bridge. Toksoy and Aktan (1994) computed the measured flexibility of a bridge and examine the cross-sectional deflection profiles with and without a baseline data set. They observe that anomalies in the deflection profile can indicate damage even without a baseline data set.

For the undamaged structure, the flexibility matrix of a structure [F] can be approximated using the unit-mass normalized modal data as:

$$[F] \approx [\phi][\Omega]^{-1}[\phi]^T \approx \sum_{i=1}^{N} \frac{1}{\omega_i^2}\{\phi_i\}\{\phi_i\}^T \qquad \text{(II.35)}$$

where $\omega_i$ is the i$^{th}$ angular natural frequency, $\{\phi_i\}$ is the i$^{th}$ unit-mass normalized mode shape, $\{\phi\}$ *is* the mass normalized modal vectors; $\Omega$ is the modal stiffness matrix (= diag ($\omega_i^2$)), and $N$ is the number of measured or calculated modes. The flexibility matrix, [$F$], in Eq. (II.35) is an approximation because it is generally calculated using the lower measured modes only. Similarly, for the damaged structure, the same expression can be used:

$$[F^*] \approx [\phi^*][\Omega^*]^{-1}[\phi^*]^T \approx \sum_{i=1}^{N} \frac{1}{(\omega_i^*)^2}\{\phi^*{}_i\}\{\phi^*{}_i\}^T \quad \text{(II.36)}$$

where the asterisks mean that the flexibility matrix and mode shapes correspond to the damaged structure. From the pre- and post-damage flexibility matrices, a measure of the flexibility change caused by the damage can be obtained from the difference of the respective matrices, i.e.

$$[\Delta F] = [F^*] - [F] \quad \text{(II.37)}$$

Theoretically, and as shown in Equation II.31, structural damage reduces stiffness and increases flexibility. Increase in structural flexibility can therefore serve as a good indicator of the degree of structural deterioration. If $\delta_{ij}$ is an element of the matrix [ΔF], then the absolute maximum value, $\bar{\delta}_j$, of the elements of each column in [ΔF] is defined as:

$$\bar{\delta}_j = max[\delta_{ij}] \qquad i = 1, \dots, n \quad \text{(II.38)}$$

The position corresponding to the largest value of $\bar{\delta}_j$ is taken to indicate the location of damage.

### II.5.2.2 - Change in uniform load surface curvature (ULS)

Zhang and Aktan (1995) combined certain aspects of the MSC method and flexibility method to develop the change in uniform load surface curvature (ULS) method by considering the flexibility matrix as the translational displacement under a unit load at j$^{th}$ DOF. The basic idea is that a localized loss of stiffness will produce a curvature increase at the same location. Since the flexibility matrices, before and after damage, can be approximated by the modal parameters (Eq. II.35 and II.36), the quantities $F_1$ through $F_n$ (with and without the asterisk) correspond to columns of the flexibility matrix. Zhang and Aktan (1995) stated that the change in curvature of the uniform load surface can be used to determine the location of damage. In terms of the curvature of the uniform load surface, the curvature change at location *i* is evaluated as follows

$$\Delta F_i'' = \sum_{i=1}^{N} \left| \{F_i^{*''}\} - \{F_i''\} \right| \quad \text{(II.39)}$$

where $F_i^{*''}$ and $F_i''$ are the damaged and undamaged curvature of the uniform load surface at the $i^{th}$ degree of freedom, respectively. $\Delta F_i''$ represents the absolute curvature change, and $N$ represent the number of the degree of freedom (or identified number of mode shapes). The elements of $\Delta F_i''$ that have comparatively large values correspond to damage location. Note that the absolute change in curvature is first evaluated for each unit load flexibility shape and then summed. The curvature of the uniform load surface can be obtained with a central

difference operator as suggested by these authors. This method requires mass-normalized mode shapes.

Zhang and Aktan (1995) studied the modal flexibility and its derivative 'uniform load surface' (ULS) to identify damage in a numerical simulation of the Cross County highway bridge near Cincinnati, OH. Results from impact and forced vibration modal tests were used to benchmark a numerical model of the bridge. Damage was introduced in the numerical model by changing the stiffness of one element in the model. The change in uniform load surface (ULS) was shown to be a sensitive indicator of this local damage. Consequently, it is less sensitive to noise compared to the mode shapes based methods.

Wu and Law (2004, 2005) applied the ULS curvature to plate structures for damage localization and quantification. The numerical examples considering different support conditions, measurement noises, mode truncation, and sensor sparsity were studied to evaluate the effectiveness of the proposed method. It is found that the ULS curvature is sensitive to the presence of local damages, even with the truncated, incomplete, and noisy measurements, making this method a good candidate for experimental damage assessment on real structures.

# CHAPITRE III

# DETECTION AND LOCALIZATION OF CHANGES: THE EFFICIENCY OF METHODS USING EIGENMODES MODELING

**Abstract -** In this chapter, we will focus on testing several methods using the variation of the mode shapes and frequencies between a damaged and undamaged condition. Several methods found in the scientific literature will be applied to a theoretical bending beam, modeled using Finite Element Method. In order to test the efficiency of the method for the three first levels LV of NDE methods, different position and severity of damage, including single and multiple damage position are tested. After describing the theoretical beam used in this chapter, the global and local methods will be presented

# III.1-Introduction

In this chapter, we propose a study based on model analysis using finite element modeling (FEM) using numerical analysis resuming on actual experimental conditions, for applying non-destructive damage evaluation (NDE) to detect and locate the damage of a clamped- free beam.

Since the final goal of this work is to provide experimental analysis of the damage, two main objectives are pursued. Since the non-destructive damage evaluation (NDE) methods listed before do not use the same number of modes, the first objectives of this analysis is to test the influences of higher modes for improving or not the localization. As often, the experimental modal analysis does not provide accurate higher modes, and the choice of the NDE method will be conditioned by its in-situ feasibility. The second objective of the numerical analysis is to evaluate the efficiency of the NDE methods for detecting and localizing the damage, by comparing several configurations (single or multiple-damage, extended or narrow damage and small or strong damage), modeling providing an accurate estimate of the mode shapes and the frequencies. In all cases, we will keep in mind the final goal of this work, i.e. applying these methods for in-situ analysis.

# III.2-The models

The modeling done in this study with finite elements modeling in 1D is made of a structural continuous Plexiglas beam anchored at the bottom and free at the extremity (i.e. clamped-free beam). The software used is RDM6, was developed by Y.Debard (IUT du Mans, Department of Mechanical and Production Engineering). Finite element analysis package is used to perform an eigenvalue analysis to generate the natural frequencies and mode shapes of the undamaged and damaged beam. The 1D model is imported into RDM6 and the modal analysis is carried out to estimate the eigenvalues and eigenvectors. Then, the theory of elastic dynamics is used for determining the natural frequencies and the corresponding mode shapes of an undamped system.

The general governing equation of motion for free vibration can be written as:

$$[M]\{\ddot{u}\} + [K]\{u\} = 0 \qquad \text{(III.1)}$$

where $[M]$ is the structural mass matrix and $[K]$ is the stiffness matrix. If the displacement $u(x, y, t)$ is written in terms of $n$ eigenvectors $\phi_i(x, y)$ and the time dependent modal coordinate $q_i(t)$ as:

$$u(x, y, t) = \sum_{i=1}^{n} \phi_i\,(x, y) q_i(t) \qquad \text{(III.2)}$$

then the eigenvalues and the corresponding eigenvectors can be calculated from the equilibrium equations:

$$[K]\{\phi_i\} = \omega_i^2[M]\{\phi_i\} \quad \text{(III.3)}$$

Based on the orthogonal properties of the eigenvectors, we obtain the expressions for modal frequencies and corresponding mode shapes:

$$\{\phi_i\}^T[K]\{\phi_i\} = \omega_i^2\,\{\phi_i\}^T[M]\{\phi_i\} \quad \text{(III.4)}$$

Let $\{\phi_i\}^T[K]\{\phi_i\} = K_i$ and $\{\phi_i\}^T[M]\{\phi_i\} = M_i$ . Then we get

$$\omega_i{}^2 = \frac{K_i}{M_i} \quad \text{(III.5)}$$

where $M_i$ and $K_i$ are the mass and stiffness of the beam in $i^{th}$ mode corresponding to the eigenvector $\phi_i$ and the resonant frequency $\omega_i$.

The software RDM6 calculates the eigenmodes of the beam by iterations. For an angular frequency $\omega$, $\omega_{i-1}$ and $\omega_i$ are the values of frequency obtained during two successive iterations. The iteration stops when the amount $\frac{|\omega_{i-1}-\omega_i|}{\omega_i}$ is smaller than the chosen precision. The precision used for the calculation of natural frequencies in this study is 0.01 Hz.

All of the modeling analysis using finite element analysis developed in this work is based on a Plexiglas beam with properties displayed in Table III.1.

| Material | Plexiglas |
|---|---|
| Length | 1 m |
| Width | 0.05 m |
| Depth | 0.01 m |
| Poisson's ratio | 0.4 |
| Mass density | 1165kg/$m^3$ |
| Modulus of elasticity | 5.4 GPa |
| Moment of inertia | $4 \cdot 10^{-9} m^4$ |

**Table III. 1 :** Geometric and material properties of cantilever beam.

The mesh consists of beam finite element and the number of elements is 200, obtained by a Delaunay triangulation. The beam is divided into twenty-eight sections having 29 nodes spread along the entire length of the beam with a 3.5 cm interval. Figure III.1 shows the modeling setup used to study the bending vibration in the 1D plane of the beam. Boundary conditions are clamped-free configuration used to validate the performance of damage detection methods aforementioned.

**Figure III. 1:** Clamped-free beam model in 1D with modal analysis using FEM by RDM6.

Each intermediate node has three degrees of freedom, translational (along *x* and *y*) and rotational (w.r.t *z*), used at each node in the finite element analysis. Since in any experimental approach (in laboratory or in-situ for real structures) rotations are not measured, only the translation degree of freedom along the *x* axis was considered in this study. Moreover, since we are interested only in flexural modes of vibration, translation along the *y* axis will be also neglected. The comparison between the theoretical computed from equation II.19 and modeling estimate of frequencies are given in Table III.2, showing a good estimate of the frequency, with a very small numerical dispersion. Finally, the mode shapes are extracted from the 29 nodes spread along the beam length.

| Mode No. | Theory [Hz] | Modal analysis using FEM [Hz] | Difference % |
|---|---|---|---|
| 1 | 3.4 | 3.4 | 0 |
| 2 | 21.3 | 21.7 | 1.8 |
| 3 | 59.7 | 61 | 2.1 |
| 4 | 117.1 | 119.5 | 2 |
| 5 | 193.6 | 197.5 | 1.9 |
| 6 | 289.3 | 294.9 | 1.8 |
| 7 | 404.1 | 411.6 | 1.8 |
| 8 | 538 | 547.7 | 1.7 |

**Table III. 2 :** Comparison of theoretical modal frequencies versus modal analysis using Finite element modeling by RDM6 of the clamped-free beam.

## III.3- Comparative study of damage detection algorithm for beams

In this study, a comparative study based on the finite element model was conducted to evaluate the four NDE algorithms considered in § II for the clamped-free beam.The four NDE methods considered are (1) Mode Shape Curvature Method (MSC), (2) Mode Shape Curvature Squared Method (MSCS), (3) Change in flexibility method (CIF), and (4) Change in uniform load surface curvature (ULS). They require the comparison of the frequencies and mode shapes before and after the damage process for locating and evaluating damage in a beam. For each scenario of damage, the structural dynamic characteristics (frequencies and mode shapes) are calculated along the beam and compared to the undamaged beam case. The damage is considered as a reduction of the Young's modulus, selecting an element of the beam where this reduction is applied. Table III.3 shows a summary of the eleven scenarios (S1 to S11) of the damage applied to the clamped-free beam with different damage severity, considering single, large and multiple damage positions. Four different severities of damage are considered, with $a$ = 0.2, 0.5, 0.7 and 0.9, where '$a$' corresponds to the reduction factor of the Young's modulus such as:

$$E^* = (1 - a) \cdot E \qquad \text{(III.6)}$$

where $E^*$ and $E$ are the damaged and undamaged Young's modulus, respectively.

| **Scenario S** | **1** | **2** | **3** | **4** | **5** | **6** | **7** | **8** | **9** | **10** | **11** |
|---|---|---|---|---|---|---|---|---|---|---|---|
| All sections | 0.9 | | | | | | | | | | |
| A – 30.0-33.5cm | | 0.9 | 0.7 | 0.5 | 0.2 | | | | 0.9 | 0.9 | 0.5 |
| B – 61.5-65.0cm | | | | | | 0.9 | | | 0.9 | 0.7 | 0.7 |
| C – 86.0-89.5cm | | | | | | | 0.9 | | 0.9 | 0.5 | 0.9 |
| D – 30.0-47.5cm | | | | | | | | 0.9 | | | |

**Table III. 3 :** Damage scenarios applied to the clamped-free beam using Finite element modeling. The values of the table correspond to '*a*', the damage severity parameter; the position of damage (POD) along the beam are presented on the first column.

The parameters of each NDE method is then computed and displayed along the height of the beam and compared to the expected position and amount of damage.

### III.3.1. – Global methods for detecting changes

To confirm the influence and sensitivity of modes shapes depending on the position of damage, we have first damaged each section of the beam from bottom to up (i.e., from section 1 to 28) with a constant damage severity *a=0.9* (S1, Table III.3). The comparison has been done with respect the undamaged beam and finally, the natural frequency change ratio (FR) is calculated. This former ratio is computed as follows:

$$FR = \left(\frac{f_u - f_d}{f_u}\right) \cdot 100 \qquad \text{(III.7)}$$

where $f_u$ and $f_d$ correspond to undamaged and damaged frequencies, respectively.

Figure III.2 shows the effects of the damage position along the beam on FR and a square of the curvature of the mode shapes. We observe that the effect of the damage on the modal frequency is closely related with its position along the beam. We note a succession of minimum and maximum values. In fact, we observed the same trend between the FR (black curve) and the square of the curvature of the mode shapes (red curve) for the first four mode shapes. This means that the FR is linearly proportional to the square of curvature mode shapes. This observation is confirmed by Morassi (1993) using this following equation:

$$FR^{(i)} = \left(\frac{F_u - F_d}{F_u}\right) \times 100 = \frac{\left[a(s)u_0^{(i)''}(s)\right]^2}{K_R F_u} \times 100$$

When $u_0^{(i)''}(s) = 0 \rightarrow FR = 0$ , s: position of the damage.

$u_0^{(i)''}(s) = max \rightarrow FR = max$ ; $u_0^{(i)''}(s) = min \rightarrow FR = min$

Where $a(x)$ is the bending stiffness, $u_0^{(i)''}(x)$ the square of the curvature of the mode shapes and $K_R$ is the severity of damage.

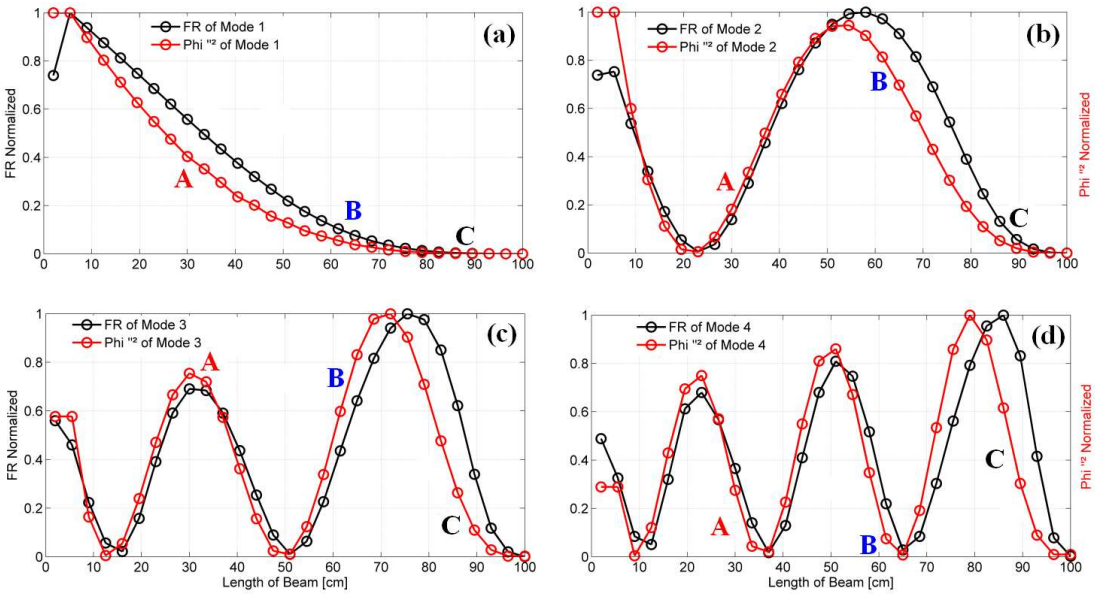


**Figure III. 2 :** Sensitivity of the four first modes with the position of the damage varying from the bottom to the top of the beam (Scenario S1). The black curves correspond to the frequency ratio (FR) normalized to the maximum, the red curve corresponds the square of the curvature of the mode shapes (normalized) and A, B and C correspond to the position of the damage corresponding to scenarios listed in Table III.3. a) Mode 1; b) Mode 2; c) Mode 3; d) Mode 4.

Considering the first modes, we observe that for this theoretical beam, the FR is strongly dependent on the position of the damage along the beam. The two extreme cases for damage position are at the bottom and at the top of the beam, for which the FR is maximal and minimal, respectively. In this case, the efficiency of the first mode for detecting and localizing the damage will be rather limited, while higher modes will be more efficient whatever the position of the damage. For the specific scenarios corresponding to the damage located at position A (S2), B (S3) and C (S4), the FR is depending on the number of mode, and the efficiency of the mode shapes for detecting and localizing damage will be also depending on its position. In fact, the extent of the shift in the natural frequency depends on the location and position of damage with respect to the mode shape of a particular mode of vibration (Moradalizadeh, 1990). A direct consequence is the impact on the mode shapes which may also depend on the configuration. This is shown in Figure III.3 which displays the variation of the eleven first modes versus the position of the damage at element A, B and C, for a damage coefficient *a* corresponding to 0.9 (scenarios S2, S6 and S7). According to the position of the damage, all modes of vibration do not react in the same way.

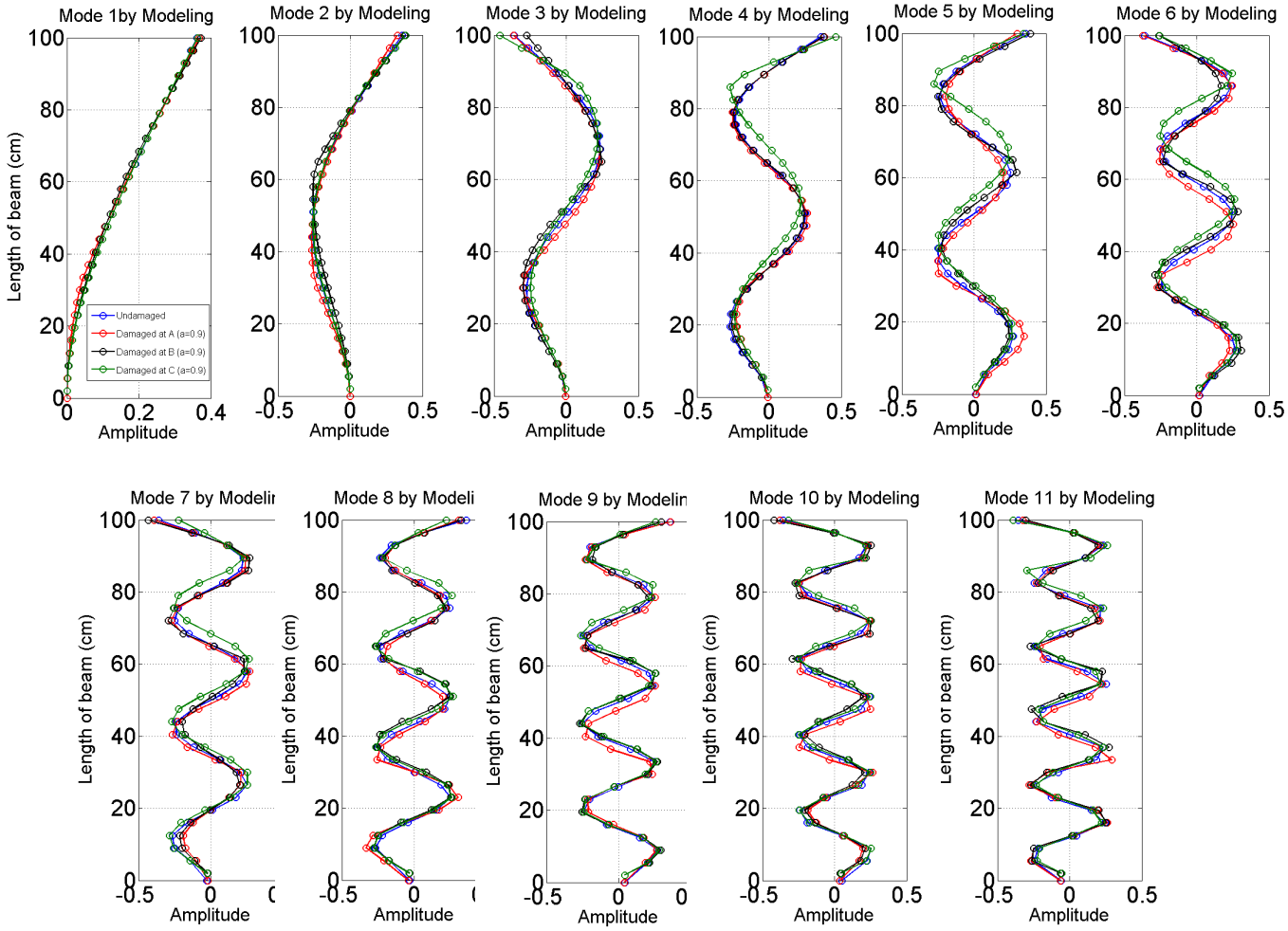


**Figure III. 3:** The first eleven mode shapes (bending modes) obtained by modal analysis using RDM6. Blue curve: undamaged state; Red curve: damage at A (S2); red, Black curve: damage at B (S6); Green curve: damage at C (S7) with damage severity a=0.9.

First, it is clear that the higher modes (e.g. modes 9, 10 and 11) are poorly sampled compared to the first eight modes, depending on the number of nodes (i.e. number of sensor for real building analysis) which cannot be sufficient for the higher modes assessment: this information must be kept in mind considering our primary goal for application to real or experimental condition, with a rather limited number of sensors.

Since the mode shapes are more or less sensitive, depending on the position of the damage, the MAC values computed for each mode will be also related to the damage position. Moreover, the severity of the damage may influence the FR and MAC value, for a given position of damage.

Table III.4 shows the variation of the FR and MAC values for the eleven first modes and considering damage at element A with four damage severity coefficients (*a=0.9* S2, *a=0.7* S3, *a=0.5* S4 and *a=0.2* S5).

| Damage severity *a* | Bending stiffness ratio, *E'I/EI* | Mode1 FR(%) / MAC | Mode2 FR (%) / MAC | Mode3 FR (%) / MAC | Mode4 FR(%) / MAC | Mode5 FR (%) / MAC | Mode6 FR (%) / MAC | Mode7 FR(%) / MAC | Mode8 FR (%) / MAC | Mode9 FR(%) / MAC | Mode10 FR (%) / MAC | Mode11 FR (%) / MAC |
|---|---|---|---|---|---|---|---|---|---|---|---|---|
| 0.2 | 0.8 | 0.58 / (1) | 0.24 / (1) | 0.73 / (0.999) | 0.14 / (1) | 0.25 / (0.999) | 0.82 / (0.999) | 0.27 / (0.999) | 0.17 / (0.999) | 0.75 / (0.999) | 0.37 / (0.999) | 0.14 / (0.999) |
| 0.5 | 0.5 | 2.19 / (1) | 0.94 / (0.999) | 2.72 / (0.999) | 0.53 / (0.999) | 0.96 / (0.997) | 2.89 / (0.995) | 0.92 / (0.996) | 0.62 / (0.997) | 2.53 / (0.989) | 1.21 / (0.992) | 0.51 / (0.997) |
| 0.7 | 0.3 | 4.89 / (0.999) | 2.05 / (0.999) | 5.63 / (0.997) | 1.07 / (0.997) | 2.02 / (0.991) | 5.53 / (0.981) | 1.72 / (0.989) | 1.27 / (0.989) | 4.57 / (0.968) | 2.14 / (0.979) | 1.14 / (0.991) |
| 0.9 | 0.1 | 15.73 / (0.998) | 6.04 / (0.991) | 13.85 / (0.981) | 2.59 / (0.987) | 5.11 / (0.951) | 10.94 / (0.923) | 3.55 / (0.965) | 3.36 / (0.956) | 8.03 / (0.901) | 4.33 / (0.939) | 3.90 / (0.945) |

**Table III. 4 :** Frequency ratio (FR) for four damage severities (scenario S2, S3, S4, S5) at point A (30-33.5 cm) / ( ) is the value of MAC.

Analysis of Table 4 shows some clear highlights. For an increasing value of damage severity, reading the table from the bottom (*a=0.9*) to the top (*a=0.2*), we observe a clear impact on the FR and the MAC value: the FR decreases as the MAC value also, whatever the mode. Even for a single damage, these global parameters are quite relevant for detecting changes. Salawu and Williams (1995) showed that the MAC values can be used to indicate which modes are being affected most by the damage. For a given value of severity, reading the rows of the table III.4 from left to right, we observe that depending on the mode, i.e. depending on the position of the damage with respect on the position of the nodes of the mode, the MAC and the FR values vary. However, we observe that the FR is more sensitive to the relative variation of the damage whatever the modes, while the MAC value is more depending on the mode number.

Figures III.4 and III.5 synthetize the variation of FR and MAC values, respectively, normalized to the maximum, depending on the number of modes and the severity of the

damage (S2, S3, S4 and S5). First, we observe that all the modes show an increase of the FR value with the damage severity, this let us conclude on the efficiency of the frequency variation for detecting low-to-strong single damage. However, non-linear trends are observed whatever the mode number, following the square root shape of the decrease of the stiffness (Eq. II.19). For a given damage state, the FR value is function of the mode number but the global trend of the FR variation is coherent with the damage severity.

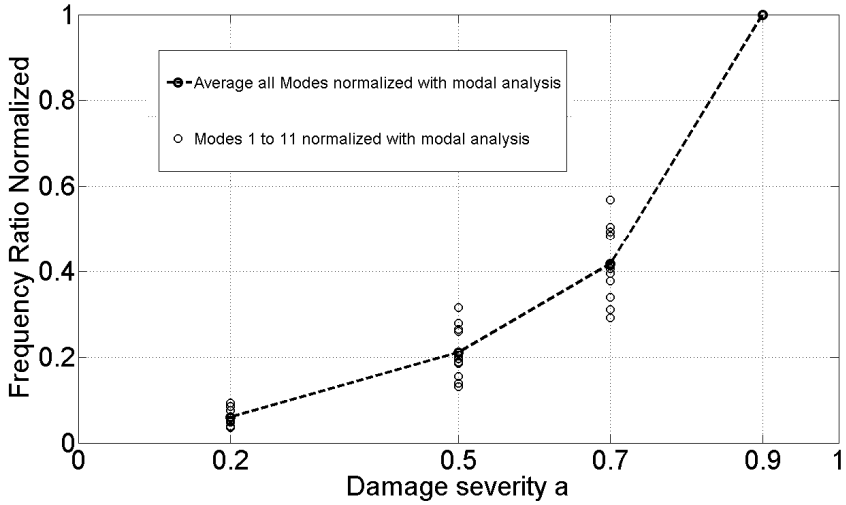


**Figure III. 4:** Frequency ratio (FR) normalized versus four damage severities at the bottom of beam (point A - 30-33.5 cm) using modal analysis (FEM) – Scenario S2, S3, S4 and S5.

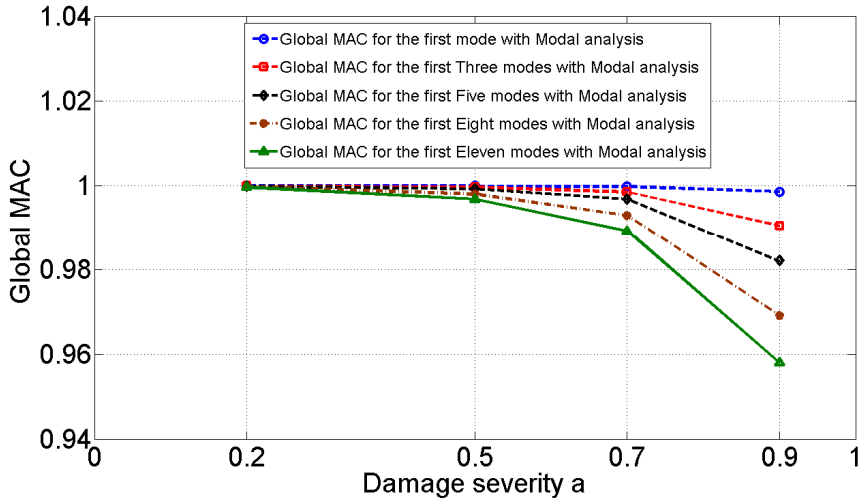


**Figure III. 5:** Global MAC value for four damage severities at the bottom of beam (position A - 30-33.5 cm) using modal analysis (FEM) and considering several number of modes.

In figure III.5, similar observations can be done considering the MAC value, but the efficiency of the detection is strongly related to the number of modes, which appears as a critical point. Indeed, as suggested by the previous results, we find that depending on the number of modes considered, the variation of the MAC value may evolve, not allowing us to quantify the damage directly. For experimental applications, the number of modes available

with a good signal to noise ratio is often limited and the MAC value will be efficient for an absolute quantification of the damage severity. Nevertheless, at the first order, even for a limited number of modes, the Modal Assurance Criterion is often applied to damage evaluation (Alvandi 2004) and its efficiency is directly connected with the number of sensors used in the structure.

In conclusion, global detection of changes is strongly related to the position of the single damage and the mode shape used. We observe that the frequency values are certainly the most sensitive parameter to changes, with limitation for the first mode in case of bending beam model. The damage at the free end of the beam will not have impact on the frequency shift. For operative damage analysis, this position is not critical for the safety of the building. Moreover, the relative variation of the FR is regular regardless of the number of modes; lets us consider the frequency shift as a relevant indicator of the damage severity. This has been already shown by Dunand et al. (2004) for operative assessment of damage severity, classifying safe and unsafe buildings after the Boumerdes earthquake with the frequency shift.

The MAC value, strongly dependent on the number of modes and sensors available for sampling the beam, is certainly not the best criterion for detecting changes. The MAC value is sensitive to damage but many modes must be considered for the best estimate. This is a major drawback for detecting changes in the field. Indeed, often based on the use of ambient vibrations, only the first mode shapes are well defined and it is not possible to link the MAC value to absolute estimate of amount of damage.

Additional methods (see § II) require mode shape and eigenfrequencies and these methods will be tested in the following section.

### III.3.2. – Local methods for detection and localization

In this section, the four NDE methods were applied to the first eleven mode shapes and frequencies before and after each damage scenario listed in Table III.3. The objectives of the research are to study the performance of the damage detection methods using finite element modeling and their application for localizing the damage of existing beams.

Since the local methods tested herein are used for the localization of the damage, a quality criterion of the estimate is defined, using the following formulation:

$$C_{AB} = \frac{\left|\sum_{k=1}^{n} (L_A)_k \, (L_B)_k\right|^2}{\sum_{k=1}^{n} ([L_A]_k)^2 \; \sum_{k=1}^{n} ([L_B]_k)^2} \qquad \text{(III.8)}$$

where $[L_A]$ is the theoretical curve representing the damage state along the beam (0 for unchanged and 1 for changed) and $[L_B]$ is the curve estimated from modeling and the use of damage localization method providing the position of changes along the beam. A $C_{AB}$ value close to 1 indicates that the NDE method is effective; a $C_{AB}$ value less than 1 implies that the

method does not localize well. This quality criteria is used for each case, following the damage scenario (Table III.3), testing the position, single, multiple and extended damages.

As example, Figure III.6 shows the two curves, theoretical in blue and estimated in red from the data of modeling using only the first mode shape and frequency corresponding to the S2 damage scenario (position A) and using the ULS method (Eq. II.39). For computing the $C_{AB}$ criterion, ULS estimate is normalized relative to its maximum.

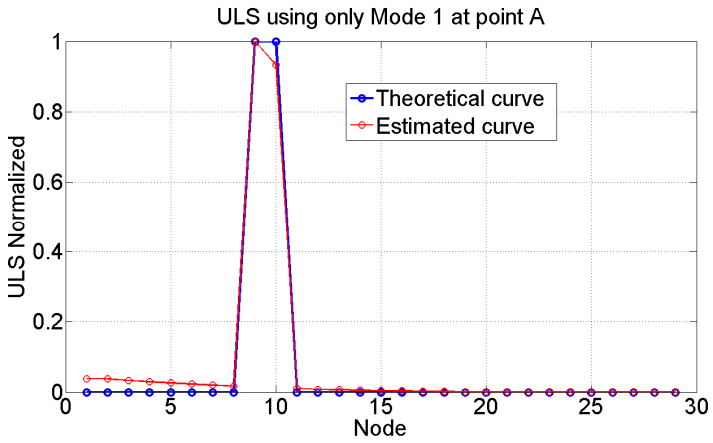


**Figure III. 6:** Example of the theoretical and estimated position of damage along the beam (node), using the ULS method for the S2 scenario.

From Equation (III.8), the correlation $C_{AB}$ between these two curves is 0.999, which means they are well correlated over the entire length of the beam. The method not only detects and locates the damage, but also no false detection is observed, the coefficient factor $C_{AB}$ representing this quality. In this example, ULS method seems very effective to locate the damage using only the first mode.

### III.3.2.1 – Comparing the four methods for scenarios S2, S3, S4 and S5

First, we compare the quality of the localization considering damages at position A for four damage severities (see Table III.3).

Using only the first mode, MSC is able to locate the damage correctly regardless of the four different damages (Figure III.7). Result shows that the difference of curvature mode shapes from undamaged and damaged beam is a good indicator of damage location, but when we consider additional modes, this method loses its effectiveness and the correlation value decreases. For strongest severity damage, the noise of the MSC curve is small, while for the smallest (*a=0.2*), some disturbances appear, providing some confusing on the localization of damage. This is particularly right considering additional higher modes (Fig. III.7.c and III.7.d) where a ghost localization is clearly observed. This observation was also reported by Pandey (1991) and Abdel Wahab (1999) who considering higher modes and the modal shape curvature (MSC), additional peaks at other positions leading to false localization.

Hence, in order to reduce the possibility of a false alarm, only the first curvature mode shapes must be used for damage identification.

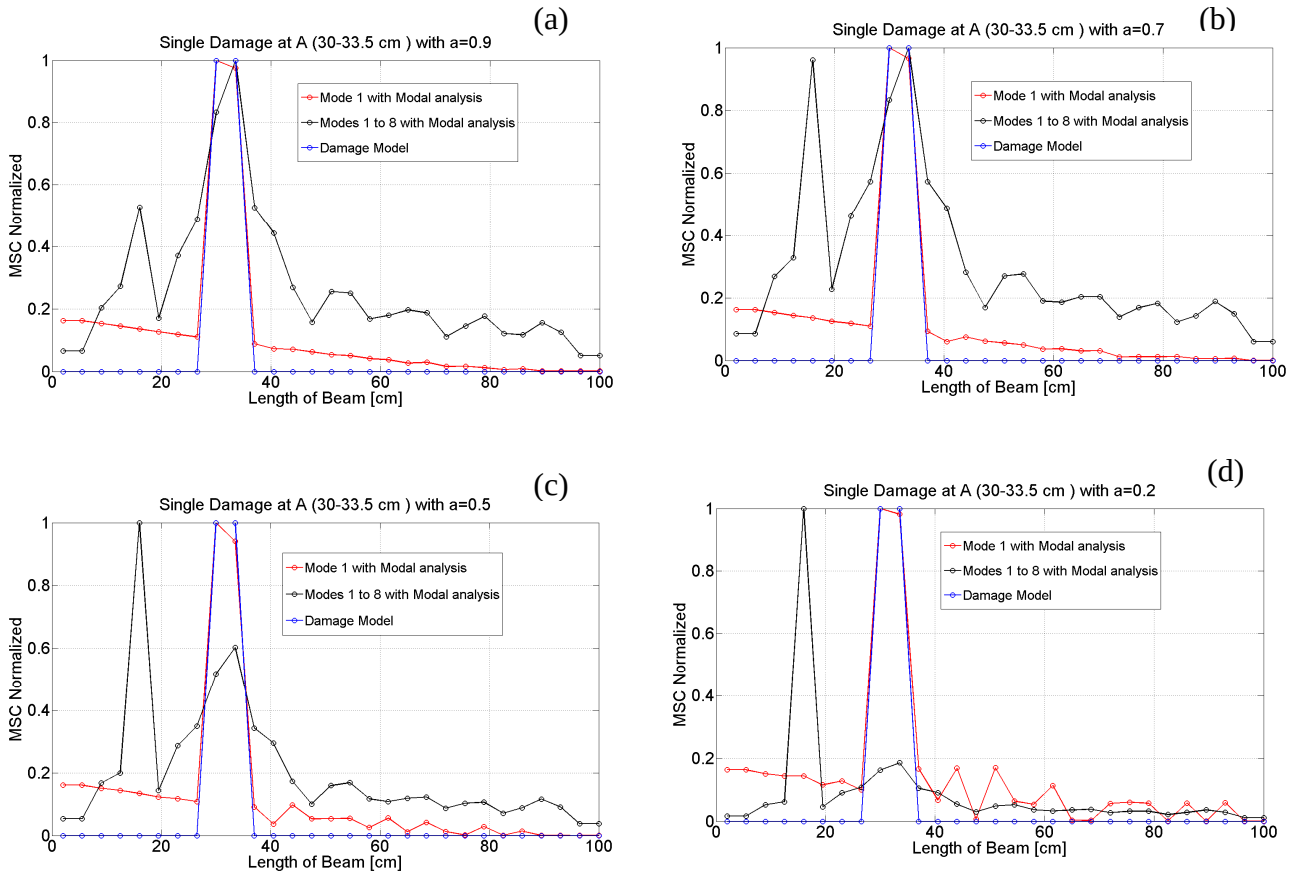


**Figure III. 7:** Theoretical (in blue) and estimated position of damage along the beam (node), using the MSC method for the scenario S2 (a), S3 (b), S4 (c) and S5 (d) using the first mode shape (red curve) and the first eight mode shapes (black curve).

Similar observation can be done also for the MSCS methods (Fig. III.8). By using the first mode, the damage at position A is precisely localized, regardless of the damage severity. False detections are provided by the MSCS method by considering higher modes and, the noise of the MSCS curve increases for the smallest damage severity.

CIF method displayed in Fig. III.9 is not able to locate the position of damage at position A using only the first mode (mode 1). No localization is observed on the CIF curve, the shape of the curve being strongly related to the shape of the mode. By adding higher modes, the localization is improved but the position of the damage is quite large and spread over several positions, reducing the efficiency of this method for small and single damage. At the free end of the beam, some false detection is observed, attenuated by incorporating additional modes in the process.

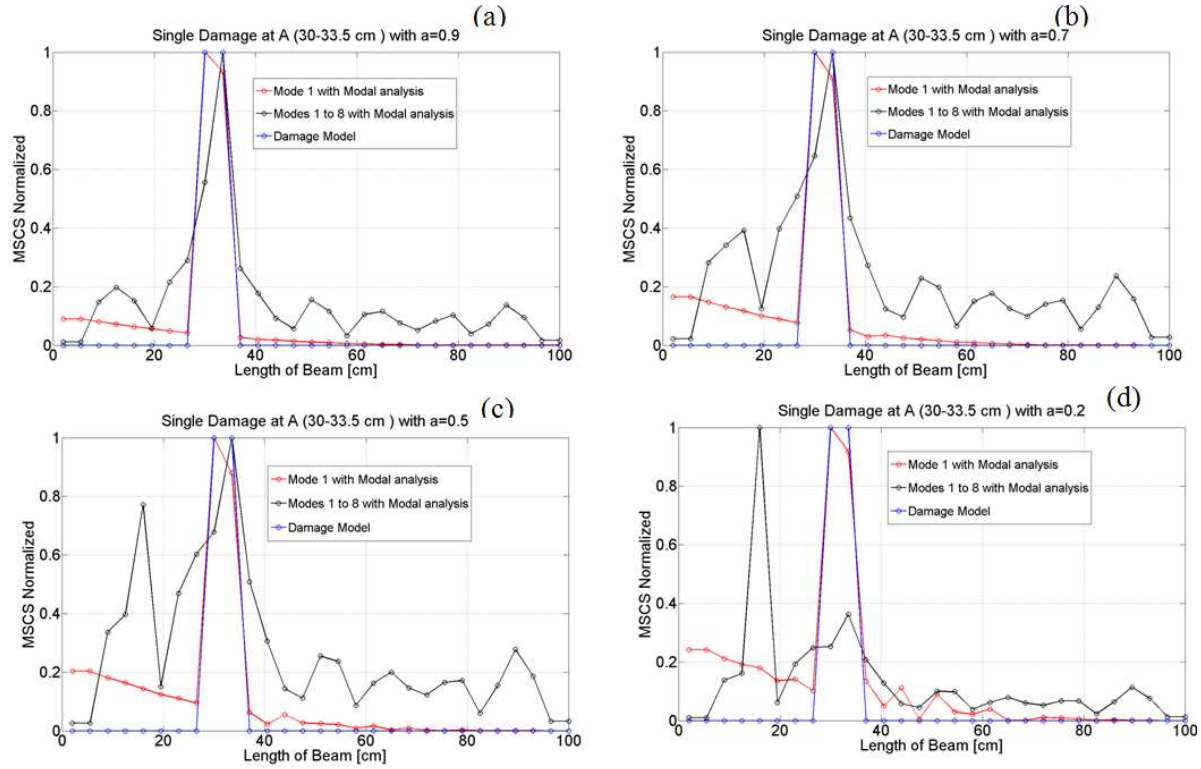


**Figure III. 8 :** same as Fig. III.7, for the MSCS method.

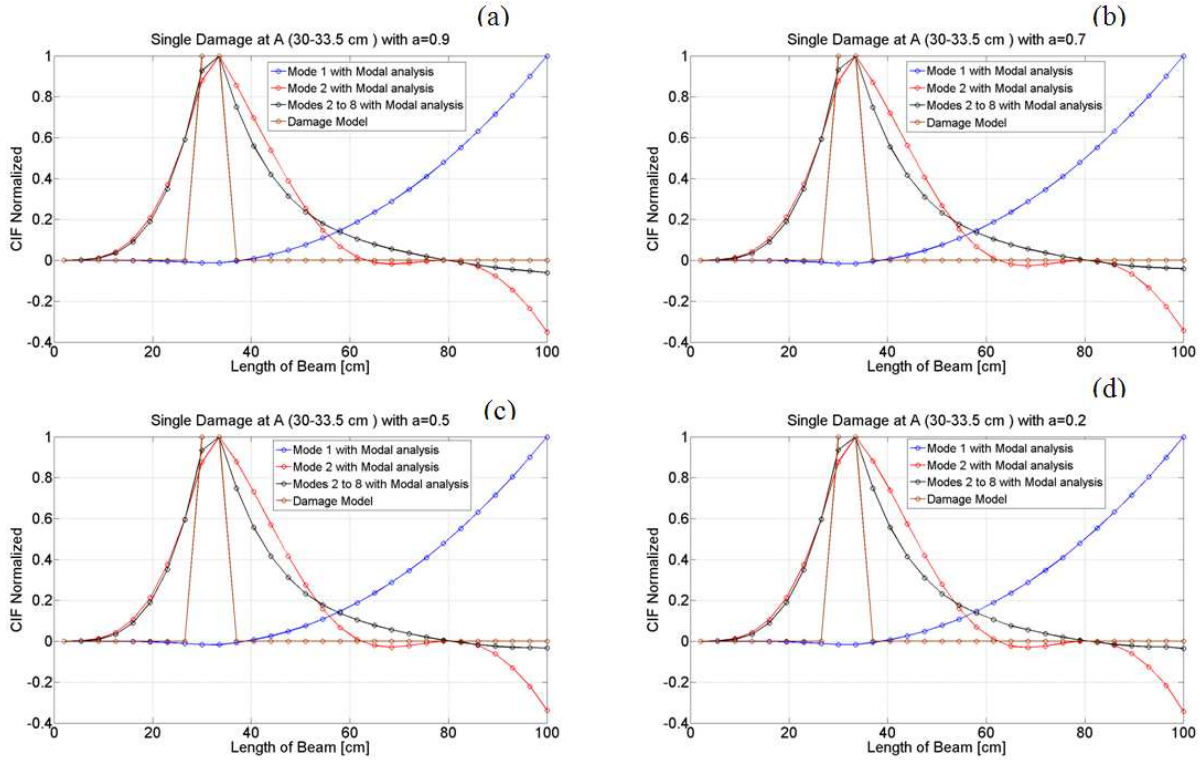


**Figure III. 9 :** same as Fig. III.7, for the CIF method.

Finally, the last methods ULS give the smallest error in the localization, using one or more mode shapes. This is particularly interesting since in practice, only the first modes are easily obtained thanks to operative modal analysis. We observed in Figure III.10 that ULS give highest noise on the estimates curve for the smallest severity damage, and a small false detection can be considered at the end.

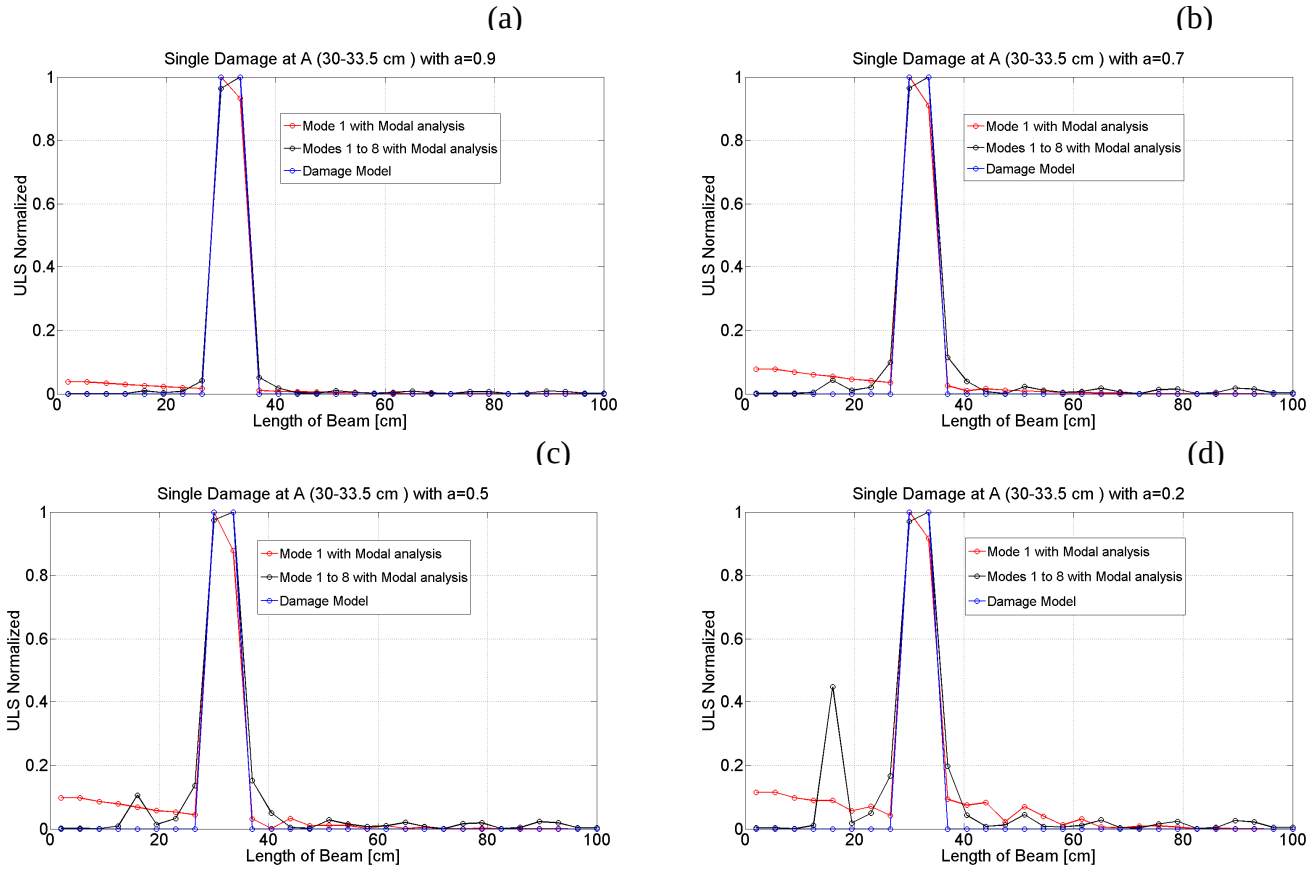


**Figure III. 10:** same as Fig. III.7, for the ULS method.

In order to have a global on the efficiency of the four methods, depending on the level of damage severity and the number of more used for the estimation, we plot on Fig. III.11 the correlation coefficient $C_{AB}$ for each configuration.

The first conclusion is the high rate of efficiency of the ULS method for localizing the damage, without introducing false detection and reducing the noise level along the ULC curve. The worst estimates appear by introducing higher modes, whatever the damage severity. It is also clear that even for small and single damage, this method provides the best solution.

The quality of the estimate using the MSC and MSCS methods decrease when higher modes are added to the process. Moreover, the result is strongly dependent on the damage severity, the smallest damage level introducing a small signal to noise ratio and then a small $C_{AB}$ coefficient. For a given number of modes (less than 7 modes), the MSC method is less sensitive to the damage severity.

Finally, the worst method is certainly the CIF (Fig. III.11.c), especially when the first mode is considered. Looking at the shape of the CIF method, this one is certainly not well adapted to the beam considered here (bending beam), the result being able to change for shear or Timoshenko beams. Keeping in mind that only the first modes are often measured by operative modal analysis methods, the MSC and ULS methods seem to be the more appropriate methods for localization of damage. However, additional position of damage along the beam must be tested, that is the objective of the next section.

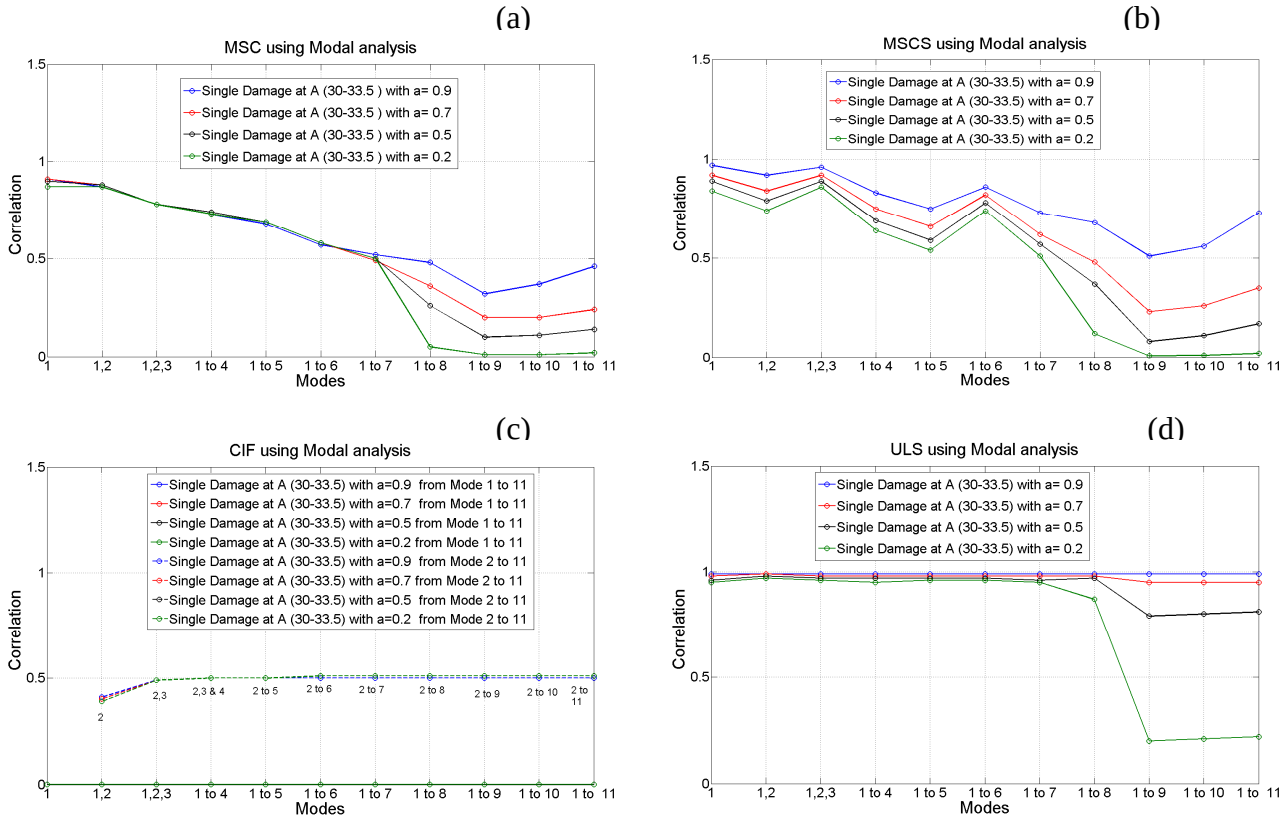


**Figure III. 11:** Correlation values $C_{AB}$ for the four methods (a: MSC; b: MSCS; c: CIF; d: ULS) considering the four damage severities at position A (scenario S2, S3, S4 and S5) and several numbers of modes.

If we considered the LV3 NDE objective, i.e. detection, localization and severity assessment, Figure III.12 confirms that the methods give a relevant assessment of the relative damage, for each method. Nevertheless, comparing method by method, it is not clear what is the absolute signification of the Normalized damage index NDI shown in Fig. III.12 and this question needs further analysis for accomplishing the LV3 objective.

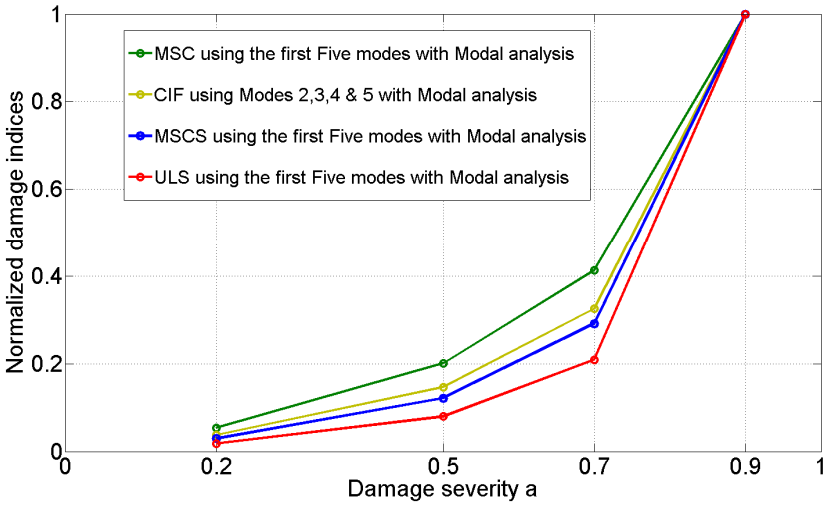


**Figure III. 12:** Peak values of the Normalized Damage Index (NDI) evaluated by the four methods (green: MSC; yellow: CIF; blue: MSCS; red: ULS) and considering the four damage severities at position A (scenario S2, S3, S4 and S5).

### III.3.2.2 – Comparing the four methods for scenarios S6 and S7

In this section, we compare the efficiency of the localization considering damages at positions B and C for the strongest damage severities (see Table III.3). The B position is located between 61.0 and 65.0 cm from the clamped extremity ($x=0$) and C between 86.0 and 89.5 cm.

Figure III.13 and III.14 show the localization between each method compared to the theoretical localization of the damage along the beam for the scenarios S6 and S7, respectively. As previously shown, the ULS method is the most efficient method tested in this work and for this sort of beam. We note a very low noise level on ULS curve and the very narrow localization of the damage, for the scenarios S6 and S7. The noise level decreases also by including additional higher modes in the analysis. This is particularly clear for the S7 scenario, when the damage position is close to the free extremity of the beam. Considering only the first mode introduces noise, which may introduce a false localization even for an expert analysis.

This is not the case for methods MSC and MSCS, for which the level of noise is moderate to strong, with a clear false estimate using the MSC method. This is worst for the scenario S7 (damage at position C, close to the free extremity), for which the fit between the theoretical and estimated curves are bad, with an extended and wide position of damage localization compared to the real case.

We observe similar trend for the CIF method, with a wide assessment of the damage position, using higher modes, while the first mode is not able to localize. This is worst for the scenario S7 (case B) than for scenario S6 (case C) the position of the damage at the free extremity introducing a big difficulty for applying the methods of localization.

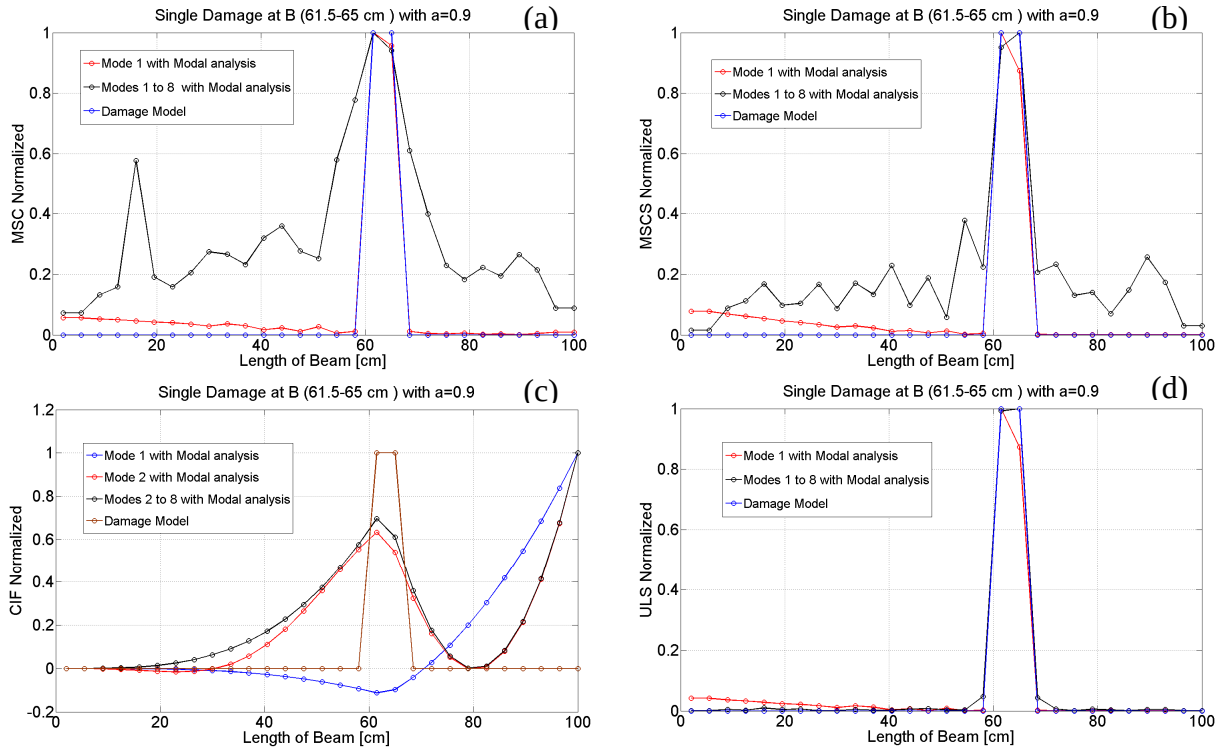


**Figure III. 13:** Theoretical (in blue) and estimated position of damage along the beam, using the MSC (a), MSCS (b), CIF (c) and ULS (d) methods for the S6 scenario using the first mode shape (red curve) and the first eight mode shapes (black curve).

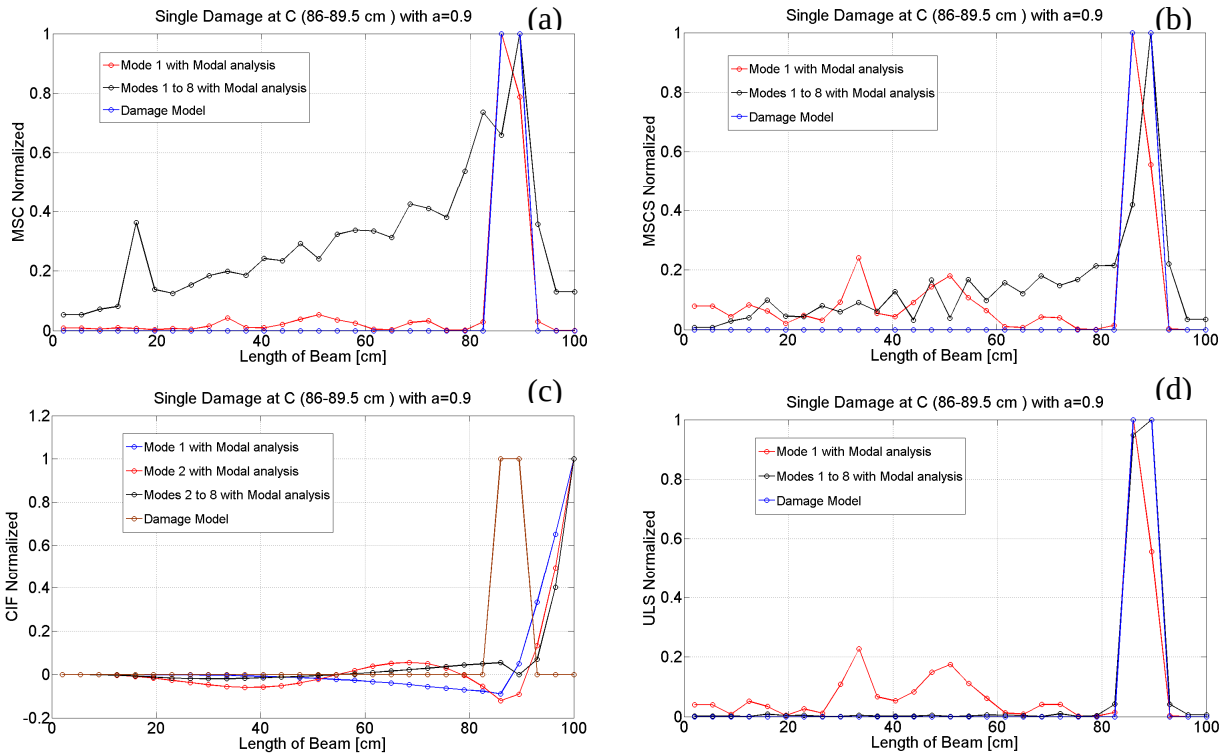


**Figure III. 14:** Same as Fig. III.13, for the S7 scenario.

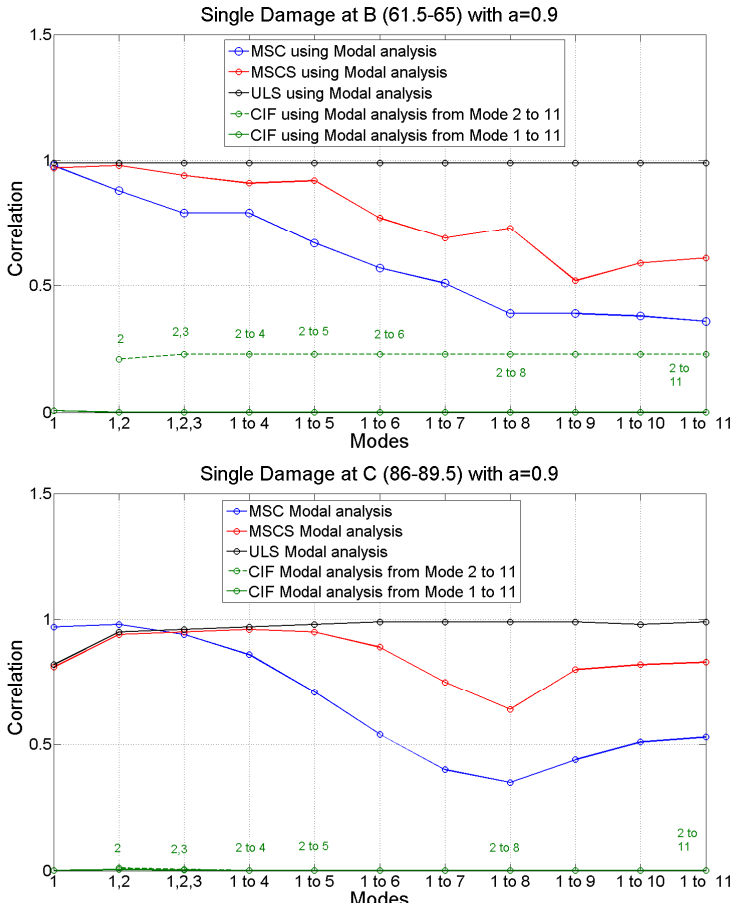


**Figure III. 15:** Correlation values $C_{AB}$ for the four methods (blue: MSC; red: MSCS; green: CIF; black: ULS) considering a=0.9 damage severity at position B (scenario S6, upper row)) and at position C (scenario S7, lower row).

The correlation coefficients $C_{AB}$ computed for each configuration and displayed in Figure III.15 show clearly the general trend of the concluding remarks. For scenarios S6 (B localization) and S7 (C localization), the most efficient method is the ULS, as previously reported for scenario S2 (Fig. III.11). This method gives a coefficient close to 0.9, and the fit between the theoretical and estimated curves for the ULS method is improved considering not only the first mode. This is the case for the C position (scenario S7) more than for scenario S2 and S6, the position of the damage along the bending beam influencing the estimate. As mentioned by authors, the MSCS method is an improvement of the MSC method, as we can observe the result on Figure III.15. For example, for the scenarios S2 and S6, $C_{AB}$ is systematically the highest with method MSCS, whatever the number of modes. For scenario S7, considering only the first mode gives reverse trend, that is to say the MSC is more efficient than the MSCS. Nevertheless, keeping in mind the objective of this work, we can conclude on the relative efficiency of MSC and MSCS methods, considering only the first mode.

The CIF method is the worst, considering single or multiple modes, whatever the scenario. CIF is unable to locate the damage at position C and also at position B, the correlation value is near to zero (green curve continuous and dashed) that means an absence of correlation with the theoretical model proposed. In addition it gives bad results compared to other methods.

### III.3.2.3 – Comparing the four methods for scenario S8

In this section, we compare (Figure III.16) the efficiency of the localization considering damage severity at position D, for large and extended damage with *a=0.9* (see Table III.3). The reduction of Young's modulus is between 30.0 and 47.5 cm from the clamped extremity of the beam (*x=0cm*).

For the MSC method, when the first eight modes (black curve) are considered in the algorithm, MSC find the damage a way less accurate than with only the first mode. It can be observed that for the higher modes, the absolute difference in modal curvatures shows several peaks not only at the position of the damaged element but also at different undamaged locations, increasing the noise level of the estimate.

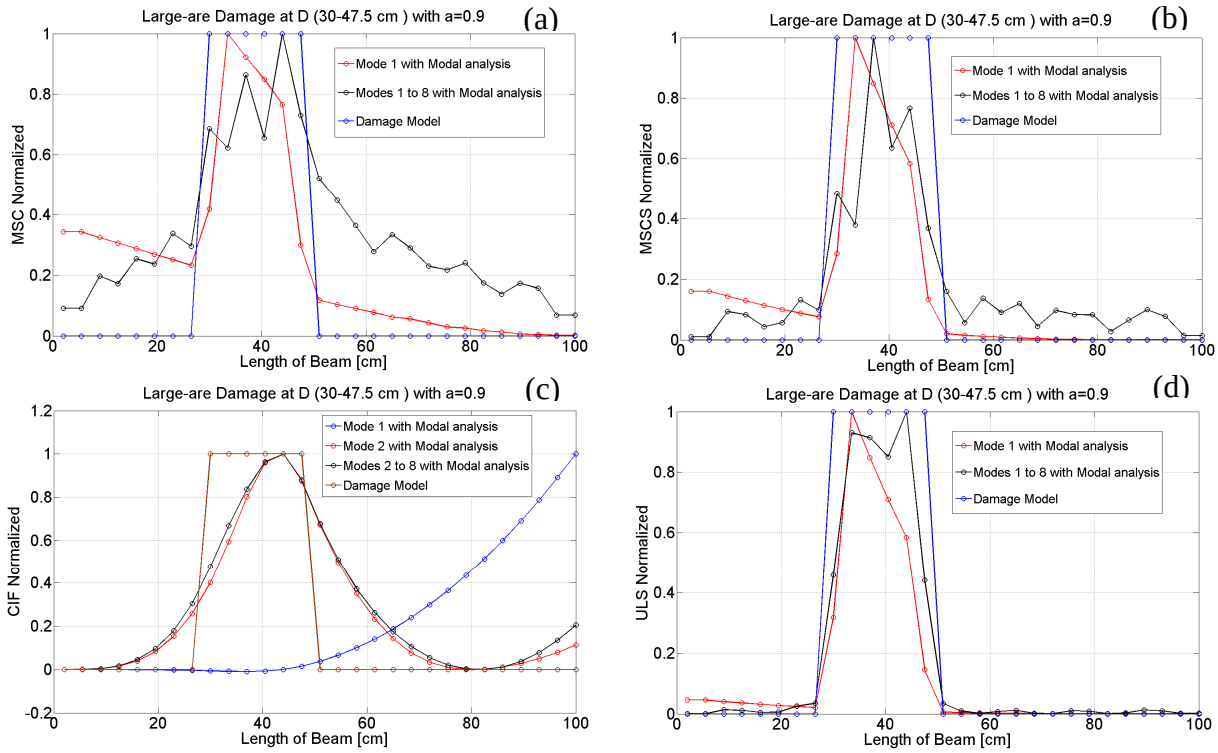


**Figure III. 16:** Theoretical (in blue) and estimated position of damage along the beam, using the MSC (a), MSC (b), CIF (c) and ULS (d) methods for the S8 scenario using the first mode shape (red curve) and the first eight mode shapes (black curve).

MSCS works as well for locating the large and strong damage at point D with the first mode, and then when the first eight modes are used, MSCS is able to locate the damage at point D better than MSC, but it gives small oscillations (noise) along the beam that could be interpreted as (false) damaged zones. Even with extensive damage, CIF failed to locate the damage position at position D, considering the first mode. This estimate is improved using the second and the second to eight higher modes, makes us assume (as previously mentioned) this method is not sensitive to higher modes. CIF remains in all cases the less efficient method to localize correctly the position of damage along the beam.

Once again, the ULS method is the most effective algorithm for damage localization, the noise level being reduced, considering the first or additional higher modes. Of course, by introducing higher modes, the fit between theoretical and estimated curves improves.

A comparison of the four algorithms for wide damage localization computing the $C_{AB}$ coefficient is displayed in Figure III. 17. Once again, the ULS method is the most efficient method and the $C_{AB}$ coefficient is from 0.8 to 0.9 depending on the number of modes. This value increases by adding higher modes to the process, as also observed for the MSC and MSCS methods. However, the latter methods do not improve the correlation compared to the CIF method considering only higher mode. For the three methods, $C_{AB}$ is close 0.6 that reflect a less accurate assessment of the wide zone of damage and/or a highest noise level along the beam that may introduce false estimate.

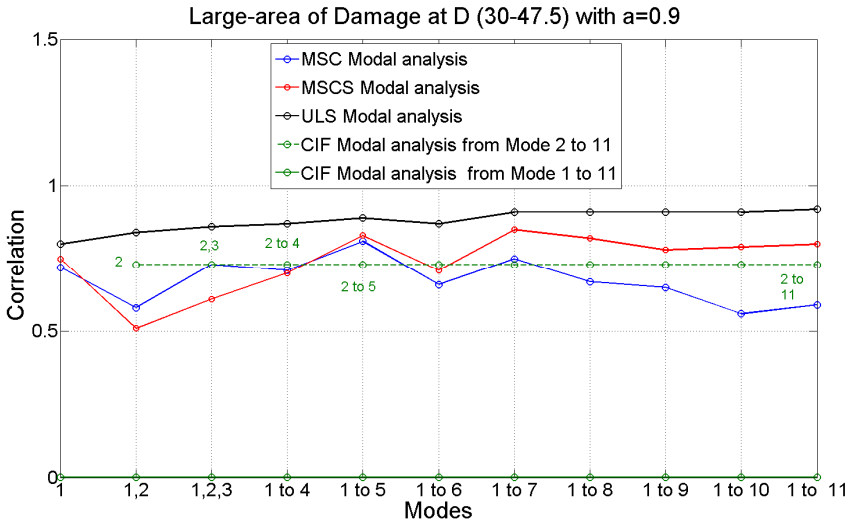


**Figure III. 17:** Correlation values $C_{AB}$ for the four methods (blue: MSC; red: MSCS; green: CIF; black: ULS) considering a=*0.9* damage severity at position D (scenario S8, wide damage).

Comparing scenarios S2 and S8, we note that these methods are more efficient for single and narrow damage rather than wide damage. This can be a key point for damage localization, applied to real-case study of existing building.

### III.3.2.4 – Comparing the four methods for multiple damage location - scenarios S9, S10 and S11

After the single and narrow damage located at different positions along the beam, a multiple damage configuration is considered and tested, using the three previous position at A (30-33.5 cm), B (61.5-65 cm) and C (86-89.5 cm) from the clamped extremity (*x=0*). Several damage severities were considered, with a homogeneous distribution of coefficient *a=0.9* (scenario S9), an increasing and a decreasing variation of damage grade at A, B, C for the scenario 10 (a=0.9(A)/0.7(B)/0.5(C)) and 11 (a=0.5(A)/0.7(B)/0.9(C)), respectively.

First, a comparative study of the four previous damage identification algorithms is provided Figure III.18 to illustrate the validity and effectiveness of the algorithms in case of multiple damages. Except for the ULS method, considering a homogenous damage distribution (*a=0.9* at A, B and C), all the methods are not efficiency, introducing a lot of noise and/or wide identification of the damage position. Only the ULS method give a relevant fit between estimated and theoretical curves along the beam, even if considering only the first mode the damage positions are detected but the amount of damage is not assessed. We can observe Figure III.18d that the damage coefficient (amplitude of damage) of the ULS along the beam change, the localization close to free extremity of the beam providing amplitude of the damage underestimated.

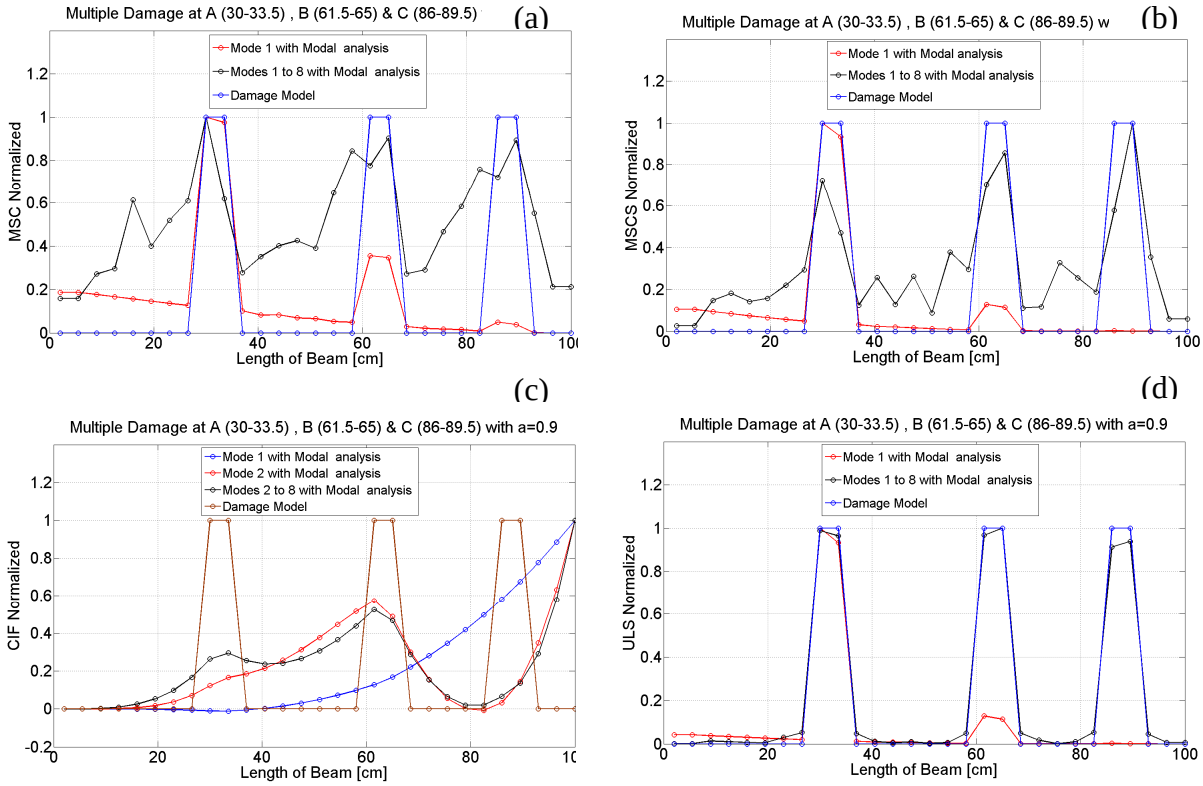


**Figure III. 18:** Theoretical (in blue) and estimated position of damage along the beam, using the MSC (a), MSC (b), CIF (c) and ULS (d) methods for the S8 scenario using the first mode shape (red curve) and the first eight mode shapes (black curve).

Once again, CIF is not suitable and not effective for multiple damage localization. It is noticeable that conversely of the relative efficiency of the MSC and MSC methods for single damage, the ULS method considering the eight first modes gives a very good fit of the damage coefficient along the beam, respecting the amount of the damage. A direct consequence displayed on Figure III.19 is the high values of the $C_{AB}$ coefficient for the ULS method, with the best estimate when considering at least 4 or 5 modes.

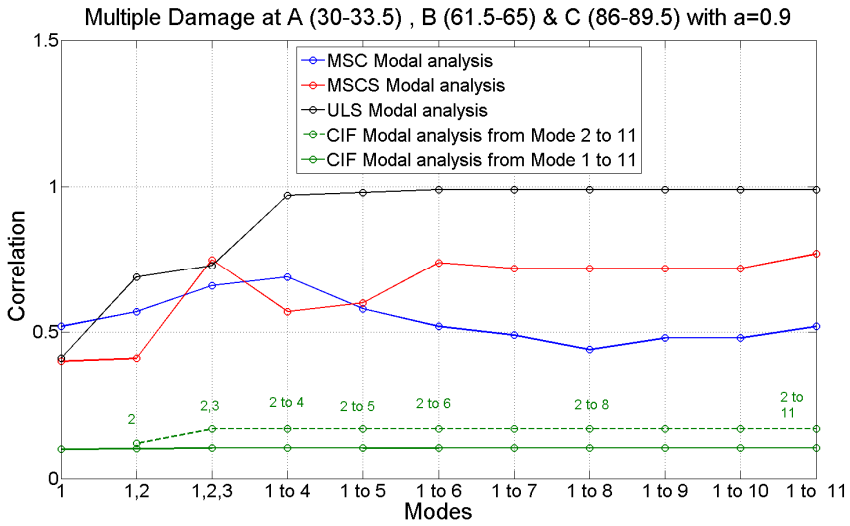


**Figure III. 19:** Correlation values $C_{AB}$ for the four methods (blue: MSC; red: MSCS; green: CIF; black: ULS) considering a=*0.9* damage severity at positions A, B and C (scenario S9).

Multiple damages with three different damage severities were applied at the bottom (A), middle (B) and at the top of beam (C) considering a descending (Scenario 10, Fig. III.20) or an ascending (Scenario 11) order of amount of damage along the beam. Only the first five modes are considered on Fig. III.20. We can confirm the very efficiency of the ULS method for localization of multiple damages, with identical ULS amplitude in the middle of the beam (point B) and ULS amplitude at positions A and C for equivalent damage coefficient whatever the order of the variation of the amount of damage

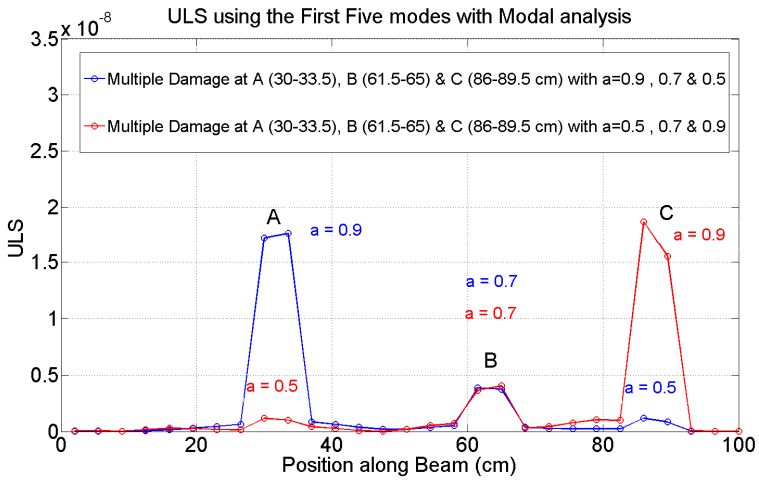


**Figure III. 20:** Estimated position of damage along the beam, using the ULS methods for the S10 (blue) and S11 (red) scenarios (multiple damage with different a coefficient) using the five first mode shapes.

### III.3.3 – Performance of the ULS method

#### III.3.3.1 – Frequency ratio versus ULS localization

According to the previous results, the ULS method localizes with success the damage along the beam, whatever the position, the number of damage position and extension of the damage. The only drawback or limitation is the number of modes required for improving the assessment.

Figure III.21 shows the effectiveness of the ULS method for different number of modes, and considering a damaged section sliding along the beam, from section 1 ($x=0$) to section 28 ($x=L$). On the same figure is displayed also the variation of the shift of the frequency, through the FR coefficient (see § III.2). Considering one, three or five modes, similar trends are observed.

First, the amplitude of ULS curve (related to the damage severity) follows the variation of the FR coefficient, since the frequency value is accounted for the ULS algorithm. It is clear that for the extreme case, for which the damaged section of the bending beam is at the free extremity, ULS and FR methods are not efficient.
Second, considering only the first mode, even if the same damage severity is applied to each section, it is not estimated the amount of damage considering only the first mode. For improving the LV3 objective of the NDE methods, we need to introduce higher modes, three modes providing a good estimate and the three first modes being often available by operative modal analysis.

Finally, considering the five first modes, it is possible to detect local, single, wide and multiple damage position and to quantify the amount of damage with a high level of accuracy. The difficulties remains for the two extreme situations, at the bottom and at the top of the beam for which the frequency shift (FR) and the ULS algorithm fail to localize.

#### III.3.3.2 – LV3 objective of the NDE-ULS method

According to the previous results, the efficiency of the ULS method is summarized in Figure III.22. In this figure, the scenarios S2, S3, S4 and S5 are compared, considering the first five modes. ULS method is able to distinguish the damage severity: when the severity of damage increased from 0.2 to 0.9, the amplitude of the ULS damage values increase. Nevertheless, previous results (Fig. III.12) seem to confirm a non-linear variation of the damage severity with the ULS amplitude, since ULS is directly related to the inverse value of the frequency square between undamaged and damaged beam (Eq. II.36 and II.37).

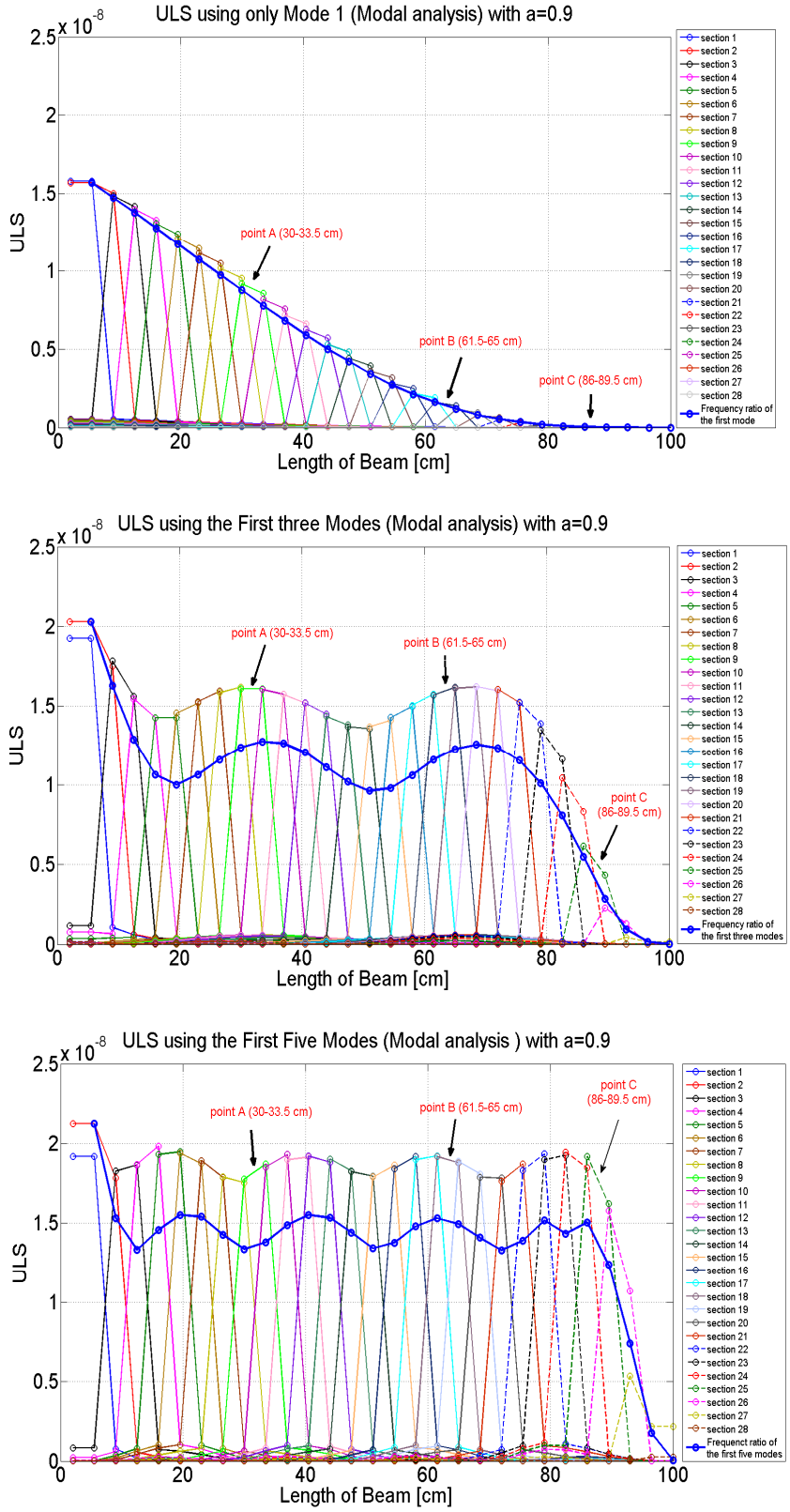


**Figure III. 21:** Amplitude and localization of damage using ULS method (multi-color legend) and the local method based on the frequency shift (Frequency Ratio FR, blue thick curve) considering damaged sections sliding along the beam and one (upper), three (middle) and five (lower) modes for the detection.

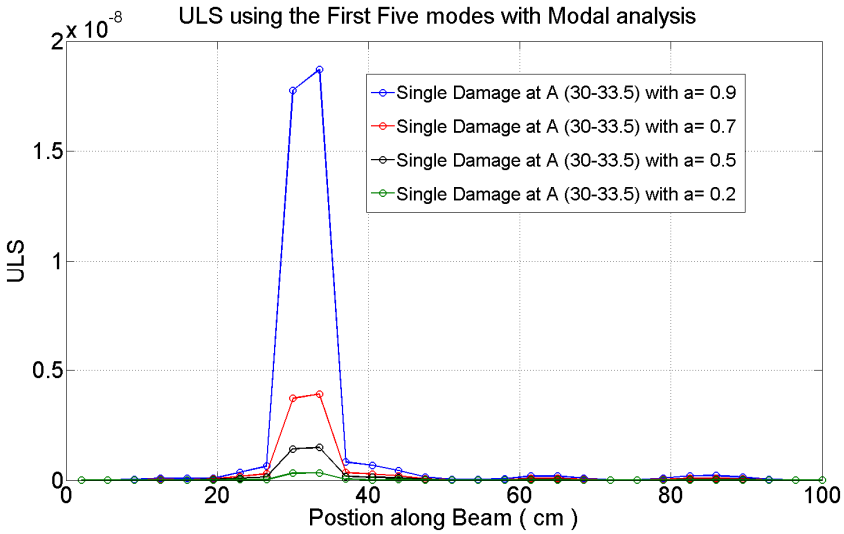


**Figure III. 22:** Estimated position of damage along the beam, and variation of the amplitude of the ULS damage value for the S2 (blue), S3 (red), S4 (black) and S5 (green) scenario considering the five first modes.

Figure III.23 summarizes the performance of the ULS method for different configurations, including multiple or single damage, with homogenous (or not) variation of the damage severity and narrow or wide damage, in complement with the results shown in Fig. III.20. Even if this method is the most efficient method tested for this beam model, one must notice the amplitude of the ULS damage value overestimates the value of damage and further analysis must be conducted.

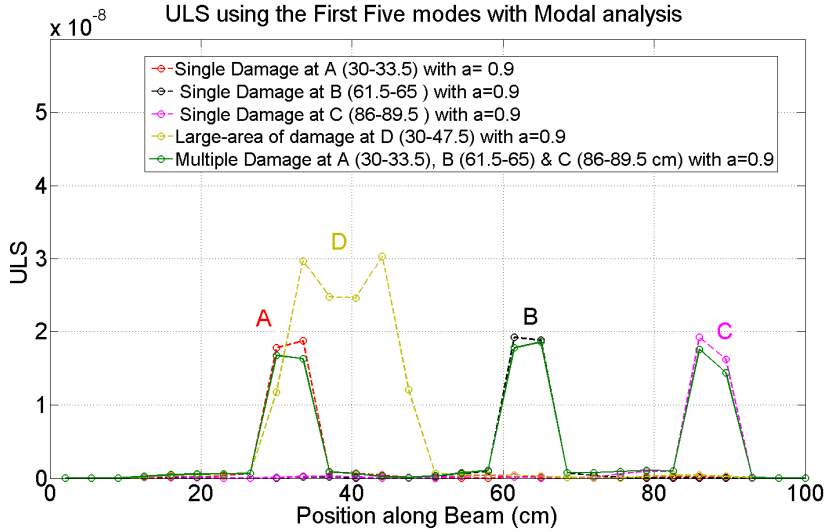


**Figure III. 23:** Summary of the performance of the ULS method considering the first five modes, for Scenarios S2 (orange), S6 (black), S7 (magenta), S8 (yellow) and S9 (green), keeping the same damage severity (*a=0.9*).

## III.4- Conclusions

In this study, modal analysis of damaged and undamaged beams was done in order to test the efficiency of several Non-destructive damage evaluation (NDE) methods.

The modeling setup, based on model analysis using finite element modeling (FEM), consisted in reduction of Young's modulus of a clamped-free beam, with material properties of Plexiglas.

The efficiency of the non-destructive damage evaluation (NDE) to detect and locate the damage is obtained by comparing the before and after damage modal parameters, numerical approach providing an accurate estimate of the frequencies and mode shapes. Several configurations were tested: single or multiple-damage, extended or narrow damage, small or strong damage. The damage is applied at different positions of the beam from the bottom to the top.

The natural frequency change ratio is a relevant indicator for detecting the damage, the position of the damage influencing the sensitivity of each mode, which does not react in the same way. The natural frequency change ratio (FR) and modal assurance criterion (MAC) between undamaged and damaged beam is used to detect the presence of changes, reflecting also the relative variation of the damage severity.

In conclusion on the global assessment methods, the frequency is the most sensitive parameter to detect damage and since only one recording point at the top of the building is required, this method is relevant for operative assessment of damage, as for emergency situation just after an extreme event.

Local methods were also tested and Figure III.24 summarizes the tests done in this section. The coefficient of correlation $C_{AB}$ is the highest for the ULS method, whatever the situation and the configuration tested. No false detections are obtained, unlike the MSC and MSCS methods.

The MSC is very sensitive to higher modes and in order to reduce the possibility of a false alarm, only the first curvature mode shape must be considered for locating the damage. MSCS method works better, even with single and narrow damage along the beam, considering the first modes. Nevertheless, situation like multiple damage or damage close to the free extremity of the beam provide a high noise level that can be interpreted as false damage localization.

The change in flexibility method CIF is the worst method, even for the single damage case. It can successfully detect and localize a single and narrow damage at the bottom of the beam, but the $C_{AB}$ value is low, that indicate a high level of noise or a less accurate localization.

The results confirm that the application of the curvature of uniform load surface (ULS) method give the more reliable results and still very robust whatever the configuration of damage.

Some drawbacks are noticed, such as the localization of the damage at the two extremity of the beam or the low reliability of the absolute damage amount, such as for the extended damage. We note also that for a blind estimate of damage (quantification and localization) at least three modes must be accounted for, improving the assessment by adding the first five modes.

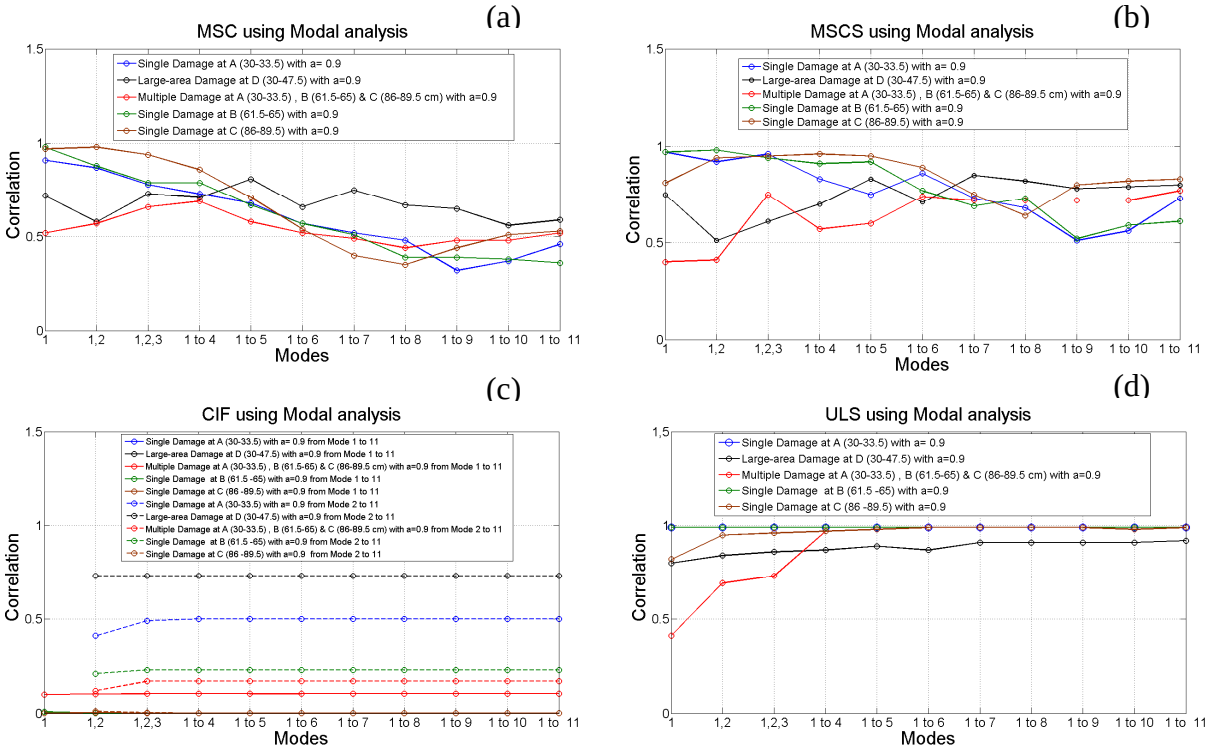


**Figure III. 24:** Correlation values $C_{AB}$ for the four methods (a: MSC; b: MSCS; c: CIF; d: ULS) considering all the scenarios of Tab. III.3 (see figures for legends).

# CHAPTER IV

# DETECTION AND LOCALIZATION OF DAMAGE USING TIME DOMAIN MODELLING

**Abstract** - In this chapter, we will consider numerical modeling equivalent to experimental conditions. The modal parameters are extracted from ambient vibrations (AV) simulated through time-domain model. For extracting mode shapes and frequencies, the two parameters necessary for applying the NDE methods (local and global) are extracted from AV synthetics using Operative Modal Analysis methods, the Frequency Domain Decomposition and the Random decrement Technique. After testing different configurations and different methods of localization and detection, a new approach is finally tested, based on the perturbation theory.

# IV.1-Introduction

In this chapter, we propose a time-based study using a numerical analysis. A white noise low amplitude excitation is applied at the bottom of the beam, and the time response is computed along the beam.

The first objective of this study is to get experimental results, i.e. by simulating ambient vibrations along the beam and by applying pseudo-experimental modal analysis. Frequency domain decomposition method (FDD) is used for extracting the frequencies and the mode shapes from synthetics, and the efficiency of the random decrement technique (RDT) is evaluated for tracking the variation of the modal frequencies in time and to detect the presence of damage.

The second goal of this study, using the frequencies and mode shapes obtained by FDD from numerical analysis, is to evaluate the efficiency of NDE methods for identify and locating the damage proposed at the beam with different kind of damage (single, large and multiple-damage). In each case, all these methods (FDD, RDT and the NDE methods) could be applied to real data.

# IV.2-Numerical simulation

### IV.2.1-Finite element discretization for a 1-D clamped-free beam

The finite element (FE) model of the uniform clamped-free 1-D beam is discretized with $n_b$=200 finite elements of the same length $\delta$ (Figure IV.1a). The Euler-Bernoulli beam theory is used for constituting the finite element matrices. The longitudinal axis of the element lies along the *x* axis. The element has a constant moment of inertia *I*, modulus of elasticity *E*, density $\rho$ and length *L*. Two degrees of freedom per node (translation $u_j$ along *y*-axis and rotation $\theta_j$ about *x*-axis) are considered. In this simulation, the shear deformation (G) and rotatory inertia (I) are neglected.

The number of degree of freedom of the beam is then $n_{dof} = 2(n_b + 1)$. The element variable vector of the $j^{th}$ beam defined by two nodes is $\{u^j\} = \{u_j \quad \theta_j \quad u_{j+1} \quad \theta_{j+1}\}^T$ where $u_j$ is the transverse displacement and $\theta_j$ the rotation of node *j*.

For a constant *E* and *I* at the $j^{th}$ beam element, the element stiffness matrix is defined as in Humar (1990):

$$K_{el}^{j} = \frac{EI^{j}}{\delta^3}\begin{bmatrix} 12 & 6\delta & -12 & 6\delta \\ & 4\delta^2 & -6\delta & 2\delta^2 \\ & & 12 & -6\delta \\ sym. & & & 4\delta^2 \end{bmatrix} \qquad \text{(IV.1)}$$

where $EI^j$ is the flexural rigidity of the $j^{th}$ beam element.

The $n_{dof} \times n_{dof}$ global stiffness matrix *K* is obtained by assembling the contribution of all $n_b$ element stiffness matrices as shown in Figure IV.1b. Boundary conditions at *x=0* are taken into account by deleting the rows and columns corresponding to $u_1 = \theta_1 = 0$. The damage made on any element of the beam is introduced by modifying the corresponding element stiffness matrix.

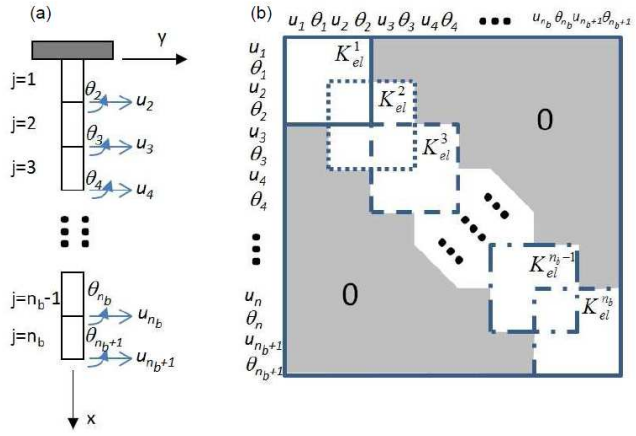


**Figure IV. 1:** (a) Finite element model of the 1-D beam discretized by *j=1, nb* Euler-Bernouilli finite elements. $\boldsymbol{u_i}$ is the transverse displacement and $\boldsymbol{\theta_i}$ the rotation of node *i*. (b) The global stiffness matrix *K* is obtained by assembling the contribution of all the nb element stiffness matrices, *j=1,nb.*from Baillet et al. (2013).

### IV.2.2-Equations of Motion of the Beam

The equation of motion for a multiple degree of freedom MDOF undamped structural system is represented as follows:

$$[M]\{\ddot{u}\} + [K]\{u\} = \{F(t)\} \qquad \text{(IV.2)}$$

where $\{\ddot{u}\}$ and $\{u\}$ are the acceleration and displacement vectors, respectively, for the whole structure, and $F(t)$ is the external force vector. Under free vibrations, the natural frequencies and the mode shapes of a MDOF system are the solutions of the eigenvalue problem. The finite element computation of the natural frequencies $\omega$ and mode shapes $\varphi$ are obtained by solving the linearized eigenvalues problem:

$$([K] - \omega^2[M])\{\varphi\} = 0 \qquad \text{(IV.3)}$$

where $\omega$ is the angular natural frequency, $\varphi$ is the mode shape of the structure for the corresponding natural frequency, *M* is the global mass matrix that is obtained in the same way as the stiffness matrix *K* by properly assembling the element mass matrices [Bathe, 1996].

### IV.2.3-Newmark Method

The wave equation at time $t + \Delta t$ governing the linear dynamic response of a complete element assemblage is defined as:

$$[M]\{\ddot{u}^{t+\Delta t}\} + [K]\{u^{t+\Delta t}\} = \{F^{t+\Delta t}\} \quad \text{(IV.4)}$$

where *M* and *K* are the global mass and stiffness symmetric matrices, respectively, *F* and *u* are the applied forces and the displacement vectors, respectively.

Newmark (1959) proposed what has become one of the most popular families of algorithms for the solution of problems in structural dynamics. His method relies on the following interpolations that relate positions, velocities, and accelerations from time t to $t + \Delta t$ . In transient dynamic simulations, the displacements are integrated using the numerical Newmark step-by-step scheme (Newmark, 1959). The constant-average-acceleration method is used as follows:

$$\dot{u}^{t+\Delta t} = \dot{u}^{t} + \Delta t[(1-\delta)\ddot{u}^{t} + \delta\ddot{u}^{t+\Delta t}] \quad \text{(IV.5)}$$

$$u^{t+\Delta t} = u^{t} + \dot{u}^{t}\Delta t + \frac{\Delta t^2}{2}[(1-2\beta)\ddot{u}^{t} + 2\beta\ddot{u}^{t+\Delta t}] \quad \text{(IV.6)}$$

where $u^t$, $\dot{u}^t$, and $\ddot{u}^t$ are approximations to the position, velocity, and acceleration vectors at time step; and β and δ are the parameters that define the method. The method is implicit, and stability is guaranteed for $2\beta \geq \delta \geq \frac{1}{2}$ (Bathe, 1982). The trapezoidal rule is a particular case of this family for which β=1/4 and δ=1/2 and Δt is the time step.

### IV.2.4-Description of numerical simulation with random noise excitation

In this study, the case of a 1-D beam in bending is studied through the numerical computation. The Finite Element Method (FEM) is used to compute the resonant frequencies $\omega_n$ and modal deformation $\varphi_n(x)$ for both the undamaged and damaged beam, before and after the reduction of the Young's modulus at local or extended zones along the beam. As previously explained in Chapter III, the damage is modeled by reducing the Young's modulus following the relation $E^* = (1-a)\cdot E$, where $E^*$ and $E$ are the undamaged and damaged Young's modulus, respectively.

The configuration of the numerical modeling is shown in figure IV.2, considering a clamped-free beam anchored at the bottom (*x=0*) and free at the extremity (*x=L*), and used to validate the performance of the NDE methods. Since the main goal of this study is to test time methods for extracting mode shapes and frequencies, time histories of the beam vibration are computed at 29 nodes, spread along the beam and considered as 29 dummy sensors.

Time analysis case-study is based on the same Plexiglas beam used in Chap.III, with the following physical properties: $L= 1\ m$ (in length); $W= 0.05\ m$ (in width), $D= 0.01m$ (in Depth), $E=5.4\ GPa$ (Young's Modulus), $\rho = 1165\ kg/m^3$ (density) and inertial moment $I=4 \cdot 10^{-9} m^4$.

The number of elements used in this simulation is two hundred (200) elements. Each element is 0.5 cm, and dummy sensors are spread along the beam with a 3.5 cm interval: the first sensor is at the node 4 ($x = 2\ cm$), the second is at the node 11 ($x = 5.5\ cm$)… and the last sensor is at the node 200 ($x=100\ cm$).

During the transient FE simulation, the white noise low-amplitude excitation is applied perpendicular to the beam axis at the boundary condition to the clamped node. The noise is generated randomly using a normal distribution with zero mean value and a standard deviation of $10^{-6}$.

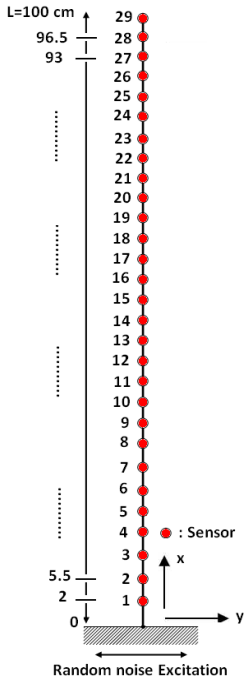


**Figure IV. 2:** Sketch of the clamped-free beam model with sensor positions.

At $x=0$, the displacement varies arbitrarily with time and its rotation remains null. The noise signal propagates into the beam and finally the time history at each node is computed. During this synthetic experiment, the noise excitation is maintained during 300 s.

One set of acceleration measurement with a sampling frequency of 5000 Hz and a time setup $\Delta t=1/5000s$ correspond to a total of 1500000 points at each sensor. Following the sampling rate and the time duration of the numerical experiment, the first eleven natural frequencies and mode shapes were considered herein.

## IV.3 – Data processing with signal processing tools (FFT, FDD, and RDT)

The aim of the numerical assess is to test the ten scenarios previously defined (Chap. III), considering a Young's modulus reduction at different places and with different severities. Since the NDE methods tested herein are based on the comparison between the undamaged (initial) and damages (final) states, the first analysis is done consider the initial state of the beam.

The ten scenarios of damage have been studied are summarized in table IV.1

| **Scenario S** | **1** | **2** | **3** | **4** | **5** | **6** | **7** | **8** | **9** | **10** | **11** |
|---|---|---|---|---|---|---|---|---|---|---|---|
| Undamaged Beam | 0 | | | | | | | | | | |
| A – 30.0-33.5cm | | 0.2 | 0.5 | 0.7 | 0.9 | | | | 0.9 | 0.9 | 0.5 |
| B – 61.5-65.0cm | | | | | | 0.9 | | | 0.9 | 0.7 | 0.7 |
| C – 86.0-89.5cm | | | | | | | 0.9 | | 0.9 | 0.5 | 0.9 |
| D – 30.0-47.5cm | | | | | | | | 0.9 | | | |

**Table IV. 1 :** Damage scenarios applied to the clamped-free beam using time domain modeling.

For example, the acceleration responses for the initial state beam at the boundary condition (top and bottom) are represented in Figure IV.3a and IV.3c. As defined in the previous section, the beam is not damped and we observe clearly the amplification of the beam motion at the top. Since most of the modal analysis methods used in this part are in the frequency domain, this artifact is not a major drawback for the processing.

Many modal extraction techniques found in the literature, which are developed to estimate the modal properties using only the output response, can be categorized into two main groups as frequency domain and time domain (Fu et al., 2001) For example, the time domain methods such as random decrement (RDT) technique (Cole (1973)), Ibrahim time domain (ITD) (Ibrahim (1977)) and the eigen-system realization algorithm (ERA) (Juang and Pappa (1985)) are widely used for damping estimation, while the frequency domain methods such as frequency domain decomposition (FDD) (Brincker et al., 2001) and enhanced frequency domain decomposition (EFDD) (Brincker et al., 2001) or the Hilbert-Huang transform (Huang and Attoh-Okine, 2005) are commonly used for the extraction of natural frequencies and mode shapes.

Additional methods exist and this is not the main goal of the work to describe and test the relevancy and the performance of all these methods. Only the methods used in this document, selected for its simplicity and operability are described.

### IV.3.1 – Fast Fourier Transform analysis - FFT

A first analysis of the beam response can be easily obtained by computing the Fourier spectrum (Fast Fourier Transform) at the clamped extremity (bottom) and the free end (top) of the beam. The results are presented in figure IV.3b and IV.3d. At the bottom, the input signal is a synthetic white noise signal, corresponding to a random and stationary time signal. In frequency, the response is a flat spectrum, corresponding to white noise signature. At the top, the signal is modulated as function of the mode shapes of the system. For that reason we observe at the free end condition of the beam the modal frequencies, varying from 3.4 Hz to 946.4 Hz from the fundamental and the 11$^{th}$ mode, respectively. As aforementioned, the peaks are narrow and with high amplitude since an undamped beam is considered for the modeling.

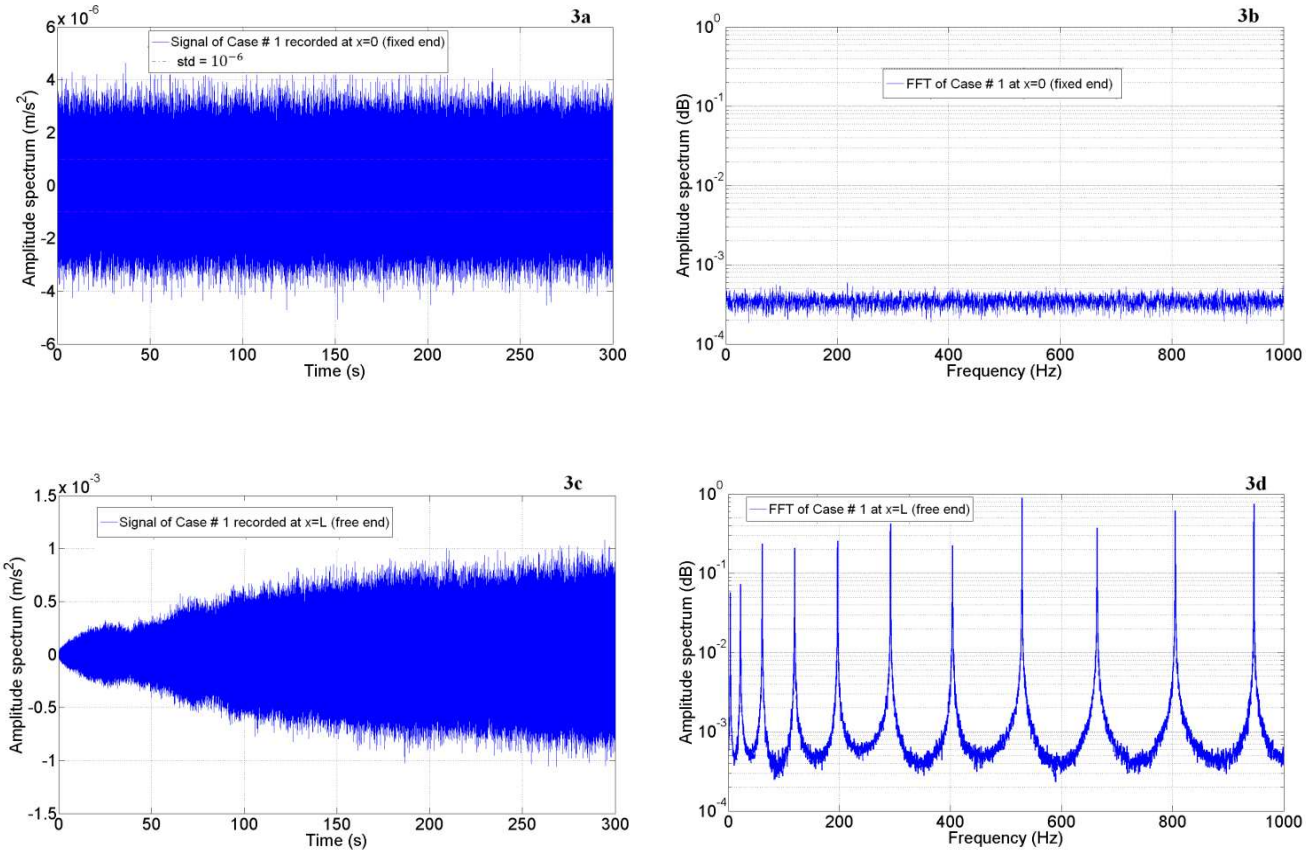


**Figure IV. 3:** Time-history of the beam motion recorded at the clamped (a) and free end (c) extremities of the beam, with frequency responses (b, clamped; d, free). The eleven peaks correspond to the modal frequencies of the beam.

Since the Plexiglas beam has the same properties as the beam described in Chap III, the table IV.2 presents a comparison of the natural frequencies obtained by modal analysis using finite element modeling with RDM6 and time domain analysis (numerical simulation). This comparison confirms the good agreement of frequency values obtained by modeling (linear modal analysis) and the numerical simulation (temporal analysis), for the first eight bending modes including the highest ones.

| Modes # | Modal analysis [Hz] | Time domain analysis [Hz] | Diff (%) |
|---|---|---|---|
| 1 | 3.47 | 3.47 | 0 |
| 2 | 21.79 | 21.79 | 0 |
| 3 | 61.00 | 61.02 | -0.03 |
| 4 | 119.52 | 119.59 | -0.05 |
| 5 | 197.51 | 197.69 | -0.09 |
| 6 | 294.93 | 295.31 | -0.12 |
| 7 | 411.76 | 412.46 | -0.17 |
| 8 | 547.94 | 549.14 | -0.21 |

**Table IV. 2 :** Natural Frequencies (Hz) by modeling (RDM6) and numerical simulation (Time domain analysis) for the undamaged beam correspond to scenario S1.

Figure IV.4 shows the shape of each mode along the beam, represent as the amplitude value of the frequency peaks along the beam, computed from the first to the twenty-ninth sensors, and considering the eleven first modes. This way of representation is equivalent to the peak-picking method for operative modal analysis, classically used for real buildings. We can clearly distinguish the node and antinode of each mode along the beam.

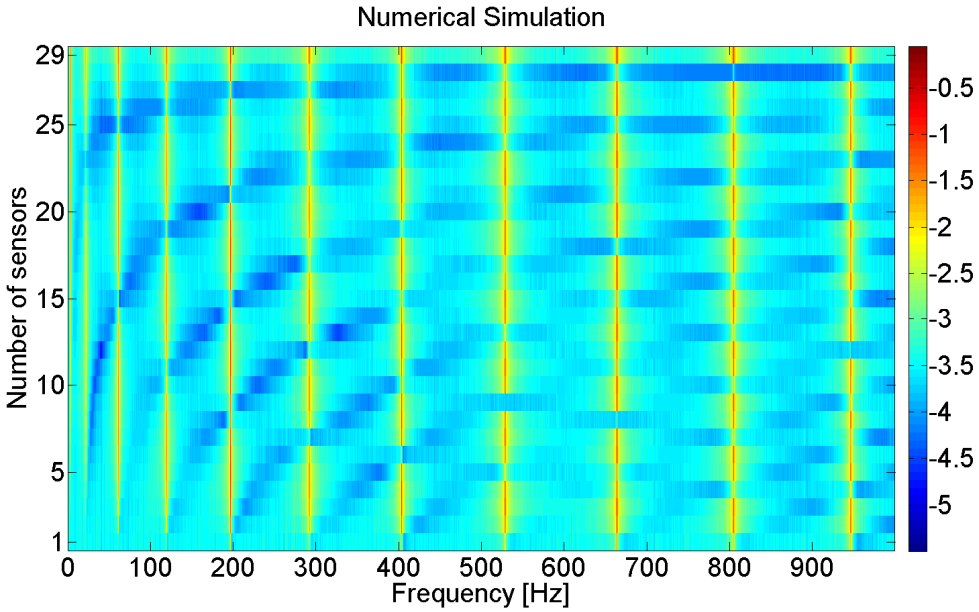


**Figure IV. 4:** Evolution of the spectral amplitude of the synthetics computed at the 29 sensors and representing the shapes of the 11 first modes of the initial (undamaged) beam.

### IV.3.2- Frequency Domain Decomposition (FDD)

The frequency domain decomposition (FDD) technique, developed by Brincker et al. (2001) is a relevant method used in modal analysis because of its accuracy and simplicity.

This method is a non-parametric Operational Modal Analysis (OMA), i.e. no prior model is needed for processing the data. It is an extension of the Basic Frequency Domain (BFD) technique, or more often called the Peak-Picking (PP) technique.

This approach uses the fact that modes can be estimated from the spectral densities calculated under the condition of a white noise input, and for lightly damped structure. The FDD technique can effectively handle close modes and noise, however it cannot provide damping information.

It has been widely used recently for output-only system identification in real buildings using ambient excitations confirming its reliability and effectiveness (Michel et al., 2008; Michel et al., 2010; Gueguen, 2012) and it is now a standard in output-only techniques having been successfully used in a number of studies and implemented in commercially available software (Magalhaes et al 2007, Gentile and Gallino 2007, Brinker et al 2001; ARTeMIS 2008).

Ventura et al. (2003) and Michel et al. (2008) also applied this method (FDD) with success using earthquake data recorded in building under the assumption of white noise spectra in the frequency range of the seismic data.

According to Ventura et al. (2003) and Michel et al. (2010), although the assumption of white noise is not too strong in the case of buildings of civil engineering, the FDD is robust enough to allow this calculation, although the time of record is very short.

A study by Peeters and Ventura (2003) reviewed various modal analysis techniques and compared them by utilizing different studies presented by different research groups who applied their methods to identify the modal parameters of the Z24 Bridge in Switzerland.

The enhanced FDD technique was used with success for the modal identification of the Z24 bridge simply because it is accurate, gives all six modes in all the damage cases, and is simple to use.

In a real application Michel et al (2010) shows the efficiency and accuracy of the FDD method to extract the first five resonant frequencies and mode shapes (Figure IV.5.a), from a test conducted using ambient vibrations and the data recorded by the sensors on bottom and at the top of City Hall of Grenoble in France.

The comparison of this test with a numerical modeling in 3D (Figure IV.5.b) of the building (City Hall of Grenoble) gave very good agreement.

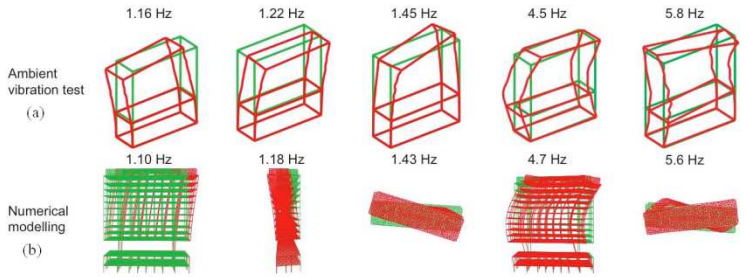


**Figure IV. 5:** (a) Modal analysis results using ambient vibration test on City Hall of Grenoble by FDD method (b) numerical modeling on City Hall of Grenoble. from Michel et al (2010).

The FDD estimates the eigenvalues of the system (mode shapes and frequencies) by diagonalizing the Power Spectral Density (PSD) matrix, i.e. by computing the Fourier spectra of the cross-correlation matrix obtained by simultaneous recordings done in the system.

Brincker et al. (2001) showed that the PSD can be decomposed into singular vectors and scalar singular values. Since the perpendicularity condition of the modes, the FDD may be considered as an approximate decomposition of the system response into a set of independent single degree of freedom (SDOF) systems. Each mode is described by one SDOF. The decomposition is performed by computing the spectral density matrices.

### IV.3.2.1 – Theoretical background

The relationship between unknown inputs *x(t)* and measured responses *y(t)* in a system can be expressed by:

$$\left[G_{yy}(j\omega)\right] = [H(j\omega)]^{*}[G_{xx}(j\omega)][H(j\omega)]^{T} \qquad \text{(IV.7)}$$

where $G_{xx}(j\omega)$ and $G_{yy}(j\omega)$ are the power spectral densities (PSD) of the input and the output, respectively, and $H(j\omega)$ is the frequency response function (FRF) matrix; * and superscript T denote complex conjugate and transpose, respectively.

The FRF matrix can be written in a typical partial fraction form (used in classical Modal analysis), in terms of poles, $\lambda$ and residues, $R$:

$$[H(j\omega)] = \frac{[Y(j\omega)]}{[X(j\omega)]} = \sum_{k=1}^{m} \frac{[R_k]}{j\omega - \lambda_k} + \frac{[R_k]^{*}}{j\omega - \lambda_k{}^{*}} \qquad \text{(IV.8)}$$

with

$$\lambda_k = -\sigma_k + j\omega_{dk} \quad \text{(IV.9)}$$

where $m$ is the total number of modes of interest, $\lambda_k$ the pole of the $k^{th}$ mode, $\sigma_k$ the modal damping and $\omega_{dk}$ the damped natural frequency of the $k^{th}$ mode, i.e.:

$$\omega_{dk} = \omega_{0k}\sqrt{1 - {\xi_k}^2} \quad \text{(IV.10)}$$

with

$$\xi_k = \frac{\sigma_k}{\omega_{0k}} \quad \text{(IV.11)}$$

where $\sigma_k$ is the critical damping and $\omega_{0k}$ the undamped natural frequency, both for mode k.

$[R_k]$ is called the residue matrix and is expressed in an outer product form:

$$[R_k] = \varphi_k {\gamma_k}^T \quad \text{(IV.12)}$$

where $\varphi_k$ is the mode shapes and $\gamma_k$ is the modal participation vector. All those parameters are specified for the $k^{th}$ mode.

Using the expression (IV.7) for the matrix $\left[G_{yy}(j\omega)\right]$, and the Heaviside partial fraction theorem for polynomial expansions, we obtain the following expression for the output PSD matrix $\left[G_{yy}(j\omega)\right]$ assuming the input is random in both time and space and has a zero mean white noise distribution, i.e. its PSD is a constant, i.e. $[G_{xx}(j\omega)] = [C]$ :

$$\left[G_{yy}(j\omega)\right] = \sum_{k=1}^{m} \frac{[A_k]}{j\omega - \lambda_k} + \frac{[A_k]^*}{j\omega - \lambda_k{}^*} + \frac{[B_k]}{-j\omega - \lambda_k} + \frac{[B_k]^*}{-j\omega - \lambda_k{}^*} \quad \text{(IV.13)}$$

where $[A_k]$ is the $k^{th}$ residue matrix of the matrix $\left[G_{yy}(j\omega)\right]$. The matrix $[G_{xx}(j\omega)]$ is assumed to be a constant value *C*, since the excitation signals are assumed to be uncorrelated zero mean white noise in all the measured DOFs. This matrix is Hermitian and is described in the form:

$$[A_k] = [R_k]C\left(\sum_{s=1}^{m} \frac{[R_s]^H}{-\lambda_k - \lambda_s{}^*} + \frac{[R_s]^T}{-\lambda_k - \lambda_s}\right) \quad \text{(IV.14)}$$

where superscript H denotes a complex conjugate and transpose. The contribution of the residue has the following expression:

$$[A_k] = \frac{[R_k]C[R_k]^H}{2\sigma_k} \quad \text{(IV.15)}$$

Considering a lightly damped model, we have the following relationship:

$$\lim_{damping \to light}[A_k] = [R_k]C[R_k]^T = \varphi_k {\gamma_k}^T C \gamma_k {\varphi_k}^T = d_k \varphi_k {\varphi_k}^T \quad \text{(IV.16)}$$

where $d_k$ is a scalar constant for the $k^{th}$ mode.

The contribution of the modes at a particular frequency ω is limited to a finite number (usually 1 or 2), and then the response spectral density matrix can be written as the following final form:

$$\left[G_{yy}(j\omega)\right] = \sum_{k \in sub(\omega)}^{m} \frac{d_k \varphi_k {\varphi_k}^T}{j\omega - \lambda_k} + \frac{{d_k}^* {\varphi_k}^* {\varphi_k}^{*T}}{j\omega - {\lambda_k}^*} \quad \text{(IV.17)}$$

where $k \in sub(\omega)$ is the set of modes that contribute at the particular frequency, $\varphi_k$ is the mode shape for the $k^{th}$ mode and $\lambda_k$ is the $k^{th}$ pole used in the determination of resonance frequency and damping and is defined as :

$$\lambda_k = -\xi_k \omega_k + j\omega_k \sqrt{1 - {\xi_k}^2} \quad \text{(IV.18)}$$

where $\xi_k$ is the damping ratio of the $k^{th}$ mode, $\omega_k$ is the eigenfrequency of the $k^{th}$ mode.

The real part depends on the natural frequency and on the modal damping ratio, whereas the imaginary part coincides with the damped natural frequency $\left(\omega_k \sqrt{1 - {\xi_k}^2}\right)$, which is close to the natural frequency when damping is small.

This final form of the matrix is then decomposed into a set of singular values and singular vectors using the Singular Value Decomposition technique (SVD). This decomposition is performed to identify single degree of freedom models of the problem.

In order to obtain the natural frequencies and mode shapes, the power spectral density matrix of the response in each frequency is decomposed by taking Singular Value Decomposition (SVD) of the matrix as:

$$\hat{G}_{yy}(j\omega_i) = U_i S_i {U_i}^H \quad \text{(IV.19)}$$

where the matrix $U_i = [u_{i1}, u_{i2}, \cdots u_{im}]$ is a unitary matrix holding the singular vectors $u_{ij}$, $S_i$ is a diagonal matrix including the singular values $s_{ij}$, and m is the rank of the matrix $G_{yy}(j\omega)$.

If only a $k^{th}$ mode is dominating at selected frequency $\omega_i$ , there would be only one singular value in (IV.19). Hence the first singular vector $u_{i1}$ is an estimate of the $k^{th}$ mode shape $\hat{\varphi} = u_{i1}$.

If two modes are dominating at this frequency peak, which means two modes are close in frequency, and if they are geometrically orthogonal, the estimates of the corresponding modal shapes are the two first singular vectors.

The FDD mode shape is used as a reference vector for a correlation analysis based on the Modal Assurance Criterion (MAC). For MAC values greater than 80%, it is considered that the point still belongs to the FRF of the mode, even on the second singular value. The MAC value controls the width of the SDOF Bell function in the frequency domain. The damping ratio as well as the natural frequency is estimated by transforming the SDOF Bell function into time domain along with regression analysis.

Damping ratios can be estimated using the Enhanced Frequency Domain Decomposition (EFDD) that is basically an extension of the FDD technique capable of providing damping information. In EFDD, the identified frequency function around each resonant peak is transferred back to the time domain using Inverse Fast Fourier transform and damping can be obtained by the logarithmic decrement of the corresponding SDOF.

### IV.3.2.2 – Data processing description by Frequency Domain Decomposition (FDD)

In practice, the FDD can be divided in the following steps:

1) Estimate spectral density matrices from the raw time series data.

2) Singular value decomposition (SVD) of the spectral density matrices.

3) In multiple data sets, the singular values are averaged over all data sets in increasing mode order.

4) Peak-pick of the singular values, either from the averaged values or for each data set separately.

In our case, the peak-pick is carried out manually for selecting the frequencies value and mode shapes to each mode of vibration corresponding to damaged and undamaged beam. Modal analysis of the clamped-free beam based on time analysis using finite element modeling (FEM) was done using the FDD, and the processing was performed using the Matlab Macity tools developed for modal analysis (Michel et al., 2010). The time histories used are computed at the 29 sensors, considering a white noise as input and generated with the Matlab function.

Brincker (2003) showed that in practice the time length of the recorded window should be at least equivalent to 1000 periods of the structure in order to calculate an accurate spectral estimate, also confirmed by Michel et al. (2008, 2010).

The synthetics were computed along the beam for 5 min of time history with a sampling rate of 5000 Hz, which is long enough with respect to the Brincker criterion.

In our case, the FDD method decomposes the original signal of 300 seconds for undamaged and damaged beam into 7 windows of 41.6 seconds, corresponding to a frequency step of 0.024 Hz.

In the beginning, the MACity toolbox was developed for operative modal analysis using the CityShark$^{TM}$ multi-channels station (Chatelain et al., 2000, 2012). Since this station allows 18 channels of recordings, the processing is based on the output format of the CityShark$^{TM}$.

For that reason, we decided to separate the 29 synthetics into two files, using the sensor #29 located at the top as reference point for normalization.

The reference point is used to normalize and combine all the components of the modal shape (Michel et al., 2008), and finally the normalized shape is obtained by dividing it by the value at the reference sensor.

Figure IV.6 shows the singular values of the power spectral density (PSD) matrix using FDD method to obtain the natural frequencies and mode shapes of the response for initial beam (without damage) Scenario S1, and for Scenarios S2, S3, S4, S5 corresponding to damage at **position** A with four damage grades.

Figure IV.6 we observe the variation of the modal frequency values with the damage states. As already mentioned, this shift is directly related with the reduction of stiffness (K) of the beam. These results confirm that the variation of frequency is very sensitive to detect the change and presence of damage on the beam.

On one side, among these modes, it is clear that Modes 1, 3 and 6 are the most sensitive to damage, because of the position of the damage (at **position** A) located to antinodes of these modes. On the other side mode 4 is the less sensitive compared to other modes, which means the node of this mode is very close to the **position** at A.

These observations are very similar to and confirmed by the modal analysis performed in Chap.III. We observe that the FDD methods using time modeling of the beam response and simulating white noise input is relevant for detecting frequencies and modes, that will be used for detecting and localizing the damage.

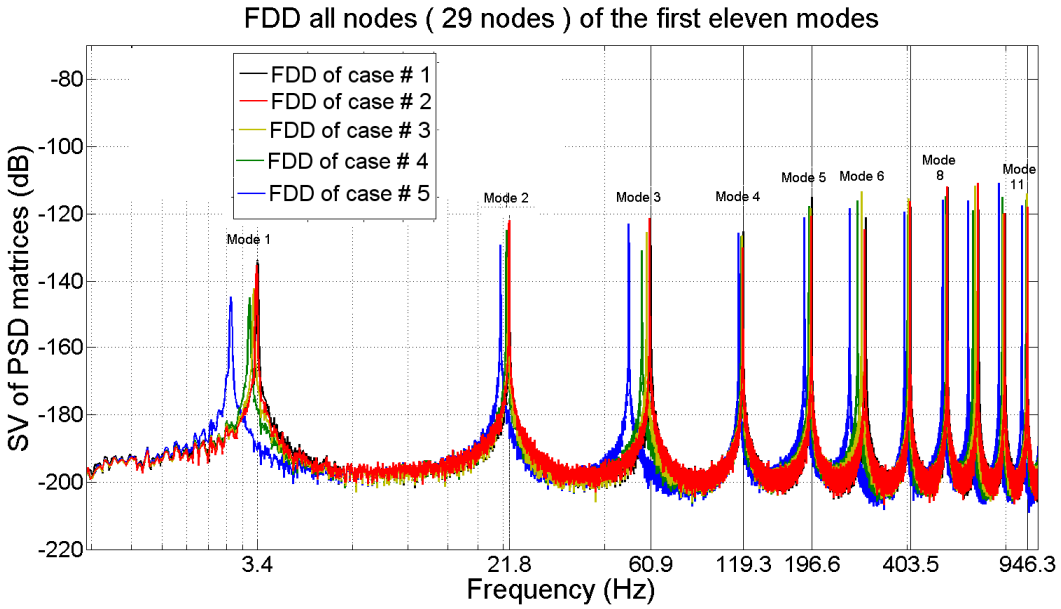


**Figure IV. 6:** Singular values of the PSD matrix of the response of the S1, S2, S3, S4 and S5 scenarios.

The identification of the first eleven bending modes for Scenario 1 (undamaged beam) and using the FDD method is displayed Figure IV.7. These mode shapes are consistent with theoretical mode shapes (Chap.III) and they will be used jointly with the frequency values for applying and testing the NDE methods.

### IV.3.3- Frequency analysis using the Random Decrement Technique (RDT)

The random decrement technique (RDT) was used in this study to track (monitor) the evolution of natural frequencies over time of the beam.

The random decrement technique (RDT), described by Cole (1971) and Asmussen et al. (1997), is a temporal non-parametric technique used for the identification of natural frequencies. Since the frequencies are sensitive to damage, we will use this method for detecting the presence of changes or damages.

#### IV.3.3.1 – Theoretical background

Initially proposed by Cole (1973), this method is based on the fact that, at any given time, ambient vibrations contain a random and a deterministic part. The response of a linear system depends on the initial conditions and the applied forcing function.

This response can be decomposed into three parts: the first caused by the initial displacement, the second caused by the initial velocity, and the third caused by the forcing function.

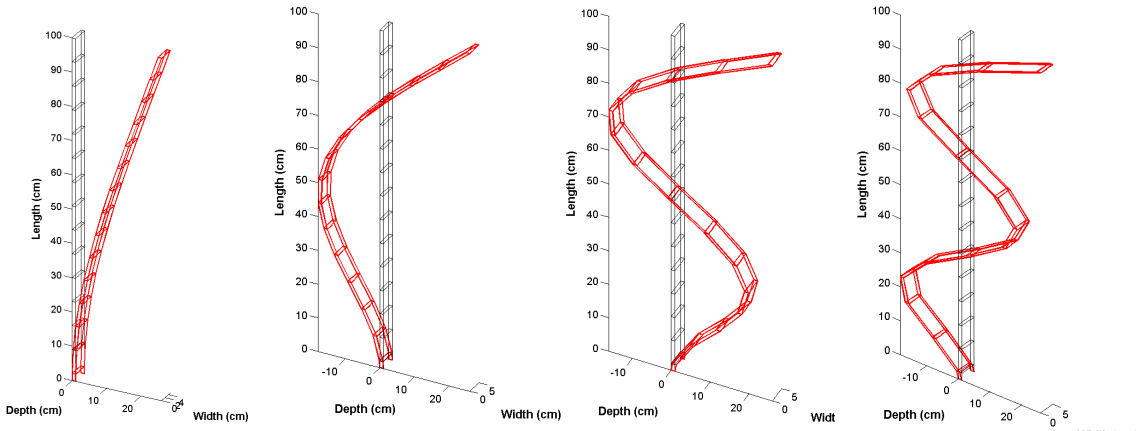


Mode 1 (3.47 Hz) Mode 2 (21.80 Hz) Mode 3 (60.97 Hz) Mode 4 (119.36 Hz)

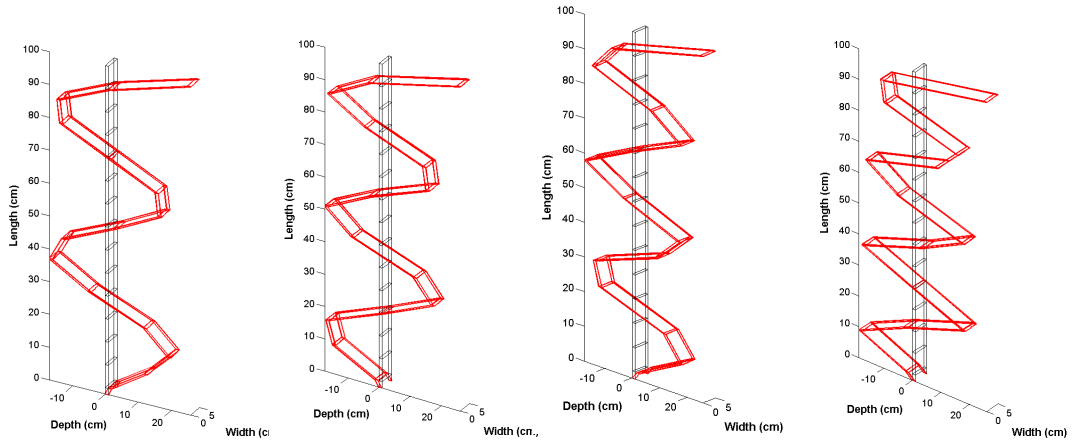


Mode 5 (196.68 Hz) Mode 6 (291.99 Hz) Mode 7 (403.59 Hz) Mode 8 (528.79 Hz)

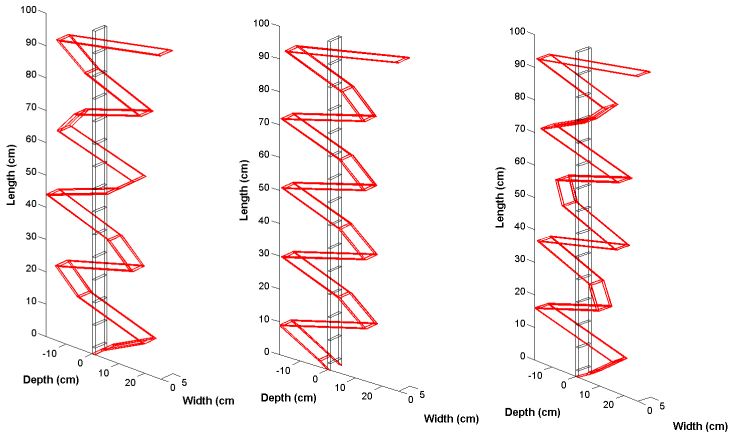


Mode 9 (663.94 Hz) Mode 10 (804.69 Hz) Mode 11 (946.36 Hz)

**Figure IV. 7:** First eleven mode shapes for Scenario 1 extracted from FDD method.

By summing a large number of finite-time windows with identical initial conditions, ambient vibrations remain stationary and the impulse response of the structure is revealed (Yang et al., 1984; Gul and Catbas, 2011). Vandiver et al. (1982) provides details of the mathematical formulation that can be simplified by:

$$RDT(\tau) = \frac{1}{N}\sum_{i=1}^{N} \dot{x}_i\,(t_i\ + \tau) \quad 0 \le \tau \le T \tag{IV.20}$$

where

$$x_i(t_i)\ =\ x_s \quad i = 1,2,3, \ldots$$

$$\dot{x}_i(t_i)\ \ge\ 0 \quad i = 1,3,5, \ldots.$$

$$\dot{x}_i(t_i)\ \le\ 0 \quad i = 2,4,6, \ldots.$$

where $N$ is the number of time windows with fixed initial conditions, $\dot{x}_i$ is the ambient vibration windows of duration τ, and $t_i$ is the time verifying the initial conditions. The choice of initial conditions is a key-point for the stability of the random decrement signature. A total of $N$ averages are taken, each of time length $T$. The starting time for each average is taken such that the initial displacement is a constant $x_s$, and the initial velocity is alternating from positive to negative value. Null displacement and positive velocity conditions proposed by Cole (1973) and verified by Asmussen et al. (1999) and Dunand (2004) are considered here. Since we assume the input (ambient vibrations) as random, then taking numerous averages will produce the response to the initial velocity. Response to the excitation will also diminish with numerous averages because the excitation is random. Therefore, only the response to the initial displacements remains and this vibration decay curve can be used to identify the resonant frequency of the structure and its damping.

### IV.3.2.2 – Data processing description by RDT

The stability of the signature also depends on the number of stacked windows of duration $\tau$ ($\tau$ corresponding to at least 10 periods $T$ of the system vibration). In general, the overall duration of the ambient vibration recording *T0* during which a large number $N$ of similar initial conditions are summed, is chosen here equal to ~1000 T, that is to say the duration T0 is adjusted to the mode period. The technique requires 400 to 500 averages to produce a repeatable signature (Jeary, 1997).

Moreover, the signal processing is done mode by mode, i.e. ambient vibrations are band-pass filtered using a second-order Butterworth filter around $\pm$10 % the mode frequency, and four periods were used to track the frequency variation of each mode over time.

During this synthetic experiment, the noise excitation using random function generated by Matlab is maintained during 1500 seconds at the boundary condition of beam (x=0). The noise signal propagates in the beam and is finally recorded at the top of the beam (free

boundary condition). The total time of the simulation is chosen long enough (1500 seconds), to monitor the frequency versus time for all modes, especially for low frequencies (3.4 Hz, 20 Hz …).

The simulation is divided into three parts:

1- From 0s to 500 seconds: Correspond to Scenario 1 (undamaged beam) with Young's modulus E = 5400 MPa.

2- From 500s to 1000 seconds: Correspond of Scenario 5 (damaged beam) following the case defined in Tab. IV.1.

3- From 1000s to 1500 seconds: Identical to the first sequence (Scenario 1).

The sampling frequency used is $f_s$= 5000 Hz. A total of 7500000 data points are obtained to simulate the measured vibration responses at the free end of the beam.

The frequency values are caught by the Random Decrement Technique applied to time-history vibrations from one sensor at the free end of the beam (x=L).

Figure IV.8 shows an example of the time variation of the modal frequencies for modes 2 to 8 tracked by the Random Decrement Technique and corresponding to Scenario 5. We observe a clear decrease of these modal frequencies due to a loss of stiffness of the beam during the part 2 (500 to1000 seconds). After removing the damage condition (part 3), we note that all frequencies of each mode of vibration increase and return to the initial state $f_0$ (relaxation on the beam). From the part 1 and 3, we observe a very low noise of the frequency value.

We note that the mode 3 is the most sensitive to damage (black curve, frequency ratio equal to 14.7%) because the position of damage for scenario 5 is located at antinode. Conversely, mode 4 (green curve) is the less sensitive compared to other modes (frequency ratio equal to 3.1%), due to the position of the damage close to node of this mode.

Table IV.3 compares the frequency values obtained using the FDD and RDT methods for the first eight frequencies obtained by numerical analysis for undamaged (Scenario 1) and damaged beam (Scenario 5).

We observe a very good agreement between these two methods (FDD and RDT) for the first eight bending modes; let us assume a relevant and accurate assessment of frequency whatever the modes and the methods.

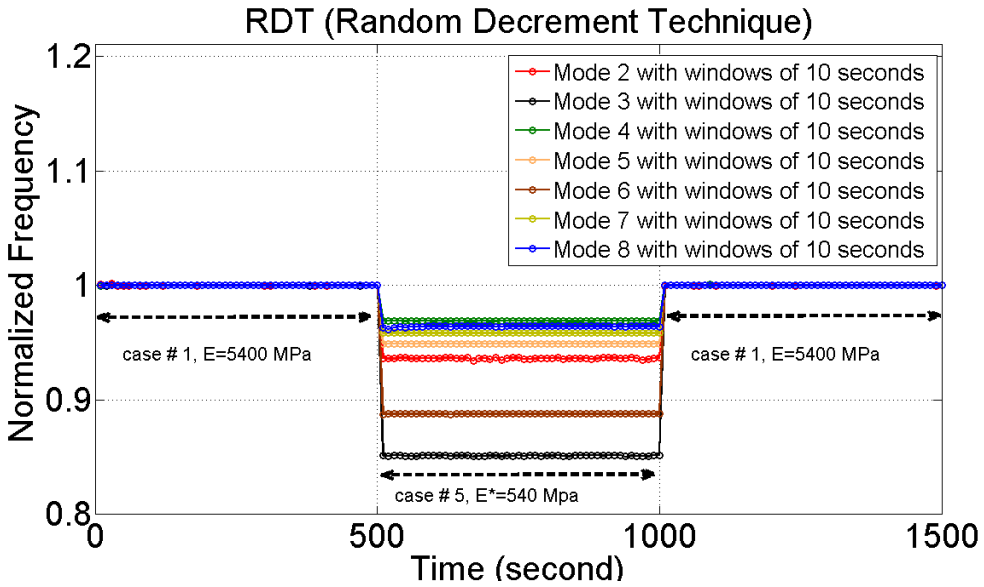


**Figure IV. 8:** Changes in normalized frequency for mode 2 to 8 versus time and tracked by the RDT method for Scenario1 and 5.

| Modes | FDD Scenario 1 [Hz] | RDT Scenario 1 [Hz] | FDD Scenario 5 [Hz] | RDT Scenario 5 [Hz] |
|---|---|---|---|---|
| 1 | 3.47 | 3.47 | 2.86 | 2.86 |
| 2 | 21.80 | 21.79 | 20.40 | 20.40 |
| 3 | 60.97 | 60.99 | 51.95 | 51.93 |
| 4 | 119.36 | 119.36 | 115.66 | 115.66 |
| 5 | 196.68 | 196.68 | 186.69 | 186.69 |
| 6 | 291.99 | 291.99 | 259.19 | 259.20 |
| 7 | 403.59 | 403.57 | 386.84 | 386.82 |
| 8 | 528.79 | 528.83 | 510.00 | 509.86 |

**Table IV. 3 :** Natural Frequencies (Hz) corresponding to Scenarios 1 and 5 extracted by the FDD and RDT methods.

Figure IV.9 shows the efficiency and robustness of the RDT method applied to mode 1. Since the frequency of mode is low, Equation IV.20 is sensitive to the length of the recording $\tau$ used for applying the RDT, as aforementioned. Ten seconds length of ambient vibrations (blue curve) is too short to get a good and accurate estimate of this frequency (i.e., noisy curves for parts 1 and 3).

To estimate the stability of the frequency measurement by RDT applied to mode 1, we tested three durations of time windows: 15, 20 and 25 seconds. For 20s and 25s length, we observe that the quality of the frequency monitoring is better than for 10 and 15 s length. Mode 1 becomes stable and accurate (less fluctuation).

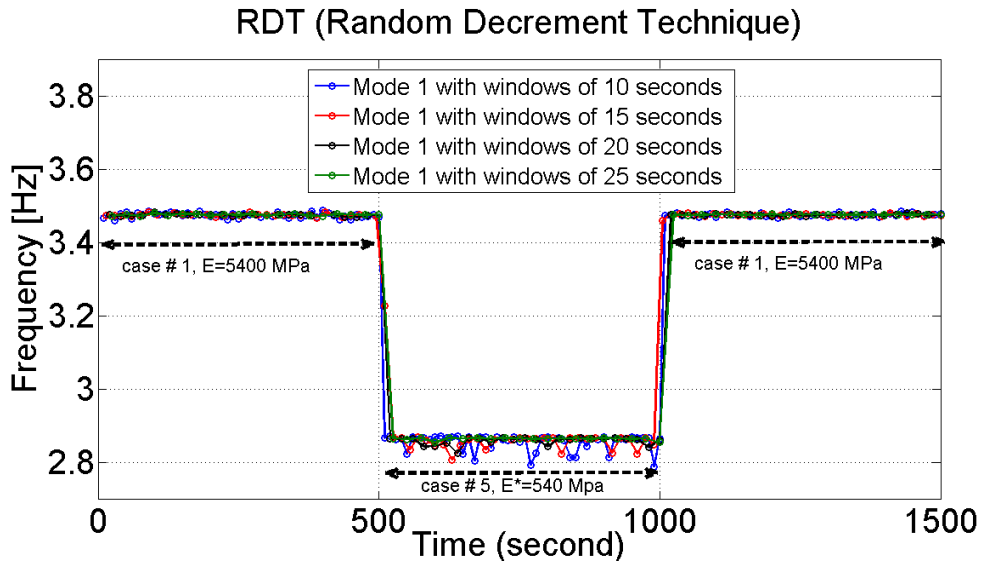


**Figure IV. 9:** Variation of the frequency assessment for mode 1 depending on the length of the time windows used for computing the RDT methods.

In order to be sure that the observed frequency variations are related to damage and not to processing, we tested different configurations for optimizing the RDT algorithm. Dunand (2005) studied the time of recording required for a relevant estimate of frequency using RDT considering real structure. He used ambient vibrations recorded at the top of several buildings in Grenoble. Figure IV.10 shows how the frequency measured by RDT converges after about 900 seconds to the measured value on 3600 seconds of recording with a relative error of 1% and Dunand assumed that 1000 periods of recording length was enough for an accurate estimate of frequency.

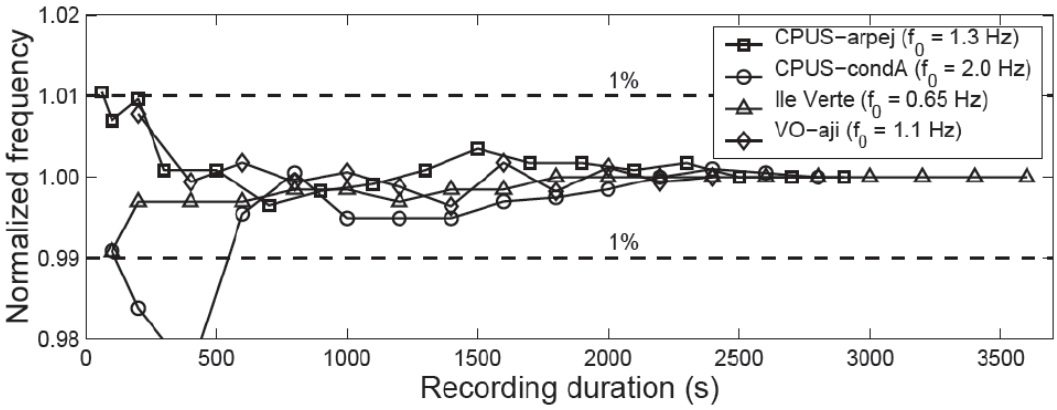


**Figure IV. 10:** Accurate of frequency measurements by random decrement technique (RDT) depending on the length of the recording on several buildings of Grenoble (after Dunand, 2005).

In our case, an oversimplified solution is considered, i.e. a synthetic signal corresponding to the response of a single-degree-of-freedom (SDOF) oscillator was used ($f_0$=3.4 Hz and damping value 5%).

During the simulation, the SDOF system was excited by a low-amplitude random noise at the base for 1200 s and the output signal at the top of the beam (free boundary condition) was computed using the Duhamel's integral solution. Figure IV.11 shows the stability of the frequency for mode 1 computed using the RDT method applied to the synthetics and according to the length of the windows stacked (i.e., $\tau$ in Eq. IV.20). The stability of the frequency is computed through the coefficient of variation, i.e.:

$$CV = {}^{\sigma}/_{\mu} \times 100 \qquad \text{IV.21}$$

with $\sigma$ the standard deviation and $\mu$ the mean value of the frequency. It is clear that for mode 1, CV is strongly dependent on the length of the windows and it decreases and becomes stable with a recording time of 100 seconds with a relative error of 0.5%.

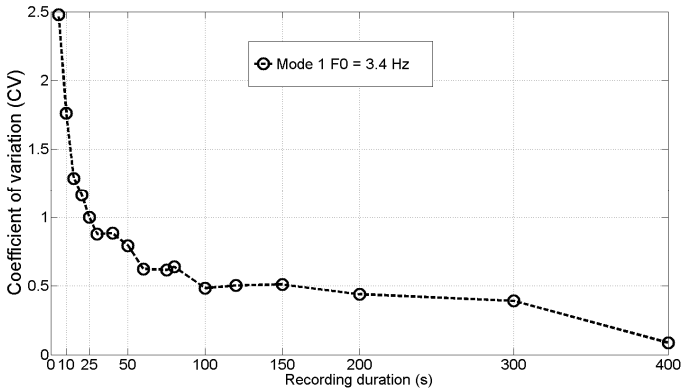


**Figure IV. 11:** Optimization of RDT tested using SDOF response to ambient vibrations.

RDT does not locate the damage and does not give an estimate of its severity. Nevertheless, the major advantage of the RDT is to provide an efficient and accurate estimate of the frequency wandering as proposed by Mikael et al. (2013) for real buildings. For this purpose, the RD technique is an efficient computational data processing procedure.

In conclusion, the random decrement technique (RDT) was used to monitor the wandering of natural frequencies of the beam using synthetic experiments. The great advantage of this method is to monitor the variation of the natural frequencies of a system so that more accurate than the Fast Fourier transform and using only one sensor at the top.

## IV.4 – Detection and localization of damages using FFT, RDT and FDD from synthetic experiments

In the following, the frequency and mode shapes will be computed for synthetics, using 300 seconds of recording at each sensors located along the beam, for the undamaged (S1) and damaged (S2 to S11) scenarios. Frequency variations are extracted from RDT methods and MAC values are computed based on mode shapes extracted using FDD.

Finally, the performance of the NDE methods is then tested under ambient noise vibration, i.e. under equivalent-to-experimental conditions, using frequencies and mode shapes computed by FDD.

### IV.4.1 – Global detection using the frequency ratio FR

Figure IV.12 displays the evolution of Frequency ratio (FR, Eq. III.7) normalized by the maximum of each mode of vibration according to the severity of the damage at **position** A (Scenarios 2 to 5). The results are for the frequency (numerical modal analysis RDM6, Chap. III) and time (FEM) domain. For increasing severity, the FR normalized also increases with the same rate whatever the modeling. We observe then a good agreement of FR values obtained by modal analysis and time analysis based on the FDD method to extract the first eleven frequencies, including the higher frequencies. In both cases, we find the same average trend, i.e. a nonlinear increase of frequency ratio with the damage severity as aforementioned (Chap. III).

### IV.4.2 – Global detection using the MAC value

The Modal Assurance Criterion (MAC, Eq. II.30) has been used in order to evaluate and detect the damage at the bottom of beam at **position** A (30-33.5 cm). The mode shapes were obtained using the FDD methods applied to the synthetics computed for the undamaged (Scenario S1) and the damaged beam, for 4 damage severities (Scenarios S2 to S5).

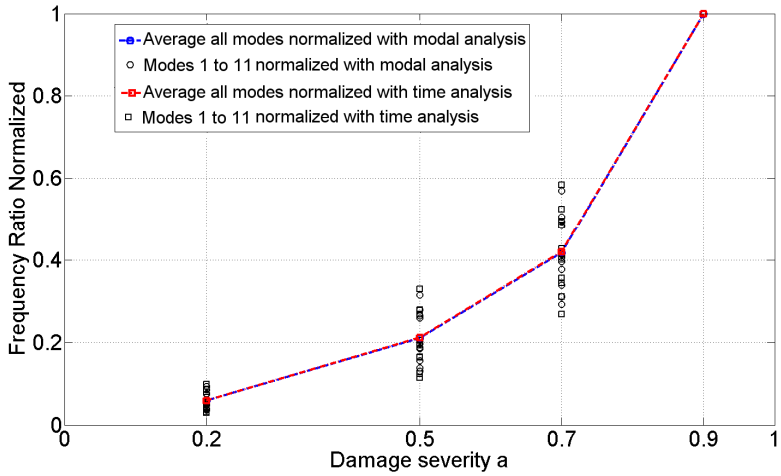


**Figure IV. 12:** Frequency ratio (FR) normalized versus four damage severities for the first eleven mode shapes using modal analysis (blue curve) and time analysis (red curve) at the bottom of beam at **position** A (30-33.5 cm) Scenario S2 to S5.

Figure IV.13a shows the variation of MAC value with respect to the number of modes considered, according to the severity of the damage. As already mentioned, the MAC value provide relative information on the level of severity, the value of MAC decreasing when degree or value of damage becomes high.

Since it depends on the number of modes considered for computing the MAC, the absolute assessment of the severity of damage is not relevant with this method. Moreover, the MAC value variation shows a very good fit between the results obtained by modal analysis and time analysis (Fig. IV.13b). In conclusion, the mode shapes extracted from synthetics are accurate enough for detecting changes by MAC values, even by considering only the first mode and this will be then tested for experimental data in the next chapter.

### IV.4.3 – Localization of damage using NDE methods

A summary of the basic process followed in this chapter is illustrated in the flowchart Figure IV.14.

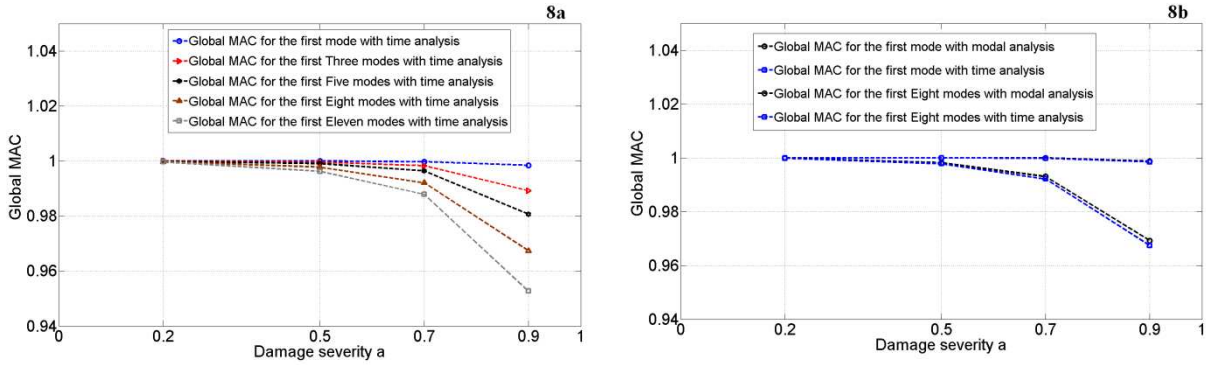


**Figure IV. 13:** (a) Global assessment of MAC with four damage severities using time analysis at **position** A (S2 to S5). (b) Comparison between modal analysis and time analysis.

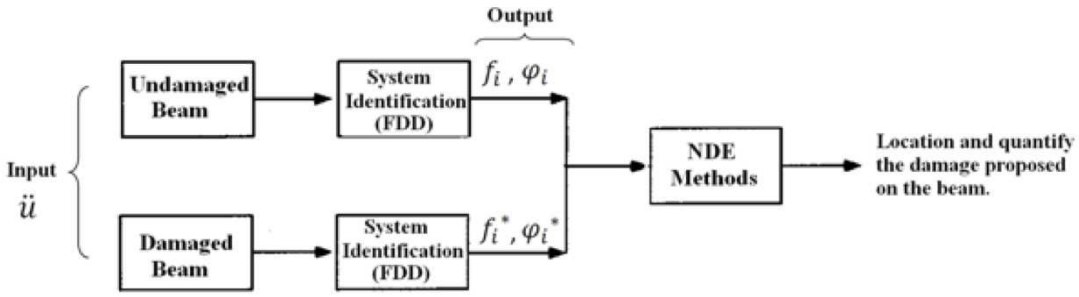


**Figure IV. 14:** Damage detection process for testing the NDE methods.

where $\ddot{u}$ is the acceleration computed at each sensor, $f_i$ and $\varphi_i$ correspond to frequencies and mode shapes to undamaged beam, and asterisk (*) corresponds to damaged beam.

#### IV.4.3.1 – Single damage detection and localization. Scenarios S2, S3, S4 and S5

First, a single and narrow damage is considered at **position** A (30-33.5 cm) with four damage severities corresponding to S2, S3, S4 and S5 (Tab. III.3). The performance of each NDE method is evaluated through the quality criterion $C_{AB}$ defined previously (Eq. III.8) and used

here for each Scenario. Among the algorithms tested, CIF and ULS require the assessment of the mode shapes and natural frequencies, while MSC and MSCS require only the mode shapes of the beam.

Figure IV.15 shows the variation of the $C_{AB}$ coefficient according to the methods and the number of modes considered. Similar observations with the results discussed in Chap. III (Fig. III.11) are done:

- We observe that for the MSC and MSCS methods, the quality of the damage localization assessment is better for a small number of modes and the efficiency decreases with the number of modes. To reduce the probability of false detections, these two methods (MSC, MSCS) need only the first two mode shapes for localization of the damage with rather good precision.
- The MSCS method is sensitive to the damage severity, the $C_{AB}$ coefficient changing for a given number of modes considered.
- The CIF is the worst method, unable to detect correctly the damage position, including or not the first mode to the process.
- The ULS remains the best method for detecting and localizing damage, with stable and constant values of $C_{AB}$ coefficient with the number of mode, value of $C_{AB}$ close to 1, which means a perfect localization.

By comparing frequency (Fig. III.11) and time (Fig. IV.15) modeling, we observe that the $C_{AB}$ values are smaller for time domain. Since the frequencies are correctly estimated using FDD methods, we can conclude on the less accurate of the FDD method for extracting the mode shapes than the numerical solution. This is also confirmed by the strong decrease of the $C_{AB}$ coefficient by including higher modes for computing NDE methods.

In fact, as shown in Fig. IV.7, the quality of the higher mode shapes is directly related to the number of sensors used along the beam. This is also the case for the experimental approach since sensors are usually placed on the slab, for a discrete assessment of shapes.

Nevertheless, for these scenarios, the FDD provides relevant mode shapes and frequencies that can be used for detected and localized singled damage close to the clamped extremity. As already mentioned, the ULS method remains the most effective solution for localizing damages.

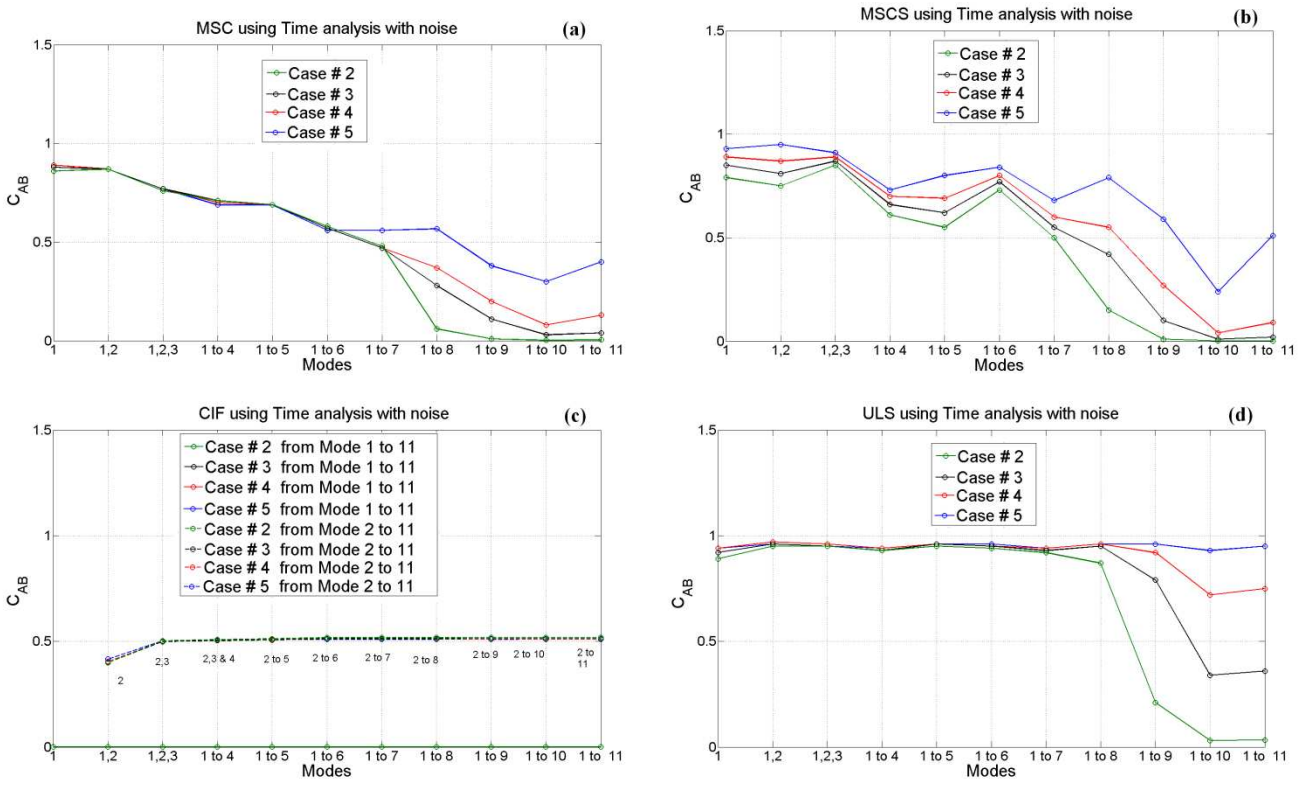


**Figure IV. 15:** Variation of the $C_{AB}$ for a single and narrow damage (Scenario S2 to S5) according to the number of modes. (a) MSC; (b) MSCS; (c) CIF; (d) ULS.

### IV.4.3.2 – Single damage detection and localization. Scenarios S6 and S7

Second, a single and narrow damage is considered at **position** B (61.5-65 cm) and C (86-89.5 cm) with one damage severity corresponding to S6 and S7, respectively (Tab. III.3). The performance of each NDE method is evaluated through the quality criterion $C_{AB}$ defined previously (Eq. III.8).

Figure IV.16 shows the variation of the $C_{AB}$ coefficient according to the methods and the number of modes considered. Similar observations with the results discussed in Chap. III (Fig. III.15) are done:

- We observe that the MSC and MSCS methods provide a bad estimate of localization even by considering only the first modes.
- The CIF is the worst method, unable to detect correctly the damage position, including or not the first mode to the process. This is above all the case for the S7 scenario, when the damage is located close to the free-end extremity, and then directly related with the model of the beam.
- The ULS remains the best method for detecting and localizing damage, with stable and constant values of $C_{AB}$ coefficient with the number of mode, value of $C_{AB}$ close to 1, which means a perfect localization.

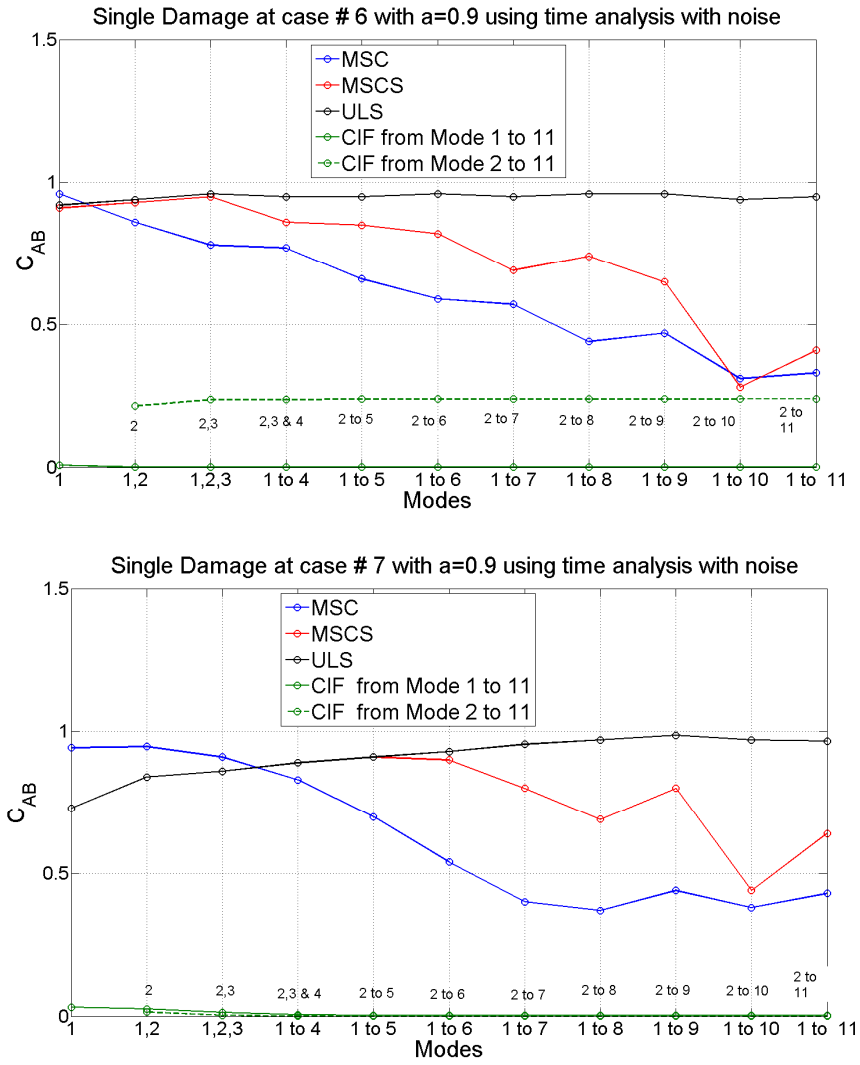


**Figure IV. 16:** Variation of the $C_{AB}$ for a single and narrow damage (Scenario S6, upper row; Scenario S7, lower row) according to the number of modes and the NDE.

As previously mentioned, the higher mode shapes introduced bias in the assessment, due to the poor accuracy of these modes for a limited number of nodes. Compared to the use of numerical mode shapes (Fig. III.15), the $C_{AB}$ values decrease when modes 8 to 11 are integrated to the process, even for the ULS method.

### IV.4.3.3 – Large and multiple damage detection and localization – Scenarios S8 and S9

Next, a large and multiple damage is considered at **position** D (30-47.5 cm) and at **positions** A, B and C for one damage severity and corresponding to S8 and S9, respectively (Tab. III.3). The performance of each NDE method is evaluated through the quality criterion $C_{AB}$ defined previously (Eq. III.8).

Figure IV.17 shows the variation of the $C_{AB}$ coefficient according to the methods and the number of modes considered. Similar observations with the results discussed in Chap. III (Figs. III.17 and III.19) are done:

- The ULS remains the best method for detecting and localizing damage, with increasing values of $C_{AB}$ with the number of modes, following an asymptotic shape up to 1. For multiple damage scenario S9, the first modes fail to localize correctly the damage and we need to consider at least the fourth mode for getting $C_{AB}$ value close to 0.9. For S9, the final $C_{AB}$ is close to 1, considering a quasi-perfect localization.
- The CIF method seems to be more effective for localizing large damage close to the clamped extremity of the beam (S8), excluding the first mode for the computing. For multiple damage (S9), this method is very bad and again the worst method for localizing.
- MSC and MSCS give a quite good localization considering the lower modes, MSCS being a little bit better than MSC. Nevertheless, they are very sensitive to the number of modes used for multiple (S9) or large (S8) damage.

### IV.4.3.4 – Multiple damage detection and localization - Scenarios S10 and S11

Finally, multiple damage are considered at **positions** A, B and C with descending and ascending damage severities, corresponding to S10 and S11, respectively (Tab. III.3). Only the performance of the ULS method is shown through the quality criterion $C_{AB}$ defined previously (Eq. III.8).

Figure IV.18 shows the variation of the $C_{AB}$ coefficient according to the scenarios and the number of modes considered. Similar observations with the results discussed in Chap. III (Fig. III.20) are done. We can confirm the very efficiency of the ULS method for localization of multiple damages, with identical ULS amplitude in the middle of the beam (**position** B) and ULS amplitude at **position** A and at **position** C for equivalent damage coefficient whatever the order of the variation of the amount of damage.

### IV.4.3.5 – Conclusions on the NDE methods using mode shapes extracted from FDD

According to the previous results, the ULS method based on mode shapes like experimental localizes with success the damage along the beam, whatever the position, the number of damage positions and extension of the damage. Figure IV.19 synthetizes the result for this method, also for assessing the amount of damage. As previously shown in Chap.III, the ULS remains the most effective and accurate methods, even when FDD frequency and mode shapes are used. Similar conclusion can be done, i.e. (1) the application of the curvature of uniform load surface (ULS) method gives the more reliable results and still very robust whatever the configuration of damage; (2) some drawbacks are noticed, such as the localization of the damage at the two extremities of the beam or the low reliability of the absolute damage amount, such as for the extended damage; (3) for a blind estimate of damage

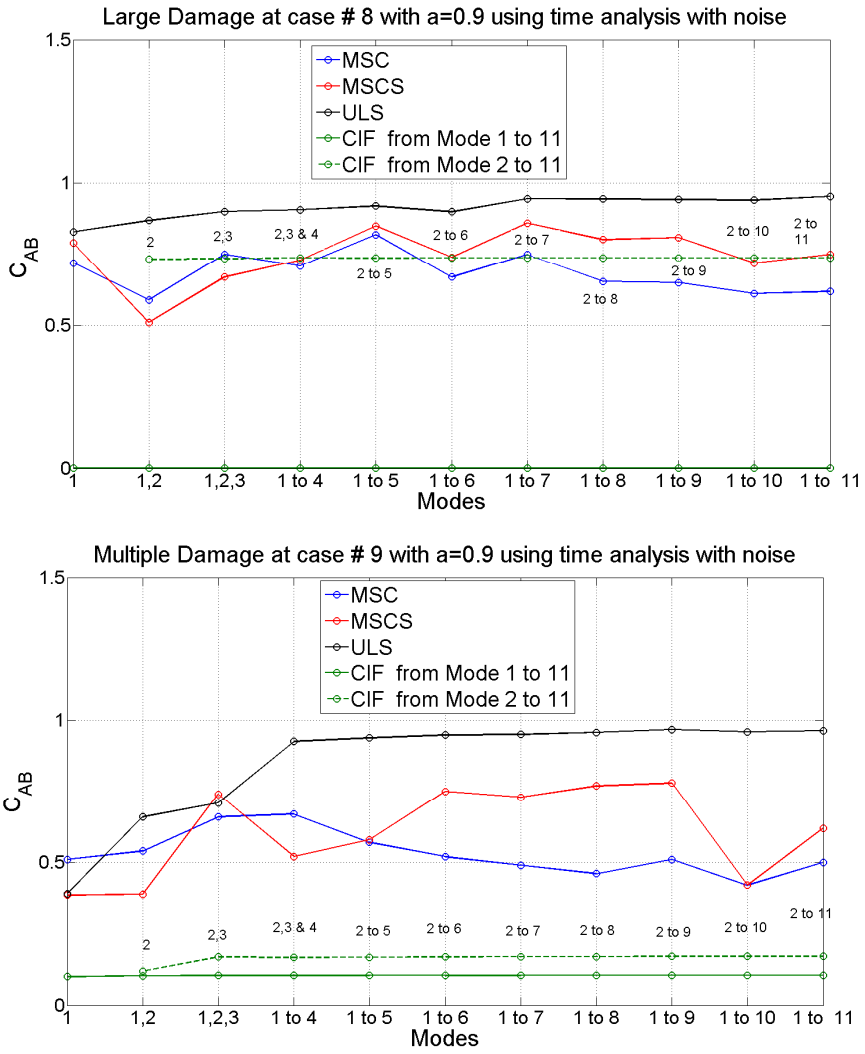


**Figure IV. 17 :** Variation of the $C_{AB}$ for a large (Scenario S8, upper row) and multiple (Scenario S9, lower row) damage scenarios according to the number of modes and the NDE methods.

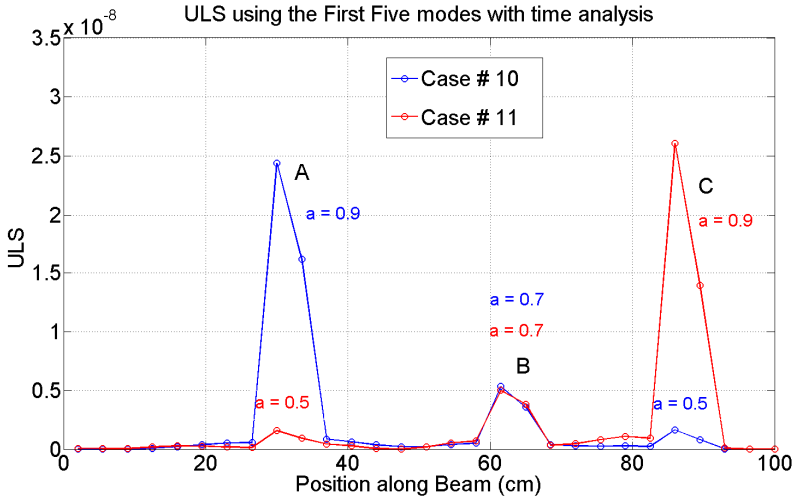


**Figure IV. 18:** Estimated position of damage along the beam, using the ULS methods for the case # 10 (blue) and # 11 (red) scenarios (with three different damage severity a).

(quantification and localization) at least three modes must be accounted for, improving the assessment by adding the first five modes.

Moreover, by comparing the time and the frequency modeling, we conclude (Fig. IV.19c) that the $C_{AB}$ values are quite similar, let us assume that the use of FDD methods for modes extraction combined with the ULS method provides an accurate and relevant assessment of damage localization. This method will be then tested for experimental data.

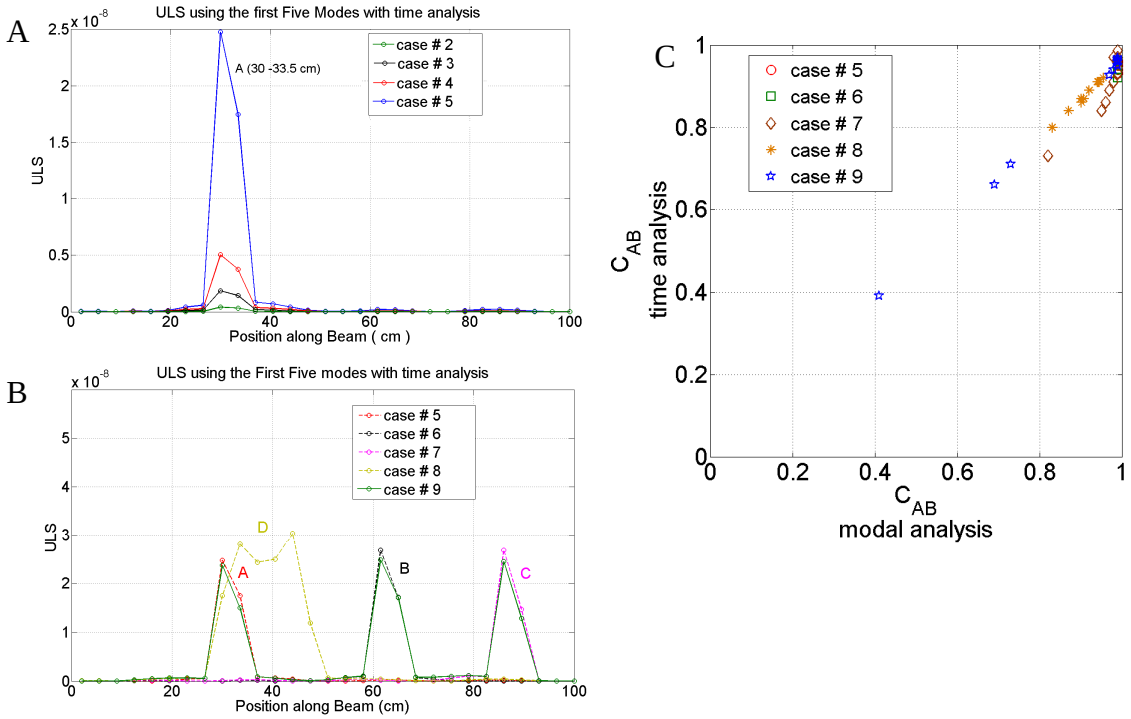


**Figure IV. 19:** Summary of the relevancy of the ULS methods applied using modes and frequencies extracted by FDD like experimental methods. A) LV3 of the NDE objective, evaluating the amount of damage (Scenarios S2, S3, S4 and S5). B) Performance of the ULS method considering the first five modes for S5, S6, S7, S8 and S9 scenario, keeping the same severity of damage (a=0.9). C) Comparing the $C_{AB}$ values computed considering the ULS method with modal and time analysis considering S5, S6, S7, S8 and S9 scenarios of damage, keeping the same severity of damage (a=0.9).

## IV.5 – Structural damage localization and monitoring through perturbation theory

Until recently, it was assumed that variations in the frequencies recorded at one point of a structure might only reflect a global change of the system properties, such as after earthquakes, and that this is often not sufficient to further locate the origin of a perturbation. For this reason, damage detection/ localization methods have been developed based on the use of multiple sensors. These provide analysis of the mode shapes, such as the four NDE methods presented before. Nevertheless, the experimental assessment of mode shapes is less accurate, and when compared with the sensitivity of resonant frequencies, these methods cannot be used for field testing for detection and location of small variations. This has been

shown in the previous paragraph, comparing the $C_{AB}$ coefficient using theoretical or pseudo-experimental mode shapes.

The first objective of this study is to propose a natural-frequency-based method for structural damage detection and localization through perturbation theory, as associated with a high-resolution deconvolution method to treat the inverse problem (Baillet et al. (2013)). The second objective is to apply this method to experimental conditions, when a structure is excited by ambient vibrations.

### IV.5.1 – Theoretical approach for a one-dimensional clamped–free beam under bending

Neglecting shear deformation, the 1-D equation governing the transverse vibration of a beam of length *L* is the Bernoulli-Euler equation:

$$\frac{\partial^2}{\partial x^2}\left( EI\left(x\right)\frac{\partial^2 \psi\left(x,t\right)}{\partial x^2}\right)+m\left(x\right)\frac{\partial^2 \psi\left(x,t\right)}{\partial t^2}=0 \qquad \text{(IV.21)}$$

where $\psi\left(x,t\right)$ is the spatial-temporal beam deformation at position *x* and time *t*, *m(x)* is the mass per unit length, and *EI(x)* is the product of the elastic Young's modulus and the inertial moment at each point on the beam. As such, *EI(x)* corresponds to the bending rigidity of the beam.

Decomposing $\psi\left(x,t\right)$ over the discrete set of natural free vibrations of the beam, we have:

$$\psi\left(x,t\right)=\sum_n \varphi_n\left(x\right)\exp\left(i\omega_n t\right) \qquad \text{(IV.22)}$$

where $\varphi_n\left(x\right)$ is the beam modal deformation that is associated with the resonant frequency $\omega_n$ (in rad/s).

For each mode n, it follows that:

$$\frac{\partial^2}{\partial x^2}\left( EI\left(x\right)\frac{\partial^2 \varphi_n\left(x\right)}{\partial x^2}\right)-\omega_n^2 m\left(x\right)\varphi_n\left(x\right)=0 \qquad \text{(IV.23)}$$

with the boundary conditions corresponding to a clamped–free beam :

$$\varphi_n\left(0\right)=\varphi_n^{''}\left(L\right)=\varphi_n^{'}\left(0\right)=\varphi_n^{'''}\left(L\right)=0 \qquad \text{(IV.24)}$$

The goal of this approach is to evaluate, to first order, the change in frequency $\omega_n$ when a slight perturbation is made to the elastic properties of the beam. This development was first introduced by Morassi (1993) in the case of a crack-induced change in a beam-like structure. In the present formulation, we assume that the stiffness coefficient *EI(x)* is perturbed at position x such that:

$$EI(x) \to \widetilde{EI}(x) = EI(x) + \delta EI(x) \tag{IV.25}$$

with the condition $\frac{\|\delta EI\|}{\|EI\|} \ll 1$; i.e. the relative change of the stiffness is small when integrated over the whole beam. This perturbation naturally induces a relative change in the modal deformation $\varphi_n(x)$ and the frequency $\omega_n$ of the beam:

$$\omega_n \to \widetilde{\omega_n} = \omega_n + \delta\omega_n$$

$$\varphi_n(x) \to \widetilde{\varphi_n}(x) = \varphi_n(x) + \delta\varphi_n(x) \tag{IV.26}$$

The perturbed system now satisfies the modified wave equation:

$$\frac{\partial^2}{\partial x^2}\left(\widetilde{EI}(x)\frac{\partial^2\widetilde{\varphi_n}(x)}{\partial x^2}\right) - \tilde{\omega}_n^2 m(x)\widetilde{\varphi_n}(x) = 0 \tag{IV.27}$$

When the perturbed solutions $\widetilde{\varphi_n}(x)$ and $\widetilde{\omega_n}$ are replaced in Eq. IV.27 by their expression in Eq. IV.26, it follows that:

$$\frac{\partial^2}{\partial x^2}\left(EI(x)\frac{\partial^2\varphi_n(x)}{\partial x^2}\right) - \omega_n^2 m(x)\varphi_n(x) \qquad \text{(zero}^{\text{th}}\text{ order)}$$

$$+\frac{\partial^2}{\partial x^2}\left(\delta EI(x)\frac{\partial^2\varphi_n(x)}{\partial x^2}\right) + \frac{\partial^2}{\partial x^2}\left(EI(x)\frac{\partial^2\delta\varphi_n(x)}{\partial x^2}\right) - 2\omega_n\delta\omega_n m(x)\varphi_n(x) - \omega_n^2 m(x)\delta\varphi_n(x)$$

(first order)

$$+\frac{\partial^2}{\partial x^2}\left(\delta EI(x)\frac{\partial^2\delta\varphi_n(x)}{\partial x^2}\right) - 2\omega_n\delta\omega_n m(x)\delta\varphi_n(x) - (\delta\omega_n)^2 m(x)\delta\varphi_n(x) \qquad \text{(second order)}$$

$$= 0$$

The zero$^{\text{th}}$ order term is null according to Eq. IV.23. It corresponds to the unperturbed solution. Neglecting the second-order term under the conditions $\frac{\delta\omega_n}{\omega_n} \ll 1$ and $\frac{\|\delta\varphi_n\|}{\|\varphi_n\|} \ll 1$, we are left with the first-order term only:

$$\frac{\partial^2}{\partial x^2}\left(\delta EI\left(x\right)\frac{\partial^2\varphi_n\left(x\right)}{\partial x^2}\right)-2\omega_n\delta\omega_n m\left(x\right)\varphi_n\left(x\right)=\omega_n^2 m\left(x\right)\delta\varphi_n\left(x\right)-\frac{\partial^2}{\partial x^2}\left(EI\left(x\right)\frac{\partial^2\delta\varphi_n\left(x\right)}{\partial x^2}\right) \tag{IV.28}$$

In perturbation theory for linear operators, the change in the modal deformation $\delta\varphi_n\left(x\right)$ is classically projected over the set of the unperturbed modes:

$$\delta\varphi_n\left(x\right)=\sum_{k\neq n}\alpha_k\varphi_k\left(x\right) \tag{IV.29}$$

According to Eqs. IV.23 and IV.29, we have, for every mode:

$$\frac{\partial^2}{\partial x^2}\left(EI\left(x\right)\frac{\partial^2\delta\varphi_n\left(x\right)}{\partial x^2}\right)=\sum_{k\neq n}\alpha_k\frac{\partial^2}{\partial x^2}\left(EI\left(x\right)\frac{\partial^2\varphi_k\left(x\right)}{\partial x^2}\right)=\sum_{k\neq n}\alpha_k\omega_k^2 m\left(x\right)\varphi_k\left(x\right) \tag{IV.30}$$

Taking into account the mode orthogonality property between the modal deformations $\int_0^L m\left(x\right)\varphi_n\left(x\right)\varphi_m\left(x\right)=\delta_{nm}$, we then project Eq. IV.28 over mode *n* to obtain:

$$\int_0^L\frac{\partial^2}{\partial x^2}\left(\delta EI\left(x\right)\frac{\partial^2\varphi_n\left(x\right)}{\partial x^2}\right)\varphi_n\left(x\right)dx=2\omega_n\delta\omega_n \tag{IV.31}$$

Finally, after two integrations by parts and using the boundary conditions in Eq. IV.24, the frequency change associated with the natural free-vibration of the beam is:

$$\delta\omega_n=\frac{1}{2\omega_n}\int_0^L\delta EI\left(x\right)\left[\frac{\partial^2\varphi_n\left(x\right)}{\partial x^2}\right]^2dx \tag{IV.32}$$

In Eq. IV.32, the integrand $\frac{1}{2\omega_n}\left[\frac{\partial^2\varphi_n\left(x\right)}{\partial x^2}\right]^2$ is classically interpreted in the framework of the first-order Born approximation as the sensitivity kernel of the frequency change for each mode associated to a stiffness perturbation.

In a second step, Eq. IV.32 is used to invert for the stiffness perturbation $\delta EI\left(x\right)$at each point *x* on the beam from the measurement of the frequency change $\delta\omega_n$ observed for each mode *n*.

In this inversion process, we assume that $\omega_n$ and $\varphi_n\left(x\right)$ are known for the unperturbed problem. This means that either: (1) the unperturbed beam has been modeled correctly so that both $\omega_n$ and $\varphi_n\left(x\right)$ are obtained from a numerical simulation for a set of modes; or (2) the resonant frequencies $\omega_n$ and the modal deformations $\varphi_n\left(x\right)$ have been experimentally measured on the beam by one or a set of sensors.

The inversion algorithm is built from the discretization of the integral in Eq. IV.32 over a finite number of segments of height $\Delta x$ on the beam, such that $x_k = k\Delta x$, with $k=1,...,M$ and $L = M\,\Delta x$.

$$\delta\omega_n = \frac{1}{2\omega_n}\frac{L}{M}\sum_{k=1}^{M}\delta EI\left(x_k\right)\left[\frac{\partial^2\varphi_n\left(x_k\right)}{\partial x^2}\right]^2 \qquad \text{(IV.33)}$$

In the summation, the amplitude factor $\frac{1}{2\omega_n}\frac{L}{M}\left[\frac{\partial^2\varphi_n\left(x_k\right)}{\partial x^2}\right]^2$ is defined in linear inversion processes as the Fréchet kernel associated to mode *n* and a perturbation *Δx* located at $x_k$ on the beam. From the linear discretization, the inversion problem can be rewritten using a matrix formulation involving *p* modes along the beam:

$$\begin{bmatrix}\delta\omega_1\\ \delta\omega_2\\ \dots\\ \delta\omega_p\end{bmatrix} = G\begin{bmatrix}\delta EI\left(x_1\right)\\ \delta EI\left(x_2\right)\\ \dots\\ \delta EI\left(x_M\right)\end{bmatrix} \qquad \text{(IV.34)}$$

where the kernel matrix G is such that:

$$G = \begin{bmatrix}\frac{1}{2\omega_1}\frac{L}{M}\left(\frac{\partial^2\varphi_1\left(x_1\right)}{\partial x^2}\right)^2 & \dots & \frac{1}{2\omega_1}\frac{L}{M}\left(\frac{\partial^2\varphi_1\left(x_M\right)}{\partial x^2}\right)^2\\ \dots & \dots & \dots\\ \frac{1}{2\omega_p}\frac{L}{M}\left(\frac{\partial^2\varphi_p\left(x_1\right)}{\partial x^2}\right)^2 & \dots & \frac{1}{2\omega_p}\frac{L}{M}\left(\frac{\partial^2\varphi_p\left(x_M\right)}{\partial x^2}\right)^2\end{bmatrix} \qquad \text{(IV.35)}$$

Note that following the same methodology the perturbation theory can be applied to the case of a 1-D shear beam. From Eq. IV.34, the solution of the inverse problem requires the estimation of $G^{-1}$. Several difficulties have to be taken into account. First, G is usually not a square matrix, and second, the number of data (the frequency perturbation $\delta\omega_n$ for each of the $p$ modes) is usually smaller than the number of unknowns (the stiffness perturbation $\delta EI(x_k)$ on the $M$ segments in the beam), which makes the problem ill-posed.

Assuming Gaussian-distributed uncertainties, the estimated inverse of G is obtained as in Tarantola (1987):

$$\widetilde{G^{-1}} = (G^T C_d^{-1} G + r * C_m)^{-1} G^T C_d^{-1} \quad \text{(IV.36)},$$

where the *a-priori* model covariance matrix $C_m$ resembles a diagonal matrix, but with Gaussian decrease outside the diagonal, such that each matrix element is:

$$Cm_{ij} = e^{-\frac{(i-j)^2 \Delta x^2}{2l^2}} \quad \text{(IV.37)}$$

The spatial correlation length $l$ is assumed to be stationary along the beam, and should be of the order of the smallest wavelength associated with the highest-order mode taken into account in the inversion. The data covariance matrix $C_d$ is diagonal, with diagonal elements that correspond to the uncertainty on the measured frequency fluctuations $\delta\omega_n$. In Eq. IV.36, the weighting between the data uncertainty $C_d$ and the model smoothing $C_m$ allows us to stabilize the inversion result through the empirical factor *r*. In practice, the optimal factor *r* corresponds to the maximum curvature of the classical L-shaped *misfit-versus-r* curve.

From the estimate of $\widetilde{G^{-1}}$, we then obtain an estimation of the stiffness perturbation as:

$$\begin{bmatrix} \widetilde{\delta EI}(x_1) \\ \widetilde{\delta EI}(x_2) \\ \cdots \\ \widetilde{\delta EI}(x_M) \end{bmatrix} = \widetilde{G^{-1}} \begin{bmatrix} \delta\omega_0 \\ \delta\omega_1 \\ \cdots \\ \delta\omega_P \end{bmatrix} \quad \text{(IV.38)}$$

### IV.5.2 – Finite-element discretization for a one-dimensional clamped–free beam

In this section, the case of a 1-D beam under bending is studied through the numerical computation of the resonant frequencies $\omega_n$ and modal deformation $\varphi_n(x)$, before and after a local change in the flexural rigidity δ*EI(x).* The beam height is 10 m, with uniform density r = 2500 kg.m$^{-3}$, elastic Young's modulus E = 10,000 e$^6$ N.m$^{-2}$, and inertial moment I = 833.3 e$^{-8}$

$m^4$ for the unperturbed case. The beam is rigidly fixed to a support at x = 0 and free at x = L (Fig. IV.1 and IV.2).

The same FEM as in section IV.2 is used. The frequencies and the modal deformation for both the unperturbed and perturbed beam are computed. The maximum error between the analytical frequencies and those obtained by the finite-element modeling is less than 0.01% over the 10 first frequencies. We limit the investigations to the first 10 modes with frequencies varying from $f_1$ = 0.32 Hz for mode 1, to $f_{10}$ = 81.8 Hz for mode 10 (with $\omega_n = 2\pi f_n$ for each mode). Figure IV.20a shows the depth-dependent modal deformation of the first five modes.

In a second step, a slight change in the Young's modulus of $\delta E = -1000\ e^6\ N.m^{-2}$ is applied to the beam at depth x = 2.3 m. The new frequencies of the perturbed beam are calculated using the same finite-element algorithm.

Figure IV.21 shows the relative changes in frequencies $\frac{\delta\omega_n}{\omega_n}$ for the first 10 modes. As expected, the changes are small (of the order of 0.1% at most), as the Young's modulus perturbation is very local on the beam. We also note that $\frac{\delta\omega_n}{\omega_n}$ strongly depends on the mode number. Indeed, the frequency change varies according to the sensitivity kernel formulation (Eq. IV.32), which is spatially modulated by the square of the second-order derivative of each modal deformation $\frac{1}{2\omega_n^2}\left[\frac{\partial^2\varphi_n(x)}{\partial x^2}\right]^2$ at the location of the stiffness perturbation (Fig. IV.20b).

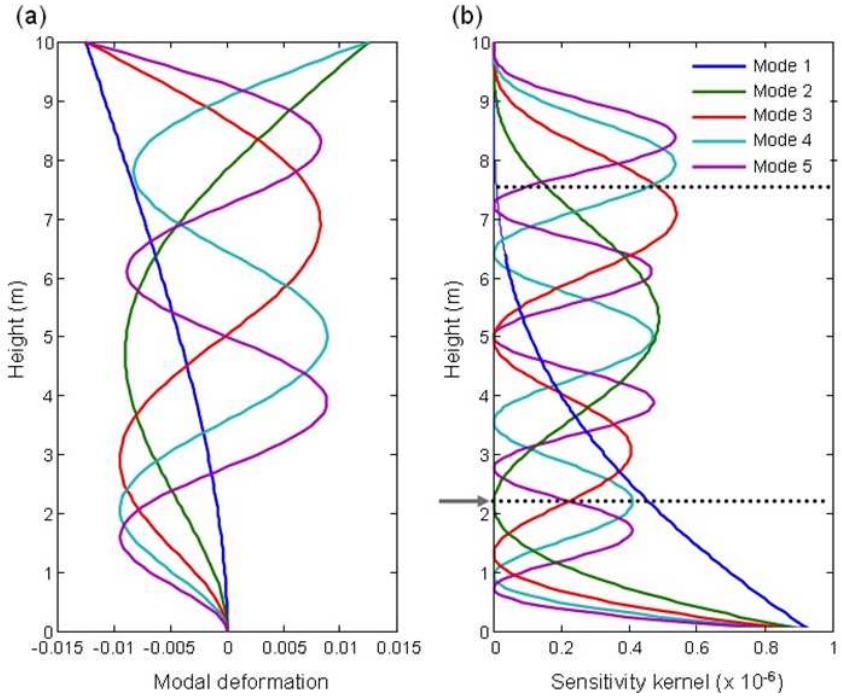


**Figure IV. 20 :** Representation of (a) the modal deformation $\boldsymbol{\varphi_n(x)}$, and (b) the sensitivity kernel of the relative frequency change $\frac{\delta\omega_n}{\omega_n}$, for the first five modes and the 10-m-long clamped–free beam. In (b), the gray arrow corresponds to the position of the stiffness perturbation at x = 2.3 m (see Fig. IV.21). The two dashed lines show the stiffness perturbation interval scanned step-by-step in Figure IV.27, between x = 2.25 m and x = 7.5 m.

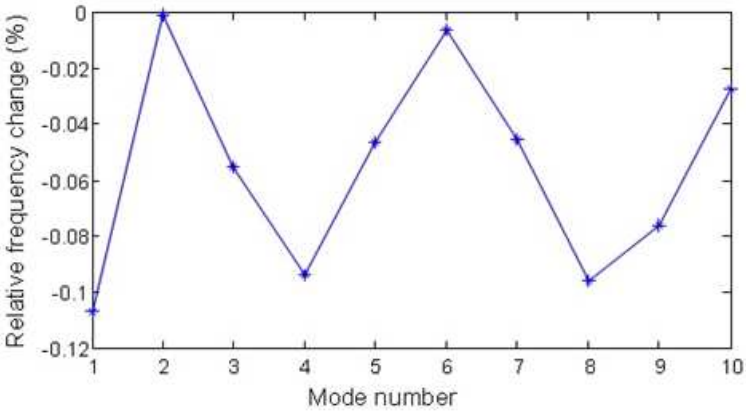


**Figure IV. 21 :** Relative frequency shift $\frac{\delta\omega_n}{\omega_n}$ of the natural frequencies of the beam *versus* mode number for a stiffness perturbation $\boldsymbol{\delta EI}$ at x = 2.3 m.

Figure IV.22a shows the inversion result for the flexural rigidity change δEI along the beam, as obtained from the relative change in resonant frequencies written into Eq. IV.38. Two points are important. First, the inversion result presents, as expected, a minimum at x = 2.3 m, with an estimation of the perturbation that is of the order of the actual δ*EI* = -8333 N.m$^2$

fluctuation. Secondly, we note the presence of a ghost of the actual fluctuation, the location of which (at x = 7.7 m) is symmetric with respect to the middle of the beam.

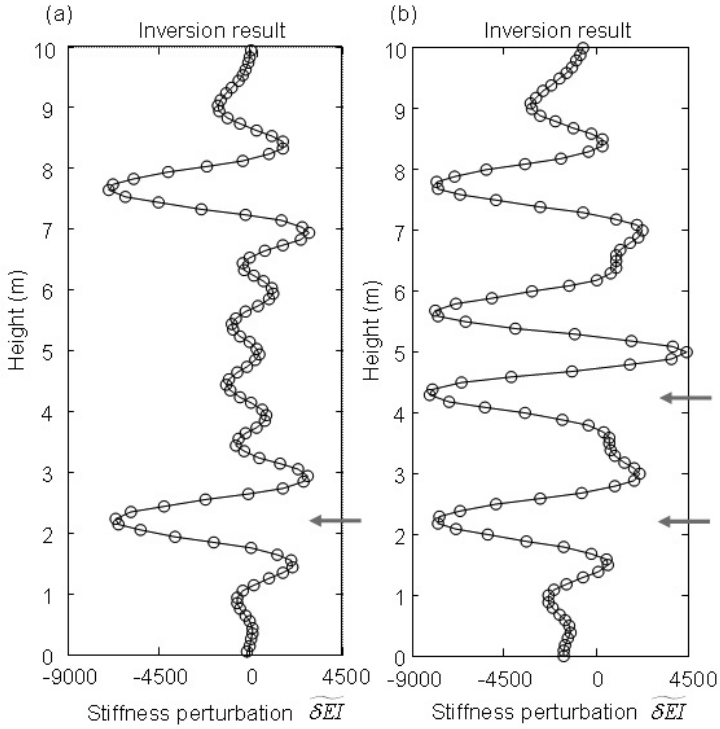


**Figure IV. 22:** Inversion result obtained with the perturbation approach for a local stiffness perturbation $\delta EI$, (a) at x = 2.3 m (gray arrow), and (b) at both x = 2.3 m and x = 4.3 m (gray arrows).

The presence of a ghost of the actual perturbation is due to the symmetric-like shape of most of the modal deformations that is imprinted in the structure of the G matrix (Eq. IV.35) from which the inversion is performed. As seen in Figure IV.22a, this ghost introduces an ambiguity in the location of the stiffness perturbation. To outperform the linear inversion result, we propose to deconvolve the perturbation estimation in a second step, through a collection of model-based inversion functions that are obtained from a set of point-like perturbations at each point of the beam.

The deconvolution algorithm is performed in three steps. In the first step, the finite-element code is used to numerically calculate the change in frequency $\delta\omega_n$ (with $n = 1,...,p$ as the mode number) associated to a set of N point-like perturbations at each height $x_j$ of the beam (with $j \in [1,N]$). From the collection of frequency perturbations $\delta\omega_{n,N}$, the second step consists of obtaining a set of N inversion results $\widetilde{\delta EI}_j(x)$ according to Eq. IV.38. In the last step, the perturbation $\widetilde{\delta EI}(x)$ is projected into the set of inversion results $\widetilde{\delta EI}_j(x)$, to deconvolve the perturbation estimation on the basis of N point-like perturbation estimations.

There are many algorithms to perform such a projection. Assuming that $\widetilde{\delta EI}(x)$ is the M-element inversion result that is discretized on the M segments of height $\Delta x$ up the beam, we

define the $M\,x\,M$ matrix $K = \widetilde{\delta EI}^t \widetilde{\delta EI}$. From the collection of N-element vectors $\widetilde{\delta EI}_j(x)$ (with $j \in [1, N]$), the deconvolution result is calculated as:

$$F(j) = \frac{\widetilde{\delta EI}^t{}_j \left(K_m^{-1} K K_m^{-1}\right) \widetilde{\delta EI}_j}{\left(\widetilde{\delta EI}^t{}_j K^{-1} \widetilde{\delta EI}_j\right)^2} \qquad \text{(IV.39)}$$

where $K_m = \widetilde{\delta EI}^t \widetilde{\delta EI} + \widetilde{\delta EI}^t{}_j \widetilde{\delta EI}_j + \widetilde{\delta EI}^t{}_{N-j} \widetilde{\delta EI}_{N-j}$ is used to minimize the deconvolution output at the ghost location. As given in Eq. IV.39, the deconvolution result is a modified version of the adaptive nulling processor that was defined in underwater acoustics to cancel sidelobes or ghosts associated with a given target location (Kim et al., 2001).

The deconvolution result F is plotted in Figure IV.23a for a set of N = M point-like perturbations created at each segment of height $\Delta x$ up the beam. As plotted, the y-axis of the deconvolution result perfectly matches the y-axis of the inversion result in Figure IV.23a, even though the representation is fundamentally different. Indeed, the inversion result $\widetilde{\delta EI}$ is projected along the M segments $\Delta x$ of the beam when the deconvolution result is back-projected along the set of N inversion functions calculated for N point-like perturbations along the beam. Compared to the inversion result in Figure IV.22a, the deconvolution result clearly distinguishes between the two symmetric solutions.

In the case where two equivalent perturbations $\delta EI$ are created simultaneously at x = 2.3 m and x = 4.3 m on the beam, the inversion result gets more difficult to interpret as the presence of the ghosts associated with each perturbation overlap on the beam (Fig. IV.22b). However, the deconvolution output still performs very efficiently, to localize the two perturbations (Fig. IV.23b).

Note, however, that the amplitude of the deconvolution output F is difficult to interpret and cannot be related to the amplitude of the perturbation. As the inverse of K is used in the denominator of Eq. IV.39, it depends non-linearly on the weight of the perturbation $\widetilde{\delta EI}(x)$ for each inversion function $\widetilde{\delta EI}_j$.

Finally, a last test is performed with a weak but extended perturbation $\widetilde{\delta EI}$= -1000 N.m$^2$ that spreads up the beam from x = 1 m to x = 3 m. The deconvolution results are presented in Figure IV.24 from the two inversion estimates $\widetilde{\delta EI}$ obtained with the first 10 modes (Fig. IV.24a) and the first five modes (Fig. IV.24b). Surprisingly enough, the deconvolution result with fewer modes greatly outperforms the result obtained with the complete set of 10 modes. The explanation for this lies in the nature of the inversion kernel in Eq. IV.35. Indeed, each element of the matrix G is built from the square of the second-order derivative $\left[\frac{\partial^2 \varphi_n(x)}{\partial x^2}\right]^2$. The modal deformation $\varphi_n(x)$ is classically robust to some mismatches, such as an inaccurate

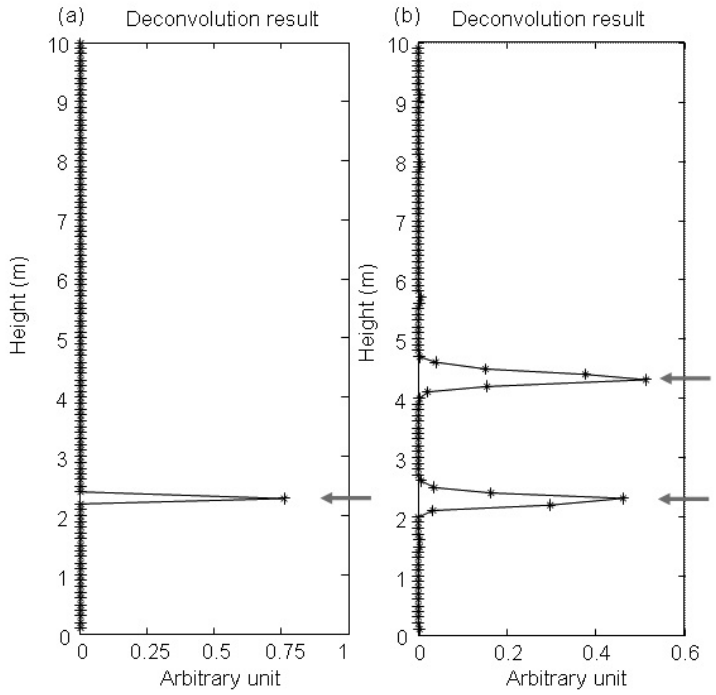


**Figure IV. 23:** Model-based deconvolution result obtained for a local stiffness perturbation $\delta\widetilde{EI}$, (a) at x = 2.3 m (gray arrow), and (b) at both x = 2.3 m and x = 4.3 m (gray arrows).

estimate of the average mass m or the average stiffness EI. However, $\frac{\partial^2 \varphi_n(x)}{\partial x^2}$ might become very sensitive to finite-length stiffness perturbations when they extend along the beam over one period or more of the mode-n oscillation. A strong change in $\frac{\partial^2 \varphi_n(x)}{\partial x^2}$ for the highest modes will then dramatically affect the matrix kernel G and the inversion and/or deconvolution result (Fig. IV.24a). To confirm this hypothesis, the change in matrix G is plotted in Figure IV.25 for one local or one extended stiffness perturbation on the beam as produced at x = 2.3 m or in the interval 1 m <x <3 m, as in Figures IV.23a and IV.24, respectively. The result in Figure IV.25b shows that the extended stiffness perturbation significantly modifies the highest mode part of the inversion kernel G, even though the two conditions $\frac{\delta\omega_n}{\omega_n} \ll 1$ and $\frac{\|\delta\varphi_n\|}{\|\varphi_n\|} \ll 1$ remain valid for all of the modes.

### IV.5.3 – A synthetic experiment with ambient-noise excitation.

The beam is now resting on a base that can support low-amplitude random noise excitation (Fig. IV.26). During the transient finite-element simulation, the white noise excitation is applied perpendicular to the beam axis as the boundary condition to the clamped node.

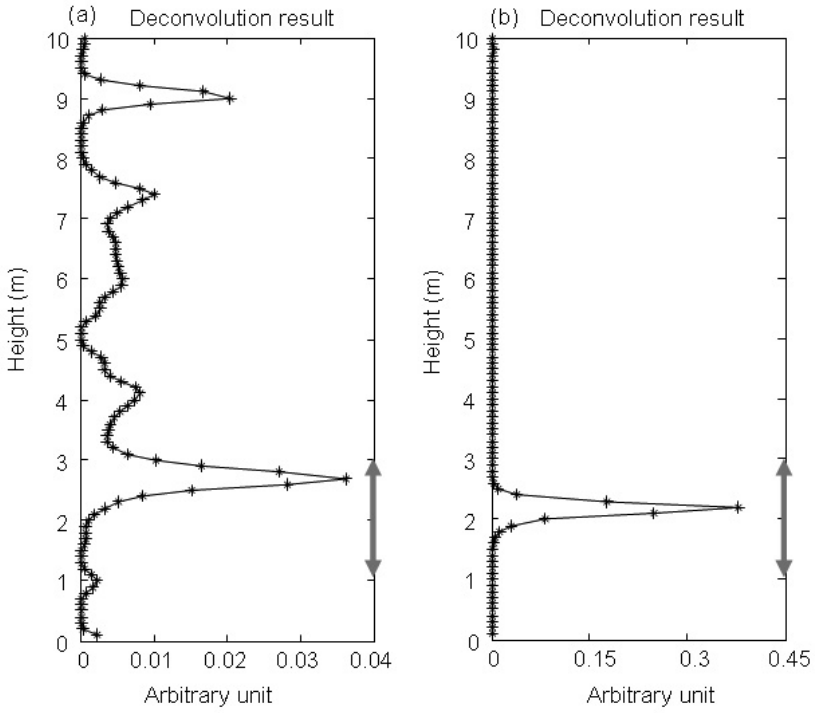


**Figure IV.24:** Model-based deconvolution result obtained for an extended stiffness perturbation between x = 1 m and x = 3 m (gray arrows) and for (a) the first 10 modes and (b) the first 5 modes.

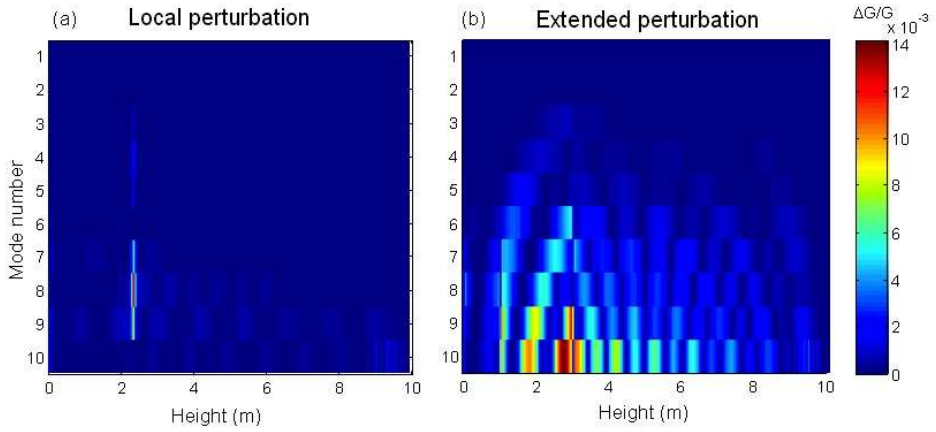


**Figure IV. 25:** Relative change ΔG/G of the inversion kernel matrix G for a stiffness perturbation associated to (a) a local perturbation (at x = 2.3 m), and (b) an extended perturbation (between x = 1 m and x = 3 m). The change in G is clearly associated with the higher-order modes for an extended perturbation.

At x = 0, the displacement varies arbitrarily with time and its rotation remains null. The noise signal propagates in the beam, and it is finally recorded at the top of the beam (free boundary condition).

During this synthetic experiment, the noise excitation is maintained over 13000 s. No change is applied to the structure during the first 3476 s. Then the same negative perturbation $\delta$EI =

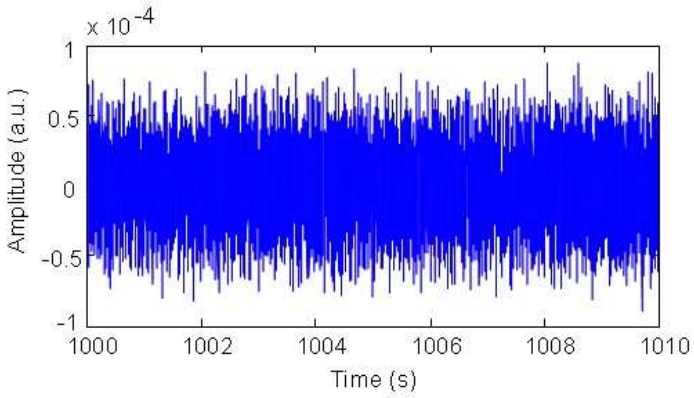


**Figure IV. 26:** Signal recorded at the top of the beam for synthetic noise excitation generated at the beam base.

-3000 N.m$^2$ is successively applied to 20 consecutive sections (each of height 0.25 m) of the beam every 476 s, starting from x = 2.25 m at t = 3476 s, up to x = 7.5 m at t = 12524 s.

An effective solution to track the frequency variation of each mode over time is to apply the random decrement technique (RDT) as shown in Chap. IV.3.3.

As the position of the damage to the beam evolves over time, we chose continuous sliding windows $T_0$ with 10% overlap. For each window $T_0$, the estimated frequency is then calculated as the dominant Fourier component of the RDT output. The frequency value is finally associated with the central time of the selected window $T_0$, which provides a continuous estimate of the frequency for every mode.

Figure IV.27 shows the frequency changes for modes 1 to 6 given as examples. For modes 1 and 2 with unperturbed frequencies of 0.323 Hz and 2.0246 Hz, the time window $T_0$ of 1000 periods T that is used to perform the RDT analysis is larger than the interval time between two successive beam perturbations. In this case, the time fluctuation of the estimated frequencies is smoothed over the perturbations that are applied to the beam. Starting with mode 3, the estimated frequency starts to follow in time the mechanical change that is applied to the beam, with perturbations occurring every 476 s. Note that the relative frequency change for every mode is always negative and is <1%, which validates the application of perturbation theory to this synthetic test. Through the perturbation approach, the frequency shifts carry the footprint of the spatial location of the beam perturbations. Indeed, the frequency change for each mode in Figure IV.27 follows the spatial modulation of the sensitivity kernel, as shown in Figure IV.20b from x = 2.25 m to x = 7.5 m.

Figure IV.28a shows the time-evolving inversion results obtained from the frequency change estimates for the first 10 modes, as in section IV.5.2. Despite the presence of the ghost, the inversion results fit the time evolution of the perturbation location along the beam perfectly (Fig. IV.28a, red line). When the deconvolution algorithm is further applied to the data (Eq.

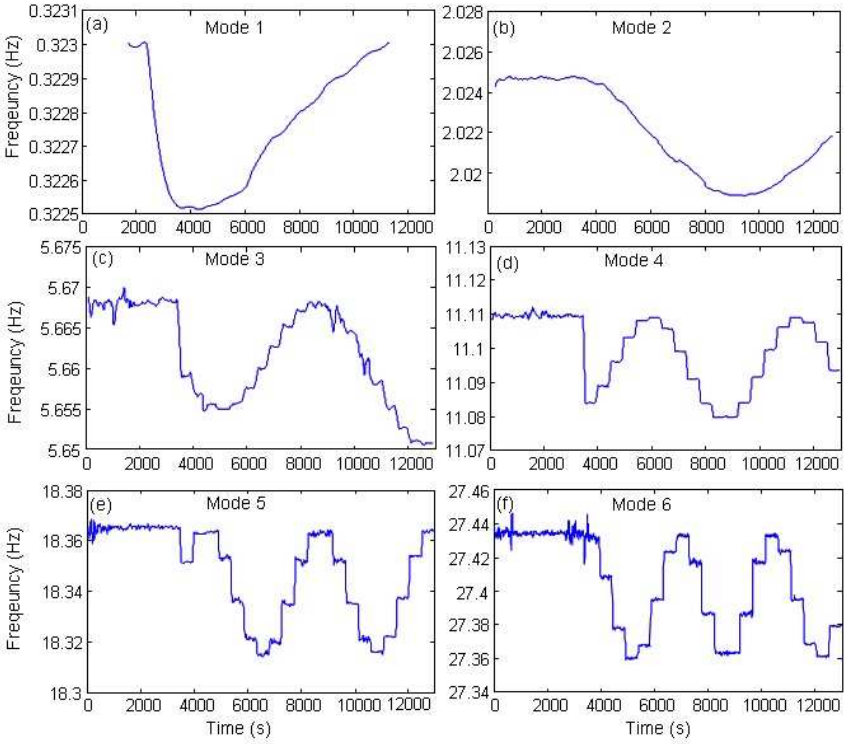


**Figure IV. 27:** Continuous track of the frequency change from the RDT algorithm for modes 1 to 6 [panels (a) to (f)] in response to a step-by-step perturbation of the stiffness beam from t = 3476 s to t = 12524 s in intervals of 476 s.

IV.39), the ghost completely disappears (Fig. IV.28b). Some uncertainty still remains when the perturbation is located close to the middle of the beam, where the ghost merges with the expected solution. Note that this spectacular result is obtained from a realistic synthetic test with some random white noise generated at the base and a unique sensor at the top of the beam, for which the theoretical modes are *a-priori* known.

### IV.5.4 – Discussion and conclusions

This study has discussed the non-invasive evaluation of damage via changes in the dynamic modal response of a structure. The basic idea is that the modification of the stiffness, mass or energy dissipation characteristics of a system can alter its dynamic response. Unlike conventional methods of detection, localization and quantification of changes, this study is devoted to the development of a novel approach of localization based only on variations of the modal frequencies tracked using a time-domain method (the RDT) and on perturbation theory.

A structure like a beam is modeled, and changes are induced by reducing the Young's modulus at local or extended zones along the beam. The interest of the proposed approach is to focus on the modal frequency variations, without a strong requirement on the modal shapes.

Indeed, the modal amplitudes determined from beam theory coupled with an accurate measurement of the modal frequency variations were sufficient to localize the local perturbation in the structure.

A new inversion method has been proposed by Baillet et al. (2013), based on the sensitivity kernel approach. Finally, to be placed under equivalent conditions as the experiment, the

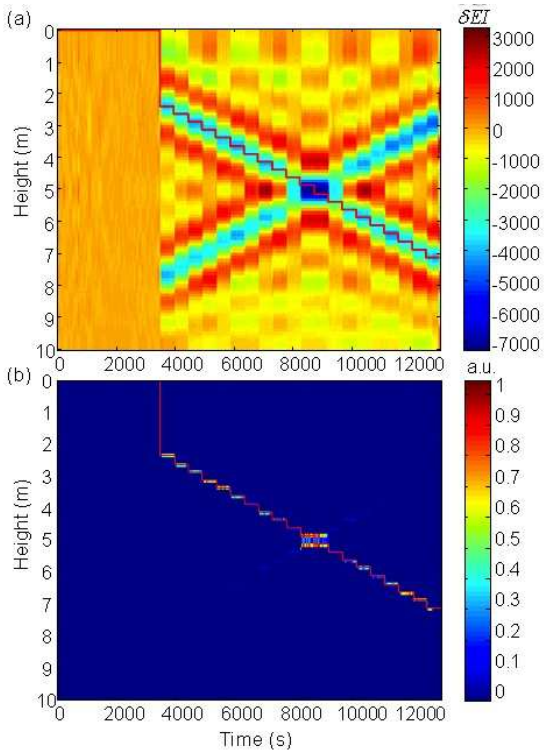


**Figure IV. 28:** Representation of the spatial-temporal (a) inversion and (b) model-based deconvolution in response to step-by-step perturbations of the stiffness beam. In both panels, the red line corresponds to the localization of the time-evolving perturbation. The color bar in (a) is the estimation of the stiffness perturbation. The deconvolution is normalized in (b).

beam is excited with equivalent white noise and its motion is recorded at the top with time-varying localization of the perturbation.

The inversion method back-projects the modal frequency variations onto the 1-D theoretical and *a-priori* (bending) model of the beam. This linear inversion is coupled to a high-resolution deconvolution approach. In this way, local and extended changes can be detected and localized even for one or two localizations, based on modal frequency shifts. The shifts tested in this study are less than 0.1% (Figs. IV.21, IV.27), which correspond to perturbations in the Young's modulus δE of about 1%; this is mandatory for the neglecting of the second-order term in the perturbation theory (Eqs. IV.27, IV.28).

For an extended zone of perturbation, the kernel matrix G, and as a consequence the inversion and/or deconvolution results of the localization, is strongly affected by the highest modes, due to the sensitivity of the second-order spatial derivative of the modal deformation (Eq. IV.33).

The highest modes introduce the perturbation, and less modes are required to improve the accuracy of the localization (Fig. IV.24). For single or multiple local changes (Fig. IV.23), detection and localization of the perturbation are effective and accurate. The errors that other methods show are thus removed, generally due to the quasi-symmetry of the mode shapes along the beam (Kim and Stubbs, 2003; Fan and Qiao, 2011; Turek and Kuperman, 1997). Spatial resolution of the local perturbation required a sufficient number of modes, which was related to the spatial wavelengths of the mode shapes (Friswell, 2007).

## IV.6 – CONCLUSIONS

In this study, a numerical analysis with low-amplitude excitation has been used in order to test the efficiency of several signal processing tools. The main goal was to show the accuracy of such method for detecting and localizing changes in a continuous beam, and to evaluate the efficiency of NDE methods under ambient vibration to localize correctly the damage for different configurations (single, extended and multi-damage). The signal processing methods tested were the FFT for extracting the frequency and the mode shapes by applying the peak-picking method, the FDD for extracting the frequencies and mode shapes, and the RDT for tracking the variation of the frequency with damage.

One important conclusion of this study is that a very clear reduction of frequency, representing a loss of stiffness of the beam, can be observed by both FDD and RDT, the frequency being certainly the most sensitive parameter to damage. As aforementioned in Chap. III, the sensitivity to changes of each mode depends on the position of the damage with respect to the node and antinode of each mode and also to the beam model.

We observe also a very accurate estimate of frequency variation using RDT; let us assume a high relevancy of this method for tracking even small changes.

For detecting changes, the variation of frequency ratio (FR) and modal assurance criterion (MAC) confirms the efficiency of these both global criteria for detecting changes. Local NDE methods applied to the synthetics provide similar conclusions as those obtained in Chap. III, i.e. the ULS method is certainly the most robust compared to MSC, MSCS and CIF, whatever the configuration and the number of modes used.

Figure IV.19c shows the correlation value of ULS method between numerical analysis (Chap. IV) and modal analysis (Chap. III) for localizing the damage considering Scenario S5, S6, S7, S8 and S9. The results present a good fit between these two methods, which means ULS

method based on operative tools for extracting frequencies and mode shapes pseudo-experimental tools provide certainly the best solution for localizing the damage.

Obviously, the localization by modal analysis is more accurate (value of $C_{AB}$ is close to 1) than the time analysis, these small differences of the location is due to the noise simulated by numerical analysis and/or by the bar error from the FDD method.

Finally, the effectiveness and robustness of the perturbation theory based method is tested in a configuration that is equivalent to that used experimentally.

Ambient vibrations are modeled at the free extremity of the beam, and the instantaneous variations in the frequencies caused by the change in the position of the perturbation along the beam are tracked by applying the RDT to the top motion.

Even for small frequency shifts (0.1% for the fundamental frequency), this new approach improves the accuracy of the damage localization, which suggests temporal and geometrical monitoring of the perturbation. For example, the effects of temperature observed in real structures can be analyzed, even if the physics of these two phenomena are different (local perturbation due to stiffness, and heat flow diffusion).

Moreover, the proposed method may only be successful in simple structures. This is the case for most of the tall buildings, with behaviour that are well approximated by continuous beam theory and more sensitive to boundary conditions.

In conclusion, the combination of the linear inversion, the high-resolution deconvolution, and the RDT provides effective tools to detect/ localize/ quantify damage in a beam-type structure.

Different beam models, actual complex structures, and different amounts of damage will be tested in the future, to further define the performance of this approach with field data.

# CHAPTER V

# DETECTION AND LOCALIZATION OF DAMAGE USING THE EXPERIMENTAL RESULTS

**Abstract** - Monitoring techniques were performed at the laboratory in order to validate the numerical results and the methods tested for detection and localization. In these experiences, damage was applied to a beam of Plexiglas forced into vibration with a white noise and for which vibrations were continuously recorded. Initial frequencies and mode shapes were first detected using signal processing methods developed before and they were compared to numerical values obtained by finite element modeling. The damage was performed through a heat flow applied at different position along the beam and with different amplitude. The variations of natural frequencies and mode shapes were then measured using signal processing algorithms (FDD and /or RDT). The perturbation theory and ULS methods were applied to localize the damage. The first gives a good localization on the first two experiments because the variation of frequency is small and mode shape unchanged, the second (ULS) provides more accurate and reliable results to locate the damage applied to the experiment 3 with a heating time of 12 minutes with a frequency variation of the order of 4% for mode 2.

# V.1-Introduction

Continuous beam theory is widely used in civil engineering and earthquake engineering for defining the dynamic response of existing structures. In fact, we may assume that, considering a regular and homogenous distribution of mass and stiffness along the beam, a building or tower behaves as a continuous beam. Several models can represent the global behavior of these structures and in order to understand their behavior under dynamic forces, and consequently to check their integrity (or health), it is imperative to define their natural frequencies and mode shapes with accuracy.

Monitoring can be done locally at critical elements of a structure (strain, stress, displacements, etc.) or globally through dynamic parameters such as the natural frequency, damping and mode shapes.

Operative modal analysis (OMA) is becoming more and more popular with the advances in the electronic capabilities of vibration monitoring instruments and the reducing cost such as instrumentation. Vibration measurements offer a non-destructive, inexpensive and effective and fast solution for recording vibrations, finally used to detect, localize and quantify the damage.

In this chapter, we propose to consider an over-simplified structure, represented by a reduce-scaled continuous beam. Laboratory tests are then conducted in order to test the algorithms presented and tested through numerical approaches (Chapter IV). Using laboratory tests allows controlling the building properties, the ambient vibrations excitation and the position and quantity of changes applied to the structure. In our case, a continuous and clamped-free Plexiglas beam was used. It was continuously excited by air jet applied directly at the top of the beam. During the experiments, changes were applied at one place and at different positions on the beam (A, B and C, see Chapter IV) using heat flow. The time of the application of the heat flow reproduces different amount of changes.

The reversible damage produced by heat flow causes a local variation of stiffness (k) of the beam due to changes of the elastic property (Young's modulus E) and affects the dynamic response of the entire beam. Considering an unchanged mass, the elastic properties reduction affects the natural frequencies ($f_i$) and the mode shapes($\varphi_i$) that can be used in detection and localization methods.

The aim of this study is composed of two parts: first, we show the effectiveness of the random decrement technique (RDT) to detect changes localized at the bottom (A), middle (B) and top (C) of the beam. Second, we compared the natural frequency-based method for structural damage detection and localization through the perturbation theory associated with a high-resolution deconvolution method to treat the inverse problem, to the classical NDE method, i.e. ULS method presented previously.

In the first case, only one sensor is required, recording ambient vibrations at the top of the beam, and considering small and transient variations of the frequencies. For this case, we consider the mode shapes remaining unchanged; while in the second case sensors are spread along the height of the beam are required for taking into account the mode shapes and the frequencies variations.

## V.2- Experiments

The goal of these tests is to obtain the dynamic characteristics (resonant frequency and mode shapes) of a structure through laboratory scaled test bed. Several configurations were selected in order to test the efficiency of methods for detecting and localizing changes. Three experiments were carried out depending on the position of changes and their amount through the duration of exposition to heat flows, used for changing elastic properties locally.

The first experimental set-up (E1) consisted of heating the continuous Plexiglas beam in three positions corresponding to the bottom at **position** A (30-33.5 cm), the middle at **position** B (61.5-65 cm) and the top of the beam C (86-89.5 cm). These positions are the same as for the numerical analysis (Chap. IV). The heat flow was applied to the beam 2, 4 and 6 hours after the beginning of the experiment at the **position** A, B and C, respectively. The duration of the heating was 30 seconds for the three cases.

The second experiment (E2) was conducted to test the influence of the amount of damage. For that, the heat flow was applied at **position** A, with different heating durations. Finally, the last experiment (E3) consisted in increasing the duration of the heating applied at **position:** $x = \frac{(2*L)}{4.938}$ correspond to 40.5 cm; with *L=100 cm* is the length of the beam (see figure V.14).

Forty five minutes after the beginning of the experiment; the heat flow was applied during 12 minutes, changing also the acquisition system for improving the continuity of the data acquisition. The structure used in this study is made of a continuous Plexiglas beam anchored at the bottom and free at the extremity (i.e. clamped-free beam). The beam used here has the elastic characteristics shown in Table V.1 and corresponding to the properties and dimension used for the numerical approach (Chap. IV).

| Material | Plexiglas |
|---|---|
| Length | 1 m |
| Width | 0.05 m |
| Depth | 0.01 m |
| Poisson's ratio | 0.4 |
| Mass density | 1165 kg/m$^3$ |
| Modulus of elasticity | 5.4 GPa |
| Moment of inertia | $4 \cdot 10^{-9} m^4$ |

**Table V. 1 :** Geometric and material properties of cantilever beam.

Figure V.1 shows the experimental setup used to study the bending vibration in the (xy) plane in a clamped-free configuration.

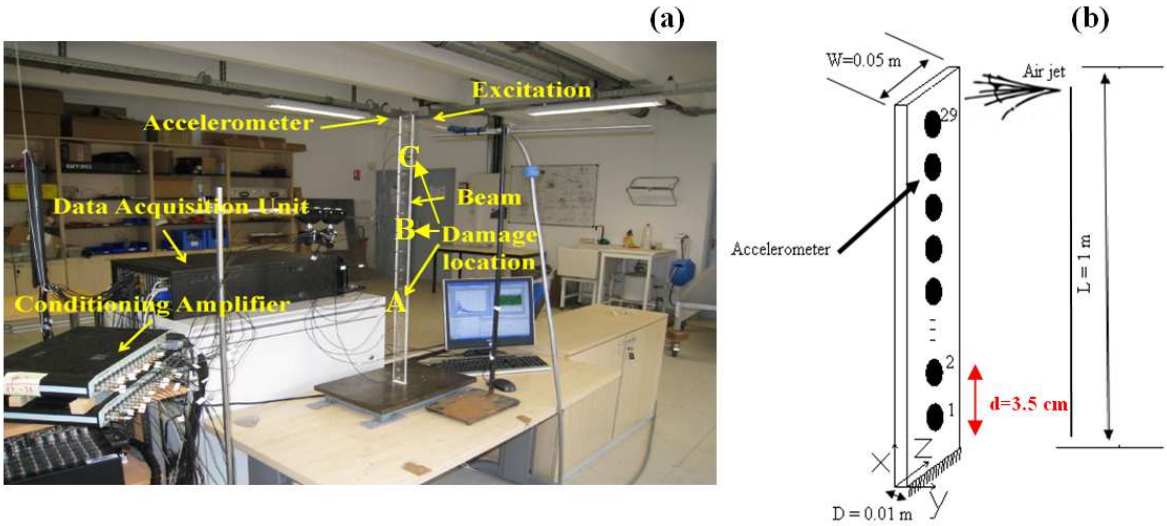


**Figure V. 1 :** Experimental bed test for detection and localization of changes used in this work (a) Clamped-free beam set up tested in the laboratory. (b) Sketch diagram with geometric dimensions and accelerometer layout.

The data acquisition is performed through 29 accelerometers powered by two conditioning amplifiers. The accelerometers are mono axial (Bruel and Kjaer, Type 4344) with 1.45 g of mass and a frequency band between 1-20 kHz. All the sensors were oriented in the horizontal direction, on the widest face of the beam in order to record the beam vibration in the *y* direction.

The amplifiers are connected to a data acquisition unit by an RS232 port that allows to define and to control some parameters of the acquisition such as the gain of each accelerometer. For the three experiments, a maximum gain of 40 dB was selected to amplify the signal recorded by each sensor. The beam vibration was gathered by these 29 accelerometers and transmitted directly to the computer through the data acquisition unit. The data acquisition is controlled through a Matlab toolbox.

The 29 accelerometers were spread along the height of the beam with a 3.5 cm interval (see figure V.1.b). The beam was continuously excited by air jet that we may assume corresponding to a white noise low-amplitude excitation applied directly at the top of the beam. By this way, the bending modes are excited in the *y* direction and the frequencies and modes detected were used for testing the detection and localization methods of changes.

With the air jet, the beam is excited continuously over a wide frequency band, reproducing the ambient vibrations conditions observed on the field. Nevertheless, the uni-directional condition of excitation is different of the 3D filed excitation and some disturbances may occur, discussed in the following section. Moreover, data was collected by windows of 10 seconds at a sampling frequency of 5000 Hz. For the two first experiments (E1 and E2) the

transfer of the data to the data acquisition unit requires about 20 seconds, that is to say the recording obtained for the experiments was not totally continuous recordings.
For the third experiment E3, the faster acquisition unit allowed the transfer in 1 second, improving the continuity of the data. For each 10s window of recording, 50000 samples were stored at each sensor and formatted in the CityShark$^{TM}$ format (Chatelain et al., 2000, 2012) used for modal analysis processing.

An example of the acceleration response of the beam is represented in Fig. V.2 for one window recorded at the top of the beam. Its Fourier transform shows the frequency response of the beam, with at least 10 modes clearly seen on the response.

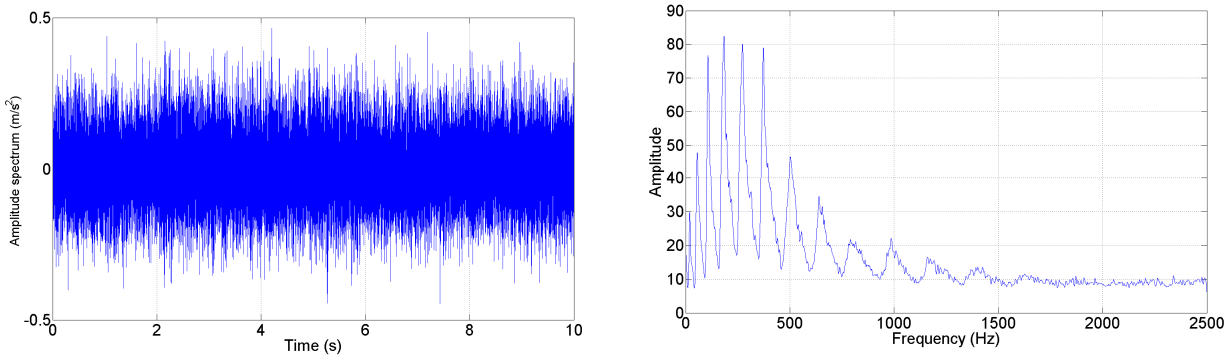


**Figure V. 2 :** Time-history of the beam motion recorded at the top (left) and its Fast Fourier Transform (right).

This figure can be compared to the Figure IV.3 corresponding to the numerical modeling of this beam, with the same conditions. Of course, in the case of the experimental beam, the damped condition is observed in frequency, the width of the peaks being proportional to the damping value, with decreasing amplitude. The amplitudes of the Fourier spectra increase up to the 5th mode and then decrease: this dynamic signature is not classical since under ambient vibrations considered as white noise; the response of the system must have decreasing amplitude related to the damping condition of the beam. In our case, the experimental solution for reproducing the excitation through air jet at the top provides some disturbances to the modes, these one having a critical influence on the definition and the detection of the mode shapes.

Table V.2 presents a comparison of the natural frequencies obtained by the finite element modeling using RDM6 (Chap. III) and experimental analysis (laboratory) for undamaged beam before applying the heat flow. The values are quite similar, keeping the order of magnitude: the differences may be due to the non-perfect fixed base condition or some variation of the elastic properties for example.

Nevertheless, the comparison confirms the good agreement of frequency values obtained by modeling (dynamic linear analysis) and by experimental analysis for the first eight bending modes.

| Modes | Numerical Modeling [Hz] | Experimental results [Hz] | Difference % |
|---|---|---|---|
| 1 | 3.14 | 3 | 4.45 |
| 2 | 19.73 | 18.99 | 3.75 |
| 3 | 55.23 | 55.33 | -0.18 |
| 4 | 108.21 | 107.37 | 0.77 |
| 5 | 178.83 | 180.73 | -0.01 |
| 6 | 267.02 | 272.52 | -2.059 |
| 7 | 372.75 | 372.94 | -0.05 |
| 8 | 495.97 | 500.24 | -0.86 |

**Table V. 2 :** Natural Frequencies (Hz) obtained by numerical and experimental analysis.

Another way to reproduce the experimental behavior of the beam is displayed in Fig. V.3, this figure shows the variation of the Fourier amplitude along the height of the beam, provided at the 29 accelerometers position. We observe clearly the theoretical behavior of continuous beam, characterized by the succession of nodes and anti-nodes corresponding to the shape of the modes.

Moreover, the frequencies ratio obtained by the experimental tests give the typical ratio defined for the bending beam (Chap. II), i.e. $f_2/f_1$=6.3 (compared to 6.3 for the theoretical beam), $f_3/f_1$=18.44 (17.5) and $f_4/f_1$=35.79 (34.3), let us assume in the rest of the document an experimental bending beam behavior.

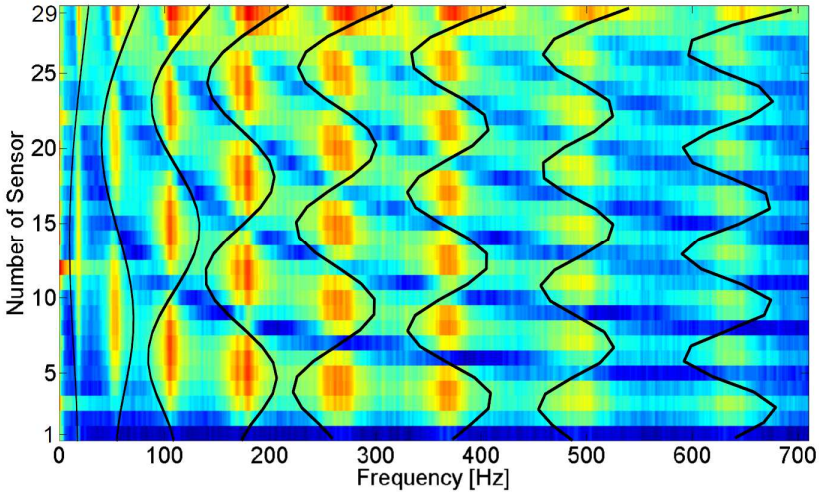


**Figure V. 3 :** Evolution of the spectral amplitude of the experimental data computed at the 29 sensors and representing the shapes of the 9 first modes of the initial (undamaged) beam (excepted for the fundamental mode). The black line is the numerical mode shapes from Chap. III.

## V.3 – Detection of damage for experiments 1 and 2

For this experiment, the variation of the frequency values are first tracked by the Random Decrement Technique presented previously (chapter IV, § IV.3.3) and applied to the recordings provided by the sensor located at the top of the beam. In this case, RDT is computed mode by mode, using a sliding window of 110 seconds that runs over the signal with 10% of overlapping. Despite the presence of gaps in recording due to the data transfer, we assumed the continuity of the data.

For each mode, the signal is filtered by a band-pass filtered using a second-order Butterworth filter, centered on ±10 % of the frequency. The length of the sliding window, the bandwidth of the filter and number of periods are chosen so as to reduce the error to estimate the frequency with a good precision. As suggested in the previous chapter of this work, four periods (see Figure V.4) were used to compute the frequency from the decrement signature.

Figure V.4 shows an example of the signature of the free-oscillation obtained by Random Decrement technique for mode 5 using data experimental recorded at the top of beam. The blue curve is called the Random Decrement signature and the frequency is computed with the zero-crossing method. Even if the RDT can provide reliable information on the damping, this information is not considered in this work.

However, as shown by Mikael et al. (2013), the RDT method provides also a very accurate estimate of the frequency of the system.

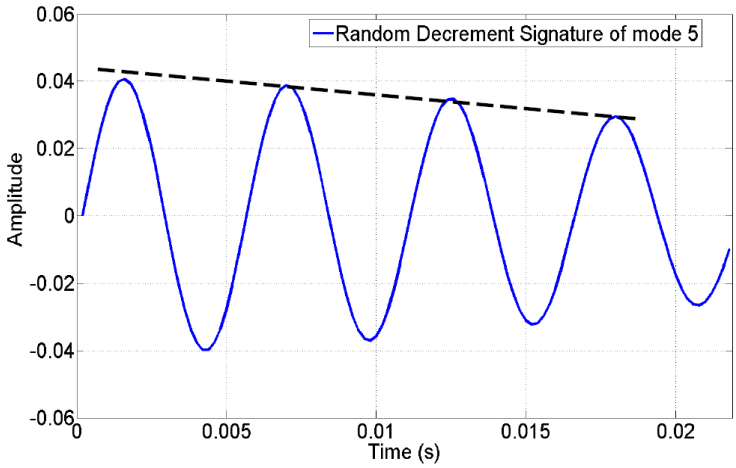


**Figure V. 4 :** Example of a random decrement signature corresponding to mode 5, obtained by RDT from recording at the top of the beam.

The RDT was applied to test its experimental performance for damage detection. In experience E1, a heat flow was applied to the Plexiglas beam at the bottom (position A: 30-33.5 cm), in the middle (B: 61.5-65 cm) and at the top (C: 86-89.5 cm) of the beam for 30 seconds after 2, 4 and 6 hours from the beginning of the experiment.

When the heat flow is applied at the beam, the flexural rigidity *EI* is locally changed, related to the stiffness K of the beam (Eq. II.21), and then affecting the frequency values of the beam (Doebling and Farrar, 1998).

### V.3.1 – Detection of changes using a single recording at the top – Experiment 1

During the heat flow (Fig. V.5), we observe a clear reduction of the frequency value. As aforementioned and related to the experimental conditions, the three first modes are less detected, with the worst signal-to-noise ratio during the experiment. This is confirmed by the variation coefficient (CV%, Eq. IV.21) given in Tab. V.3, considering the first part of the experiment, i.e. the unchanged state of the beam before heating. We observe the highest CV values for the three first modes, while modes 4 to 9 have a small wandering of their frequency.

| Modes # | 1 | 2 | 3 | 4 | 5 | 6 | 7 | 8 | 9 |
|---|---|---|---|---|---|---|---|---|---|
| CV (%) | 0.6074 | 0.2655 | 0.0945 | 0.0737 | 0.0528 | 0.0470 | 0.0281 | 0.0433 | 0.0295 |

**Table V. 3 :** Variation coefficient (CV %) of the frequency value of the first 9 modes obtained using the RDT and considering the first part of the experience (unchanged beam condition before heating).

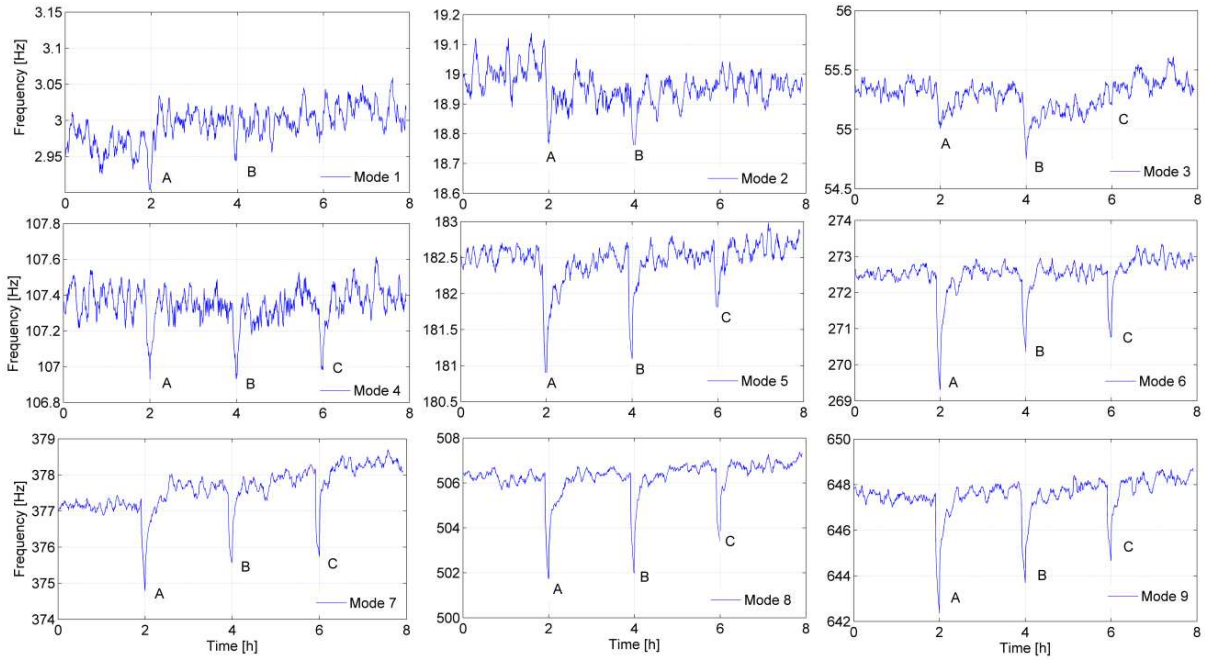


**Figure V. 5 :** RDT applied to the beam considered for the experiment E1, with three positions of changes (A, B and C) tested successively. The data used for this experience is provided by the sensor located at the top of the beam.

The highest modes (4 to 9) are sensitive to the changes for the three localizations of heating (A, B and C), with more or less the same magnitude of decay considered mode by mode.

Figure V.6 compares the time variation of normalized frequency for modes 4 to 9, according to the three positions of heating. This normalization is done with respect to the average value of the mode frequency computed at the first part of the experiment, i.e. considering the undamaged condition (before heating).

We observe that considering a quite identical amount of change, related to the exposure duration to the heat flow, the amount of variation is strongly related to the position of the changes (A, B and C) whatever the mode. With this observation, we can assume that the position of the changes along the height of the beam may have a strong influence on the estimate of the damaged amount and this must be accounted for in the next section.

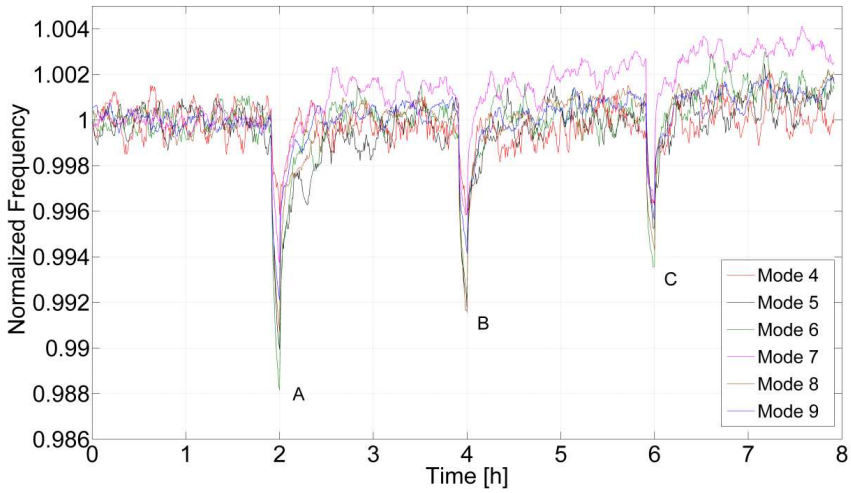


**Figure V. 6 :** Time variation of the normalized frequencies of modes 4 to 9 computed by RDT using sensor located at the top of the beam (free condition) for experiment E1. A, B and C mark the time when the heat flow was applied for 30 seconds at positions A,B and C respectively.

This result shows the efficiency and robustness of the RDT to detect a small variation of elastic properties of the beam, some having order of magnitude less than 0.2%. This observation has been recently done by Mikael et al. (2013) using real data recorded at the top of existing buildings. Based on the frequency ratio (FR, see Chap 3), the experimental results confirm also that the mode 4 is certainly the less sensitive to changes located at **position** A, B or C (FR equal to 0.43%), that was already seen with modeling (Chap III) and numerical simulation (Chap IV) and due to the position of the damage close to node of this mode.

After stopping the heating, the Young's modulus E of the beam increases again, which implies that the frequency of all modes increases and recovers its initial state $f_0$. The recovery time is proportional to the time of relaxation of the changes applied to the beam.

We used a smoothing function to compare the rate of recovery: $f(t) = \alpha t^{\beta} + \gamma$ (curve fitting), "*t*" varies between the time of the minimum value of frequency and 2 hours after this point. Other solutions of fitting were tested and this solution provided the best fit in term of error to the curve. Figure V.7 displays an example of the fit given by this solution considering the mode 6.

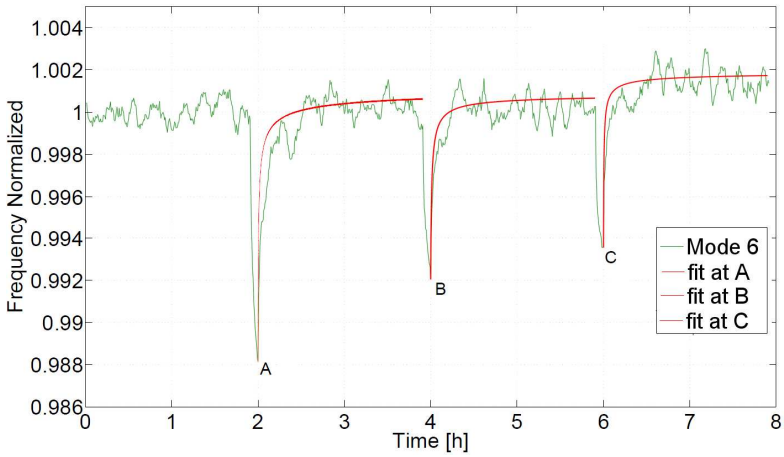


**Figure V. 7 :** Example of fitting curve applied at points A, B and C after stopping the heat flow. The data corresponds to the vibration recorded at the top of the beam; the frequency is tracked with RDT and normalized by the average frequency of the undamaged state.

Table V.4 summarizes the β values for each mode and each position of changes. As previously observed, for modes 1 to 3, the signal to noise ratio of the variation is not good enough to be confident with the results. We notice that the rate (β) varies from one mode to another, because the modes do not react in the same way since they depend on the location and position of damage applied at the beam. Even if the material remains the same, the global behavior of the beam, tracked using only the modal frequency variations, may be influenced by the position of the change along the beam and depending on the mode considered.

However, the number of results is not enough and it could be interesting to confirm these results by increasing the number of tests for performing a statistical analysis and to conclude on the rate of the time recovery.

| Modes # | 1 | 2 | 3 | 4 | 5 | 6 | 7 | 8 | 9 |
|---|---|---|---|---|---|---|---|---|---|
| $\beta\ (A)$ $(10^{-4})$ | -7710 | -6610 | -1029 | -2471 | -1945 | -4361 | -3495 | -3292 | -3842 |
| $\beta(B)$ $(10^{-4})$ | -7613 | -5716 | -1518 | -2683 | -4680 | -6825 | -2947 | -3966 | -2991 |
| $\beta(C)$ $(10^{-4})$ | ----- | ----- | -3212 | -4918 | -4081 | -5531 | -4781 | -5505 | -3924 |

**Table V. 4 :** β value of the time recovery of the modal frequencies computed using the RDT and observed after stopping the heat flow at **position** A, B and C, using the same time of heating of 30 seconds.

### V.3.2 – Detection of changes using a single recording at the top – Experiment 2

The objective of experiment 2 is to test the variation of the frequencies by RDT, considering different values of damage. In this experiment, only damage at **position** A will be considered, as a function of amount of heating. Similar processes and experiments as for experiment E1 were decided, for the signal processing of the RDT, the data acquisition and the excitation through air jet. The total duration of acquisition (10 s) is chosen in a manner to get precisely the first nine resonance frequencies of the beam. In order to test the RDT for detect / quantify the damage, a heat flow is applied at the bottom of beam (A), with different heating duration corresponding to 10, 20, 30, 40, 50 and 60 seconds of exposition, after 1, 2, 3, 4, 5 and 6 hours from the beginning of the experiment, respectively. The total duration of the experiment was 8 hours**.**

Figures V.8 and V.9 present the variation of the modal frequencies for each damage applied to the beam, using the sensor located at the top of the beam. Only the nine first modes are considered. As previously mentioned for experiment E1, the three first modes are quite undefined, showing a bad signal-to-noise ratio for tracking the frequency and the highest coefficient of variation of the frequency centered on the average value (Tab. V.5).

| Modes # | 1 | 2 | 3 | 4 | 5 | 6 | 7 | 8 | 9 |
|---|---|---|---|---|---|---|---|---|---|
| CV (%) | 0.5976 | 0.1723 | 0.1418 | 0.0673 | 0.0657 | 0.0454 | 0.0313 | 0.0251 | 0.0398 |

**Table V. 5 :** Variation coefficient (CV %) of the frequency value of the first 9 modes obtained using the RDT and considering the first part of the experience (unchanged beam condition before heating).

On figure V.8, we clearly observe an increase of the frequency decay with the duration of the heat flow exposure, regardless of the mode. That corresponds to the relation between the frequency decay and structural integrity. This decrease is due to a loss of stiffness (*EI*) caused by the increase of temperature injected by the heat flow and affecting directly the mechanical properties. When we observe the frequency ratio FR, displayed in Fig. V.10, we may consider the same relationship that the FR versus a curve (a: coefficient of Young's modulus reduction) obtained using numerical modeling (Chap III and IV). Even with experimental data, the dispersion of the result is the highest, especially for the two first modes, the same trend is observed with a non-linear relationship between frequency shift and amount of damage. This relation should be confirmed using a measure of the reduction of stiffness but considering the RDT as a very accurate method for tracking the frequency, the FR could be directly related to the integrity. This has been shown yet, after the Boumerdes earthquake by Dunand et al (2004) who tested buildings with ambient vibrations, having suffered the Algerian earthquake. They observed a close correlation between the frequency shift and the classification done by expert judgments in the field and the three color scale used: red (strong damage), orange (moderate) and green (low).

On figure V.9, the comparison of the recovery time for each mode and each amount of damage is not easy. The normalized frequency for modes 4 to 9 over 8 hours confirms the efficiency and robustness of the RDT for quantifying the damage (or change) level. All the

modes react following the same trend, with increasing decay with increasing duration of heat exposure. The recovery time is quite similar and the value of the power law used for fitting the recovery curve vary a lot for each mode and each damage level, as previously observed in Tab. V.4. The recovery function should have a special attention for having a good evaluation of this property.

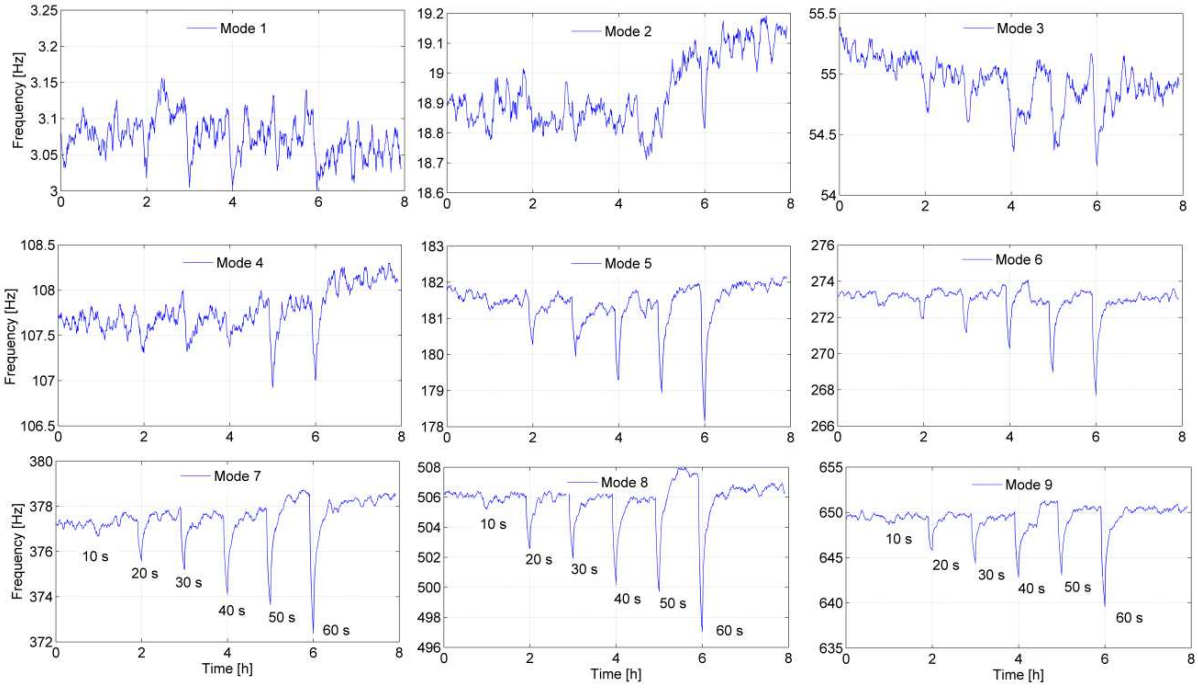


**Figure V. 8 :** RDT applied to the beam considered for the experiment E2, with one position of change (**position** A) and 6 amounts of damage reproduced by the time duration of the heat flow exposure (from 10 to 60 seconds). Data used for this experience are provided by the sensor located at the top of the beam.

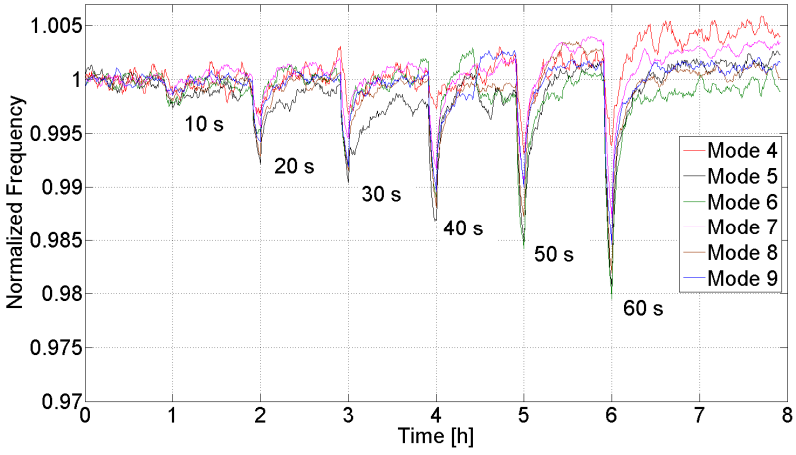


**Figure V. 9 :** Time variation of the normalized frequencies of modes 4 to 9 computed by RDT using sensor located at the top of the beam (free condition) for experience E2. The heat flow was applied for 10 to 60 seconds at **position** A.

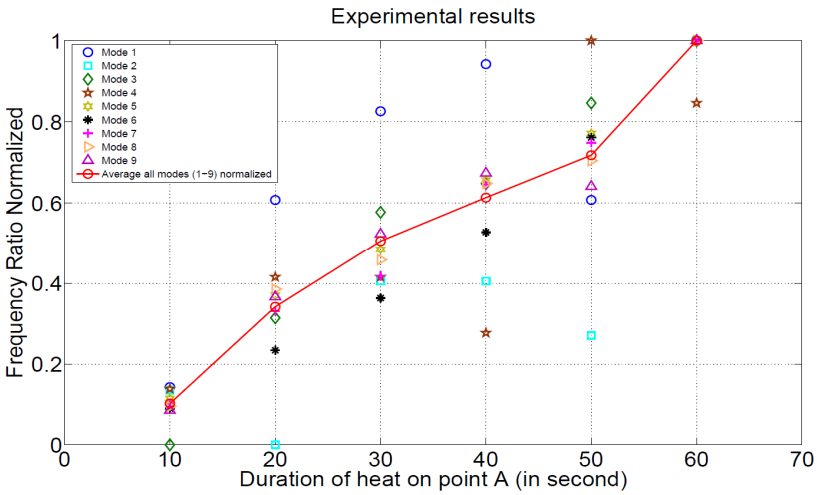


**Figure V. 10 :** Frequency ratio (FR) of the 9 first modes for 10s to 60 seconds of heat flow exposure, applied at the bottom of the beam (**position** A).

### V.3.2 – Localization of damage using ULS and perturbation theory for experiment E1

Two methods of localization were applied to this experiment: (1) the first one corresponds to the ULS method presented in the Chap. IV and corresponding to the method providing the best localization result using modeling; (2) the second is the method based on the perturbation theory and presented in Chap IV. The major differences between these two methods are:

- Perturbation theory method requires only one sensor located at the top while ULS needs the mode shapes provided by sensors spread along the height of the beam.
- ULS uses frequencies and mode shapes of the beam and the damage is obtain by comparing the undamaged and damaged states of the beam, while the perturbation theory uses only the variation of the frequencies compared to the initial (undamaged) frequencies and back projected on the theoretical mode shapes.

Consequently, the ULS method requires data length enough for extracting the mode shapes. The damage must be strong enough to influence the modes and not only the frequencies. Conversely, the perturbation theory uses only the variation of the frequencies, provided by small changes that do not influence strongly the mode shapes. As supported by Kim and Stubbs (2003) and Xu et al. (2007), the efficiency of frequency analysis for damage detection is known, considering fundamental mode and overtones, even for very small changes.

Figure V.11 gives the experimental mode shapes extracted using the FDD method (Chap. IV) and applied to the experimental data. The modal analysis method used is the Frequency Domain Decomposition, a non-parametric frequency domain method (Brincker et al., 2001).

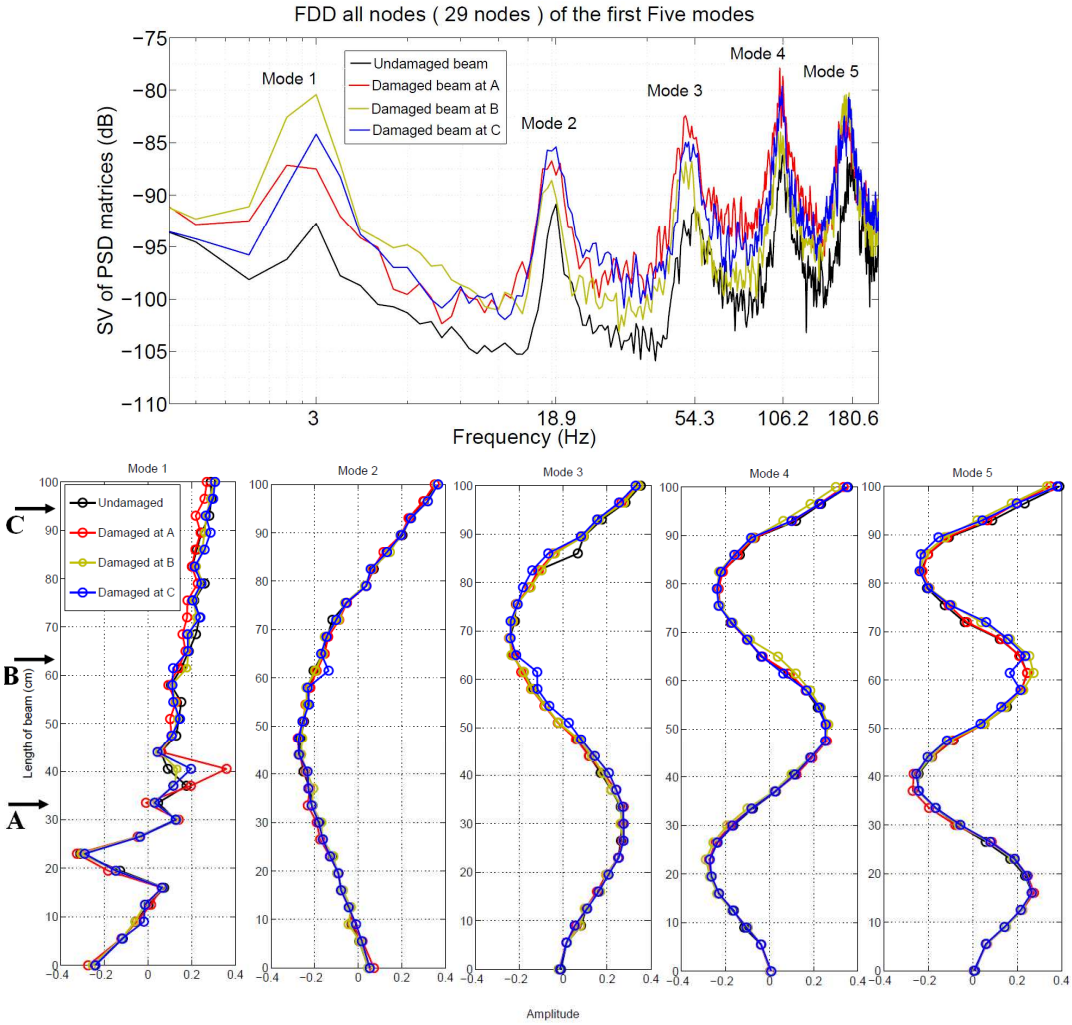


**Figure V. 11 :** First five singular values (upper row) and mode shapes (lower row) of the beam extracted from ambient vibrations recorded on the beam using the 29 accelerometers, corresponding to the undamaged and damage (positions A, B and C) of the experiment E1.

It consists of decomposing the spectral densities matrix (cross power spectral densities between all simultaneous recordings) into independent degrees of freedom using the singular value decomposition. It therefore allows the accurate estimation of the natural frequencies and mode shapes of structures. More details and theoretical background of this method was presented previously (Chap. IV) on synthetics and can be found in Brincker et al (2001).

FDD was applied to the data recorded by the 29 accelerometers located along the beam. Two analyses were done, considering the undamaged and the damage states for detecting and localizing the damage using the ULS method. For this second state, because of the small and transient variation of the frequency during the experiment, only one time window (10 s of length) was used to analyze the modal parameters, corresponding to the window having the lowest value of frequency. The processing was performed using the Matlab Macity routine developed for modal analysis (Michel et al., 2010). In order to optimize the processing, raw data were re-sampled at 500 Hz, that is to say dividing by 8 the number of samples (from 4 kHz to 500 Hz).

By this way, the mode shapes considered here are from the 1st to the 5th, i.e. from 2.9 Hz to 177.5 Hz, respecting the Nyquist frequency condition. Considering only the first 5 frequencies allows us to consider a real case, experimental analysis performed in real buildings providing generally only the first modes.

Figure V.11 confirms the bad resolution of the first mode, due to the solution applied for the excitation. Since the first mode has a low signal-to-noise ratio, only modes 2 to 5 were considered for this analysis. In chapters III and IV, we observed that the use of the first mode was not a crucial issue for improving the quality of the estimate using the ULS method. Moreover, as shown previously, the length of the damage state file (10 seconds) was not long enough for having a good estimate of the mode shape following the criteria defined in Michel et al. (2008, 2010) and also discussed in Chap IV. The singular value decomposition represented in Fig. V.11 gives an overview of the frequency shifts and consequently the variation of the mode shapes for the cases A, B and C.

Considering damaged and undamaged states, we can apply the ULS method for detecting and localizing the damage. We observe Fig. V.12 the ULS estimate for the A, B and C positions of the damage. The curve represents the value of the ULS function along the beam. In this case, the localization of the damage position is bad, showing some information for A localization, a lot of fluctuation along the beam for case B and a ghost of the damage not defined at the good position for the case C. Because of the small and transient nature of the change, mode shapes used for the ULS method are not modified enough for being accounted for the application of the ULS.

Since the experimental mode shapes are noisy (compared to the numerical modeling) we need a strong modification to be detected by this method. Moreover, due to short and fast variation of the properties, and then of the frequencies and mode shapes, it is not possible to have a good assessment of the mode shapes and frequencies values with only 10 seconds of ambient vibrations recording. This is one requirement for using the FDD method with a good accuracy to have a long enough recordings of ambient vibrations.

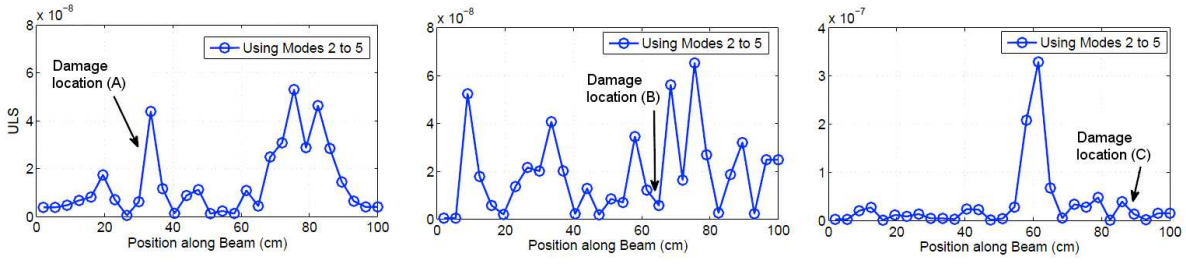


**Figure V. 12 :** Localization of the damage at position A, B and C using the ULS method and considering modes 2 to 5 for experiment E1.

The second method used for detecting the damage is based on the perturbation theory as presented at the end of Chap. IV with numerical simulation. The main principle of this method is to back project the variation of frequencies observed at the top of the beam on the theoretical mode shapes since as observed previously, depending on the position of the damage along the beam, all the modes do not react in the same way.

With this method, only one recording at the top of the beam is required and it is not necessary to define the mode shapes, certainly the element the most difficult to extract experimentally with a good resolution (at least compared to the frequencies) for small variations. Moreover, for small and fast changes, the frequencies react immediately while the mode shapes remain unchanged or at least with changes that could not be detected. For this application, we considered the variation of the frequency observed in Fig. V.6 for cases A, B and C.

The method is based on three steps: (1) the inverse problem of the perturbation of stiffness polluted by the symmetry of the beam that gives a localization and its ghost (See Chap. IV, Fig. IV.22); (2) the deconvolution of the perturbation estimation through a collection of model-based inversion functions that are obtained from a set of point-like perturbations at each point of the beam (Chap. IV); and (3) the perturbation of stiffness is projected into the set of inversion results in order to improve the localization (Chap. IV).

Figures V.13 shows the three steps of the localization process based only on the variation of the modal frequencies obtained with the RDT method. The three steps of the localization method are described for the three cases of damage, i.e. at the positions A, B and C. The results are different from one case to another one, depending on the number of modes used and the position of the damage along the beam. For case A, the number of modes used is 4 to 9, since the position of the damage is close to the zone having the worst estimate of the first three modes, with the highest variation coefficient CV.

Because of the theoretical model of the beam (bending beam) and the bad resolution of the first modes, the inversion scheme has difficulties to distinguish the real to the ghost localization. Similar difficulties are also observed for the case B, considering modes 1 to 9, the position of the damage being localized close to the symmetry axis of the beam, and then of the modes.

For cases A and B, even if the symmetrical ghost of localization is not completely removed, the amplitude of the inversion permits us to discriminate the position of the damage, which could be more difficult in case of blind analysis. For the last case, position C, the method is very efficient for localizing the changes, considering modes 1 to 9. Even after the second step, because of the distance of the damage to the symmetry axis of the beam, the localization is quite effective.

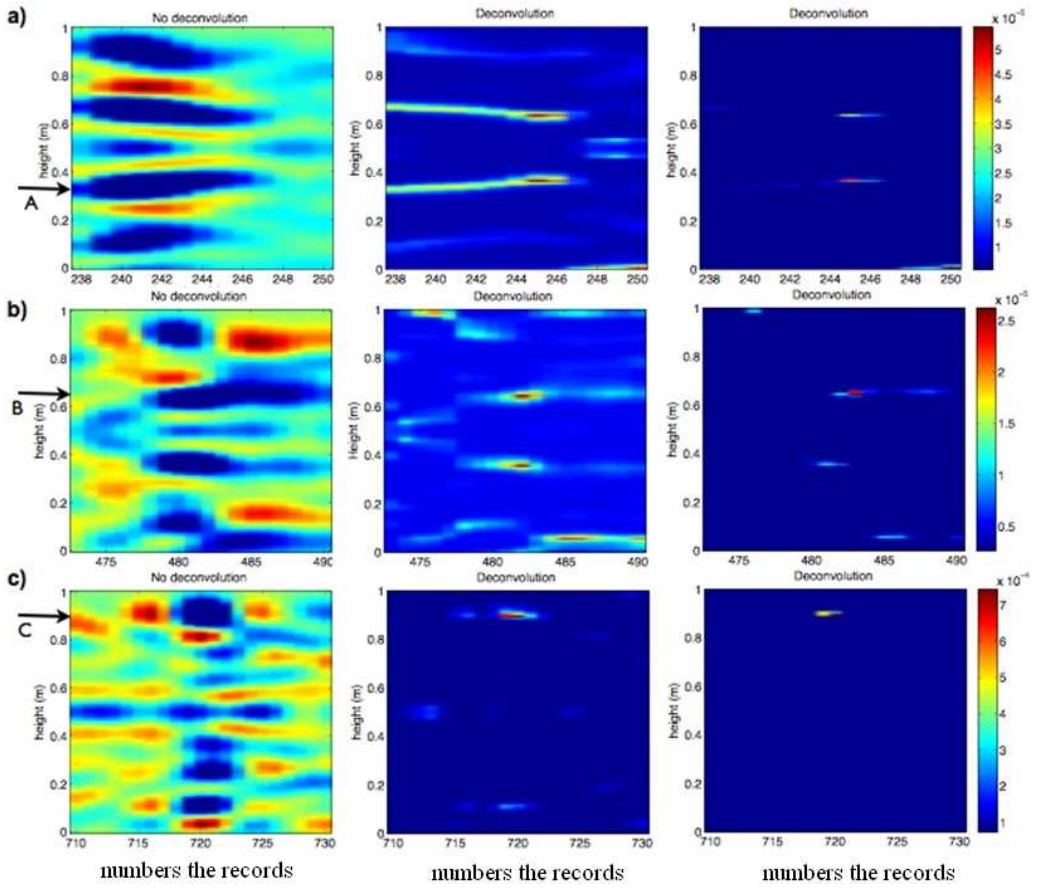


**Figure V. 13 :** Results of the damage localization method applied to the experimental data (experience E1) for the three cases of change (a: at position A; b: at position B; c: at position C), where the heat flow applied at 2, 4 and 6 hours from the beginning of the experiment corresponds to the numbers of recording following: 240, 480 and 720 respectively (each record duration is 10 s, a total of records is 960).

## V.4 – Detection and localization of damage for experiment 3

Figure V.14 shows the experimental setup used for this experiment. The beam and the configuration of the experiment were the same as for experiment E1 and E2.

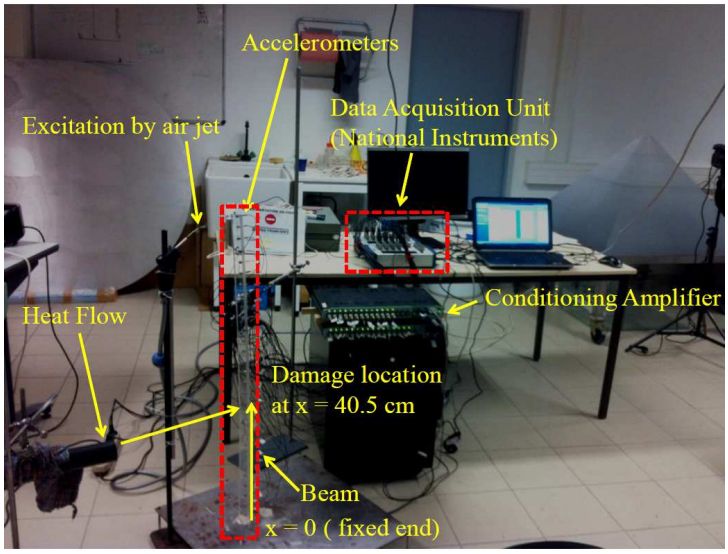


**Figure V. 14 :** Experimental setup with faster prototype.

The difference with experiments E1 and E2 is the data acquisition unit. The conditioners are connected via serial port to the computer to define the gains for each accelerometer. Ambient vibrations recorded by each accelerometer are transmitted to the computer via two National Instrument acquisition boxes and USB communication system.

These two National Instrument acquisition boxes are much faster than the first data acquisition unit previously used for experiments E1 and E2. The instrumentation consisted in 29 accelerometers regularly spaced along the beam and the excitation was done by air jet applied at the top of beam. Data acquisition parameters remain unchanged except that the sampling frequency changed from 5 to 4 kHz.

The total duration of the experiment was 2.2 hours, divided into three parts:

1- 0- 45 minutes: acquisition at ambient temperature (undamaged state).

2- 45-57 minutes: a local damage is applied to the beam through heat flow applied during about 12 minutes at the bottom of the beam (*x=40.5 cm*).

3- 57-132 minutes: acquisition after stopping the heating (recovery time of the beam).

Data was collected in fragments of 10 seconds at a sampling frequency of 4 kHz. Data transfer for the 29 accelerometers to computer is done in 2 seconds, which allows having 5 acquisitions per minute.

The total duration of the experiment is composed of 650 acquisitions for a total duration of 2.2 hours. Figure V.15 presents the evolution of the first nine modal frequencies in bending of the undamaged beam corresponding to the first step of the experience (0-45 minutes).

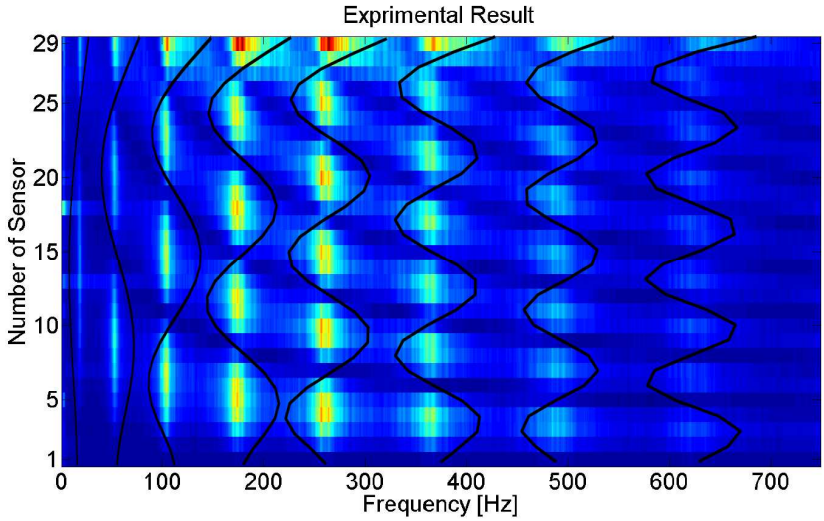


**Figure V. 15 :** Evolution of the spectral amplitude of the experimental data computed at the 29 sensors and representing the shapes of the 9 first modes of the initial (undamaged) beam (excepted for the fundamental mode). The black line is the numerical mode shapes from Chap. III.

For doing figure V.15, the FFT of ambient vibrations recorded at the 29 accelerometers position, from the bottom (1) to the top (29) were calculated, corresponding to the classical peak picking method used for mode detections and representation. We can clearly distinguish the position of nodes and antinodes of each mode along the beam.

The Plexiglas beam has the same geometric dimensions as the beam described in experiment 1 and 2. Table V.6 gives a comparison of the natural frequencies obtained by experimental analysis for the first eight bending modes for undamaged state before applying the heat flow.

The value of modal frequencies obtained for experiment E3 is a little smaller than the initial state of the beam used for experiments E1 and E2, certainly due to local changes of Young's modulus ($E$) caused by using a repetitive heat flow for previous experiment. In this condition, we consider a new initial beam, its mass remaining unchanged in all experiments.

| Modes | Experimental results 1 | Experimental results 3 |
|---|---|---|
| 1 | 3 | 2.90 |
| 2 | 18.99 | 18.65 |
| 3 | 55.33 | 53.59 |
| 4 | 107.37 | 106.27 |
| 5 | 180.73 | 179.36 |
| 6 | 272.52 | 267.36 |
| 7 | 372.94 | 375.08 |
| 8 | 500.24 | 498.34 |

**Table V. 6 :** Natural Frequencies (Hz) obtained by experimental analysis for experiment 1 and 3 respectively before applying the damage (heat flow) in both cases correspond to intact beam.

First, the variation of the frequencies in time is tracked using RDT applied at the top of the beam. Thanks to this new equipment, we observe figure V.16 and Tab. V.7 that the variation of the first frequencies (1 to 3) are lesser than for experiments E1 and E2.

We also observe a clear decrease of the modal frequencies during the heating phase, related to the loss of the stiffness, and the amount of lost being strongly related with the exposure duration (FR of about 4% for mode 2 for example). After this phase, we observe the same recovery time whatever the modes.

The damage localization was performed using the ULS methods. The perturbation theory method developed before was not considered here since this method is less efficient for strong and long period changes, affecting the shape of the mode, as suggested in the previous paragraph and in Chap. IV. For ULS method, the frequencies and mode shapes were computed using the 29 accelerometers thanks to the FDD methods presented before.

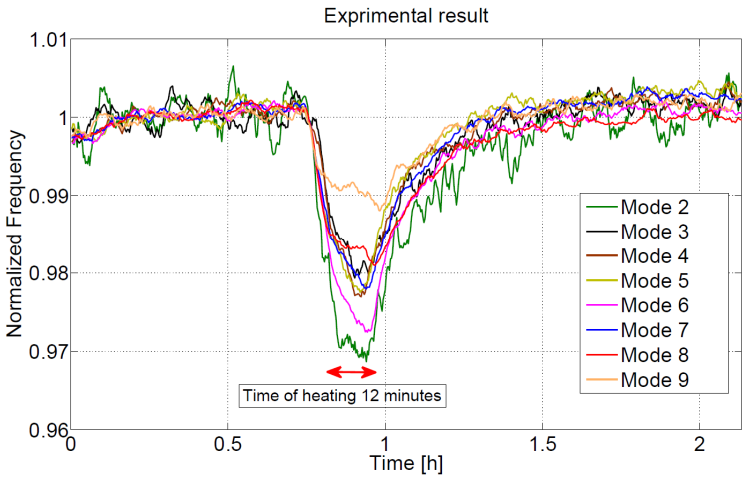


**Figure V. 16 :** Time variation of the normalized frequencies of modes 2 to 9 computed by RDT using sensor located at the top of the beam (free condition) for experience E3. The heat flow was applied for 12 minutes at *x=40.5 cm*.

| Modes # | 1 | 2 | 3 | 4 | 5 | 6 | 7 | 8 | 9 |
|---|---|---|---|---|---|---|---|---|---|
| CV (%) | 0.5838 | 0.2351 | 0.1507 | 0.1254 | 0.1423 | 0.1324 | 0.1230 | 0.1193 | 0.0920 |

**Table V. 7 :** Variation coefficient (CV %) of the frequency value of the first 9 modes obtained using the RDT and considering the first part of the experience (unchanged beam condition before heating).

For the first parts of the experiment (undamaged state), the ambient vibrations windows of 2000 seconds signal was divided into 48 windows of 41.6 seconds for computing the mode shapes. For the second part of the experiment, 400 seconds of recording were considered, that allows a better estimate of the mode shapes compared to the fast and small variation used for experiments E1 and E2. By increasing the length of heating, the available signal corresponding to the damage state improves the accuracy of the mode shapes assessment for this phase.

In order to have equivalent condition as for in-situ experiment, only the first 5 modes are considered here. Figures V.17 and V.18 show the singular values of the power spectral density (PSD) matrix using FDD method and the mode shapes of the damaged and undamaged states.

We observe clearly the effect of the heating on the frequencies, the shift value being related to the position of the damage versus the mode considered. Using frequencies and mode shapes variations, Table V.8 gives the FR parameters related to the frequency shift and the MAC value related to the variation of the shape of the modes.

As already mentioned, this change is directly related with a loss of stiffness (EI) of the beam. These results confirm that the variation of frequency ratio (FR in table V.8) is very sensitive to detect the change and presence of damage on the beam. Looking at the result of the frequency ratio given Tab. V.8, it is very clearly that modes 1, 2 and 5 are the most sensitive to damage, because of the position of the damage location (at *x=40.5 cm*) located to antinodes of these modes.

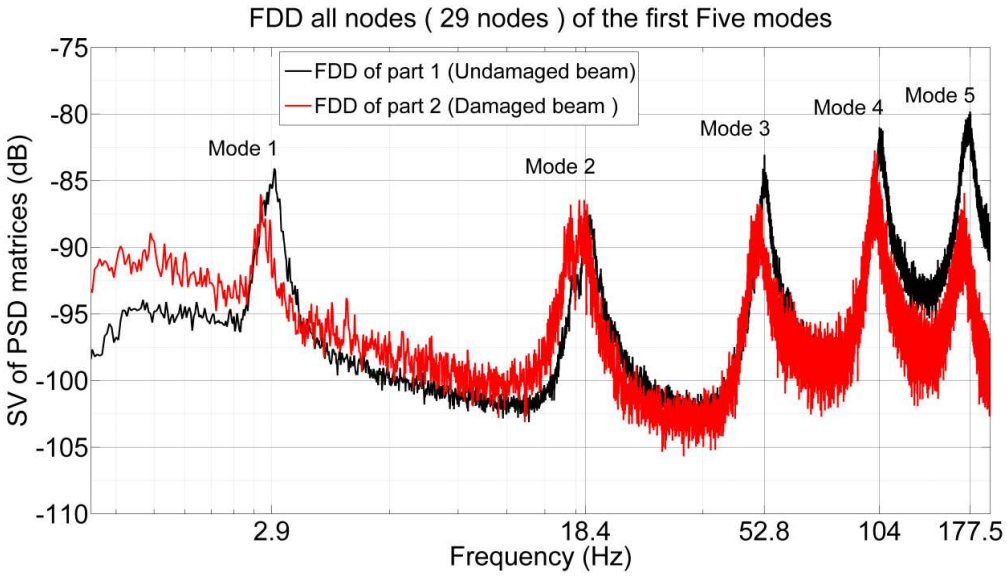


**Figure V. 17 :** Singular values of the PSD matrix of the recordings provided by the 29 accelerometers along the height of the beam computed through the FDD methods.

| Modes | Freq. undam. [Hz] | Freq. dam. [Hz] | Frequency ratio (FR) [%] | MAC-Value |
|---|---|---|---|---|
| *1* | 2.945 | 2.716 | 7.783 | 0.9713 |
| *2* | 18.478 | 17.761 | 3.880 | 0.9130 |
| *3* | 52.872 | 51.544 | 2.511 | 0.9811 |
| *4* | 104.034 | 102.544 | 1.432 | 0.8968 |
| *5* | 177.521 | 171.646 | 3.309 | 0.9579 |

**Table V. 8 :** Natural frequencies of undamaged and damaged beam for the first five modes. Frequency ratio (FR) calculated by Eq. III.7 and Modal Assurance Criterion (MAC) calculated by Eq. II.30.

Mode 4 is the least sensitive compared to other modes, which means the node of this mode is very close to the position of the damage location (*x=40.5 cm*) . This observation on mode 4 is very similar to and confirmed by the modal and numerical analysis performed in Chap III and IV.

Knowing frequencies and mode shapes, the ULS method (Equation II.39) was applied considering the two states (before and after heating). With experimental data, the choice of ULS is the best to identify and locate the damage among other non-destructive methods (NDE), as shown previously on modeling and numerical simulation (chapter III and IV).

Since the accuracy of the first mode is quite low, especially at the bottom of the beam where the damage was localized (Fig. V.18), mode 1 is not accounted for localization of the damage by ULS method.

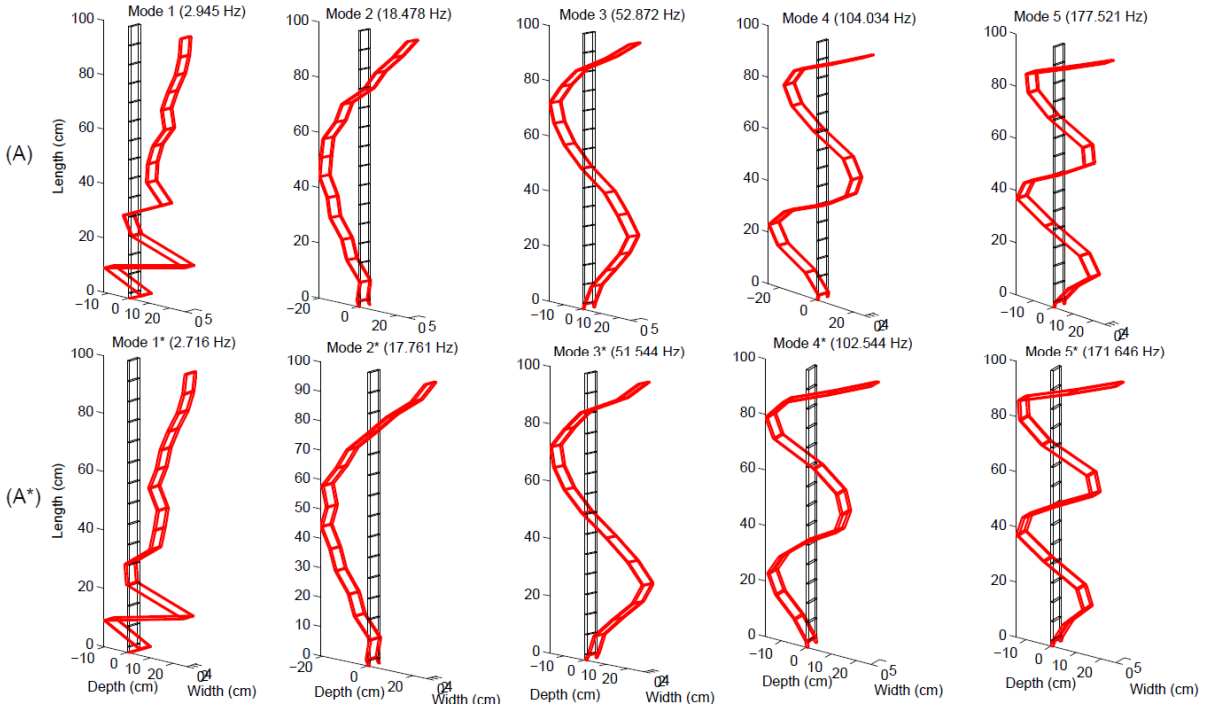


**Figure V. 18 :** First five mode shapes of the beam extracted from ambient vibrations recorded using the 29 accelerometers, corresponding to the undamaged (A) and damaged (A*) states of the experiment E3.

Figure V.19 summarizes the performance of ULS method applied to the beam, considering modes 2 to 5 separately, but also all together.

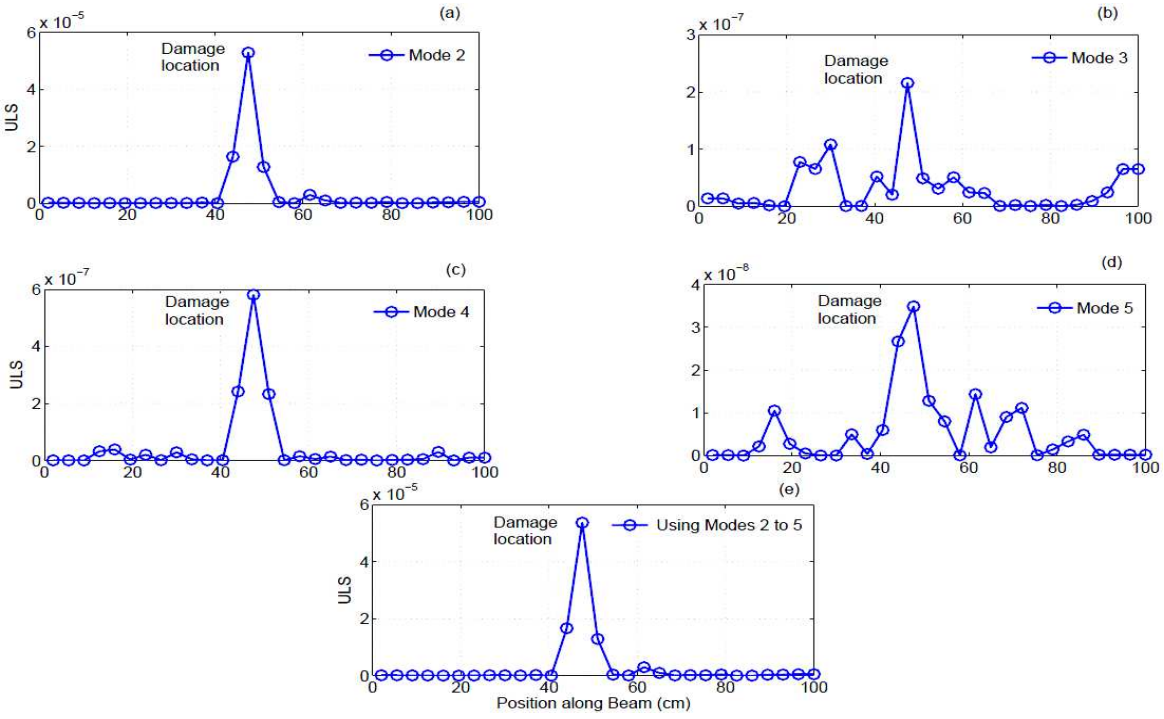


**Figure V. 19 :** Summary of the performance of the ULS methods to locate the damage at the bottom of the beam (*x=40.5 cm*) using modes and frequencies extracted by FDD from the experiment E3. (a) Mode 2; (b) Mode 3; (c) Mode 4; (d) Mode 5; (e) Modes 2 to 5.

Few modes were used in order to keep our work close to real case, where few number of mode shapes can be detected using ambient vibrations.

We observe a very good estimate of the localization of the damage proposed in the bottom of beam at $x = 40.5\ cm$, the efficiency of the mode considered separately depending on the position of the damage with respect to the position of the node and antinode.

By taking into account the largest number of modes as possible, the detection of huge amount of damage can be easily obtained. Nevertheless, we have to keep in mind that this test was performed only for bending beam model. For shear beam, the position of the damage may have different influence on the estimate.

## V.5 – Conclusions

In this study, experiments in the laboratory were performed for confirming on the results provided by the numerical analysis conducted in Chap. III and IV. Damaged and undamaged beams were tested in order to detect and localize damage with Random Decrement Technique (RDT), perturbation theory and ULS method.

The experimental setup consisted of locally heating a continuous Plexiglas beam, at three positions (A, B and C, experience E1) with the same duration of exposure (30 seconds), at one position (A, experience E2) with different duration of exposure, and finally, at one **position** ($x = 40.5\ cm$) with a longer duration of heating (about 12 minutes).

During all the experiments, the beam was forced into vibration by an equivalent white noise, produced by a continuous air jet applied at the top of beam. Modal analysis was then performed using the ambient vibrations recorded along the beam to detect and localize the damage.

We can confirm RDT is a very efficient and robust method for detecting the variations of the frequency values. RDT offers the precision required for controlling the integrity of the structures, allowing the detection of changes of less than 1%, with a low variation coefficient.

This method requires only one sensor located at the top of the beam and the amount of the damage can be related to the value of the frequency shift.

We observe the same average trend, i.e. a nonlinear increase of frequency ratio normalized with the damage severity of heating (heat flow) obtained by experimental data and modeling given in the previous chapters (III and IV).

After stopping the heating, we observe time of recovery of the initial frequencies, this process observed and tracked by RDT. On the three experiments performed in the laboratory, we have seen that the increment rate ($\beta$) corresponding to the recovery of the elastic properties of the

beam after the changes are quite different, depending on the position of the damage versus the mode.

These results are not enough for concluding at this time and further experiment must be planned for improving the physical observation.

ULS method applied for the damage localization is not efficient for small and local variations of elastic properties, compared to the perturbation theory. In the first case, the mode shapes are not affected enough by the changes for being used in the localization process and in the second case, the frequencies are so sensitive to changes that they are enough for improving the localization.

Some improvements must be done in the experimental analysis, such as the quality of the excitation in order to have a better assessment of the first mode that could be crucial for removing the ambiguity of the real and ghost positions. However, the perturbation theory requires a large number of modes that is not always possible for real buildings.

For the last experiment, ULS method was so efficient, even without considering the first mode, and using only the 5 first modes as in a real case. The localization is good enough and this observation confirms the results given in Chap IV with numerical approach.

Since we need a good estimate of the modes shapes and the frequencies with ambient vibrations, this method is not efficient for fast and short changes but it could be very robust for comparing two states: before and after an earthquake for example, by having tested the building before the extreme event and by testing the building for taking a decision concerning the integrity of the building and then its safety.

# Conclusion générale et perspectives

Les développements scientifiques décrits dans ce mémoire s'inscrivent dans le contexte du suivi de l'état de santé des structures (SHM) pour l'application au génie civil par l'analyse des mesures vibratoires afin de détecter, localiser et quantifier l'endommagement.

La détection de l'endommagement est un problème majeur dans le cadre de la surveillance des structures. Ce processus mène en général à des changements de la réponse dynamique de la structure étudiée, et bien souvent à des modifications des paramètres modaux de la structure tels que les fréquences propres, les coefficients d'amortissement et les déformées modales.

En premier lieu, une étude bibliographique sur l'importance de la surveillance de santé des structures, et sur les méthodes non-destructives d'évaluation (NDE) globales et locales avec leurs applications numériques et expérimentales a été réalisée dans les deux premiers chapitres (I et II).

Dans le deuxième, notre intérêt a essentiellement porté sur la détection de changement de façon expérimentale suite à des dommages sismiques. Des méthodes globales et locales de NDE basées sur la variation de fréquences ou sur les déformées modales ou sur les deux en même temps ont été appliquées à nos études avec les trois approches proposées dans ce manuscrit : modélisation, simulation et enfin en condition réelle qui a été testée au laboratoire (poutre en plexiglas).

Le chapitre III présente une étude détaillée par modélisation éléments finis de l'efficacité des méthodes de localisation et d'endommagement appliquée à une poutre encastrée-libre. La modélisation en dynamique linéaire fournit une estimation précise des fréquences propres et des déformées modales à la fois pour une poutre intacte et endommagée. Cet endommagement est local, il consiste en une réduction locale du module d'Young.

Les méthodes globales de NDE tels que la variation de fréquence et le MAC (Modal Assurance Criterion) basées respectivement sur la variation de fréquence et sur la forme des modes, pour une poutre intacte (saine) et endommagée, montrent que la détection de l'endommagement a été identifiée avec une bonne précision. Nous avons remarqué que lorsque la sévérité de l'endommagement augmente progressivement on observe une augmentation non linéaire de la variation des fréquences et une diminution non linéaire des valeurs du MAC.

Une autre observation indique que, suivant la position de l'endommagement appliqué à la poutre (aux deux extrémités ou au milieu) chaque mode de vibration ne réagit pas de la même façon. Quand la position de l'endommagement est à coté d'un nœud d'un mode, on trouve une faible variation de fréquence pour ce mode (exemple du mode 4 pour une poutre encastrée-libre). A l'inverse, une forte variation est produite si la position est au niveau d'un ventre d'un mode (exemple du mode 3) (voir la figure III.2).

Pour conclure ces deux méthodes globales sont très sensibles à l'endommagement mais de façon non-linéaire et dépendent de la position de l'endommagement.

Des méthodes locales de NDE, telles que MSC, MSCS, CIF et ULS, ont également été testées dans ce travail en utilisant les paramètres extraits d'un modèle aux éléments finis. Les variations des fréquences et des déformées modales avant et après l'endommagement sont obtenues par les simulations numériques.

La Figure III.24 résume l'efficacité et la sensibilité de ces quatre indicateurs proposés dans cette étude par rapport à différentes configurations incluant la position (du bas vers le haut), l'extension (étroite, large et multiple) et l'amplitude de l'endommagement. Là encore, suivant les modes utilisés, l'efficacité des méthodes varie, en fonction de la position de l'endommagement.

Les résultats confirment que la méthode (ULS) est la plus fiable et la plus robuste pour localiser l'endommagement quelle que soit la configuration de dommage, avec le moins d'erreur possible par rapport aux autres méthodes. Nous notons également que, pour une bonne estimation aveugle des dommages (quantification et localisation) avec peu de modes de vibration, au moins les trois premiers modes de vibration doivent être pris en compte, ce qui est le cas de la plupart des expériences de terrain effectuées sur des ponts et des bâtiments.

Pour l'amélioration de l'évaluation et la précision de l'amplitude des dégâts, nous avons utilisé les cinq premiers modes. On remarque certains inconvénients par exemple l'amplitude détectée des dégâts est très faible lorsque l'endommagement est localisé aux deux extrémités fixe et libre de la poutre. Cela dépend fortement du modèle de poutre analysé, le cas cisaillement devant présenter un comportement différent.

Le chapitre IV a été consacré à la simulation numérique par éléments finis (analyse temporelle) de conditions expérimentales, c'est-à-dire en excitant la structure à l'aide de vibrations ambiantes et en évaluant les paramètres modaux sur les enregistrements le long de la poutre. Nous avons utilisé une fonction aléatoire qui génère des vibrations ambiantes (bruit blanc de faibles amplitudes).

Ces vibrations ont été appliquées à la base de la poutre pour tester l'efficacité de plusieurs outils de traitement du signal et des méthodes non-destructives (NDE) sous excitation temporelle. Les résultats montrent la faisabilité et les performances des méthodes de traitement du signal telles que la technique du décrément aléatoire (RDT), et la méthode de FDD (Frequency Domain Decomposition), pour suivre l'intégrité des structures, dans le cas d'un faible ou d'un important endommagement. Ces deux méthodes révèlent et indiquent la présence de l'endommagement appliqué à la poutre, ce qui implique que la variation de fréquence est très sensible à l'endommagement même avec l'existence de bruit.

La détection de l'endommagement à partir de ces deux critères globaux, i.e. le rapport de fréquence (FR) et le Modal Assurance Criterion (MAC), aboutit à des résultats qui confirment de nouveau leur efficacité pour détecter les changements. Les résultats de localisation par la méthode locale (ULS) utilisant les paramètres modaux (pseudo-expérimentaux) extraits par le FDD sur les signaux simulés sur le long de la poutre, montre une très bonne corrélation (voir la figure IV.19c) avec ceux obtenus par la modélisation (chapitre III).

Évidemment, la localisation en utilisant la méthode ULS à partir des résultats issus de l'analyse modale est plus précise (la valeur de la corrélation est proche de 1) que ceux issus de l'analyse temporelle.

Les petites différences de l'emplacement de l'endommagement sont dues au bruit simulé par l'analyse numérique et / ou aux erreurs d'évaluation des formes modales à partir de la méthode FDD.

La théorie des perturbations qui est basée sur l'évolution de la fréquence pour chaque mode de vibration en fonction du temps via les données détectées par le RDT à partir d'un seul capteur, a été testée dans une configuration qui est équivalente à celle d'une condition expérimentale.

Cette méthode est efficace pour localiser l'endommagement surtout pour un petit changement de l'ordre de 0.1 % sur la première fréquence fondamentale.

Le chapitre V a porté essentiellement sur un volet expérimental. L'objectif de l'application expérimentale a été de tester au laboratoire les conclusions obtenues par modélisation. Au cours de toutes les expériences réalisées au laboratoire, la poutre a été excitée par des vibrations (bruit blanc) de faibles amplitudes.

Ces vibrations produites par une soufflette d'air en continu est appliquée à la partie supérieure (libre) de la poutre. L'analyse modale est ensuite effectuée en utilisant les vibrations ambiantes enregistrées le long de la poutre pour identifier et extraire les fréquences et les déformées modales par la méthode FDD. Ensuite la méthode de localisation (ULS) est appliquée. Le suivi de l'évolution des fréquences est obtenu par RDT et la méthode basée sur la théorie des perturbations est appliquée.

D'après les résultats expérimentaux pour les trois expériences réalisés (E1, E2 et E3), nous pouvons confirmer que la RDT est une technique très efficace pour suivre en continu et détecter l'intégrité de la poutre (SHM) à partir des signaux enregistrés par un seul capteur situé en partie supérieure de la poutre.

Cette technique montre qu'il est possible de détecter des petits changements de fréquence (moins de 1%) avec un coefficient de variation (CV) très faible. Ces changements sont dus à un flux de chaleur appliqué à différentes positions sur la poutre. En augmentant progressivement la sévérité de l'endommagement, nous avons observé les mêmes tendances que celles obtenues par la modélisation et la simulation numérique dans les chapitres précédents (III et IV) à savoir un comportement non linéaire entre la réponse fréquentielle et l'amplitude du dommage.

Après l'arrêt du flux de chaleur, les fréquences modales reviennent à l'état initial et un processus de relaxation en fonction du temps est observé et bien suivi par la RDT. Nous avons remarqué aussi que le coefficient ( $\beta$ ) qui correspond au taux de relaxation pour chaque mode n'est pas le même, ce qui signifie que suivant la position de l'endommagement tous les modes ne réagissent pas de la même façon.

Dans les deux premières expériences (E1 et E2), la méthode ULS n'est pas efficace pour localiser l'endommagement par rapport à la théorie des perturbations pour deux raisons :

-Premièrement, les déformées modales ne sont pas affectées par des changements assez bien marqués ; en effet, le temps d'exposition du flux de chaleur appliqué à la poutre est court et ne modifie que très faiblement le comportement de la structure.

-Deuxièmement, bien que les fréquences soient très sensibles aux changements, le temps pour obtenir ces modes de façon précise est supérieur au temps imposé dans les manipulations.

La méthode des perturbations fonctionne bien car elle est basée sur les fréquences qui sont sensibles à de très faibles changements de structure et que l'on peut les évaluer sur de temps d'enregistrement très courts. Cependant, elle nécessite un grand nombre de modes pour la localisation, ce qui n'est pas toujours disponible sur les bâtiments réels.

Pour la dernière expérience (E3), la méthode ULS est efficace pour localiser l'endommagement appliqué à la poutre. La localisation de l'endommagement avec la méthode ULS est assez bonne, et cette observation confirme les résultats présentés dans le chapitre IV par la simulation numérique. Par contre, puisque les modes ont été perturbés, la méthode des perturbations est moins efficace.

# Perspectives

Les résultats obtenus au cours de ce travail de thèse concernant le suivi de l'intégrité de structure (Détection, localisation et quantification de l'endommagement) sur la poutre par la modélisation numérique et l'application expérimentale, ont montré l'intérêt de suivre en temps réel les changements fréquentiels au cours du temps et de localiser l'endommagement.

En perspectives, nous pouvons proposer les extensions suivantes de ce travail :

- Amélioration de la qualité de l'excitation sur l'approche expérimentale pour avoir une bonne évaluation de la forme du premier mode fondamental : le plus énergétique, qui pourrait être crucial pour localiser l'endommagement avec une bonne estimation des dégâts.

- Entailler la poutre et suivre sa réponse vibratoire par la technique RDT en fonction du niveau d'excitation (faible, linéaire et fort) appliqué à la poutre d'une manière continue pour voir l'effet de l'ouverture et la fermeture des fissures au cours du temps. Il serait également intéressant de tester la localisation avec la méthode ULS.

- Tester différents types des matériaux (acier, aluminium, matériaux composite) sous l'effet thermique ou de chargement (ajout de petite masse sans abimer la poutre), pour voir leurs comportements mécaniques après l'endommagement, et de comparer avec le phénomène de relaxation que nous avons observé sur le plexiglas, pour conclure si cette observation est liée aux processus physique ou peut être à une autre condition externe (sollicitation,… etc.).

- Valider et examiner la méthode locale ULS sur un vrai bâtiment ou un pont en condition in-situ, avant et après un événement sismique comme un tremblement de terre par exemple, pour pouvoir évaluer l'intégrité de structure et prendre des mesures de sécurité pour la protection des personnes.

# Bibliographie

Abdel Wahab, M. and De Roeck, G. "Damage detection in bridges using modal curvatures: application to a real damage scenario," *Journal of Sound and Vibration* (226:2), 1999, pp. 217-235.

Aktan, A. E., Farhey, D. N., Helmicki, A. J., Brown, D. L., Hunt, V. J., Lee, K. and Levi, A. "Structural identification for condition assessment: experimental arts," *Journal of Structural Engineering* (123:12), 1997, pp. 1674-1684.

Alampalli, S. "Influence of in-service environment on modal parameters" 'PROCEEDINGS-SPIE THE INTERNATIONAL SOCIETY FOR OPTICAL ENGINEERING', SPIE INTERNATIONAL SOCIETY FOR OPTICAL, 1998, pp. 111-116.

Alampalli, S., Fu, G. and Dillon, E. W. "On the use of measured vibration for detecting bridge damage" (7) 'Transportation Research Board Conference Proceedings', 1995.

Allemang, R. J. and Brown, D. L. "A correlation coefficient for modal vector analysis "Proceedings of the 1st international modal analysis conference", SEM, Orlando, 1982, pp. 110-116.

Alvandi, A. "Contribution a l'utilisation pratique de l'évaluation dynamique pour la détection d'endommagements dans les ponts", 2003.

Askegaard, V. and Mossing, P. "Long term observation of RC-bridge using changes in natural frequency," *Nordic concrete research* (:7), 1988, pp. 20-27.

Asmussen, J., Brincker, R. and Ibrahim, S. "Statistical theory of the vector random decrement technique," *Journal of sound and vibration* (226:2), 1999, pp. 329-344.

Asmussen, J. C. "Modal analysis based on the random decrement technique: application to civil engineering structures", 1997.

Baillet L., Gueguen P., Roux P. "Structural damage localization and monitoring through perturbation theory, " submitted to *Structural Control and Health Monitoring* , 2013.

Balageas, D., Fritzen, C. and Güemes, A. "Structural health monitoring," (493), 2006.

Bathe, K. *Finite Element Procedures in Engineering Analysis*, Prentice-Hall, Englewood Cliffs, NJ, 1982.

Bathe, K. *Finite element procedures*, Vol. 2, Prentice hall Englewood Cliffs, NJ, 1996.

Biswas, M., Pandey, A. and Samman, M. "Diagnostic experimental spectral/modal analysis of a highway bridge," *The International Journal of Analytical and Experimental Modal Analysis* (5:1), 1990, pp. 33-42.

Boutin, C., Hans, S., Erdin, I. and Loriot, M. "Approche de la vulnérabilité sismique par l'étude du comportement de bâtiments réels," *Rapport de recherche ENTPE, Lyon*, 1999.

Brincker, R., Ventura, C. and Andersen, P. "Why output-only modal testing is a desirable tool for a wide range of practical applications" 'Proc. Of the International Modal Analysis Conference (IMAC) XXI, paper', 2003.

Brincker, R., Zhang, L. and Andersen, P. "Modal identification of output-only systems using frequency domain decomposition," *Smart materials and structures* (10:3), 2001, pp. 441.

Carder, D. S. "Observed vibrations of buildings," *Bulletin of the Seismological Society of America* (26:3), 1936, pp. 245-277.

Celebi, M. "Comparison of damping in buildings under low-amplitude and strong motions," *Journal of wind engineering and industrial aerodynamics* (59:2), 1996, pp. 309-323.

Celebi, M., Phan, L. and Marshall, R. "Dynamic characteristics of five tall buildings during strong and low-amplitude motions," *The structural design of tall buildings* (2:1), 1993, pp. 1-15.

Chance, J., Tomlinson, G. and Worden, K. "A simplified approach to the numerical and experimental modelling of the dynamics of a cracked beam" 'PROCEEDINGS-SPIE THE INTERNATIONAL SOCIETY FOR OPTICAL ENGINEERING', SPIE INTERNATIONAL SOCIETY FOR OPTICAL, 1994, pp. 778-778.

Chang, F. "Structural Health Monitoring 2011: Condition-Based Maintenance and Intelligent Structures," , 2011.

Chang, F., Markmiller, J. F., Ihn, J. and Cheng, K. Y. "A potential link from damage diagnostics to health prognostics of composites through built-in sensors," *Journal of vibration and acoustics* (129:6), 2007, pp. 718-729.

Chase, S. "The role of smart structures in managing an aging highway infrastructure"'Keynote Presentation, SPIE Conference on Health Monitoring of Highway Transportation Infrastructure', 2001.

Chatelain, J., Gueguen, P., Guillier, B., Frechet, J., Bondoux, F., Sarrault, J., Sulpice, P. and Neuville, J. "CityShark: A user-friendly instrument dedicated to ambient noise (microtremor) recording for site and building response studies," *Seismological Research Letters* (71:6), 2000, pp. 698-703.

Chatelain, J., Guillier, B., Guéguen, P., Fréchet, J. and Sarrault, J. "Ambient Vibration Recording for Single-Station, Array and Building Studies Made Simple: CityShark II," *International Journal of Geosciences* (3:6), 2012, pp. 1168-1175.

Chopra, A. K. *Dynamics of Structures (Theory and Applications to Earthquake Engineering) Prentice Hall*, 1995.

Chopra, A. K. and Naeim, F. "Dynamics of structures—theory and applications to earthquake engineering," *Earthquake Spectra* (23), 2007, pp. 491.

Clinton, J. F., Bradford, S. C., Heaton, T. H. and Favela, J. "The observed wander of the natural frequencies in a structure," *Bulletin of the Seismological Society of America* (96:1), 2006, pp. 237-257.

Clough, R. W. and Penzien, J. *Dynamics of structures. 1993*, McGraw-Hill, New York, 1993.

Cochran, E. S., Lawrence, J. F., Christensen, C. and Jakka, R. S. "The quake-catcher network: Citizen science expanding seismic horizons," *Seismological Research Letters* (80:1), 2009, pp. 26-30.

Cole Jr, H. A. "On-line failure detection and damping measurement of aerospace structures by random decrement signatures," (NASA), 1973.

Cole Jr, H. A. "Failure detection of a space shuttle wing flutter model by random decrement," (NASA), 1971.

Cornwell, P., Doebling, S. W. and Farrar, C. R. "Application of the strain energy damage detection method to plate-like structures," *Journal of Sound and Vibration* (224:2), 1999, pp. 359-374.

Creed, S. "Assessment of large engineering structures using data collected during in-service loading," *Structural Assessment: The Use of Full and Large Scale Testing*, 1988, pp. 55-62.

Cremona, C. "Surveillance de santé structurale, la démarche du projet s3,", 2009.

Deraemaeker, A., Reynders, E., De Roeck, G. and Kullaa, J. "Vibration-based structural health monitoring using output-only measurements under changing environment," *Mechanical Systems and Signal Processing* (22:1), 2008, pp. 34-56.

Doebling, S. W. "Damage detection and model refinement using elemental stiffness perturbations with constrained connectivity", Technical report, Los Alamos National Lab., NM (United States), 1996.

Doebling, S. W. and Farrar, C. R. "Statistical damage identification techniques applied to the I-40 bridge over the Rio Grande River" 'Society for Experimental Mechanics, Inc, 16 th International Modal Analysis Conference.', 1998, pp. 1717-1724.

Doebling, S. W., Farrar, C. R. and Prime, M. B. "A summary review of vibration-based damage identification methods," *Shock and Vibration Digest* (30:2), 1998, pp. 91-105.

Doebling, S. W., Farrar, C. R., Prime, M. B. and Shevitz, D. W. "Damage identification and health monitoring of structural and mechanical systems from changes in their vibration characteristics: a literature review", Technical report, Los Alamos National Lab., NM (United States), 1996.

Dunand, F. "Pertinence du bruit de fond sismique pour la caractérisation dynamique et l'aide au diagnostic sismique des structures de génie civil" , 2005.

Dunand, F., Ait Meziane, Y., Guéguen, P., Chatelain, J., Guillier, B., Ben Salem, R., Hadid, M., Hellel, M., Kiboua, A., Laouami, N. and others "Utilisation du bruit de fond pour l'analyse des dommages des batiments de Boumerdes suite au séisme du 21 mai 2003," *Mémoires du Service Géologique de l'Algérie* (12), 2004, pp. 177-191.

Dunand, F., Guegen, P., Bard, P., Rodgers, J. and Celebi, M. "Comparison of the dynamic parameters extracted from weak, moderate and strong motion recorded in buildings" 'PROC (CD) First European Conference on Earthquake Engineering and seismology, Geneva, Switzerland', 2006, pp. 3-8.

Ewins, D. *Modal testing: theory and practice, 1985*, Research Studies Press LTD.

Ewins, D. J. *Modal testing: theory, practice and application*, Vol. 2, Research studies press Baldock, 2000.

Fan, W. and Qiao, P. "Vibration-based damage identification methods: a review and comparative study," *Structural Health Monitoring* (10:1), 2011, pp. 83-111.

Farrar, C. R. and Doebling, S. "Damage detection II: field applications to large structures," *Modal Analysis and Testing, JMM Silva and NMM Maia, edts., Nato Science Series, Kluwer Academic Publishers, Dordrecht, Netherlands*, 1999.

Farrar, C. R., Doebling, S. W., Cornwell, P. J. and Straser, E. G. "Variability of modal parameters measured on the Alamosa Canyon Bridge" 'PROCEEDINGS-SPIE THE INTERNATIONAL SOCIETY FOR OPTICAL ENGINEERING', SPIE INTERNATIONAL SOCIETY FOR OPTICAL, 1997, pp. 257-263.

Farrar, C. R., Doebling, S. W. and Nix, D. A. "Vibration-based structural damage identification," *Philosophical Transactions of the Royal Society of London. Series A: Mathematical, Physical and Engineering Sciences* (359:1778), 2001, pp. 131-149.

Farrar, C. R. and Worden, K. "An introduction to structural health monitoring," *Philosophical Transactions of the Royal Society A: Mathematical, Physical and Engineering Sciences* (365:1851), 2007, pp. 303-315.

Farsi, M. N. "Identification des structures de Génie Civil a partir de leurs réponses vibratoires et vulnérabilité du bâti existant" , 1996.

Fox, C. "The location of defects in structures-A comparison of the use of natural frequency and mode shape data"'10th International Modal Analysis Conference', 1992, pp. 522-528.

Friswell, M. I. "Damage identification using inverse methods," *Philosophical Transactions of the Royal Society A: Mathematical, Physical and Engineering Sciences* (365:1851), 2007, pp. 393-410.

Fu, Z. and He, J. *Modal analysis*, Butterworth-Heinemann, 2001.

Fujino, Y., Abe, M., Shibuya, H., Yanagihara, M., Sato, M., Nakamura, S. and Sakamoto, Y. "Forced and ambient vibration tests and vibration monitoring of Hakucho suspension bridge," *Transportation Research Record: Journal of the Transportation Research Board* (1696:-1), 2000, pp. 57-63.

Fujino, Y. and Yoshida, Y. "Wind-induced vibration and control of Trans-Tokyo Bay crossing bridge," *Journal of Structural Engineering* (128:8), 2002, pp. 1012-1025.

Genest, M., Martinez, M., Mrad, N., Renaud, G. and Fahr, A. "Pulsed thermography for non-destructive evaluation and damage growth monitoring of bonded repairs," *Composite Structures* (88:1), 2009, pp. 112-120.

Gentile, C., Gallino, N., Lourenço, P., Oliveira, D. and Portela, A. "Ambient vibration-based investigation of the" Victory" arch bridge"'Proc, 5th Int. Conference on Arch Bridges (ARCH'07)', 2007, pp. 63-70.

Giurgiutiu, V. *Structural health monitoring with piezoelectric wafer active sensors*, Academic Press, 2008.

Gueguen, P. "Experimental analysis of the seismic response of one base-isolation building according to different levels of shaking: example of the Martinique earthquake (2007/11/29) Mw 7.3," *Bulletin of Earthquake Engineering*, 2012, pp. 1-14.

Gul, M. and Catbas, F. N. "Damage assessment with ambient vibration data using a novel time series analysis methodology," *Journal of Structural Engineering* (137:12), 2010, pp. 1518-1526.

Guo, T., Li, A. and Wang, H. "Influence of ambient temperature on the fatigue damage of welded bridge decks," *International Journal of Fatigue* (30:6), 2008, pp. 1092-1102.

Hamey, C. S., Lestari, W., Qiao, P. and Song, G. "Experimental damage identification of carbon/epoxy composite beams using curvature mode shapes," *Structural Health Monitoring* (3:4), 2004, pp. 333-353.

Hemez, F. M. and Doebling, S. W. "Review and assessment of model updating for non-linear, transient dynamics," *Mechanical Systems and Signal Processing* (15:1), 2001, pp. 45-74.

Ho, Y. and Ewins, D. "On the structural damage identification with mode shapes" 'Proceedings of the European COST F3 conference on system identification and structural health monitoring', 2000, pp. 677-686.

Hua, X., Ni, Y., Ko, J. and Wong, K. "Modeling of temperature--frequency correlation using combined principal component analysis and support vector regression technique," *Journal of Computing in Civil Engineering* (21:2), 2007, pp. 122-135.

Huang, N. "Introduction to Hilbert-Huang transform and some recent developments," *Hilbert-Huang Transform in Engineering. Taylor & Francis, Boca Raton*, 2005, pp. 1-24.

Huang, N. E. and Attoh-Okine, N. O. *The Hilbert-Huang transform in engineering*, CRC, 2005.

Humar, J. "Dynamics of Structures" , Prentice Hall, *Englewood Cliffs, NJ*, 1990.

Humar, J., Bagchi, A. and Xu, H. "Performance of vibration-based techniques for the identification of structural damage," *Structural Health Monitoring* (5:3), 2006, pp. 215-241.

Ibrahim, S. "Random Decrement Technique for Modal Identification of Structures," *Journal of Spacecraft and Rockets* (14), 1977, pp. 696.

Inman, D. J., Farrar, C. R., Junior, V. L. and Junior, V. S. *Damage prognosis for aerospace, civil and mechanical systems*, Wiley, 2005.

Ivanovic, S., Trifunac, M., Novikova, E., Gladkov, A. and Todorovska, M. "Ambient vibration tests of a seven-story reinforced concrete building in Van Nuys, California, damaged by the 1994 Northridge earthquake," *Soil Dynamics and Earthquake Engineering* (19:6), 2000, pp. 391- 411.

Jeary, A. "Damping in structures," *Journal of wind engineering and industrial aerodynamics* (72), 1997, pp. 345-355.

Juang, J. and Pappa, R. "An Eigensystem Realization Algorithm (ERA) for modal parameter identification and model reduction,", 1985.

Just-Agosto, F., Shafiq, B. and Serrano, D. "Development of a damage detection scheme applicable to sandwich composites," *Journal of Sandwich Structures and Materials* (9:4), 2007, pp. 343-363.

Kim, J., Song, H. and Kuperman, W. "Adaptive time-reversal mirror," *The Journal of the Acoustical Society of America* (109), 2001, pp. 1817.

Kim, J. and Stubbs, N. "Crack detection in beam-type structures using frequency data," *Journal of Sound and Vibration* (259:1), 2003, pp. 145-160.

Kohler, M. D., Davis, P. M. and Safak, E. "Earthquake and ambient vibration monitoring of the steel-frame UCLA Factor building," *Earthquake Spectra* (21:3), 2005, pp. 715-736.

Lestari, W., Qiao, P. and Hanagud, S. "Curvature mode shape-based damage assessment of carbon/epoxy composite beams," *Journal of intelligent material systems and structures* (18:3), 2007, pp. 189-208.

Li, H., Li, S., Ou, J. and Li, H. "Modal identification of bridges under varying environmental conditions: temperature and wind effects," *Structural Control and Health Monitoring* (17:5), 2010, pp. 495-512.

Maeck, J., Abdel Wahab, M., Peeters, B., De Roeck, G., De Visscher, J., De Wilde, W., Ndambi, J. and Vantomme, J. "Damage identification in reinforced concrete structures by dynamic stiffness determination," *Engineering structures* (22:10), 2000, pp. 1339-1349.

Magalhães, F., Caetano, E. and Cunha, Á. "Challenges in the application of stochastic modal identification methods to a cable-stayed bridge," *Journal of Bridge Engineering* (12:6), 2007, pp. 746-754.

Maia, N., Silva, J., Almas, E. and Sampaio, R. "Damage detection in structures: from mode shape to frequency response function methods," *Mechanical Systems and Signal Processing* (17:3), 2003, pp. 489-498.

Mazurek, D. F. "Modal sensitivity to damage in multigirder bridges" 'PROCEEDINGS-SPIE THE INTERNATIONAL SOCIETY FOR OPTICAL ENGINEERING', SPIE INTERNATIONAL SOCIETY FOR OPTICAL, 1997, pp. 1892-1898.

Mazurek, D. F. and DeWolf, J. T. "Experimental study of bridge monitoring technique," *Journal of Structural Engineering* (116:9), 1990, pp. 2532-2549.

Meola, C., Carlomagno, G. M. and Giorleo, L. "The use of infrared thermography for materials characterization," *Journal of materials processing Technology* (155), 2004, pp. 1132-1137.

Messina, A., Williams, E. and Contursi, T. "Structural damage detection by a sensitivity and statistical-based method," *Journal of Sound and Vibration* (216:5), 1998, pp. 791-808.

Michel, C. and Gueguen, P. "Time-frequency analysis of small Frequency variations in civil engineering structures under weak and strong motions using a reassignment method," *Structural health monitoring* (9:2), 2010, pp. 159-171.

Michel, C., Gueguen, P. and Causse, M. "Seismic vulnerability assessment to slight damage based on experimental modal parameters," *Earthquake Engineering & Structural Dynamics* (41:1), 2011, pp. 81-98.

Michel, C., Guéguen, P. and Bard, P. "Dynamic parameters of structures extracted from ambient vibration measurements: An aid for the seismic vulnerability assessment of existing buildings in moderate seismic hazard regions," *Soil Dynamics and Earthquake Engineering* (28:8), 2008, pp. 593-604.

Michel, C., Guéguen, P., El Arem, S., Mazars, J. and Kotronis, P. "Full-scale dynamic response of an RC building under weak seismic motions using earthquake recordings, ambient vibrations and modelling," *Earthquake Engineering & Structural Dynamics* (39:4), 2010, pp. 419- 441.

Mikael, A., Gueguen, P., Bard, P., Roux, P. and Langlais, M. "The Analysis of Long-Term Frequency and Damping Wandering in Buildings Using the Random Decrement Technique," *Bulletin of the Seismological Society of America* (103:1), 2013, pp. 236-246.

Moradalizadeh, M. "Evaluation of crack defects in framed structures using resonant frequency techniques" , 1990.

Morassi, A. "Identification of a crack in a rod based on changes in a pair of natural frequencies," *Journal of Sound and Vibration* (242:4), 2001, pp. 577-596.

Morassi, A. "Crack-induced changes in eigenparameters of beam structures," *Journal of Engineering Mechanics* (119:9), 1993, pp. 1798-1803.

Nayeri, R. D., Masri, S. F., Ghanem, R. G. and Nigbor, R. L. "A novel approach for the structural identification and monitoring of a full-scale 17-story building based on ambient vibration measurements," *Smart Materials and Structures* (17:2), 2008, pp. 025006.

Ndambi, J., Vantomme, J. and Harri, K. "Damage assessment in reinforced concrete beams using eigenfrequencies and mode shape derivatives," *Engineering Structures* (24:4), 2002, pp. 501-515.

Newmark, N. M. "A method of computation for structural dynamics" (3) 'Proc. ASCE', 1959, pp. 67-94.

Palacz, M. and Krawczuk, M. "Vibration parameters for damage detection in structures," *Journal of Sound and Vibration* (249:5), 2002, pp. 999-1010.

Pandey, A. and Biswas, M. "Damage diagnosis of truss structures by estimation of flexibility change," *Modal Analysis-the International Journal of Analytical and Experimental Modal Analysis* (10:2), 1995, pp. 104-117.

Pandey, A. and Biswas, M. "Damage detection in structures using changes in flexibility," *Journal of sound and vibration* (169:1), 1994, pp. 3-17.

Pandey, A., Biswas, M. and Samman, M. "Damage detection from changes in curvature mode shapes," *Journal of sound and vibration* (145:2), 1991, pp. 321-332.

Park, K., Reich, G. W. and Alvin, K. "Structural damage detection using localized flexibilities," *Journal of intelligent material systems and structures* (9:11), 1998, pp. 911-919.

Parloo, E., Guillaume, P. and Van Overmeire, M. "Damage assessment using mode shape sensitivities," *Mechanical systems and signal Processing* (17:3), 2003, pp. 499-518.

Peeters, B. and De Roeck, G. "One-year monitoring of the Z 24-Bridge: environmental effects versus damage events," *Earthquake engineering & structural dynamics* (30:2), 2001, pp. 149-171.

Peeters, B. and De Roeck, G. "Stochastic subspace system identification of a steel transmitter mast" 'Society for Experimental Mechanics, Inc, 16 th International Modal Analysis Conference.', 1998, pp. 130-136.

Peeters, B. and Ventura, C. "Comparative study of modal analysis techniques for bridge dynamic characteristics," *Mechanical Systems and Signal Processing* (17:5), 2003, pp. 965-988.

Perrault, M. "Évaluation de la vulnérabilité sismique de bâtiments à partir de mesures in situ" , 2013.

Raghavendrachar, M. and Aktan, A. E. "Flexibility by multireference impact testing for bridge diagnostics," *Journal of Structural Engineering* (118:8), 1992, pp. 2186-2203.

Ratcliffe, C. P. "A frequency and curvature based experimental method for locating damage in structures," *Journal of vibration and acoustics* (122:3), 2000, pp. 324-329.

Ratcliffe, C. P. "Damage detection using a modified Laplacian operator on mode shape data," *Journal of Sound and Vibration* (204:3), 1997, pp. 505-517.

Risitano, A., Giacomo, R. and Clienti, C. "Fatigue limit by thermal analysis of specimen surface in mono axial traction test" 'EPJ Web of Conferences', EDP Sciences, 2010.

Roach, D. P. and Neidigk, S. "Does the Maturity of Structural Health Monitoring Technology Match User Readiness?.", Technical report, International Workshop on Structural Health Monitoring 2011, 2011.

Rytter, A. "Vibrational based inspection of civil engineering structures", 1993.

Salane, H. and Baldwin Jr, J. "Identification of modal properties of bridges," *Journal of Structural Engineering* (116:7), 1990, pp. 2008-2021.

Salawu, O. and Williams, C. "Review of full-scale dynamic testing of bridge structures," *Engineering Structures* (17:2), 1995, pp. 113-121.

Salawu, O. and Williams, C. "Damage location using vibration mode shapes" 'Society of Photo-Optical Instrumentation Engineers (SPIE) Conference Series', 1994, pp. 933.

Salawu, O. S. and Williams, C. "Bridge assessment using forced-vibration testing," *Journal of structural engineering* (121:2), 1995, pp. 161-173.

Sohn, H., Farrar, C. R., Hemez, F. M., Shunk, D. D., Stinemates, D. W., Nadler, B. R. and Czarnecki, J. J. "A review of structural health monitoring literature: 1996-2001", Los Alamos National Laboratory Los Alamos,, New Mexico, 2003.

Structural Vibration Solution, "ARTeMIS Extractor Pro, release 3.43", Denmark, 2004.

Srinivasan, M. and Kot, C. "Effect of damage on the modal parameters of a cylindrical shell", Technical report, Argonne National Lab., IL (United States), 1992.

Stubbs, N., Kim, J. and Topole, K. "An efficient and robust algorithm for damage localization in offshore platforms" 'Proc. ASCE Tenth Structures Congress', 1992.

Surendra, P. S., Popovics, J. S., Subramaniam, K. V. and Aldea, C. "New directions in concrete health monitoring technology," *Journal of engineering mechanics* (126:7), 2000, pp. 754-760.

Tarantola, A. *Inverse problem theory: Methods for data fitting and model parameter estimation*, Elsevier, 1987.

Todorovska, M. I. and Al Rjoub, Y. "Effects of rainfall on soil--structure system frequency: examples based on poroelasticity and a comparison with full-scale measurements," *Soil Dynamics and Earthquake Engineering* (26:6), 2006, pp. 708-717.

Todorovska, M. I. and Trifunac, M. D. "Earthquake damage detection in the Imperial County Services Building I: The data and time-frequency analysis," *Soil Dynamics and Earthquake Engineering* (27:6), 2007, pp. 564-576.

Toksoy, T. and Aktan, A. "Bridge-condition assessment by modal flexibility," *Experimental Mechanics* (34:3), 1994, pp. 271-278.

Trifunac, M., Ivanovic, S. and Todorovska, M. "Apparent periods of a building. I: Fourier analysis," *Journal of Structural Engineering* (127:5), 2001, pp. 517-526.

Turek, G. and Kuperman, W. "Applications of matched-field processing to structural vibration problems," *The Journal of the Acoustical Society of America* (101), 1997, pp. 1430.

Ulm, F. J., J. L. Clément, and P. Argoul. "Coefficient de comportement: approche chute de fréquence." *3e Colloque national de Génie Parasismique*. 1993.

Vandiver, J., Dunwoody, A., Campbell, R. and Cook, M. "A mathematical basis for the random decrement vibration signature analysis technique," *Journal of Mechanical Design* (104:4), 1982, pp. 307-313.

Ventura, C., Liam Finn, W., Lord, J. and Fujita, N. "Dynamic characteristics of a base isolated building from ambient vibration measurements and low level earthquake shaking," *Soil Dynamics and Earthquake Engineering* (23:4), 2003, pp. 313-322.

West, W. M. "Illustration of the use of modal assurance criterion to detect structural changes in an orbiter test specimen" 'International Modal Analysis Conference, 4 th, Los Angeles, CA, Proceedings.', 1986, pp. 1-6.

Williams, E. J. and Messina, A. "Applications of the multiple damage location assurance criterion," *Key Engineering Materials* (167), 1999, pp. 256-264.

Worden, K. and Dulieu-Barton, J. "An overview of intelligent fault detection in systems and structures," *Structural Health Monitoring* (3:1), 2004, pp. 85-98.

Worden, K., Manson, G. and Allman, D. "An experimental appraisal of the strain energy damage location method," *Key Engineering Materials* (204), 2001, pp. 35-46.

Wu, D. and Law, S. "Sensitivity of uniform load surface curvature for damage identification in plate structures," *Journal of vibration and acoustics* (127:1), 2005, pp. 84-92.

Wu, D. and Law, S. "Damage localization in plate structures from uniform load surface curvature," *Journal of Sound and Vibration* (276:1), 2004, pp. 227-244.

Wu, M., Chen, X. and Liu, R. "Highway crack monitoring system" 'Proc. SPIE Conf., San Diego, March', 2002.

Xu, G., Zhu, W. and Emory, B. "Experimental and numerical investigation of structural damage detection using changes in natural frequencies," *Journal of vibration and acoustics* (129:6), 2007, pp. 686-700.

Yang, J., Chen, J. and Dagalakis, N. "Damage detection in offshore structures by the random decrement technique," *Journal of energy resources technology* (106:1), 1984, pp. 38-42.

Zhang, Z. and Aktan, A. "The damage indices for the constructed facilities" 'PROCEEDINGS SPIE THE INTERNATIONAL SOCIETY FOR OPTICAL ENGINEERING', SPIE INTERNATIONAL SOCIETY FOR OPTICAL, 1995, pp. 1520-1520.